Fall 2014

A Computational Analysis Of The Aerodynamic And Aeromechanical Behavior Of The Purdue Multistage Compressor

David Monk
Purdue University

Graduate School Form 30
(Revised 08/14)

PURDUE UNIVERSITY
GRADUATE SCHOOL
Thesis/Dissertation Acceptance

This is to certify that the thesis/dissertation prepared

By David James Winchester Monk

Entitled
A COMPUTATIONAL ANALYSIS OF THE AERODYNAMIC AND AEROMECHANICAL BEHAVIOR OF THE PURDUE MULTISTAGE COMPRESSOR

For the degree of Master of Science in Mechanical Engineering

Is approved by the final examining committee:

Dr. Nicole Key

Dr. Jun Chen

Dr. Gregory Blaisdell

To the best of my knowledge and as understood by the student in the Thesis/Dissertation Agreement, Publication Delay, and Certification/Disclaimer (Graduate School Form 32), this thesis/dissertation adheres to the provisions of Purdue University's "Policy on Integrity in Research" and the use of copyrighted material.

Dr. Nicole Key

Approved by Major Professor(s): _____

Approved by: Dr. Ganesh Subbarayan 12/05/2014

Head of the Department Graduate Program Date

A COMPUTATIONAL ANALYSIS OF THE AERODYNAMIC AND AEROMECHANICAL BEHAVIOR OF THE PURDUE MULTISTAGE COMPRESSOR

A Thesis

Submitted to the Faculty

of

Purdue University

by

David James Winchester Monk

In Partial Fulfillment of the

Requirements for the Degree

of

Master of Science in Mechanical Engineering

December 2014

Purdue University

West Lafayette, Indiana

To my family of yesterday, today, and tomorrow.

ACKNOWLEDGMENTS

First and foremost I would like to thank my advisor, Dr. Nicole Key, for the opportunity to work in the Purdue Compressor Lab, and for her assistance and guidance during my two years here at Purdue University. Her support, expertise, and, at times, difficult questions forced me to stretch my capacity and broaden my understanding in the field of compressor research. In addition, I would like to thank Rolls-Royce for financial support in funding a portion of my graduate studies as well as allowing me access to computational tools and high-performance computing cluster. In particular I would like to thank Dr. Roy Fulayter for his endless support in the CFD modeling of compressor aeromechanics, Dr. Aaron King for bestowing his CFD expertise when I was just starting out in this field, and Moujin Zhang for technical support in generating complex CFD grids. I would also like to thank the GUIde 5 Consortium for their funding and support during a portion of my Master's Degree.

I would like to acknowledge my labmates, past and present, for their support and patience as I started out as a new grad student, as well as for the good times we had in the lab. Reid, Natalie, Lou, Nick, Patrick, Bill, Evan, Bryce, Matt, Jeanne, Nyansafo, Trey, and John. I am grateful for their advice and value our friendships.

Most importantly I thank my wife, Megan, for encouraging me to pursue my educational and career dreams. Her support during these two years, most especially during the hectic and stressful times, meant the world to me. I would have never been able to do this without her. I also thank my family for their love and support during my educational endeavors.

TABLE OF CONTENTS

Page

Page

LIST OF TABLES

LIST OF FIGURES

Figure Page

Figure Page

Figure Page

Figure Page

Figure Page

Figure Page

NOMENCLATURE

Symbol	Definition
1B	1st Bending mode
1T	1st Torsion mode
ADPAC	Advanced Ducted Propfan Analysis Code
AIP	aerodynamic interface plane
CFD	computational fluid dynamics
DCA	double circular arc
DNS	direct numerical simulation
EO	engine order
FEA	finite element analysis
FSI	fluid-structure interaction
FT	Fourier transform
HCF	high-cycle fatigue
HL	high loading condition
HPC	high pressure compressor
IBRs	integrally bladed rotors

Symbol	Definition
IGV	inlet guide vane
JACC	Joint Axial Compressor Code
LE	leading edge
LES	large-eddy simulation
ND	nodal diameter
NL	nominal loading condition
NSMS	non-intrusive stress measurement system
NUVS	non-uniform vane spacing
PE	peak efficiency loading condition
P_o	total pressure
P_s	static pressure
PS	pressure surface
R	rotor
RANS	Reynolds-averaged Navier-Stokes
R_c	pressure ratio
S	stator
SS	suction surface
TE	trailing edge
T_o	total temperature

Symbol	Definition
URANS	unsteady Reynold-averaged Navier-Stokes
W_c	corrected mass flow rate

Lowercase Symbol	Definition
$\dot{m}_c$	corrected mass flow
y^+	dimensionless wall distance

ABSTRACT

Monk, David James Winchester, M.S.M.E., Purdue University, December 2014. A Computational Analysis of the Aerodynamic and Aeromechanical Behavior of the Purdue Multistage Compressor. Major Professor: Nicole L. Key, School of Mechanical Engineering

Compressor design programs are becoming more reliant on computational tools to predict and optimize aerodynamic and aeromechanical behavior within a compressor. Recent trends in compressor development continue to push for more efficient, lighter weight, and higher performance machines. To meet these demands, designers must better understand the complex nature of the inherently unsteady flow physics inside of a compressor. As physical testing can be costly and time prohibitive, CFD and other computational tools have become the workhorse during design programs.

The objectives of this research were to investigate the aerodynamic and aeromechanical behavior of the Purdue multistage compressor, as well as analyze novel concepts for reducing rotor resonant responses in compressors. Advanced computational tools were utilized to allow an in-depth analysis of the flow physics and structural characteristics of the Purdue compressor, and complement to existing experimental datasets.

To analyze the aerodynamic behavior of the compressor a Rolls-Royce CFD code, developed specifically for multistage turbomachinery flows, was utilized. Steady-state computations were performed using the RANS solver on a single-passage mesh. Facility specific boundary conditions were applied to the model, increasing the model fidelity and overall accuracy of the predictions. Detailed investigations into the overall compressor performance, stage performance, and individual blade row performance were completed. Additionally,

separation patterns on stator vanes at different loading conditions were investigated by plotting pathlines near the stator suction surfaces. Stator cavity leakage flows were determined to influence the size and extent of stator hub separations.

In addition to the aerodynamic analysis, a Rolls-Royce aeroelastic CFD solver was utilized to predict the forced response behavior of Rotor 2, operating at the 1T mode crossing of the Campbell Diagram. This computational tool couples aerodynamic predictions with structural models to determine maximum Rotor 2 vibration amplitudes excited by both vortical and potential disturbances. A multi-bladerow, full-annulus unsteady simulation was performed to capture the aerodynamic forcing functions and understand the influence of bladerow interactions on these flow disturbances. The strength and frequency content of the S1 vortical field and S2 potential field were examined to quantify the aerodynamic forces exciting resonant vibrations. Detailed comparisons were made to experimental datasets acquired on the Purdue compressor which characterize the forced response behavior at the 1T mode crossing.

Lastly, stator asymmetry was examined as a means of reducing forced response vibration amplitudes. For this study, a new Stator 1 ring was designed with a reduced vane count, creating the ability to isolate the relative contribution of the S1 wakes on R2 vibrational amplitudes. A second Stator 1 ring was then designed with asymmetric vane spacing such that two stator half-sectors of different vane counts were joined together to form a full stator ring. By joining two stator half-sectors with different vane counts, the energy of the wakes is spread into additional frequencies, thereby reducing the overall amplitudes. The aeroelastic CFD solver was again used to perform steady-state and unsteady simulations, capturing the effect of the stator asymmetry on resonant vibrational amplitudes. The resulting blade deflection amplitudes are presented and discussed in detail.

CHAPTER 1: INTRODUCTION

1.1 Motivation

Each day across the world thousands of aircraft streak across the sky, driven by advanced gas turbine engines. A core feature gas turbine engine are compressors, which perform work on the incoming air to raise the total pressure, temperature, and enthalpy. Air flow through a compressor is inherently unsteady due to the relative motion of rotating blades and stationary vanes. This complex, three-dimensional flow has been the focus of aerodynamic and aeromechanic research for much of the past century. As our understanding of the flow physics inside compressors has increased, so to have compressor performance demands. Current compressor design trends have pushed for lighter, more efficient, and more powerful systems. This has led to more highly loaded stages with reduced axial gaps between blade rows; all of which lead to increased secondary flow effects and blade row interactions.

Vital to our continued progress in compressor design is understanding the effects of secondary flows and blade row interactions on compressor aerodynamics and aeromechanics. Increased loadings across blade rows create larger pressure gradients and therefore more influential secondary flows. Two examples of secondary flows are rotor tip clearance flows, and stator shroud cavity flows. The viscous nature of internal fluid flows also create complex flow features such as boundary layers on all viscous surfaces as well as viscous wakes propagating downstream from each blade or vane. As experimental campaigns are costly to conduct, designers

must rely primarily on computational fluid dynamics (CFD) to model the interaction of these complex flow features.

Additionally, the reduction of axial spacing between blade rows creates stronger forcing functions impinging on blade rows which can excite dangerous vibrations when the forcing occurs at or near resonance frequencies. Airfoils in turbomachines produce wakes, or vortical disturbances which propagate downstream of its trailing edge, as well as inviscid potential disturbances that propagate both upstream and downstream from the airfoil. Reduced axial spacing increases the strength of this aerodynamic forcing and increases the susceptibility of a compressor to large vibrations and high-cycle fatigue (HCF). Recent designs have also seen an increased number of integrally bladed rotors (IBRs) which are full blade rows machined out of a solid piece of metal. Stronger aerodynamic forcing functions, coupled with IBR design which have considerably less damping than traditional slotted-disks with individual blade inserts, have led to increased potential for dangerous vibrational responses in compressors.

As modern trends continue to push the envelope of compressor performance, designers must increasingly rely on computational models to accurately predict the complex flow physics. However, experimental data are still necessary to validate and improve such computational models. Comparisons of experimental and computational results help identify regions where computational improvements are needed. Therefore, detailed analysis of CFD and experimental measurements in compressors flow is vital to gain a more complete picture of compressor aerodynamics and aeromechanics.

1.2 Development of Three-Dimensional CFD for Turbomachinery

Engine demands for increased power and efficiency with reduced weight have driven compressor designs toward higher stage loading and reduced aspect ratio blading (Wisler, 1985).

Cumpsty (2004) suggests that the increasing cost and difficulty of conducting experimental studies on test rigs have resulted in fewer experiments being conducted before progressing to full engine tests. One of the primary difficulties in performing detailed experimental investigations is obtaining quality measurements in regions of interest. For example, understanding flow behavior within the passage between adjacent rotor blades is crucial to developing high efficiency designs, yet it is very difficult to measure aerodynamic properties within this region due to the high rotational speeds of the blades. For this reason, designers must rely more on computation tools to predict compressor performance throughout the design process.

Modern CFD solves the full 3-D Navier-Stokes equations in a computational domain representing as many geometric features as possible. Even with advancements in computing power and capability, computational tools still have difficulty accurately predicting the inherently unsteady and complex flow behavior in turbomachinery. Designers must understand the limitations of CFD and interpret results with a degree of caution (Denton, 2010). While it is possible for CFD to model and capture a large portion of geometric and flow features present in compressors, the computational cost of doing so increases which each additional feature. Engineers are constantly balancing the trade-off of higher accuracy models with the desired quick convergence time and low computational cost. Many advancements have been made to lessen the trade-off between these two requirements.

1.2.1 General Three-Dimensional CFD Methods for Turbomachinery

The relative motion between rotating blade rows (rotors) and stationary vane rows (stators) makes compressor flows difficult to model in a computational domain. One difficulty lies in passing fluid properties between stationary domains and rotating domains. Several techniques have been developed to accommodate the passing of such information, each with

unique advantages and disadvantages. Two methods for passing data between these relative blocks in steady-state simulations are the mixing plane approach and the average passage approach.

The most common method of passing flow properties between stationary and rotating frames is the implementation of mixing plane boundaries at the interface of each relative motion mesh block. Mixing planes are defined at fixed axial locations, typically midway between adjacent blade rows. In the mixing plane approach, non-uniform flow properties are assumed to "mix out" in the distance between the trailing edge of each blade row and the mixing plane, generating a pitch-wise uniform enthalpy and entropy (Denton, 2010). In essence, the mixing plane circumferentially averages flow properties at each radial level on the mesh, losing passage profiles while maintaining radial profiles for axisymmetric assumptions. This uniform flow at each radial level is then passed to the next blade row as uniform, steady flow. The circumferential averaging of flow properties allows mass, momentum, and energy to be conserved as data are passed between mesh blocks in relative motion. Because the mixing plane approach increases the mixing effect of the flow in a shorter distance, mixing losses are naturally increased and, therefore, an increase in entropy is also predicted. The weakness of the mixing plane approach is that because flow properties are assumed to mix out, non-uniform flow features such as viscous wakes and blade row interactions cannot be passed between mesh blocks in relative motion. Still, the mixing plane approach is commonly employed as it is easily implemented and robust in giving realistic results when compared to experimental data (Mansour, 2008).

The Average-Passage approach, developed by John Adamczyk (Adamczyk, 1985), uses an alternate method for passing data between rotating and stationary mesh blocks in steady Reynold-averaged Navier-Stokes (RANS) simulations. Instead of separating blade rows by mixing planes, the Average-Passage approach employs a technique where each blade row mesh block is extended upstream and downstream to overlap adjacent blade rows. The influence of

neighboring blade rows is incorporated by imposing body forces and deterministic stresses on overlapping mesh blocks which represent viscous wakes and potential interactions, allowing the realistic development of mixing to occur. This novel approach captures the effects of non-uniform flow perturbations as they occur in turbomachinery and has been successful in modeling both commercial and industrial compressor performance (Adamczyk, 1999).

1.2.2 Mesh Generation

Three-dimensional CFD codes solve the full Navier-Stokes equations at each node in a computation domain, or mesh. Therefore, the computational mesh is constrained around all relevant geometric features included in the model. Features such as annulus geometry, blade or vane geometry, secondary flow paths, and tip clearance gaps must be defined prior to generating a mesh. The decision of which geometric features to include in a model most often governs which type of mesh to generate. Two types of mesh are possible; namely structured and unstructured. Structured grids are comprised of hexahedral elements arranged in such a way that each node in the mesh can be defined by (i,j,k) node indices. Numerically speaking, structured grids generate simple connectivity arrays, which allow more efficient computations of higher-order derivatives, such as those found in flows dominated by viscous interactions. As a result, structured grids are almost universally used in endwall regions where boundary layer resolution is important. Structured grids are also somewhat limited to more simplistic geometries.

Unstructured grids allow for more complicated geometries, but the non-simple connectivity between nodes changes the way each node is defined. Unstructured mesh nodes cannot be defined by simple (i,j,k) indices, but rather replace indices with node numbers in a connectivity table. Both hexahedral and tetrahedral elements can be used in an unstructured format. Tetrahedral grids can often conform to complex geometries while allowing fewer nodes

than hexahedral grids. For these cases, tetrahedral unstructured meshes are commonly coupled with structured grids in the endwall region to reduce cell count while still resolving important boundary layer flows.

Mesh resolution is also a critical aspect of mesh generation, as it can significantly alter computational results. More finely resolved grids are likely to produce higher-fidelity results, but at the expense of computational time. Much effort is placed on finding the balance between adequate grid resolutions with economical run times.

1.2.3 Turbulence Modeling

One of the key factors in determining the necessary grid resolution in endwall regions is the selection of a turbulence model. Turbulence models are sets of assumption-based equations that close the Navier-Stokes equations. When deriving the 3-D Navier-Stokes equations for unsteady (fluctuating) fluid flow, the resulting equation, written in Cartesian tensor notation, appears as:

$$\rho\left[\frac{\partial U_i}{\partial t}+U_j\frac{\partial U_i}{\partial x_j}\right]=-\frac{\partial P}{\partial x_i}+\frac{\partial}{\partial x_j}\left[T_{ij}^{(v)}-\rho\left\langle u_i u_j\right\rangle\right]. \tag{1.1}$$

Capital letters represent mean or average values while lowercase letters represent fluctuating terms. The last two terms in the equation represent the stresses, T as a viscous stress and u_iu_j termed “Reynolds Stresses”. The difficulty with this equation is that the addition of the fluctuating velocities in the Reynold Stress term create more unknowns than equations, with no additional known relationships to close the equation. This is called the “turbulence closure problem”. Hence, turbulence models are introduced as a means of making certain assumptions to create additional turbulent relations to close the Navier-Stokes equations.

Many turbulence models exist, varying in complexity from simple algebraic turbulence relations to two-equation partial differential equations relating turbulent viscosities to assumed parameters. One of the more basic, but still very common, turbulence models used in turbomachinery simulations is the Baldwin-Lomax model (Baldwin and Lomax, 1978). This simple algebraic model was created and fine-tuned for boundary-layer flows in aeronautical applications. Because of this, the Baldwin-Lomax model performs very well in turbomachinery applications. Much has been written about the accuracy, computational stability, and overall success of the Baldwin-Lomax turbulence model in turbomachinery simulations (See Dawes, 1985; Adamczyk et al., 1990; and Rai, 1989). However, this turbulence model, as with most algebraic models, breaks down in the presence of large boundary layer separations. Common one-equation turbulence models include Spalart-Allmaras (Spalart and Allmaras, 1994) and Baldwin-Barth (Baldwin and Barth, 1990). Yet many more models exist which use 2 equations to close the Navier-Stokes equations, with countless modifications. In general, as the complexity of the turbulence model increases (algebraic, 1-eqn, 2-eqn), the number of assumptions decreases. Each successive level generates a more comprehensive description of the turbulence, removing qualitative deficiencies present in earlier models (Pope, 2000).

However, with each increase in complexity comes increased computational cost. Many of the 2-equation turbulence models require extremely refined grids in the boundary layer regions to yield the most accurate results, thus greatly increasing CFD run times. One way to avoid excessive grid resolution requirements in boundary layers is to impose “wall functions” on all viscous surfaces. Wall functions apply boundary conditions based on “law of the wall” relations at a specified distance away from the wall (Pope, 2000). Therefore, turbulence-model equations are not solved in this region where wall functions are imposed. The benefit of this is that the first computational grid point is located outside of the boundary layer’s viscous sublayer, and the turbulent profile within this sublayer is assumed to follow log-law or modified log-law relations.

The parameter $y+$ is a non-dimensional parameter used to describe the distance between a wall and the first grid point, and it is defined by the friction velocity u_τ, the distance to closest wall y, and the kinematic viscosity υ:

$$y^+ = \frac{u_\tau y}{\upsilon}. \tag{1.2}$$

Many turbulence models require a y+ value on the order of $y+\sim1$ to yield the most accurate results. Imposing wall functions on viscous surfaces allows the y+ value to be relaxed 1-2 orders of magnitude, or roughly $y+\sim20$-200, saving significant CPU time. As with most simplifying assumptions, physical fidelity is decreased. However, for many applications where near-wall turbulent boundary layer profiles are not critical to the solution, wall-functions can be a beneficial simplifying assumption.

1.2.4 Steady vs. Unsteady Simulations

The vast majority of computations performed on compressor flows utilize steady CFD where the solution is iteratively solved until all flow transients average out and a steady-state condition is reached. When transient analyses of compressor flows are desired, a time-dependent, or unsteady, simulation is required. Tucker (2011) outlines the available techniques for modeling transient flow physics. Linear Harmonic models, Unsteady Reynold-Averaged Navier-Stokes (URANS), Large-Eddy Simulation (LES), and Direct Numerical Simulation (DNS) are all unsteady CFD methods. Each successive method listed improves the model fidelity while significantly increasing computational cost. In fact, the CPU time required for most unsteady simulations is substantial enough that designers rarely utilize these methods in the design process.

Nevertheless, the simulation of many flow features require the use of unsteady CFD. For example, to study the effect of blade row interactions, it is necessary to capture the transient

propagation of wakes, shocks, or other non-uniformities as they convect through the compressor. Time-accurate URANS CFD was utilized to show that the axial spacing between a stator and a downstream transonic rotor significantly affects the stage loss. The computational results revealed that the bow shock from the downstream rotor interacts with the upstream stator to form larger shed vortices at closer axial spacing (Gorrell et al., 2005). Likewise, aeroelastic computations for forced response analyses require a transient analysis to capture the vibration-inducing unsteady blade loading caused by non-uniform wakes and potential fields.

1.3 Effect of Secondary Flows on Compressor Performance

Air flow through a compressor can be generically labeled into two categories; main gas path (primary) flow, and secondary flows. The main gas path flow is the bulk flow in the streamwise direction through the annulus of a compressor. The performance of a compressor is primarily governed by the controlled behavior of this bulk flow. Current understanding of the primary flow is substantial. This flow, for the most part, behaves in a way that is easily and accurately predicted by simple analytical techniques. The difficulty in modeling compressor flows lies in the prediction of secondary flows and their interaction with the main gas path. Secondary flows can be broadly described as minor streams or jets of fluid that flow in opposing directions or speeds to the primary flow. Although the behavior of the primary flow determines in large part the overall performance of the compressor, secondary flows have significant influence on aerodynamic behavior and are the primary causes of blockage and loss. Two of the most fundamental forms of secondary flow are shrouded stator cavity leakage flows and rotor tip clearance flows.

1.3.1 Stator Hub Cavity Flows

Leakage flows in compressors are inevitable due to mechanical restrictions in the design. Many compressor stators utilize shrouded hubs as a means of reducing vibrations. Figure 1.1 depicts a general shrouded stator configuration, showing the rotating wheel drum beneath the hub shroud. Mechanical considerations require a small clearance between the inner shroud surface and the rotating drum to avoid material rubs. Since stator vanes act as diffusers in that absolute velocity is reduced from leading edge to trailing edge, the static pressure at the outlet of the stator is greater than at the inlet. This pressure gradient drives a leakage flow from the exit of the stator row through the cavity where it re-enters the main gas path upstream of the stator leading edge. A labyrinth, or knife seal, also depicted in Figure 1.1, is placed under the hub shroud to reduce this leakage flow through the cavity. The interaction of this secondary flow as it re-enters the main gas path is a significant source of blockage and loss and alters the momentum and velocity fields. The low momentum cavity flows reduce the momentum of the primary flow in the hub region, creating flow blockage and increased incidence, leading to stator hub corner separations, and total pressure and efficiency losses (Wellborn, 1996). Additional CFD studies on a low speed multistage compressor concluded that for every 1% increase in seal tooth clearance-to-span ratio, there is a 1 point decrease in efficiency and 3% decrease in total pressure rise (Wellborn, 1999).

1.3.2 Tip Leakage Flows

Just as mechanical considerations require a clearance between the stator inner shroud surface and the rotating wheel drum, there must also exist a small clearance gap between the tip of rotor blades and the casing endwall. This clearance gap reduces the likelihood of blade rubs during engine operation. During engine operation, centrifugal forces lead to growth in blade

heights, while thermal expansion in both the rotor blade rows and the compressor casing affect the clearance size. The size of the clearance gap is determined by the minimum transient clearance needed to avoid a blade-rub while keeping steady-state performance losses to a minimum (Freeman, 1985).

The curvature of rotor blades create a higher static pressure on one side of the blade (pressure surface) and a lower static pressure on the other (suction surface). This pressure difference between the pressure surface and suction surface causes flow to spill over the tip gap. The leakage flow then mixes with the main passage flow, rolling into a vortex structure, Figure 1.2. This secondary flow vortex structure is a significant source of entropy and loss in compressors. Larger tip clearance gaps increase the leakage flow across the tip and thus increase the size of the resulting vortex structures. As a general rule, a 1% increase in tip clearance corresponds to a 1% decrease in compressor efficiency (Freeman, 1985). It is also reported that for a low-speed four-stage compressor, increasing the tip-clearance-to-span ratio from 1.6% to 3.4% reduced the peak pressure rise by 9.7% and the stall margin by 11% (Wisler, 1985).

It is, thus, seen that the stability of a compressor is influenced greatly by the formation and dynamics of the tip leakage vortex. At higher loading, the primary compressor mass flow is reduced while an increased pressure gradient between pressure and suction surfaces increases tip leakage flow. As a result, the leakage vortex develops with greater tangential momentum and less axial momentum. The trajectory of this vortex then becomes more circumferential than axial and becomes a major blockage source to incoming flow. Vo et al. (2008) suggested that when the clearance vortex trajectory becomes completely tangential and impinges on the adjacent blade leading edge, large separations occur and lead to the formation of rotating stall. Computational models suggest that as the leakage vortex gains strength and becomes more tangential in trajectory, the structure separates from the suction side of the blade and forms a “tornado-like”

vortex structure which propagates across the passage and leads to rotating stall (Pullan et al., 2012).

1.3.3 Computational Modeling of Secondary Flows

Since secondary flows have such critical effects on the performance and stability of compressors, computational models must be able to accurately predict these flows if designers are to improve the aerodynamic performance in these regions. Unfortunately for CFD, these regions are the most difficult to model. The interaction of secondary flows with main gas path flows, boundary layers, and viscous wakes creates a highly turbulent and complex flow regime. CFD codes must be able to capture these interactions to produce accurate predictions. The difficulty in modeling tip leakage flows is in obtaining sufficient grid resolution through the clearance gap to resolve the small length-scale flows formed in the leakage vortex. For this reason, many early tip leakage models used simple periodicity models in the tip region to avoid gridding the clearance (Chima, 1998). More recent models grid the clearance gap but with mixed results. Adamczyk et al. (1993) assumed the vena-contracta effect in modeling tip clearance flows on a transonic fan. This study found that computational results closely matched experimental measurements only when the clearance gap size was reduced in the CFD model. Because of the complex nature of the tip clearance vortex interactions, the accurate prediction of these flows is still a difficult task in compressor simulations.

Likewise, the modeling of stator hub cavity flows encounters similar difficulties. The cavity under shrouded stators is much larger than the gap above rotor tips and often doubles the mesh size if this region is included in the mesh. It is generally not feasible for designers to mesh this cavity region. Simplified stator cavity models are often used to simulate the effect of the leakage path flow without physically gridding the region. These models use parameters such as

wheel speed, cavity and seal geometry to calculate windage losses, discharge coefficients, and cavity static pressures to estimate the mass flow rate through the cavity and the flow properties at re-entry into the main gas path (see Wellborn et al., 2000; Tipton et al., 1986). The inclusion of cavity models improves CFD fidelity and almost always yields more realistic results. The additional CPU time added by including cavity models is only a fraction of the added CPU time in gridding the entire cavity geometry.

1.4 Compressor Forced Response

Complex aeroelastic phenomena commonly occur in turbomachines as a result of the inherently unsteady and turbulent flows which influence the dynamics of the blade rows upon which they act. This fluid-structure interaction is a critical concern in the design of compressors, with extensive effort and research given to the accurate prediction and measurement of these complex interactions. One class of aeroelastic phenomena is termed flutter and is brought about by self-excited aerodynamic instabilities. The second class is termed forced response and is excited by external forcing.

Recent trends in compressor blade design push for higher loaded blades with reduced axial spacing. These trends, although successful in maximizing power-to-weight ratio, elevate the potential for dangerous forced response conditions. An embedded rotor in a multistage compressor is forced externally by potential fields from both upstream and downstream vane rows, as well as vortical disturbances from upstream wakes, Figure 1.4. Although potential disturbances decay rapidly in space for lower Mach number flows, the close proximity of adjacent blade rows allow these unsteady features to contribute to the aerodynamic forcing. The main contributors to forced response are vortical disturbances, which most commonly are viscous wakes from upstream vane rows. Unlike potential disturbances, viscous wakes persist for several

blade rows. As the rotor rotates, it encounters the shed wakes at a frequency, or periodicity, dependent on the rotational speed. When this frequency coincides with a natural vibrational mode of the blade, vibrations occur and can lead to High Cycle Fatigue (HCF) failures. HCF occurs when blades endure cyclic stresses beyond the endurance limit of the material. The Campbell Diagram is a useful tool for engineers to use in predicting shaft speeds associated with dangerous engine vibrations. In this diagram, shaft speed is plotted on the abscissa with frequency on the ordinate, Figure 1.3. Engine order (EO) lines extend from the origin and correspond to all known excitations that could be produced, as a function of shaft speed. Natural mode frequencies of the blade are also plotted as a function of RPM. The intersection of EO lines with natural mode frequencies identifies shaft speeds corresponding to possible dangerous vibrational responses of the blade. While Campbell Diagrams are beneficial in identifying potentially dangerous operational speeds, they do not yield information on the aerodynamic forcing or vibrational response magnitudes associated with a specific resonant operating speed. To gather this data, experimental or computational tools must be utilized.

Forced response vibrations are often modeled as 2nd order harmonic oscillators using the traditional spring-mass damper equation, Eqn. 1-3, where m, c, and k are the mass, damping, and stiffness of the blades, respectively. Wakes, gusts, and potential fields from surrounding stator rows acts as periodic forcing functions in exciting the vibrations. These aerodynamic forcing functions can be lumped into a single periodic term, $Fe^{i\omega t}$.

$$m\ddot{x} + c\dot{x} + kx = Fe^{i\omega t} \tag{1.3}$$

1.4.1 Aerodynamic Forcing

Much research has been conducted to characterize the aerodynamic forcing which excites blade vibrations. Potential fields propagate as acoustic waves in both directions from stator vanes

and, thus, act as excitation sources on the rotor blade from both upstream and downstream. Although potential fields decay rapidly in time, the close proximity of adjacent blade rows in modern engines increases the strength of this forcing. Miller et al. (2003, Part 1) tested the strength of both upstream and downstream potential fields by isolating the forcing in a vane-rotor and also rotor-vane configuration. The potential fields from both upstream and downstream were found to create nearly equal unsteady pressure fluctuations on the embedded rotor blade surface. Murray, (2014, a) characterized the potential field strength from a downstream stator on the embedded rotor in a 3-stage axial compressor. The strength of the upstream propagating acoustic wave was such that changes in flow angle of up to 4° were measured at mid-gap between the rotor trailing edge and stator leading edge at a high loading condition, locally back-pressuring the rotor.

Vortical disturbances, or wakes shed from upstream vanes, provide the strongest forcing to blade rows. Unlike potential fields, viscous wakes persist for several bladerows (Chen and Eastland, 1990). Murray (2014, a) performed detailed measurements of an upstream stator wake and found that the deeper and wider wakes generated at a high loading condition increase the amplitude of the spectral analysis 1_{st} harmonic up to 300% when compared to a nominal loading condition.

1.4.2 Vibrational Response of Rotor Blades

The aerodynamic forcing on rotor blades by periodic disturbances excite vibrational responses when the frequency of such disturbances coincide with natural vibrational mode frequencies of the blade. The amplitude of the response is dependent upon the strength of the forcing function as well as the aerodynamic and mechanical damping of the rotor. Traditional rotor construction consists of a slotted disk to which individual blades are inserted via a “fir-tree”

groove. The surface contact area of the fir-tree design provides significant mechanical damping. In recent years, IBRs have gained popularity due to decreased manufacturing cost and time, lighter weight, and eliminated assembly complexities. However, the solid structure of IBRs virtually eliminates any mechanical damping and leave aerodynamic damping as the only source of vibrational damping.

Traditional forced response vibrational measurements utilize strain gages surface-mounted on the rotor blades. This measurement is trusted to yield accurate results, but it is often expensive and complex in nature as a slip ring is required to transfer the measurement signals taken in the rotating frame to stationary data acquisition systems. Richards (2012) employed strain gages on a high-speed centrifugal compressor in a vaneless diffuser to measure the vibrational response. A large response was measured for a 30/rev excitation, corresponding to 30 impeller blade wakes reflecting off downstream channels and impacting the impeller trailing edge.

Choi et al. (2008) used a non-intrusive stress measurement system (NSMS) tip timing system to measure the effects of clocking on the resonant vibration amplitudes of the embedded rotor in a multistage compressor. They found that at nominal loading conditions, the maximum blade deflection changed up to 80% between different clocking configurations. Clocking effects at high loading changed the maximum vibrational amplitudes 168%. Additionally, Murray (2014, b) was able to detect rotor vibrations from high frequency Kulite pressure sensors embedded in a downstream stator as the compressor RPM was swept through resonance. Vibrations in the rotor blades create unsteady acoustic waves that propagate downstream. The Kulite transducers embedded in the downstream stator were able to measure distinct fluctuations in the pressure signal as the compressor passed through resonance speeds, signifying an increased vibrational magnitude in the upstream rotor. This is an important find as such a measurement technique could be utilized as an on-board diagnostic tool used during engine operation.

1.4.3 Computational Modeling of Forced Response

Experimental testing of forced response is often a complex task. To effectively evaluate compressor designs, it is crucial that computational models be able to predict accurate aerodynamic forcing and resulting vibrational responses. The nature of such a simulation is complex as the CFD must capture the fluid-structure interaction (FSI) between the unsteady flow physics and structural rotor properties. The ability to accurately predict the vibrational response, or amplitude, of turbomachinery blades operating at resonant speeds is not yet a simple endeavor. One of the formidable challenges of numerically modeling aeroelasticity is that the analysis must accurately represent the interaction of disturbances between bladerows, as well as the coupling of aerodynamic and structural properties. Advancements in computational power have allowed aeroelastic codes to model many of these interactions. It takes significant engineering judgment to decide how many interactions, or bladerows, need to be included in a model to capture the primary aerodynamic forcing and obtain accurate results.

Vahdati et al. (2007) utilized an advanced numerical model to investigate the importance of the number of modeled bladerows on the forced response of an embedded rotor. One simulation was run with only an upstream vane row compared to a second simulation with 5 modeled bladerows. The computed response of the 2-blade-row simulation gave peak-to-peak deflections nearly twice the magnitude as the 5-blade-row simulation. This discrepancy was attributed, in part, to the 2-blade-row simulation lacking important harmonics present in the larger simulation. The interaction and relative phasing of the additional harmonics can have an important effect on the magnitude of the main passage harmonic. The 5-blade-row simulation predicted peak-to-peak deflections within a fraction of a millimeter of the measured rotor displacement. Sayma et al. (2003) modeled the forced response of 2 rotors in a 6-blade-row liftfan. For vane-pass excitations, the aeroelastic code matched very closely to measured

deflections. As a means of reducing lengthy aeroelastic computational times, one practice is to model only a three bladerow section, including the blade rows immediately upstream and downstream of the blade row of interest. Sound engineering judgment is necessary, however, to determine the extent to which reduced blade row models should be used. Some compressor geometries may necessitate the inclusion of additional rows if non-standard aerodynamic forcing functions are known or presumed to exist.

1.5 Research Objectives

The work presented herein focuses on computational modeling of the aerodynamic and aeromechanical properties of the Purdue 3-stage axial compressor. This work is unique in that rarely are such highly detailed experimental datasets available for direct comparison to CFD results run with detailed facility-specific boundary conditions. Previous experimental campaigns on the Purdue multistage compressor have compiled an extensive dataset characterizing both the aerodynamics and forced response. The initial research utilizes an industry-maintained steady CFD code to analyze the aerodynamics of the multistage compressor flow. Comparisons will be made to experimental measurements to understand the ability of the numerical model in predicting compressor aerodynamic performance. Specific comparisons will include overall performance, stage matching, radial profiles, blade and vane incidence, and flow separation patterns. Next, a proprietary aeroelastic CFD code is utilized to investigate aerodynamic forcing and the resultant vibrational response of the embedded blade row operating at resonant speed. CFD results will compare the strength of the vortical flows and potential fields exciting the vibrations in Rotor 2 (R2), as well as maximum blade deflections, to measured data.

Lastly, a new Stator 1 (S1) is designed with a reduced vane count from the current model. The reduced vane count changes the EO line on the Campbell diagram and thus increases the

shaft speed at which the vibrational mode of interest is excited. A variation to this reduced vane S1 design is also created in which the number of vanes is unequally distributed such that one half-annulus sector has a different vane count than the other half annulus sector. As no experimental data are taken as of yet for the new S1 designs, a computational study will investigate the predicted changes in aerodynamic forcing and vibrational response created by the introduction of the geometric asymmetry in Stator 1.

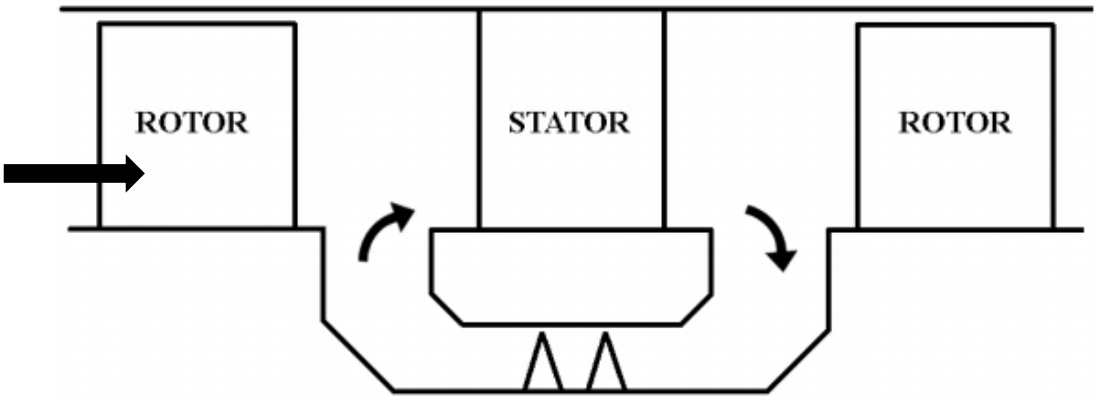

Figure 1.1: Generic shrouded stator hub cavity showing leakage flow direction.

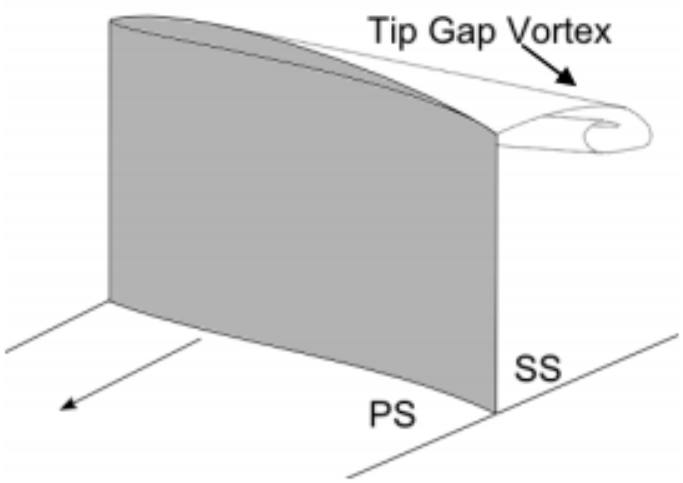

Figure 1.2: Tip clearance flows resulting in a leakage vortex.

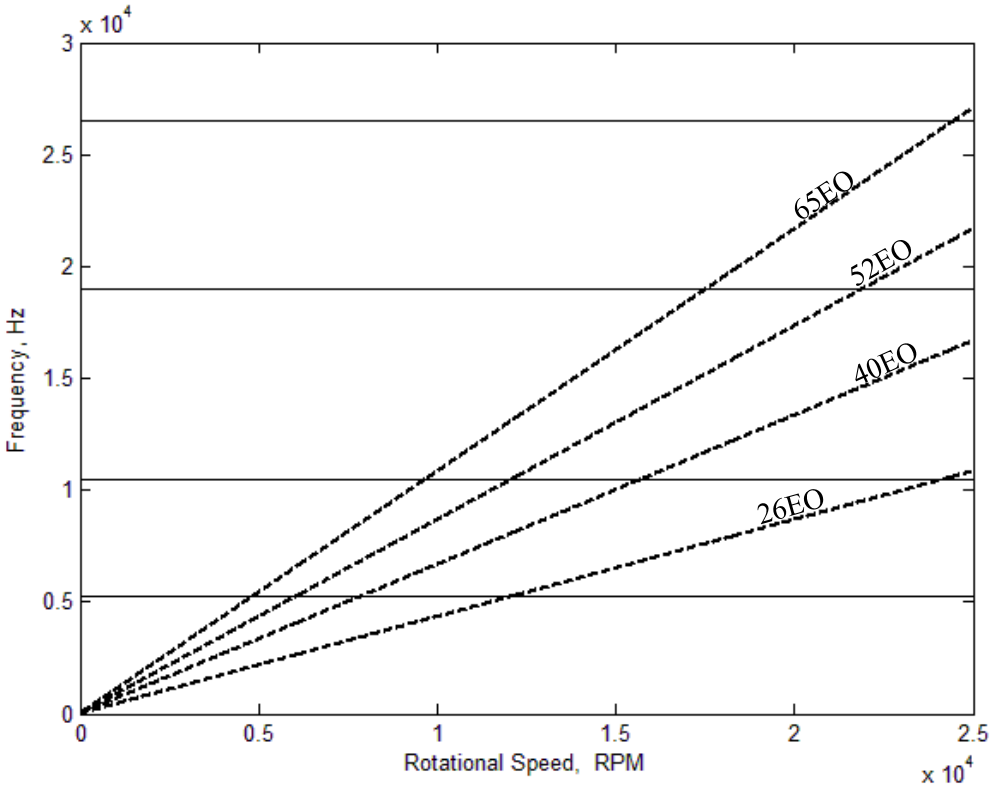

Figure 1.3: Campbell Diagram showing 4 EOs and 4 modes.

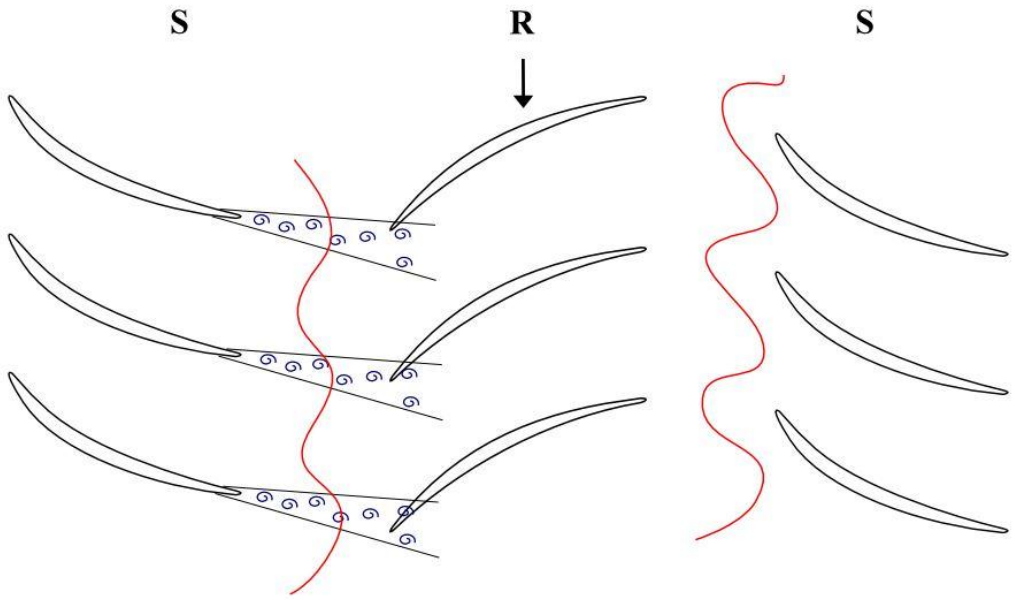

Figure 1.4: Sources of blade excitation including potential fields and vortical disturbances.

CHAPTER 2: COMPUTATIONAL MODEL OF PURDUE COMPRESSOR

2.1 Purdue 3-Stage Axial Research Compressor

The Purdue 3-stage research compressor is modeled after the rear stages of a Rolls-Royce high-pressure compressor (HPC). This geometry is a scaled-up model to allow for greater resolution in measurements, while still matching engine representative Mach and Reynolds numbers that exist in the rear stages of HPC's. This compressor features an inlet guide vane (IGV) followed by three stages. All rotor blade rows, plus the IGV vane row are comprised of double circular arc airfoil (DCA) profiles. Meanwhile, each of the three shrouded stators are designed with NACA 65-series airfoils. Blade and vane counts in the compressor are as follows: 44 vanes for the IGV, Stator 1 (S1), and Stator 2 (S2), while Stator 3 (S3) has 50 vanes. Rotor 1(R1), Rotor 2 (R2), and Rotor 3 (R3) each decrease by 3 blades and have 36, 33, and 30 blades, respectively. The compressor features hub and tip diameters of 20 inches and 24 inches, yielding a constant annulus height of 2 inches. Figure 2.1 shows a cross-section of the compressor. The compressor operates at a corrected design speed of 5000 rpm. Instrumentation ports are located at mid-gap – relative to the 50% span geometry, between all interstage blade rows, as well as at the IGV inlet, S3 exit, and aerodynamic interface plane (AIP) located 5 chord lengths upstream of the IGV leading edge. All vane rows can be circumferentially traversed past stationary instrumentation to allow for detailed flow measurements in the pitchwise direction. A complete description of the Purdue research compressor facility is given by Talalayev (2011).

2.2 Computational Setup for Steady Aerodynamic Performance Calculations

The computational code used to calculate the aerodynamic performance was a Rolls-Royce proprietary code called *JACC* (Joint Axial Compressor Code), a derivative of the former NASA code ADPAC (Advanced Ducted Propfan Analysis Code), and developed specifically for turbomachinery applications. *JACC* is a three-dimensional Reynolds-averaged Navier-Stokes (RANS) solver. Aerodynamic calculations are based on a four-stage Runge-Kutta time marching finite volume solution technique with added numerical dissipation (Hall et al., 1999). The Baldwin-Lomax algebraic turbulence model is the default choice and was used in all aerodynamic calculations. Mixing planes were placed at axial locations mid-gap between adjacent blade rows as a means of passing flow variables between mesh blocks in relative motion. These interfacial planes numerically "mix out" circumferential non-uniformities at each radial level, and the resulting flow properties are then interpolated onto the inlet mesh of the next mesh block as uniform flow at each radial level on the grid. Mixing planes conserve mass, momentum, and energy and are a stable and efficient means of transferring data between stationary and rotating mesh blocks.

The *JACC* solver allows the use of a multi-block mesh domain, where the grid system is subdivided into smaller grid blocks. The multi-block format allows the flow variables in each sub-block (density, pressure, temperature, and velocities) to be solved simultaneously. Shared interfaces between all sub-blocks communicate these flow variables with adjacent blocks, thereby ensuring conservation of mass, energy and momentum. Multi-block grid structures allow solutions to be computed in parallel, thereby allowing larger computations to be computed on multiple processors simultaneously in a quick and efficient manner.

JACC accelerates convergence by employing a multi-grid mesh scheme. Multi-grid should not be confused with multi-block mesh structures. Multi-grid convergence acceleration

refers to a numerical solution technique that solves the governing equations on multiple levels of grid coarseness. After a satisfactory grid is generated, the multi-grid conversion generates additional meshes where every other node is removed for each successively coarse mesh, Figure 2.2. *JACC* employs a 3-level multi-grid scheme by default. Multi-grid techniques accelerate convergence by damping out low frequency perturbations in the computational domain. In a discretized domain, high frequency errors - short length scale errors due to unconverged solutions, are eliminated quickly as they are averaged out by adjacent nodes. The solution domain is then left with low frequency (large length scale) errors which take much longer to propagate and average out. Low frequency errors on a fine grid become higher frequency errors on a coarse grid. Therefore, solving initially on a coarse grid and interpolating flow properties from coarse grids onto finer grids quickly eliminates low frequency errors and accelerates convergence. The recommended practice for starting simulations in *JACC* is to run 500 iterations on the full 3-level multi-grid mesh in order to get the flow field started and reduce low frequency errors. The finest grid is then used for the remainder of the iterations until convergence is reached.

2.2.1 Mesh Generation

Grids used in all *JACC* calculations were generated using proprietary Rolls-Royce tools, based on the mesh described by Mulac (1988). As the Purdue compressor consists of 7 blade rows, the mesh is divided into 7 mesh blocks, one for each blade row. The mesh generated using the Rolls-Royce tools is a single passage, multi-bladerow, structured, sheared-H mesh, Figure 2.3. Each mesh block consists of 53 radial points and 45 circumferential points. Each of the interstage mesh blocks consist of 93 axial nodes. Since the inlet and exit planes in the computational domain were both extended approximately one chord length upstream and downstream of the blading, the IGV and S3 blocks require additional axial points (105). In total, the multi-bladerow

mesh contains 1.7 million nodes, distributed among 7 mesh blocks. To obtain better resolution in viscous boundary layer regions, nodes are clustered tighter around the airfoil, the hub endwall, and the casing endwall, Figure 2.4. An important parameter in determining mesh quality is to compute y^+ values at all endwalls. Figure 2.5 shows the average y^+ values at all viscous surfaces in the computational domain. Y^+ values for near-blade mesh range from 10-15 while hub and casing endwall grids range from 15-25. Such near-wall grid resolution is not sufficient to fully resolve boundary layer development, but it is adequate for *JACC* prediction accuracy. The Purdue multistage compressor has fillets of 0.15 inches on all rotors and 0.09375 inches on all stators. These fillet sizes were included in the computational mesh, increasing model fidelity. To avoid fully gridding the region over the rotor tips, periodic boundaries are implemented, with 4 cells defining the gap between rotor tip and casing. Although no mesh sensitivity study was conducted to verify proper grid resolution, the grid produced is consistent with those typical of most Rolls-Royce compressors (King, 2013).

2.2.2 Boundary Conditions

Inlet boundary conditions used in the CFD calculations were based on detailed experimental total pressure and total temperature measurements taken at the AIP (station 0 in Figure 2.1). Since the AIP is located 5 chord lengths upstream of the IGV leading edge, and the inlet plane of the *JACC* calculations is defined 1 chord length upstream of the IGV leading edge, the experimentally measured inlet total pressure profile was modified for a thicker boundary layer such that the computational total pressure profile matched the measured profile at the IGV leading edge. The inlet plane of the computational domain could also have been moved back to match the distance of the AIP to produce similar results. The radial profiles used for the inlet

boundary conditions are shown in Figure 2.6. At the compressor exit a single static pressure was defined, which is adjusted to throttles the compressor to the desired loading conditions.

To capture the effects of shrouded stator cavity flows, this secondary flow must be accounted for in the numerical model. Generating a mesh in the cavity to directly resolve the leakage flow properties becomes computationally expensive and will often double the mesh size. Therefore, to avoid meshing the stator cavity region, a leakage model was used to estimate flow velocities and mass flow through the cavity. In the Purdue multistage compressor, Stator 1 and Stator 2 have leakage cavities beneath the hub shroud, Figure 2.7. The leakage path under the IGV shroud is sealed, preventing any flow, while leakage under Stator 3 is exhausted out the compressor through the bearing housing and measured in an orifice flow meter (this "bleed" flow was also included in numerical model). The leakage model used in the *JACC* simulations is a proprietary knife seal model developed by Rolls-Royce and similar to that described by Wellborn (2000). To incorporate this model into the existing mesh, patches were defined on the hub surface in the regions both upstream and downstream of S1 and S2. The added patch allows a new mass inflow and outflow boundary condition. The boundary conditions on the patch are the outputs from the knife seal leakage model. Inputs to the model include cavity geometry, knife seal height, and clearance. From these inputs, an integral over the surface area of the rotating and stationary surfaces is computed and multiplied by the respective radii from the rotational axis. This allows windage losses to be computed as well as the effect of the rotating and stationary surfaces on the secondary flow. Outputs from the knife seal model include temperatures, pressures, velocity components, and mass flow at the inlet and exit of the shroud cavity. These outputs are then applied as boundary conditions on the mesh patch surfaces.

2.2.3 Monitoring Convergence and Post-Processing Solutions

At each loading condition along the compressor characteristic, pressure ratio, efficiency, and mass inflow and outflow are monitored for convergence. When a steady-state is reached in each of these parameters, the solution is considered to be converged. Convergence for the Nominal Loading operating point on the compressor is shown in Figure 2.8. The simulations were throttled until the maximum stability point was reached, which is the maximum loading possible before *JACC* falls in to numerical stall. Figure 2.9 shows the full *JACC* characteristic for the compressor operating at the design speed of 5000 rpm.

Post-processing of the numerical data was accomplished using Rolls-Royce tools and scripts. All performance data presented in this work are area-averaged values to keep consistent with area-averaged experimental results. Steady 1-D performance results are area-averaged both circumferentially across a single passage as well as radially across the span. Radial profiles are area-averaged in the circumferential direction only. To reduce the influence of the mixing plane on the area-averaged flow properties, the post-processing extracts flow variables at a location of roughly 7 grid points away from the airfoil leading and trailing edge. Data are then processed further using Matlab and Tecplot scripts developed by the author.

2.3 Computational Setup for Unsteady Forced Response Calculations

The numerical code used for Rotor 2 forced response calculations is a proprietary code available to Rolls-Royce, and is similar to the codes described by Sayma et al. (2000) and Vahdati et al. (2007). This code is a time-accurate solver for 3-D steady and unsteady aerodynamics, aeroelasticity, and aeroacoustic computations. This code is routinely employed to investigate forced response, flutter, rotating stall, surge, and other flow instabilities in

turbomachinery. It is an implicit, nonlinear, unstructured, compressible flow solver which can simulate steady and unsteady solutions for single passage - single blade row problems, as well as multi passage - multi blade row geometries. In the unsteady state this code can be coupled with a forced response solver to capture the fluid-structure interaction. Dynamic mesh deformation and flexible disks are additional capabilities of the aeroelasticity solver that create realistic and accurate forced response prediction. The latter feature, flexible disks, allows for different disk nodal diameter excitations, based on the number of vanes upstream and downstream of the vibrating blade row. The capability of mesh deformation allows the blade surface mesh to deform after each iteration. During the setup process, mode shapes obtained from finite element analysis (FEA) are interpolated onto the computational blade mesh. After each successive iteration, unsteady pressures on the blade surface are converted to modal forces at each node and subsequently to blade deflection magnitudes. Each node on the computational blade mesh is then moved, with the magnitude of the movement dependent on the modal forces and specific mode shapes of the blade. This type of fully-coupled analysis is necessary for calculations on fan blades and low pressure compressor stages where blade heights and vibration amplitudes are large and significantly influence local aerodynamics. For core compressor blades where blade heights and vibration amplitudes are much smaller, the dynamic mesh feature can be omitted and blade vibration amplitudes computed in the post processing stages (Vahdati et al., 2002). In this "uncoupled" analysis, time-dependent modal forces are written to a file where they can be applied to the structural mesh during post-processing for blade vibration amplitudes. The uncoupled analysis is suitable for the current forced response investigation in the Purdue axial compressor.

Figure 2.10 shows the Campbell Diagram for Rotor 2 of the Purdue Compressor. The focus of the present research is to investigate R2 forced response at the 1st Torsional mode resonance conditions. Three different test cases will be run, each with a different S1 configuration. Rotor 2 and Stator 2 remain unchanged in all test cases. Case 1 will model the

current compressor geometry with 44 Stator 1 vanes. Case 2 will analyze forced response with a new S1 where the vane count is reduced to 38 equally spaced vanes. Lastly, Case 3 will modify the new 38-vane S1 configuration by distributing the 38 vanes unequally across the stator ring such that one 180° sector has 18 equally-spaced vanes and the other half-sector has 20 equally spaced vanes. Each of these modifications changes the EO excitation line on the R2 Campbell Diagram (see Figure 2.10) and, therefore, changes the compressor RPM at which the modal excitation occurs. Before the unsteady forced response computation can be initiated, a steady computation at resonant speeds must first be completed. Although the three cases to be studied each have unique aspects, the process by which the steady and unsteady computations are set up is equivalent and will be detailed in the following sections.

2.3.1 Steady Flow Computation at Resonance Speed

The initial step in preparing for the steady CFD computation is to generate the multi-bladerow, single passage mesh representing the Purdue 3-stage compressor. This was accomplished using Rolls-Royce in-house mesh generation software. A separate mesh is created for each blade row and the user has complete flexibility regarding the meshing parameters. The forced response solver is designed to run unstructured layers of mesh which are connected radially in a structured fashion. Typically, tetrahedral grids are chosen for the bulk of the mesh block, with a structured O-mesh wrapped around the airfoil. Due to the grid generation software's limitations in creating a full annulus tetrahedral mesh for the asymmetric S1 vane spacing, hexahedral and quadrilateral elements were used for all blade rows to maintain consistency between each case. This HOH grid was generated as a structured grid and then converted to an unstructured format to comply with the solvers mesh requirements. The individual mesh blocks were then assembled into a single-passage, multi-bladerow mesh, Figure 2.11. It should be noted

that for Case 3 (S1 asymmetric spacing), the steady state simulation was run with a full annulus S1 vane row while all other blade rows were run with a single passage. Total node counts were roughly 2.4 million for the single passage multi-bladerow grids, and 13 million for Case 3 with the full annulus S1 mesh.

The forced response code offers multiple turbulence models, including Baldwin and Barth, Spalart-Allmaras, and q-ζ. Spalart-Allmaras was chosen as the turbulence model along with a 2nd order time integration scheme. Additionally, wall functions were implemented on all viscous surfaces. Wall functions further reduce the required mesh resolution in the endwall regions as the first mesh point is moved outside the viscous sublayer. The number of nodes needed in the boundary layer mesh is significantly reduced by not resolving the viscous sublayer region of the boundary layer. Instead of near-wall nodes on the order of $y^+ \sim 1$, best results were obtained for near wall spacing on the order of $y^+ \sim 40$.

After generating a suitable mesh, several boundary conditions were applied to the mesh surfaces. Periodic boundaries were applied to all suction and pressure side boundaries of the single passage mesh blocks. Mixing planes, which circumferentially average flow properties, were inserted on all block interfaces as a means of passing flow information between mesh blocks in relative motion. For inlet and exit boundary conditions, the code requires all three velocity components defined at arbitrary radial locations, along with static pressure and temperature. These inlet and exit profiles were taken from *JACC* simulation results run at the R2 1st Torsion resonant speeds. The exit static pressure profile is then scaled to throttle the compressor to the desired loadings. To validate the prediction of the computational model, a speedline was computed at the design speed of 5000 rpm. A comparison of the computed speedline and the experimental speedline at 5000 rpm is shown in Figure 2.12. As is common in many computational turbomachinery predictions, the mass flow rate of the compressor is numerically

over predicted by 1-3%. However, the shape of the computed speedline follows closely the shape of the experimental curve, suggesting that the numerical model is capturing the large-scale behavior of the flow. Y^+ values of the O-mesh surrounding the airfoils used in the final mesh are shown in Figure 2.13.

At the R2 1st Torsion mode crossing speeds, only a nominal loading and high loading condition were computed. The loadings were selected to match experimental measurements taken on the Purdue compressor. Murray (2014, a) performed detailed aerodynamic and forced response measurements at nominal and high loading conditions at the 1st Torsion resonant speed. These loading conditions are matched computationally by matching the ratio of overall total pressure ratio (Rc) over corrected mass flow rate (Wc). Since the numerical model over predicts mass flow rate, matching the same flow rate would not result in equivalent loading conditions. Matching the Rc/Wc parameter tends to provide a better comparison of the loading conditions. Once steady solutions were obtained for each Stator 1 configuration, they were then used as the flow initialization for the unsteady forced response simulation.

2.3.2 Setup for Unsteady Forced Response Calculation

After the steady solution is obtained for each test case, modifications must be made to the mesh in preparation for the forced response calculations. Since the forced response of R2 is the focus of this research, the unsteady mesh must encompass the vortical and potential forcing from upstream vane rows and potential forcing from the downstream vane row. Therefore, the unsteady mesh included three blade rows, namely S1, R2, and S2. Since the numerical code prevents the implementation of phase lag boundary conditions, multi-passage blade rows are required to capture the convection of wakes and potential fields through the R2 blade row. When possible, it is desirable to generate a reduced sector mesh to prevent the meshing of a full

annulus. For the baseline test case with 44 vanes for S1 and S2 and 33 blades for R2, it is possible to reduce the blade and vane counts by a factor of 11 to create a 4-3-4 configuration. However, when S1 is reduced to 38 vanes for Case 2 and Case 3, no such common factor exists and the full annulus mesh cannot be reduced. Therefore, full annulus blade and vane rows were used for all unsteady grids to maintain consistency between each case. Figure 2.14 shows an example of the S1-R2-S2 unsteady mesh for the baseline Case 1 stator configuration. The new full annulus grids each contain approximately 40 million nodes.

New boundary conditions were created for the new S1-R2-S2 multi-passage grids. The final solution of the steady simulations provides detailed boundary conditions. For the new inlet and exit boundary conditions, circumferentially averaged steady flow properties at the S1 inlet mixing plane and S2 exit mixing plane were applied at the unsteady mesh inlet and exit. These were applied as Riemann Invariants. Additionally, mixing planes were replaced by sliding planes. Mixing planes circumferentially average flow properties across mesh blocks, causing stator wakes and potential fields to be mixed out and not propagate as a forcing function to R2. Sliding planes do not average or mix flow properties, but rather interpolate flow properties directly onto the adjacent mesh block, thus preserving unsteady and non-uniform flow features. As a final step, the flow solution from the steady computation was duplicated across all passages and used as a flow initialization for the unsteady run.

With the fluid domain setup complete, the structural domain must be initialized. A Rolls-Royce developed FEA code provided a modal analysis on the R2 blisk, including both mode shapes and frequencies (see Figure 2.15 for 1st Torsion mode shape). Mode shapes are then interpolated onto the computational blade mesh using additional Rolls-Royce tools and scripts. In this process it is possible to specify exactly which disk nodal diameters (ND) to analyze in the forced response computation. The disk nodal diameter excitation is determined by the difference

between vane counts of upstream and downstream stators and the vibrating rotor blade count. For the baseline case with 44 stator vanes upstream and downstream and 33 rotor blades, an 11 ND disk excitation is created. Figure 2.16 shows the 11 ND excitation of a disk. Likewise, when S1 is reduced to 38 vanes in Case 2, the 33 blades in R2 are now excited by 38 upstream vanes and 44 downstream vanes, generating a 5 ND and 11 ND disk excitation. The final test case where S1 is modified to have an 18 vane half sector and a 20 vane half sector corresponds to R2 disk excitations of 3 ND, 7 ND, and 11 ND. Table 1 lists vane and blade counts for each test case run, along with the associated R2 disk nodal diameters. The specific disk nodal diameter excitations are analyzed in the forced response computation.

Each simulation was run for 10,000 time steps, for which convergence is easily obtained. Within each time step, 20 Jacobi iterations and 5 Newton iterations are performed as a means of accelerating convergence. Figure 2.17 shows the modal force convergence for Case 1. Core compressor forced response simulations typically converge within 15-20 vibration cycles. The modal force history shown in Figure 2.17 was run for 23 vibration cycles. With both the fluid field and structural field fully converged, recorded modal forces can be processed to represent vibrational amplitudes, and the unsteady flow field can be analyzed to understand the unsteady aerodynamic forcing which excites the R2 1T resonance.

	Blade and Vane Configurations				
Test Case	**S1**	**R2**	**S2**		**Nodal Diameter Excitations**
1	44	33	44		11
2	38	33	44		5, 11
3	38: 18 vane half-sector 20 vane half-sector	33	44		3, 11 7, 11

Table 2.1 : Nodal diameter disk excitations for three S1 vane configurations.

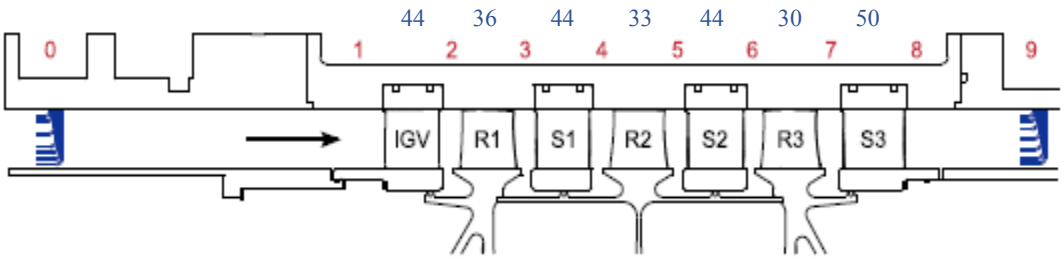

Figure 2.1: Cross-section of Purdue compressor, showing measurement locations and blade counts.

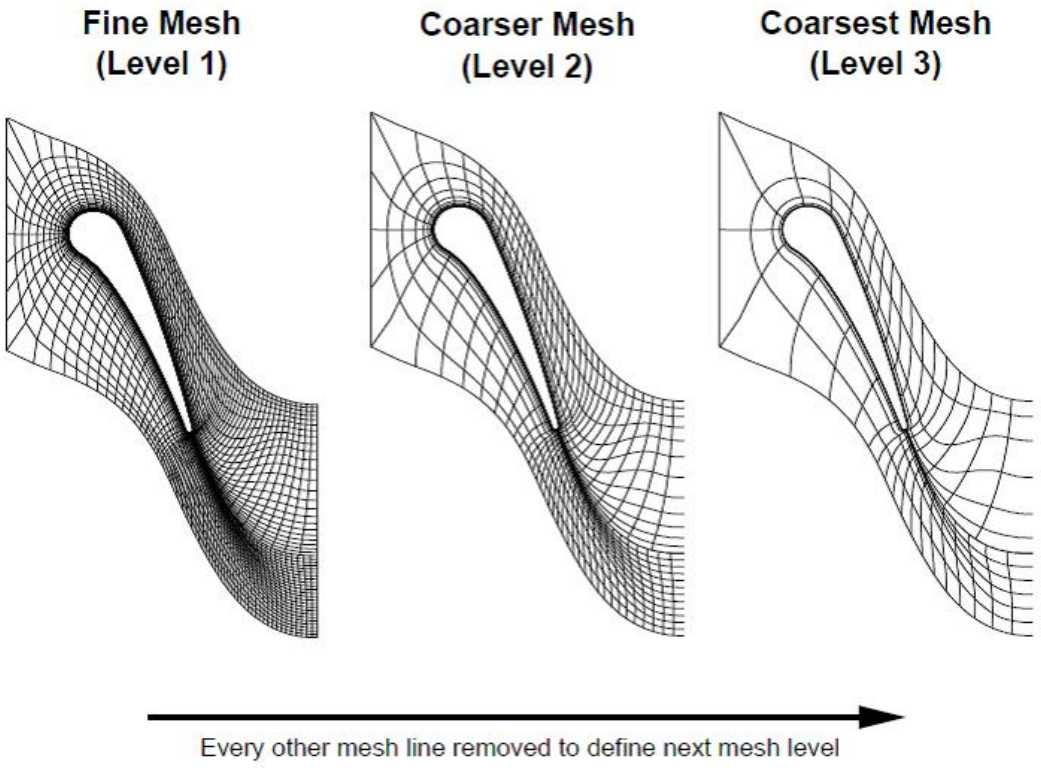

Figure 2.2: 3-level multi-grid mesh scheme. (Hall, 1999)

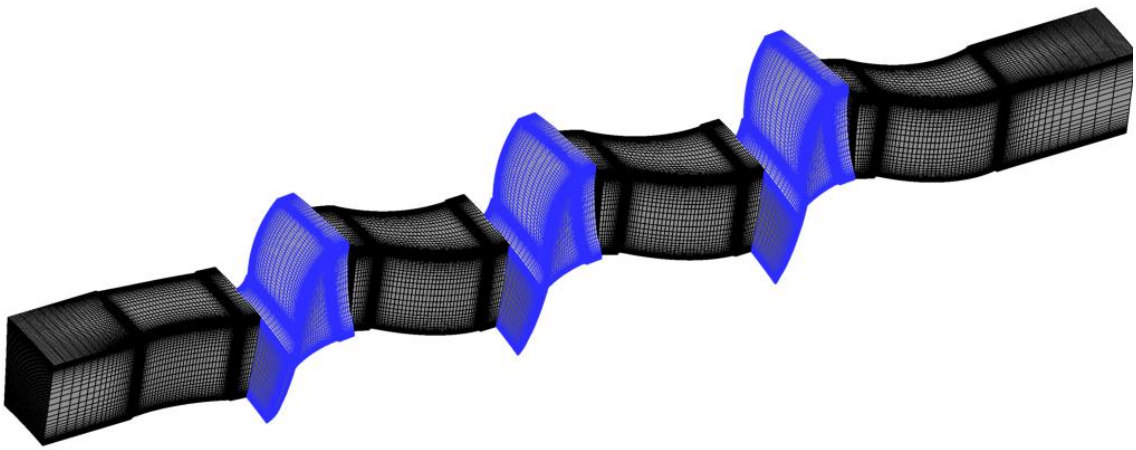

Figure 2.3: *JACC* 3-Stage, multi-block mesh.

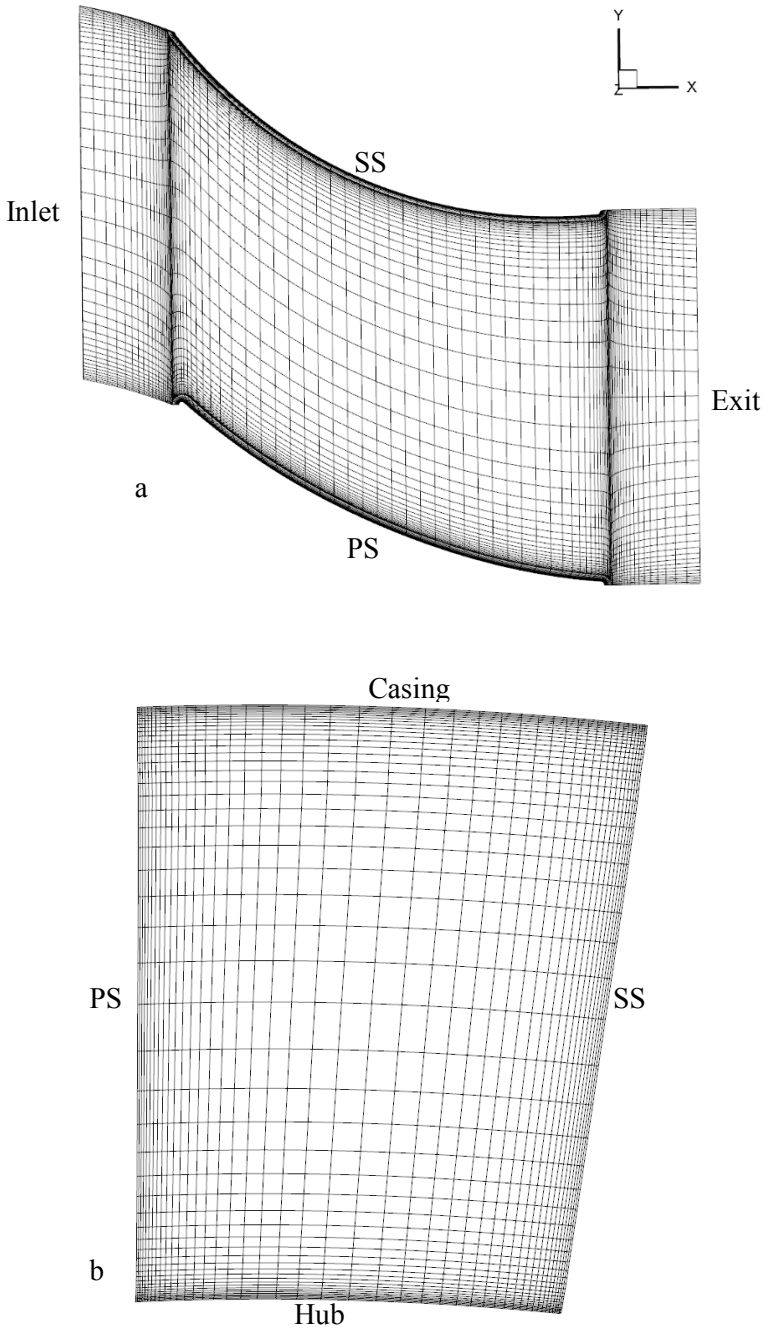

Figure 2.4: View of S1 mesh showing mesh clustering around viscous surfaces at casing surface (a) and exit mixing plane surface (b).

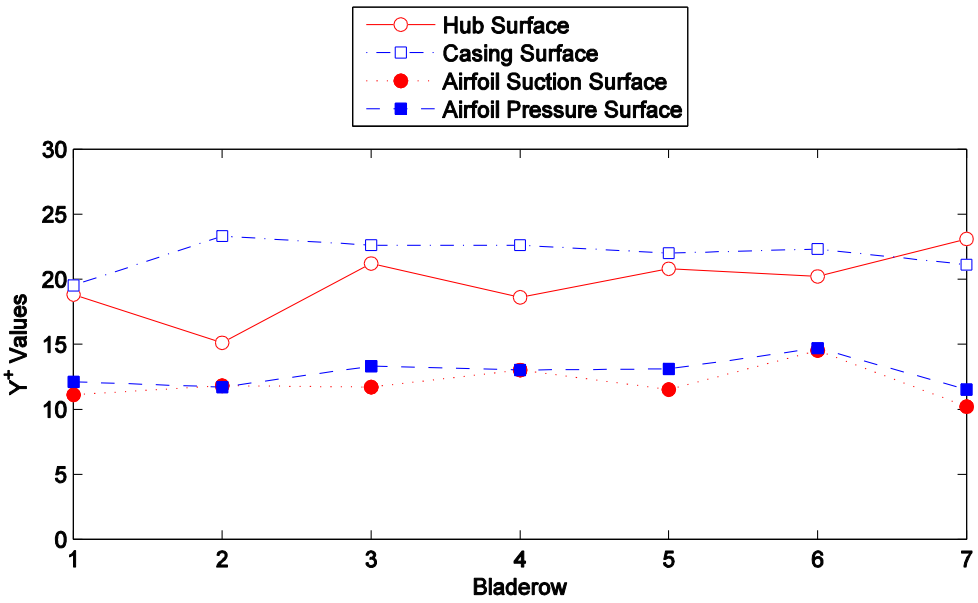

Figure 2.5: Average Y^+ values on viscous surfaces of *JACC* mesh.

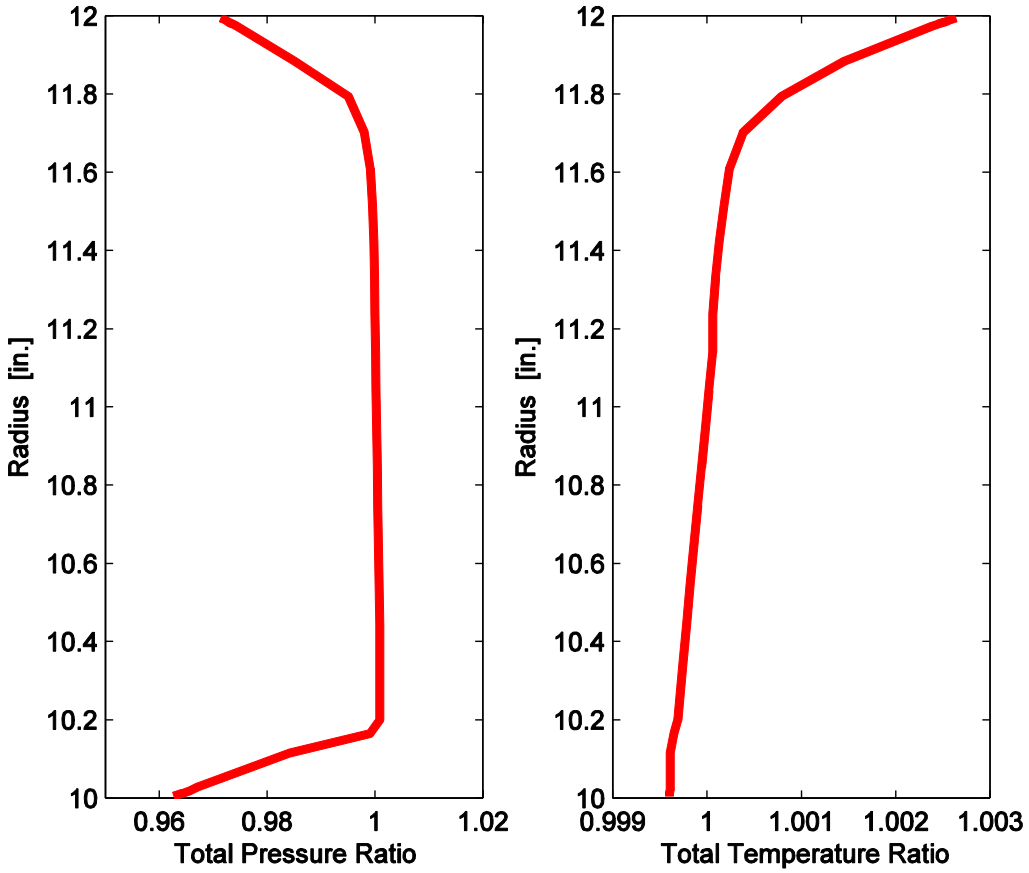

Figure 2.6: Inlet Total Pressure and Temperature profiles used in *JACC* simulations.

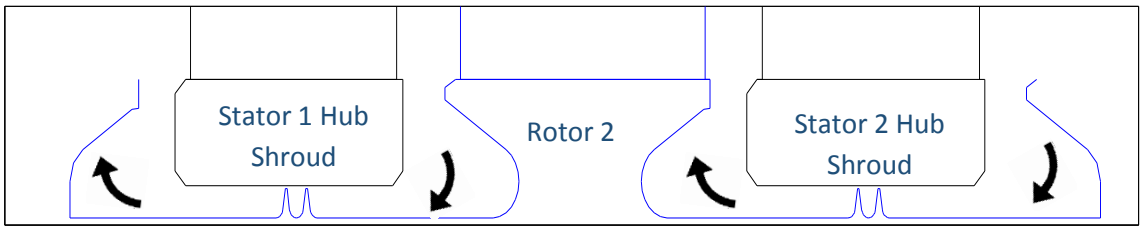

Figure 2.7: Stator cavity leakage paths in Purdue compressor.

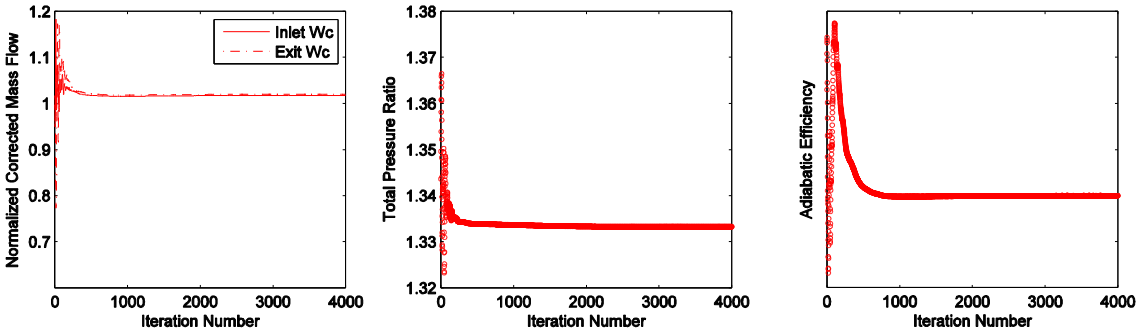

Figure 2.8: Convergence plots for *JACC* solution: mass flow (left), Total Pressure Ratio (middle), Adiabatic Efficiency (right).

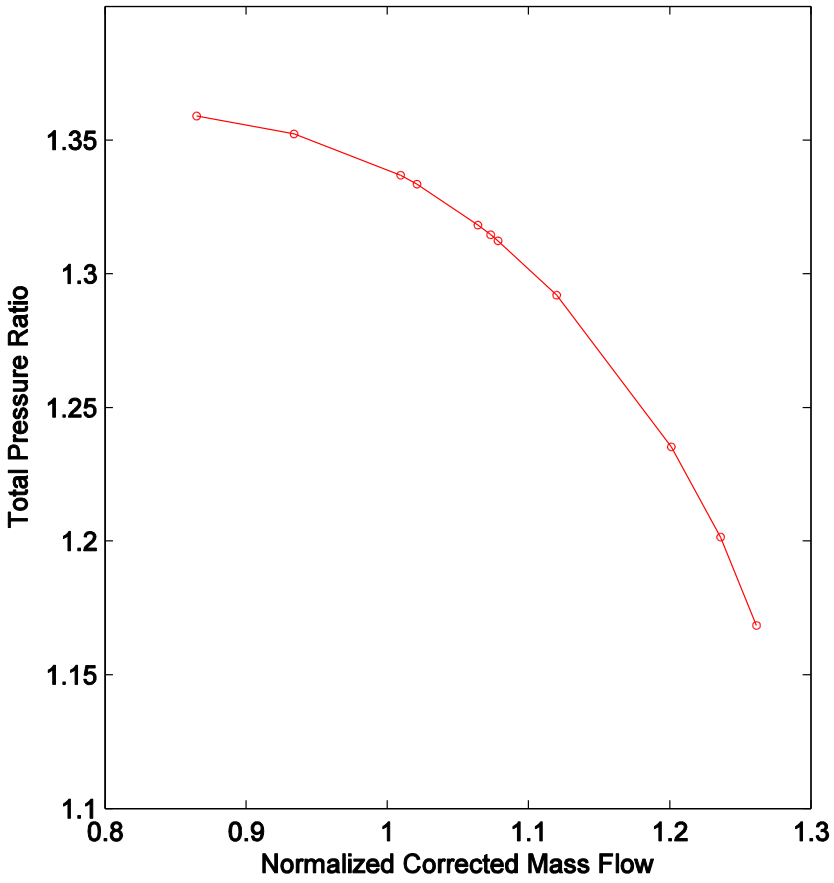

Figure 2.9: *JACC* overall compressor characteristic at design speed (5000 rpm).

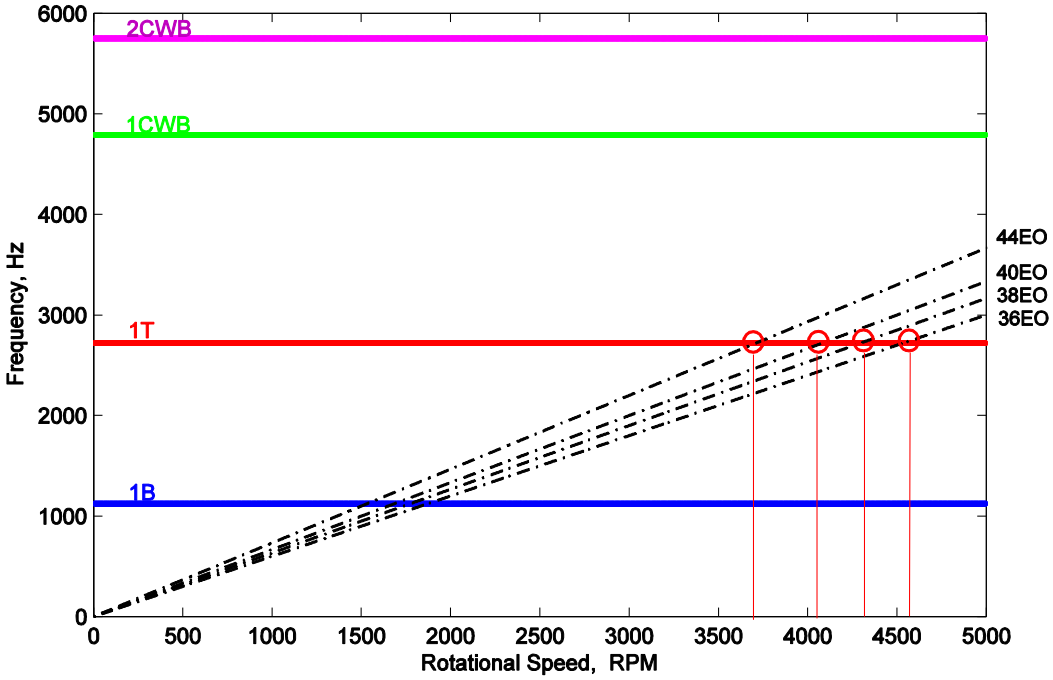

Figure 2.10: R2 Campbell Diagram with EO excitations from three S1 configurations.

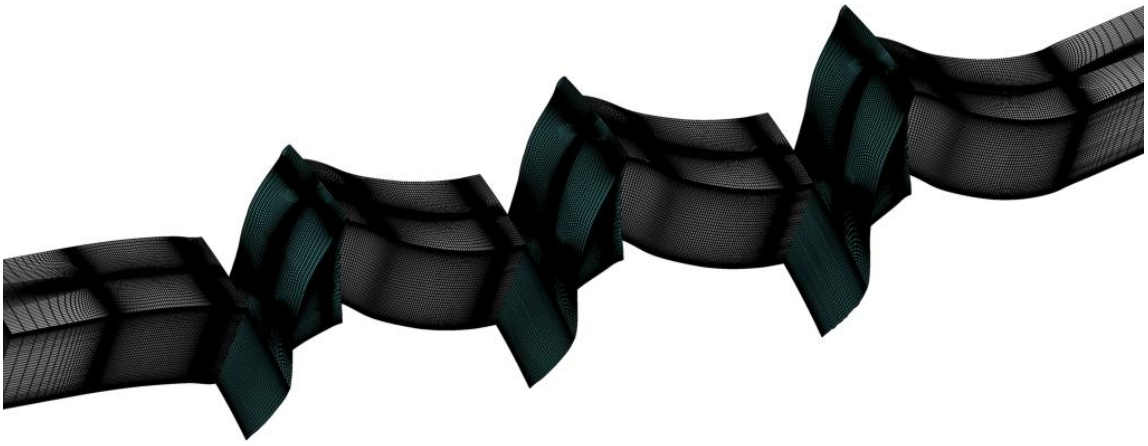

Figure 2.11: Multi-bladerow, single passage HOH mesh for forced response computation.

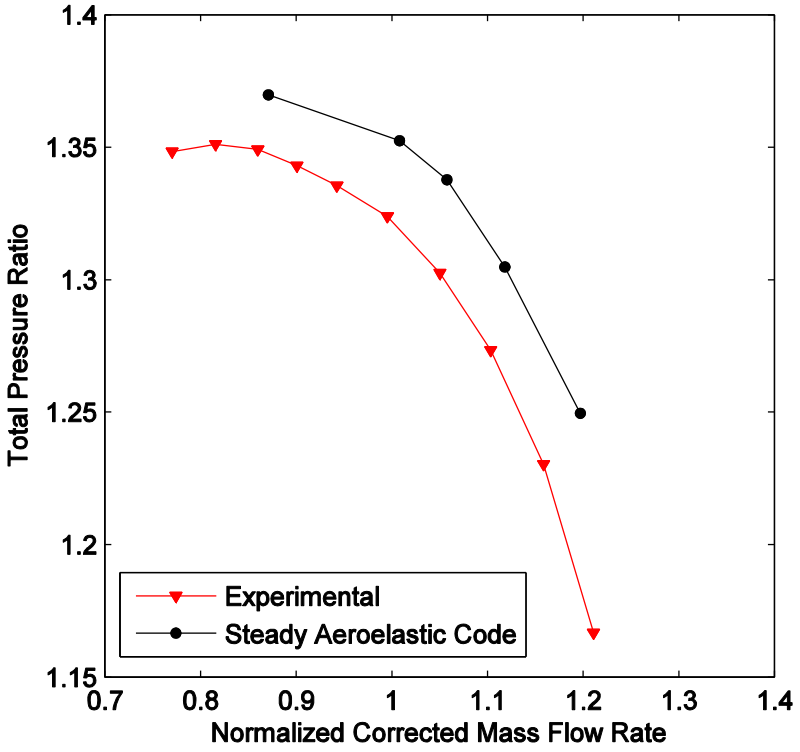

Figure 2.12: Experimental and Computational Speedline at 5000 RPM.

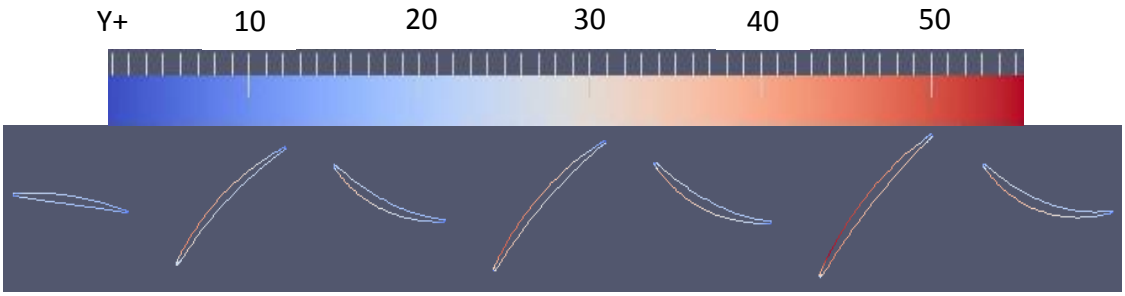

Figure 2.13: Y^+ values of single-passage steady CFD for aeromechanics computations.

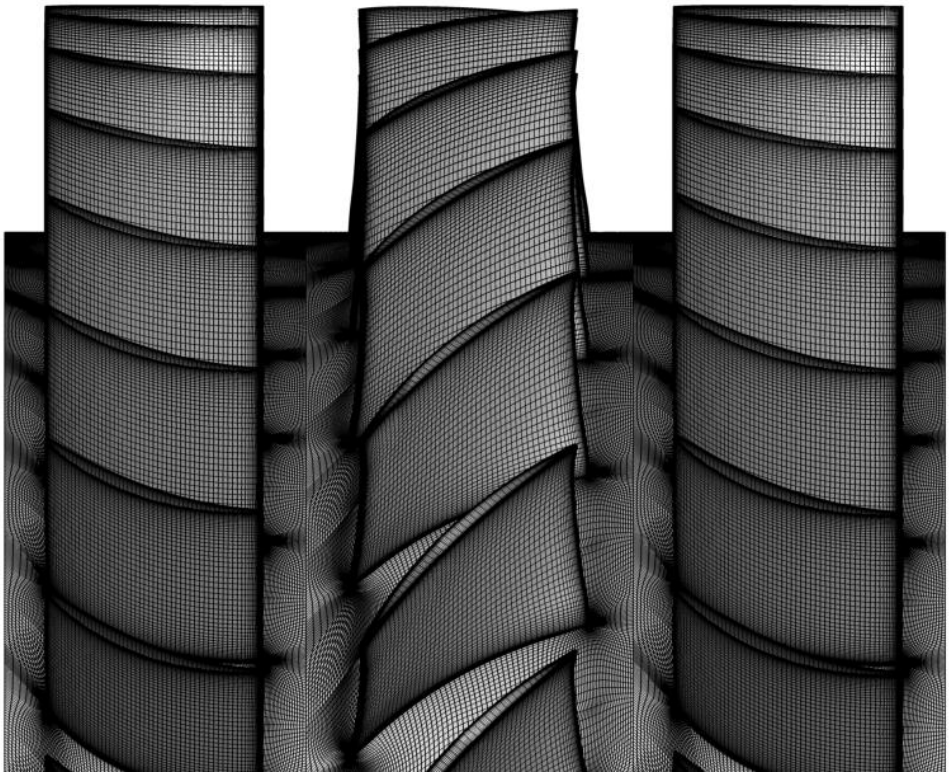

Figure 2.14: Section of the full annulus S1-R2-S2 mesh for unsteady simulation.

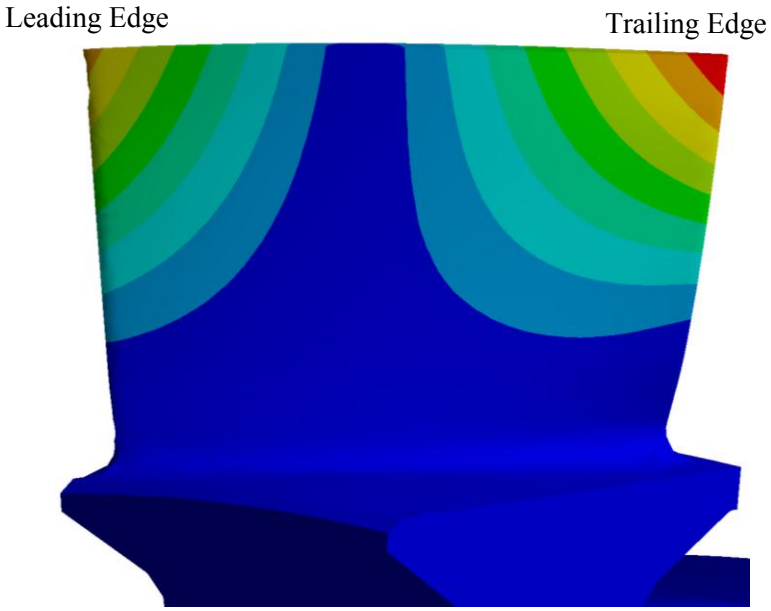

Figure 2.15: R2 1st Torsion mode shape.

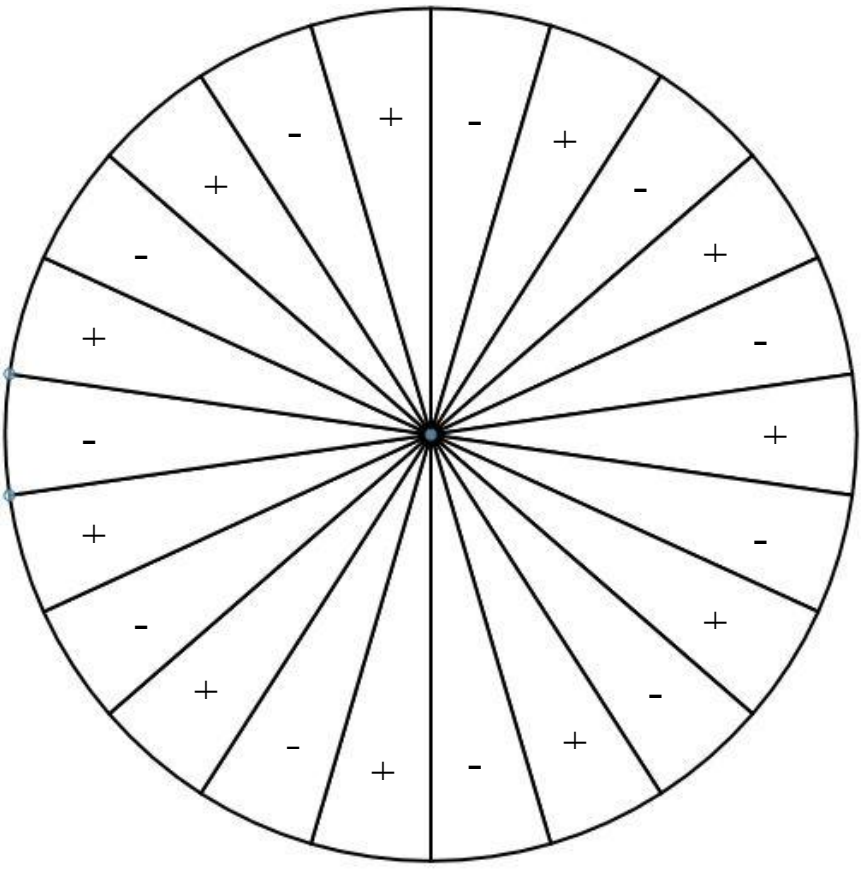

Figure 2.16: 11 nodal diameter excitation of the Rotor 2 Disk.

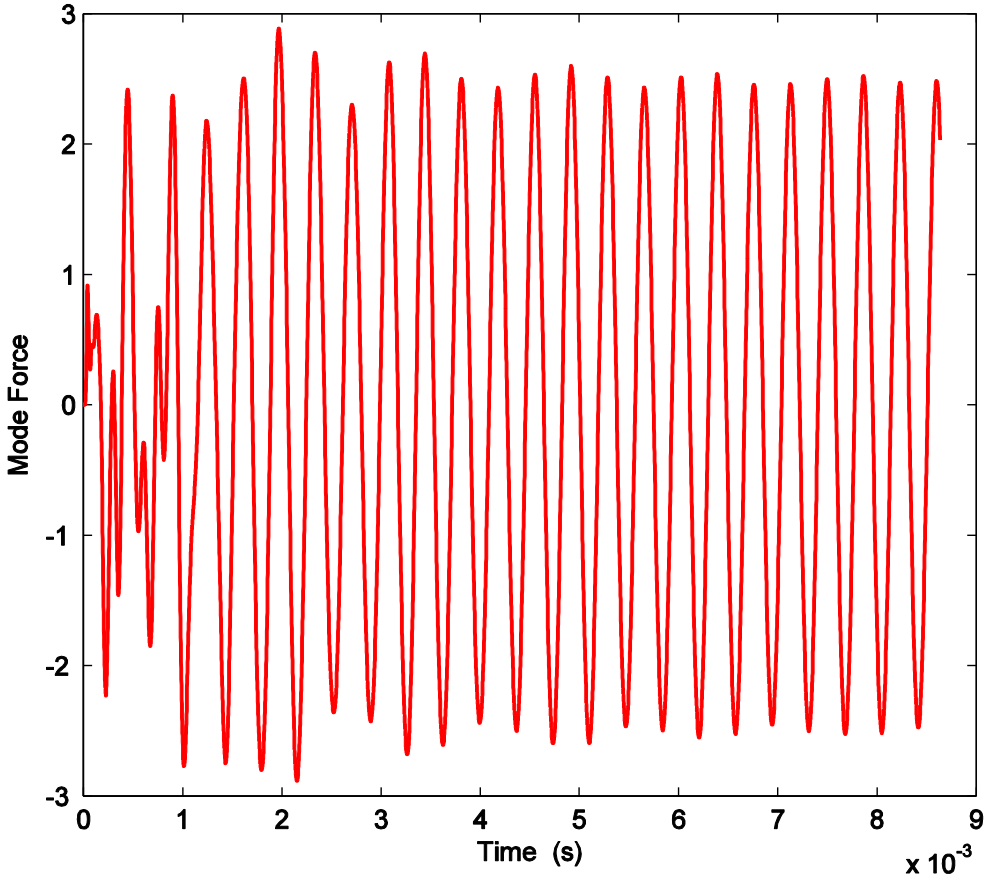

Figure 2.17: Modal Force convergence.

CHAPTER 3: COMPUTATIONAL ANALYSIS OF PURDUE COMPRESSOR

CFD analyses of compressor aerodynamics have improved through the years to where it now is the primary tool used for aerodynamic design and analysis of compressor blading. Crucial to the accuracy of these computational predictions are the defined boundary conditions. The *JACC* flow solver requires total pressure and total temperature radial profiles as boundary conditions at the compressor inlet plane, along with other geometric and turbulence parameters. Brossman et al. (2014) computed the sensitivity of computational predictions to different total pressure and total temperature profiles, including uniform flat and experimentally measured inlet profiles. The results show large differences in total pressure and isentropic efficiency after the first stage of the compressor. It is critical to the accuracy of CFD predictions to model correct inlet boundary conditions to the machine. As mentioned in section 2.2.2, detailed measurements were previously taken at the compressor inlet plane on the Purdue 3-stage compressor (Ball, 2013).

The compressor inlet plane is located approximately 5 chord lengths upstream of the IGV leading edge (see measurement location 0 in Figure 2.1). To avoid excessively increasing the computational node count by extending the compressor inlet duct 5 chord lengths upstream, the inlet plane was instead defined only 1 chord upstream of the IGV leading edge. Applying the experimentally measured inlet profile (measured 5 chords upstream of IGV) at the computational inlet (1 chord upstream of IGV) yields an incorrect prediction of boundary layer thickness flowing into the compressor blading. Figure 3.1 compares total pressure profiles at the IGV leading edge for *JACC* results with measured inlet boundary conditions applied at the computational inlet, to measured total pressure profiles just upstream of the IGV. Applying the

measured inlet profiles at the computational compressor inlet does not allow proper boundary layer development and thus, does not model accurate flow into the compressor. To correct this, the measured inlet total pressure profile at the compressor inlet was modified to increase the boundary layer thickness such that the new profile produced accurate flow properties at the leading edge of the IGV. The modified inlet profile used as the CFD inlet boundary condition is shown in Figure 3.2, and the resulting total pressure measurement upstream of the IGV is shown in Figure 3.3. Increasing the boundary layer thickness on the compressor inlet boundary conditions increases model fidelity and matches the predicted flow properties to the experimentally measured properties at the IGV inlet location. With correct CFD boundary conditions, a detailed computational analysis can be performed to increase understanding of the aerodynamic performance of the Purdue multistage compressor.

3.1 Overall Compressor and Stage Performance

The overall performance of a compressor is often analyzed through the computation of a speedline, or characteristic curve. Such a speedline shows total pressure ratio on the ordinate and corrected mass flow rate on the abscissa at various flow rates as the compressor is throttled from high mass flow (choked) to lower mass flow (high loading), while operating at a constant corrected shaft speed. Figure 3.4 compares the experimentally computed compressor characteristic to *JACC* computational results. Note that the mass flow rate is normalized by the compressor Peak Efficiency mass flow rate. The shape of the *JACC* prediction matches very well the shape of the experimental curve. When comparing computational flow predictions to experimental measurements it is often encouraged to look more at profile shapes and trends than to compare quantitative values, which is appropriate for this speedline comparison. *JACC* implements the Baldwin-Lomax algebraic turbulence model which, when used for

turbomachinery applications, is known to over predict mass flow by 1-2% for matching loading conditions (Hall et al., 1999). Between the two speedlines presented, three loading conditions have been matched (see Nominal Loading (NL), Peak Efficiency (PE), and High Loading (HL), in Figure 3.4). At these conditions, *JACC* predicts mass flow rates in the range of 1.1-1.5% higher than experimentally measured values. It is also noted that the *JACC* results do not reach the experimental stall limit of the compressor. This is a result of numerical stall. Steady CFD will always predict stall sooner than it actually occurs. The flow physics leading to compressor stall are inherently unsteady and involve large separated regions called stall cells. Steady CFD breaks down in the presence of these large-scale instabilities, leading to numerical instabilities and premature stall. However, as the shape of the characteristic matches so closely to the experimentally measured curve, it appears the computational model is capturing the general flow physics through the compressor.

Analyzing the individual stage characteristics also yields insight into the compressor behavior. Figure 3.5 compares the individual stage characteristics. The values on the ordinate are corrected mass flow rates at the inlet of the specific stage, again normalized by the overall PE mass flow rate. In general, *JACC* stage characteristic shapes agree well with experimental trends. Stage 1 matches well until high loading, where the computational model over predicts stage performance. Stage 2 has the best general comparison to experimental trends in that the predicted curve maintains the general shape for the entirety of the operating range. *JACC* again predicts Stage 3 performance very well except for differences in the near-stall region. These differences are attributed to which stage is the predicted weak stage. It is noticeable in the experimental results that Stage 1 is the weakest. In this stage, the characteristic falls off at the highest loading point, signifying that peak pressure rise has been reached and any further reduction in mass flow deteriorates the stage performance until stall is reached. Stage 2 and Stage 3 do not have the performance deterioration as is shown in Stage 1. Conversely, in the computational model Stage 3

is the weak stage. Stages 1 and 2 show healthy pressure rises at the last loading condition whereas Stage 3 is clearly starting to fall over. Figure 3.6 displays this further, where the computational stage characteristics and efficiency curves are shown for all 3 stages together. It is most notable in the efficiency curve that Stage 3 performance begins to deteriorate more rapidly than the previous stages. This difference in which stage first deteriorates in performance is the principal cause for variances in stage characteristic shape between *JACC* and experimental curves. However, in terms of general shapes and trends, the predicted overall performance of *JACC* simulations agree well with measured experimental trends, suggesting that the computational model is capturing the large scale aerodynamic behavior of the compressor.

3.2 Comparison of Blade Row Performance

To further analyze the capability of *JACC* to accurately predict aerodynamic behavior of the Purdue multistage compressor, it is beneficial to analyze radial profiles at the exit of each blade row. In the computational model, radial profiles are generated by circumferentially area-averaging flow variables at a location 7 grid points downstream of the blade or vane trailing edge. Taking the circumferential average at such a proximity to the airfoil reduces artificial mixing losses produced by mixing plane effects. Experimental data are taken in the Purdue compressor at a mid-gap distance between each blade row, based on midspan geometry. The physical distance between experimental and computational measurement planes is roughly 0.25 inches. Total pressure and total temperature measurements are acquired with 7-element rake probes at this mid-gap location. Rake measurements are acquired at spanwise locations of 12%, 20%, 35%, 50%, 70%, 80%, and 88%. Vanes are traversed circumferentially past stationary rakes to obtain passage-averaged results. The experimental data presented in this section result from 20-point vane passage traverses. Comparisons are made at three loading conditions: namely Nominal

Loading, Peak Efficiency Loading, and High Loading (refer to Figure 3.4). At each condition, *JACC* solutions were adjusted to match Rc/Wc ratios of the experimental measurements.

Figure 3.7 compares total pressure profiles at Nominal Loading at the exit of each blade row. Each of the rotor profiles match very well with the shape of the experimental rake data. Rotor 1 yields an almost perfect match. Each successive rotor starts to differ slightly more, especially in the tip region. At R3 exit, *JACC* also slightly over predicts the work output from the blade. Observing the stator performance, the overall agreement is not as good. The S1 computational prediction matches generally well with rake data except for discrepancies in the upper span region. These differences become more pronounced in each successive vane row. It is clear that experimental measurements point to a significant pressure loss in the tip region. Each of the stators shows a reduction in pressure for the upper 20-30% span, while rotors exhibit similar behavior to a lesser radial extent. The experimental rotor profiles start to fall over at the 88% span rake position in each of the blade rows, while maintaining a healthier hub region. Alternatively, *JACC* shows somewhat different trends in the endwall regions. *JACC* predicts healthy rotors, meaning that no large scale separations or high loss regions appear in the radial profiles, as shown by relatively flat profiles. Stators show similar behavior. Stators 1 and 2 remain primarily flat through most of the span. Stator 3 shows signs of a weak hub region, with pressure loss apparent in the lower 25-30% span. Figure 3.8 compares total temperature profiles at the Nominal Loading condition. Computational results slightly under-predict the temperature rise through the machine. The over prediction of total pressure and under prediction total temperature result in a higher predicted efficiency than what actually occurs in the compressor, a common feature of computational predictions.

Figure 3.9 and Figure 3.10 compare experimental and *JACC* total pressure and total temperature profiles at Peak Efficiency Loading. Again, observing the total pressure profiles of

the rotors reveals that *JACC* is capturing the aerodynamic behavior of the rotors extremely well. Computational profiles match nearly perfectly. Behavior at the hub agrees well with experimental data, while only the 88% span location starts to show discrepancies. *JACC* predicts a strong rotor tip performance, while actual compressor rig measurements suggest the performance starts to fall over in the tip region. Overall, the aerodynamic prediction of the rotors on the Purdue compressor is excellent. The stators again show much larger differences. Stator 1 has the best agreement, matching well in the lower 50% span. The predicted overall performance trend of the stators shows that performance degrades primarily in the hub region, with greater losses in each successive vane row. Stator 1 shows a relatively flat profile through the majority of the span. The slope of the bulk flow changes noticeably for Stator 2 and Stator 3, with the radial profiles suggesting much stronger tip regions and weaker hub regions moving back in the compressor. These profiles suggest that flow separations grow in magnitude for each successive stator, thus creating a larger hub region blockage, reducing axial velocity and creating larger regions of loss. The higher loss is evident in the total temperature profiles shown in Figure 3.10. Large blockage regions in the hub force more flow through the tip region at a higher velocity. The higher momentum tip flows decrease incidence, thereby reducing separations and improving performance. Hence, the total pressure profiles slope from a strong tip to a very weak hub. The opposite trend is observed in experimental results, which show the tip becoming weaker as flow progresses through the compressor.

Figure 3.11 sheds further light on the *JACC* predicted blade performance, where total pressure contours at the exit of each stator are shown. The axial plane at which the data are acquired is roughly the same location at which radial profiles are computed. S1 has a very small hub separation, as shown by darker blue regions in the contour plot, with the extent of the blockage in the passage is less than 10% at the hub. This corresponds to the uniform and flat S1 total pressure profile in Figure 3.9. The small blockage at the hub does not alter the aerodynamic

behavior at greater span locations. However, the size of the separation and resulting blockage in the hub region increases with each vane row. S2 develops a blockage region occupying roughly 25% span and 20% passage. S3 blockage envelops even more radial distance and, therefore, drives a larger portion of the incoming flow towards high span regions. Higher mass flow rates in the upper span increase the fluid momentum and performance in the tip region.

Figure 3.12 compares radial total pressure profiles at High Loading. This loading condition is the second to last stable operating point on the compressor characteristic before *JACC* enters into numerical stall. Results at this condition clarify the flow physics leading to predicted stall. As with the previous loading conditions, predicted performance in the rotors agree well with measured data. Profiles for the rotors, both numerical and experimental, remain predominately flat, suggesting clean flow without major loss sources. Profile shapes agree well between the two data, with experimental rake data showing a slight decrease in rotor performance in the upper 30% span. Stator performance, however, is again not predicted well. On the experimental side, S1 appears to be the weak bladerow which causes instabilities in the compressor. The total pressure performance clearly shows the tip region losing pressure rise capability. The formation of large separation and blockage is apparent by the increased performance in the hub region. As more flow is forced from the tip region to the hub region, separations in the hub diminish and performance improves. The experimental results suggest that R2 is able to overcome the weak tip from S1 and the extent of total pressure loss seen in S1 is not observed through the rest of the compressor. *JACC* predicts the S3 hub region as the weak point. S1 appears to have significant separations at both the hub and tip, causing increased flow toward midspan and peak performance at 60% span. S2 indicates a large hub separation, and S3 suggests blockage that occupies a majority of the span. Interestingly, even though S1 and S3 predictions are far from matching experimental measurements, S2 predictions agree well for the lower 50% span.

Figure 3.13 helps visualize the predicted flow behavior in the stators for the High Loading condition. S1 generates separated regions at both the hub and tip, forcing increased mass flow through the mid span section of the vane. This explains why radial profiles show peak performance at roughly 60% span. The primary separation on S2 occurs in the hub region, occupying nearly 50% of the passage near the hub and more than 50% of the span. S3 separations produce blockage occupying an ever greater extent of the passage and span than S2, and it is predicted to be the weakest location in the compressor. *JACC* results would point to S3 being the location where stall is initiated in the compressor. Experimental data suggests otherwise, with the Stator 1 tip region being the weakest and the likely location where separations and blockage lead to compressor instabilities.

The overall ability of *JACC* to predict bladerow performance is still very good. Rotor performance is predicted almost perfectly, with profile shapes following the same trends as experimental measurements. Only the very tip region showed differences, where *JACC* under predicted losses in the tip region. Stator performance was not predicted as well, primarily due to *JACC* predicting larger separations in the hub than in the tip. However, the bulk of the design process is spent designing a compressor at a peak efficiency, or nearby design loading. Flow at this loading condition is understood the best and many CFD codes are calibrated and optimized to give the best prediction at this condition. Recall the total pressure profile comparison at Peak Efficiency Loading in Figure 3.9. The overall agreement between *JACC* and measured data are very good. Even S1 and S2 predicted performance matches reasonably well. Thus, *JACC* is very capable of predicting the complicated aerodynamic behavior in the Purdue multistage compressor operating near design loading conditions.

3.3 Separation Patterns

Smith et al. (2014) utilized flow visualization techniques in the Purdue compressor to qualitatively map separation patterns on each vane row. In this study, a mixture of a fluorescent powder paint and kerosene is injected into the inlet of the compressor at flow rates low enough such that the paint particles in the mixture follow streamtubes of air. As the mixture propagates, kerosene eventually evaporates out leaving streaklines of paint on flow surfaces, most especially in regions of separation and recirculation. This is particularly useful as a qualitative means of analyzing aerodynamic behavior in turbomachinery. Images captured in this research are compared with surface streaklines from *JACC* results. Using the 3-D graphics software Tecplot, computational mesh and flow solutions were visualized. CFD surface streaklines were generated by creating a surface at the desired location and generating "particles" which propagate on the surface according to the computed velocity field. The surfaces created for visualizing streaklines are 5 grid points away from the vane suction surfaces. This location remains well inside the airfoil boundary layer, while maintaining enough distance from the no-slip vane surface boundary condition to capture the aerodynamic flow behavior.

Comparisons of *JACC* separation patterns to experimental Flow Vis results are given in Figures 3.14 - 3.16 for Nominal Loading, Peak Efficiency Loading, and High Loading. Observing the comparison at Nominal Loading in Figure 3.14, it is clear that *JACC* is not computing the separations in the tip region to the extent at which they occur in the compressor. Flow visualization techniques in the compressor show recirculation regions at the tip which span roughly half-chord and 30% span in S1 to nearly 50% span and 75% chord in S3. *JACC* results do show small-scale streamline shifting in the tip region, but it is not nearly the size of actual separation regions. *JACC* does predict separation zones much better at the hub. The size and

extent of the regions predicted by *JACC* match very well the separation bubbles present in experimental results.

Figure 3.15 shows the same comparison at Peak Efficiency Loading. Again, computational results agree well in the hub region, where both size and shape compare very well to experimental flow visualization. The predicted location of the node, or saddle point, on Stator 3 appears at roughly 30% span on the trailing edge. The location of this flow structure matches nearly identically to the actual saddle point observed in the experimental results. Flow in the tip region still does not compare nearly as well between the computational and experimental results. Computational results for S3 do show roughly the same chordwise extent of separation, but the radial extent of the recirculating region is only a fraction of the actual size. Separation patterns at Peak Efficiency Loading have the best agreement between *JACC* and experimental results. This is not surprising as most CFD codes used in turbomachinery are calibrated to yield accurate results near design operating conditions. Off-design conditions have not yet reached the level of reliability to where numerical predictions are read with high confidence. Figure 3.16 highlights this principle, comparing separation patterns at the off-design condition of High Loading.

Computational prediction are again not far off when comparing size and extent of flow separations in the hub region. Saddle point locations for S1 and S2 appear very close to those observed experimentally. CFD results for S3 at High Loading confirm that numerical stall initiates in the hub region of this vane. This High Loading condition is the final stable operating point on the compressor characteristic before *JACC* falls into numerical stall, which occurs because steady CFD numerics break down in the presence of large separations. In the case of S3, the separation near the tip is small enough that little flow is pushed back down to lower spans. As a result hub separations continue to grow until the stability limit is reached.

The question must be asked as to why *JACC* has difficulty predicting the observed flow physics in the tip region of the compressor. It is the opinion of the author that *JACC* does not fully capture the interactions, blockage, and losses associated with rotor tip leakage vortices. As the compressor is throttle towards stall, the pressure difference between suction and pressure surfaces on the rotor blade increase, driving an increased flow across the tip gap. Higher mass flows across the tip gap create larger tip leakage vortex structures which grow radially as they propagate downstream, creating a larger radial blockage. Figure 3.17 compares CFD entropy contours of R2 at Peak Efficiency Loading and High Loading. The images on the left column compare entropy contours at 95% span, while the images on the right show entropy contours on an axial plane at roughly 66% chord. The results at 95% span show very little difference in vortex size and trajectory between Peak Efficiency and High Loading. The axial slice contour shows the influence of the tip leakage vortex at High Loading (near stability limit for *JACC*) still only propagates from the casing to 90% span, only about 3% span further than the vortex structure at Peak Efficiency. The axial location at 66% R2 chord was chosen such that the core of the vortex travels through the axial plane, giving valid estimation of the size of the leakage vortex. It is believed that the tip leakage vortex in the Purdue compressor generates more loss and blockage than is predicted in *JACC*, influencing the aerodynamics to a greater extent in the tip region and causing large separations on the stator vanes.

3.4 Effects of Stator Cavity Leakage Flow on Vane Performance

The re-introduction of stator cavity leakage flow into the main gas path is the greatest source of hub endwall losses (Cumpsty, 2004). The Purdue compressor has four shrouded leakage cavities. The cavity under the IGV is sealed in the nosecone. Therefore, flow across this knife seal is not expected. Cavities under S1 and S2 result in recirculating flow under the vane, while

S3 leakage flow exits to atmospheric conditions. Only the effects of the cavity leakage flow through S1 and S2 cavities are included in this section. Stator vanes act as diffusers in that velocities are decreased and static pressure increased from leading to trailing edge. Pressure gradients created by this diffusion drives flow through the stator shroud cavity from the trailing edge side to the lower pressure leading edge side. As the leakage flow re-enters the main gas path upstream of the stator vane, the low momentum leakage flow reduces the momentum of the main gas flow in the hub region, affecting the axial and tangential velocities as well as the flow angles. Mixing of the two air streams occurs as the flow passes through the vane, and the effect is most noticeable at the stator exit. The vane performance degradation resulting from leakage flow is heavily dependent on the size of the knife seal clearance and the mass flow of fluid passing through the cavity. Current knife seal clearance height-to-stator span ratios for S1 and S2 are 1.75% and 1.85%, respectively. Additionally, the Purdue compressor features knife seals with double-tooth configurations, intended to reduce the cavity mass flow more than a single tooth configuration. The magnitude of leakage flow predicted in the *JACC* knife seal model at each point on the speedline is shown in Figure 3.18, with leakage mass flow plotted as a percent of the compressor inlet mass flow. The trend is nearly linear, with larger pressure gradients driving increased leakage flows at higher loading conditions. At Peak Efficiency Loading, the cavity leakage flows are 1.12% and 1.16% for S1 and S2, respectively.

Predicted leakage rates are higher than would be expected through stator cavity passages. As mentioned previously, the mixing of the secondary flow stream with the primary flow has substantial effects on the blade performance. A large tangential velocity component is imparted to the leakage flow due to viscous interactions with the rotating wheel drum. Cavity geometry also results in a very small axial velocity component. To analyze the effect of the predicted leakage flow on the blade performance, stator exit aerodynamic properties for a *JACC* simulation with the

knife seal model and a *JACC* simulation with zero cavity leakage flows, are sown for Peak Efficiency loading, Figure 3.19.

According to the computational predictions, the influence of the cavity leakage flow extends from the hub endwall all the way to midspan for tangential velocity and flow angle. The low momentum leakage flow re-entering the gas path creates a blockage in the hub region, which leads to increased incidence and ultimately greater flow separation in the hub endwall region. This is apparent as flow velocities are decreased in the lower 10% span. This forces more flow to higher spans where higher velocities are encountered from about 15% span to midspan. For both Stator 1 and Stator 2, the predicted cavity leakage flow changes the absolute flow angle by up to 20° compared to the same loading with a cavity leakage model. It is evident that secondary flows through the hub cavity influence the magnitude of stator hub corner separations, generating much larger separation regions.

3.5 Stator Surface Isentropic Mach Numbers and Incidence Evaluation

Flow separation can be influenced by many things. One property that tends to increase separation potential is high incidence levels. Incidence is a measure of the angular difference between the incoming air flow and the blade or vane leading edge metal angle. Different airfoil profiles have different optimum incidence values, but in general most airfoils have maximum performance at incidence values at or slightly less than zero degrees (Cumpsty, 2004). Higher incidence angles require more flow turning to follow the profile of the airfoil, and hence require higher momentum to follow the blade profile unseparated. For this reason, flows with higher incidence tend to separate prematurely compared to similar flows with lower incidence values.

Different airfoil designs have varying sensitivities to incidence levels, making it difficult to design to a predetermined incidence.

A useful tool for analyzing incidence and diffusion levels on a compressor blade or vane is the Isentropic Mach Number vs. Chord graph (Iso plot). Such a figure shows the isentropic Mach number of both the pressure and suction surfaces against axial chord location. The shape of the two curves near the leading edge region gives a qualitative measure of incidence. If the incoming flow is perfectly aligned with the leading edge metal angle (zero incidence) then the Mach number on the two airfoil sides will be identical right at the leading edge region before the suction side flow accelerates around the airfoil curvature. If the airflow approaching the blade or vane has a positive incidence then the stagnation point shifts to the pressure side of the leading edge and the suction side air flow accelerates around the leading edge at a higher Mach number. Figure 3.20 illustrates isentropic Mach number plots for zero incidence and positive incidence. Only the results of the embedded stage will be presented as both the R2 and S2 isentropic Mach number plots are representative of the other blade and vane rows.

Figure 3.21 shows Iso plots at several radial locations for R2 operating at Peak Efficiency Loading. At this loading, the hub regions at 10% and 20% span are operating at a somewhat high incidence while the rest of the span is operating with an incidence of only a few degrees. The region most susceptible to incidence induces separation is the tip region, and hence the rotors are not predicted to operate with large regions of separation. The Iso plots for S2 operating at Peak Efficiency Loading, Figure 3.22, show a different story. The 80% and 90% span regions of S2 operate at a high incidence level while the rest of the radial locations appear to read only slightly positive. Interestingly, previous analyses showed that the hub region of the stators produced large separations while the tip region separated much less. This is likely caused by the continued mixing of the stator shroud cavity leakage flow with the main stream through the stator passage.

Although the incidence at the hub does not appear to be unreasonably elevated, the continued mixing of the two streams through the passage reduces momentum to the point that separations occur. Incidence levels are much reduced at Nominal Loading, where the Iso plots for R2 and S2 are shown in Figure 3.23 and Figure 3.24, respectively. At this loading condition, R2 incidence levels are only slightly positive in the hub region and slightly negative to zero at all other radial locations. The slightly negative incidence levels are often targeted in the blade and vane design stage. The same trends exist in S2 as R2, but in reverse. All spanwise locations operate at slightly negative incidence levels except for at 90% span, which is only slightly positive. The incidence levels at Nominal loading are more in line with values typically sought for in the design phase of blade design.

3.6 Conclusion from Numerical Predictions of Aerodynamic Performance

JACC predictions of the Purdue 3-stage compressor agree well with measured results on an overall level. The computed compressor characteristic follows very closely the trend and shape of the measured curve. Individual stage characteristics also agree well, with only minor differences showing up at maximum loadings. The computational results show that Stage 3 is the weak stage, deteriorating in performance before the other stages, while experimental measurements show Stage 1 as the first to deteriorate in performance.

Looking more closely at individual blade row performance, *JACC* predicted rotor performance almost perfectly at each loading condition. Only slight variations occurred in the upper 15% span of the blade. These differences likely arise from *JACC* missing the mixing and losses generated by the interactions of the tip leakage vortex with the main gas path. The large majority of the spanwise predicted performance matched experimental measurements in shape, trend, and quantitative value. Stator performance predictions were not as good as the rotor

predictions. *JACC* results consistently showed large separations in the hub region and only minor separations in the tip region. While the predicted hub separations matched well with flow visualization experiments performed in the Purdue compressor, the large stator tip separations observed in the research compressor are not predicted in *JACC*. This is again likely a result of the computer model not fully capturing losses in the tip leakage vortex which could significantly influence stator performance and produce larger tip separations in downstream stators.

A knife seal leakage model implemented in the *JACC* simulations predicted mass flow rates of over 1% of the compressor inlet mass flow around the compressor design operating ranges. This large secondary flow alters the aerodynamics of the flow through the stator passage and produces much larger stator separations than *JACC* simulations run without accounting for leakage flow interactions.

Overall, *JACC* is a very effective tool in modeling compressor aerodynamics. Future work can be done to modify the model in an attempt to capture more of the losses associated with the tip leakage vortex. Greater losses in the tip region of the rotor blade rows would force larger separations in the stator tip regions, more closely matching experimental results. The additional blockage created in the tip region would force more mass flow toward the hub region and alleviate, to a degree, the predicted performance loss associated with very large separated regions at higher loadings.

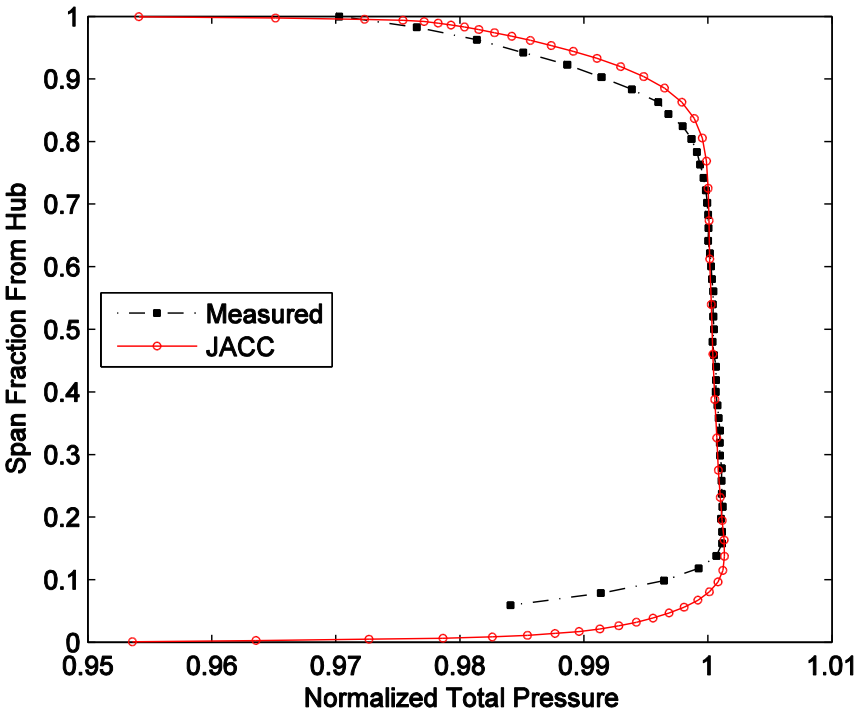

Figure 3.1: Total pressure profiles at IGV leading edge with *JACC* using incorrect inlet boundary conditions.

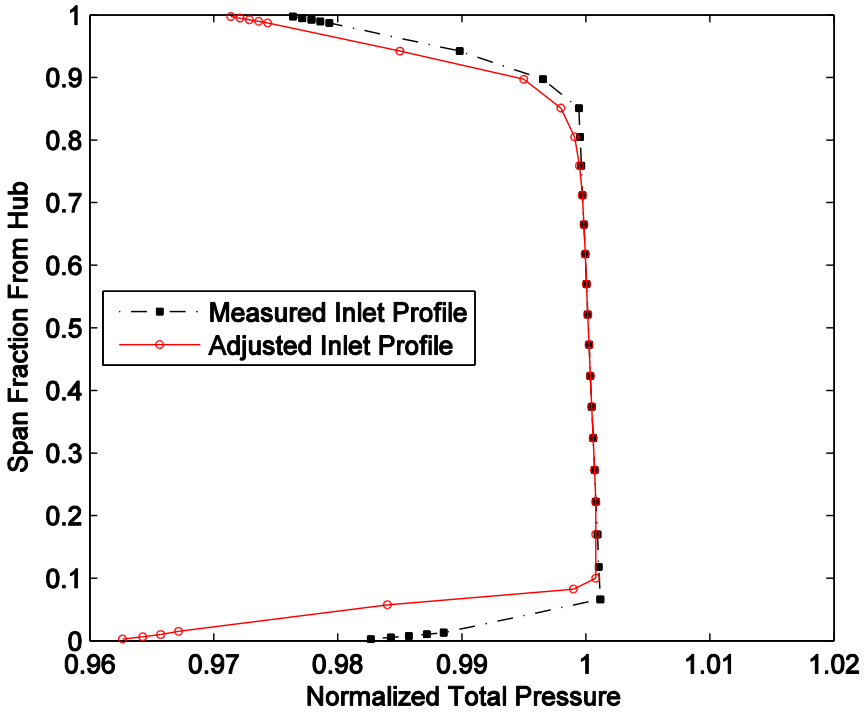

Figure 3.2: Comparison of measured inlet total pressure profile to modified profile used in *JACC*.

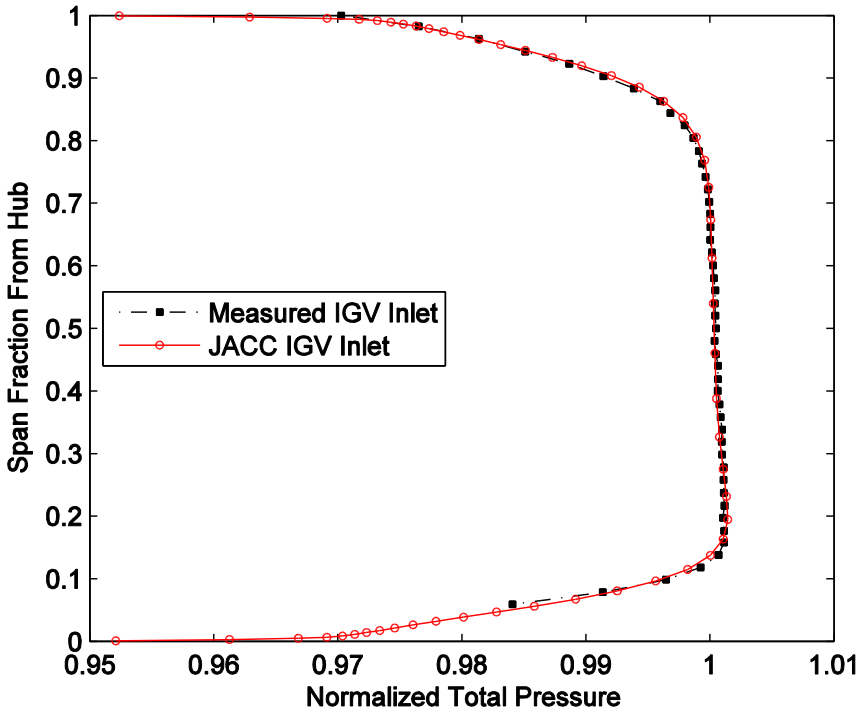

Figure 3.3: Radial total pressure profiles near IGV leading edge.

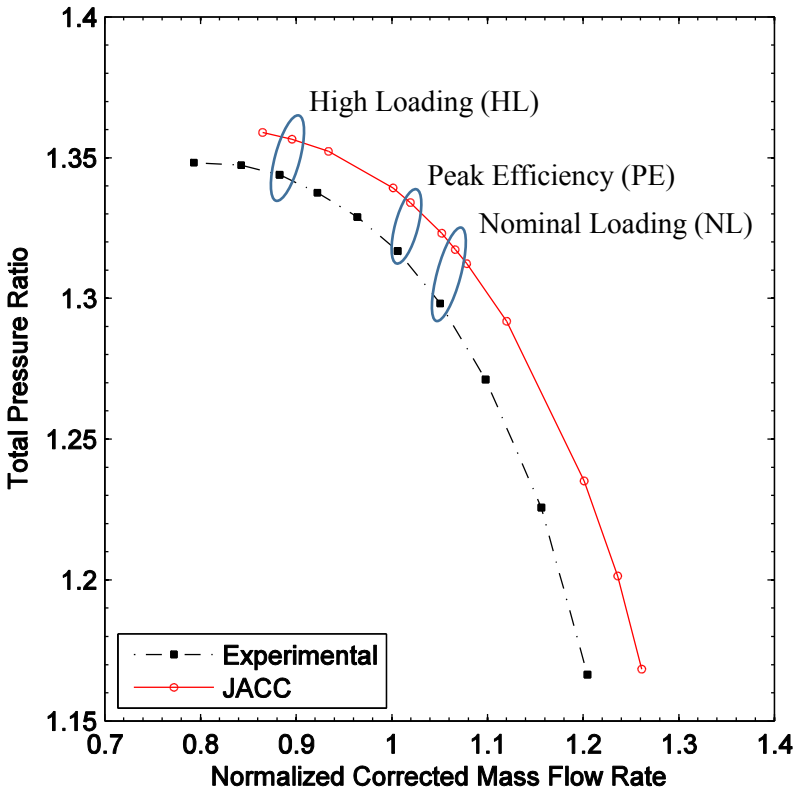

Figure 3.4: Comparison of compressor characteristics.

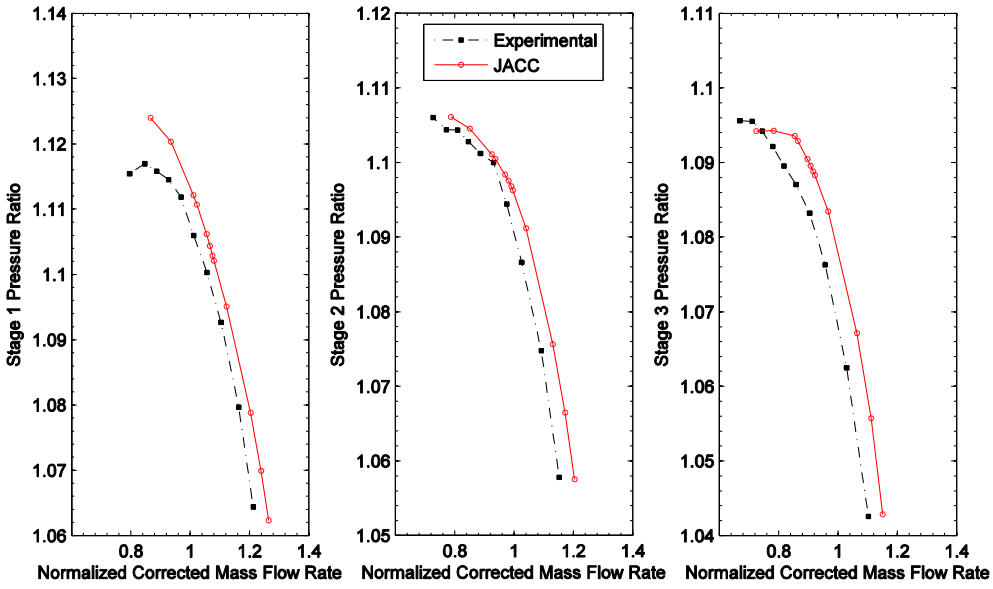

Figure 3.5: Individual stage characteristics, Stage 1 (left), Stage 2 (middle), Stage 3 (right).

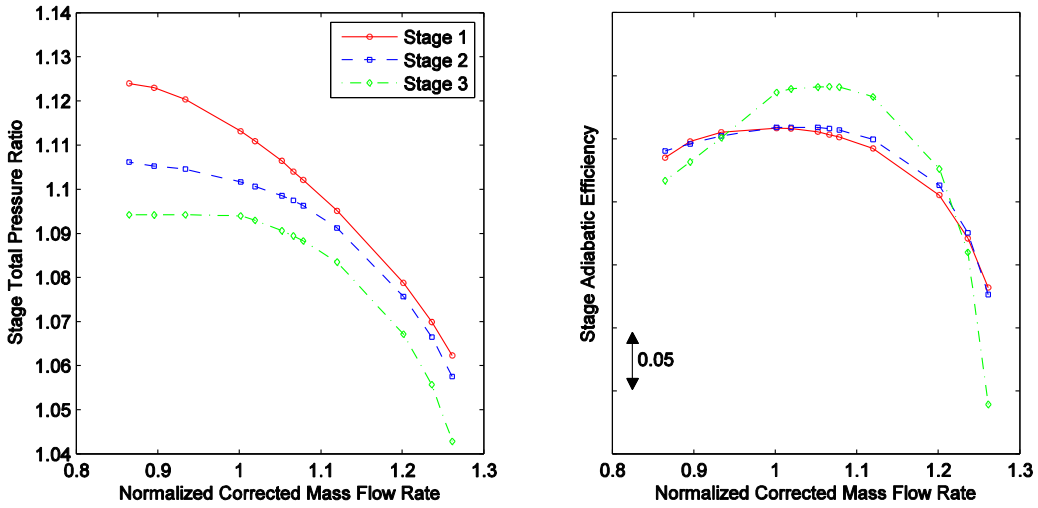

Figure 3.6: *JACC* stage characteristics and efficiency curves.

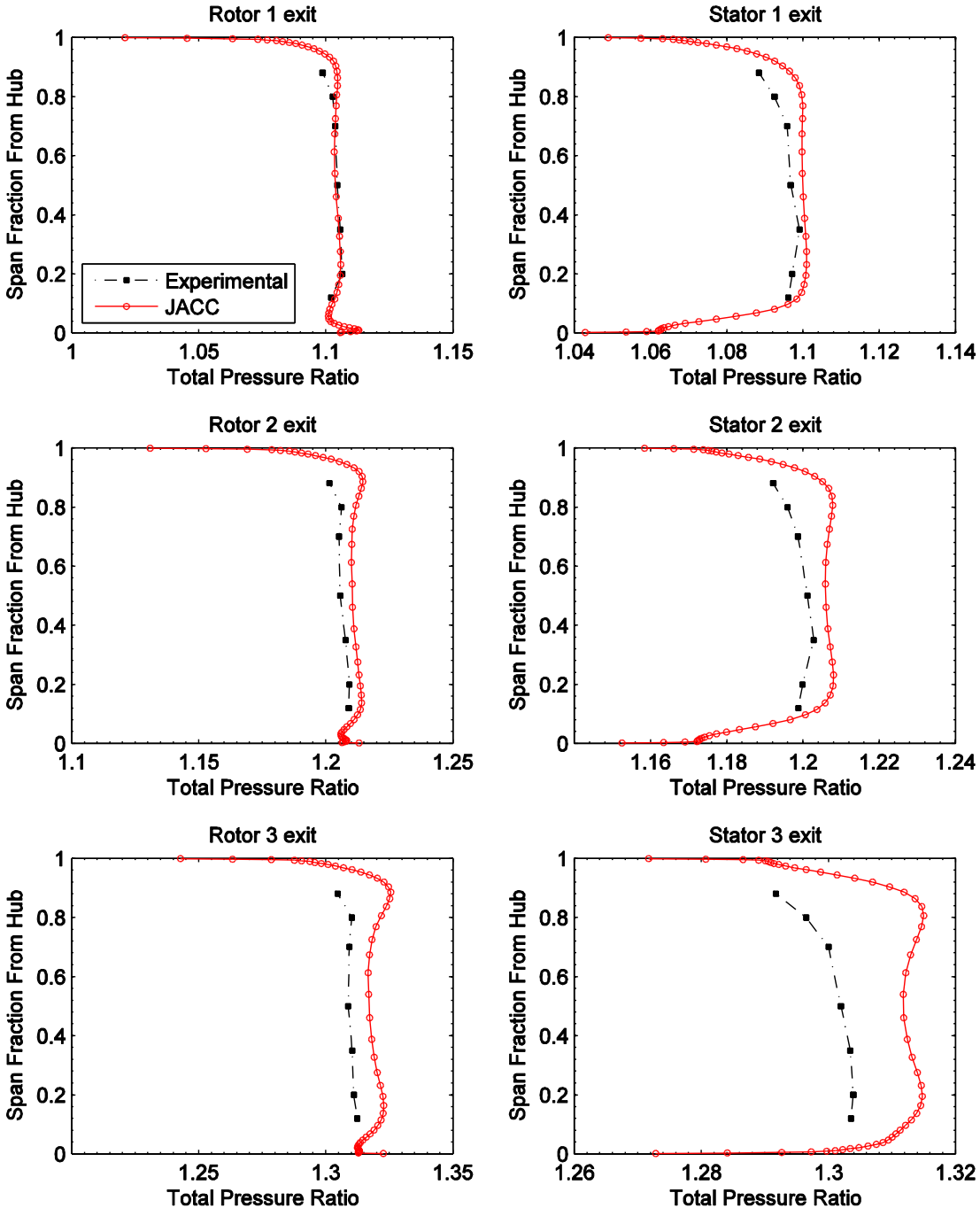

Figure 3.7 : Radial total pressure profile comparison at Nominal Loading condition.

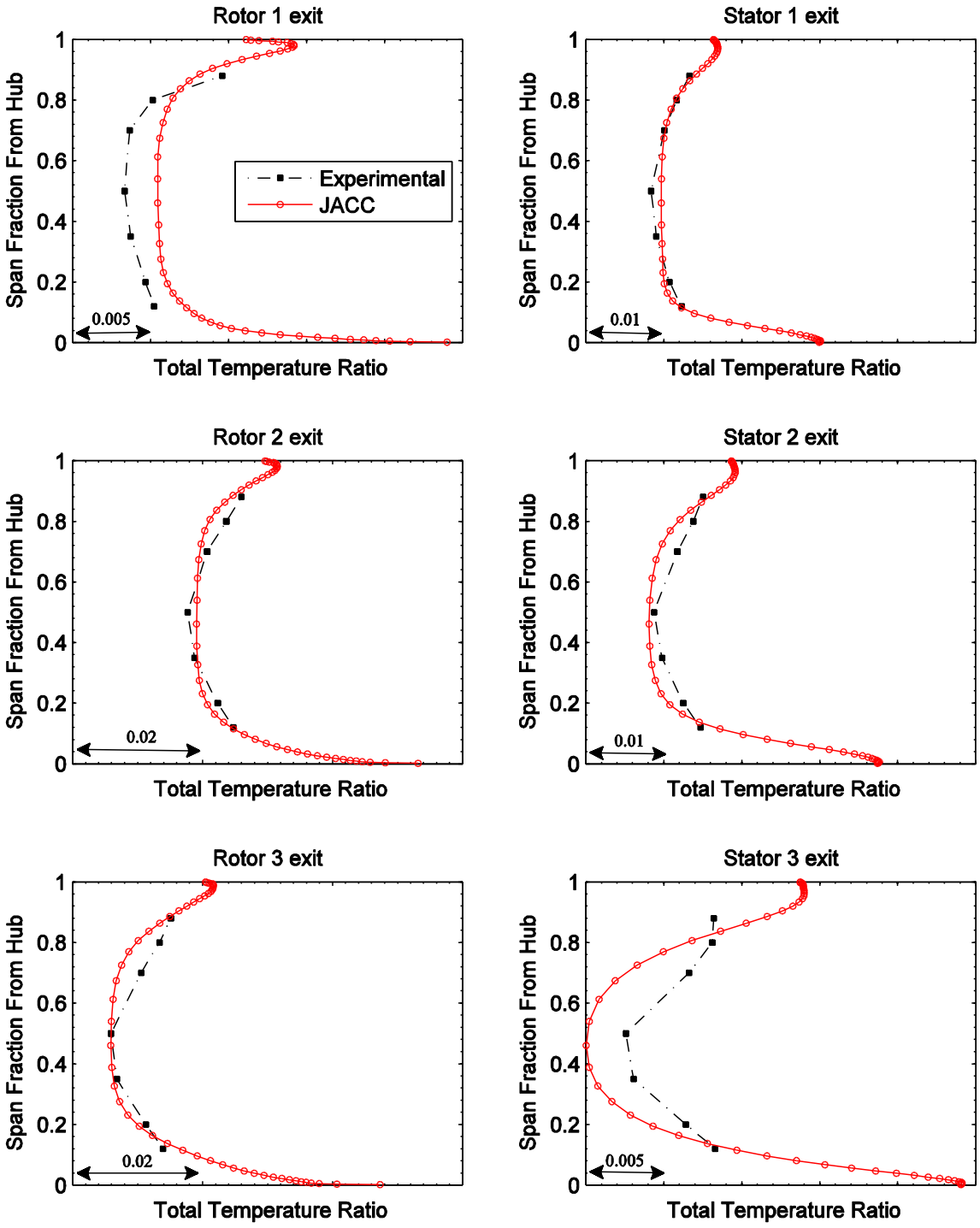

Figure 3.8: Radial total temperature profile at Nominal Loading condition.

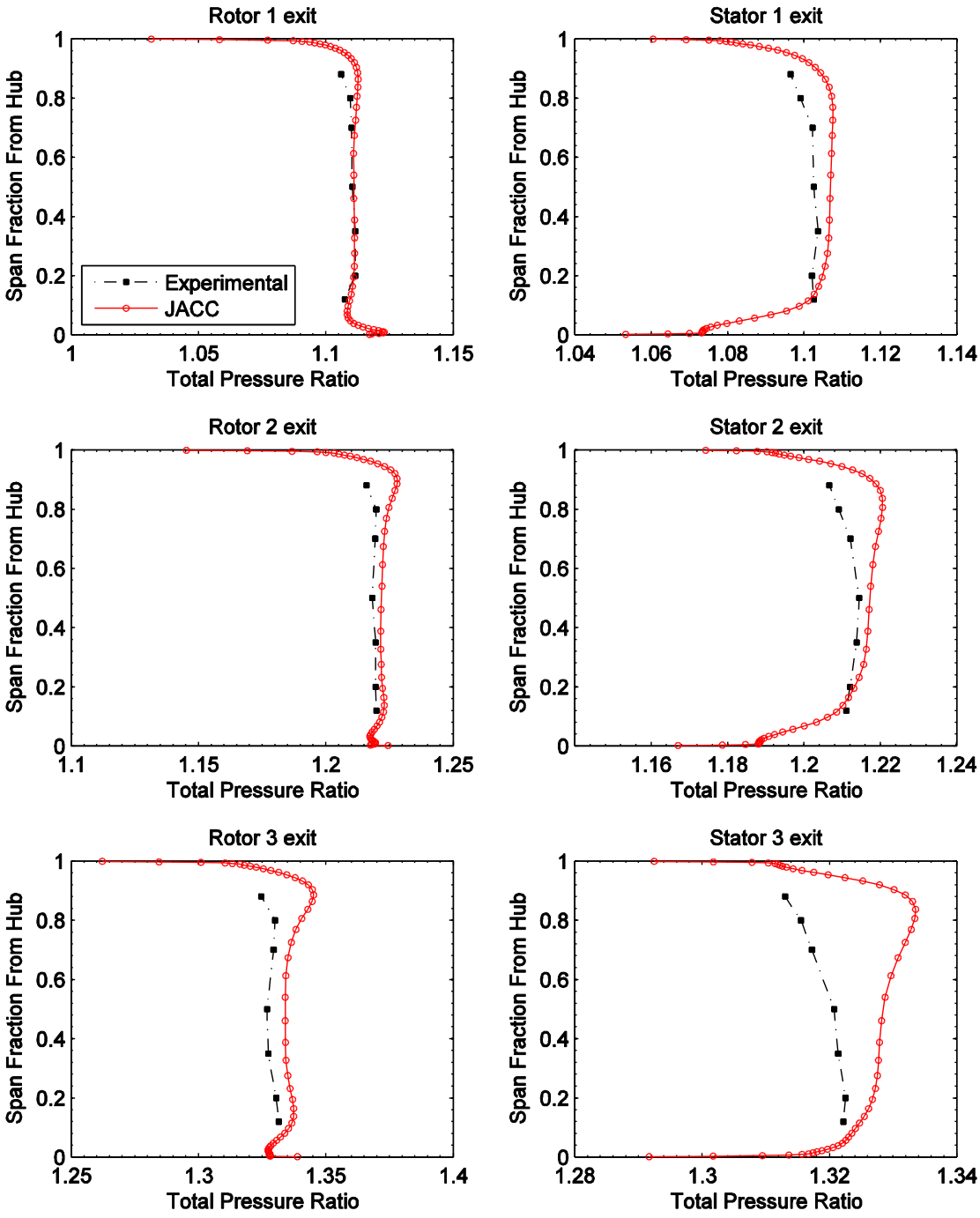

Figure 3.9: Radial total pressure profile comparison at Peak Efficiency loading condition.

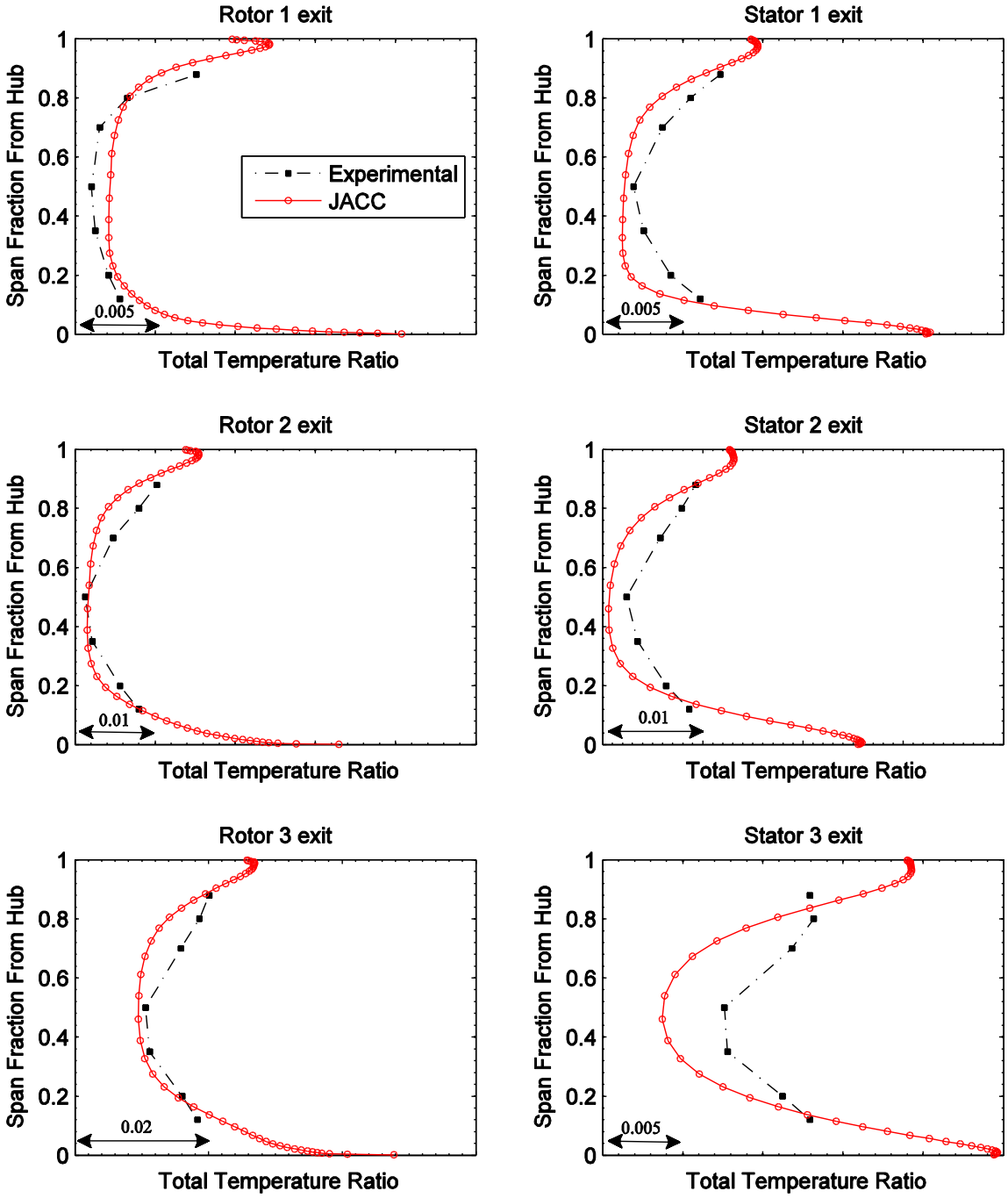

Figure 3.10: Radial total temperature profile comparison at Peak Efficiency loading condition.

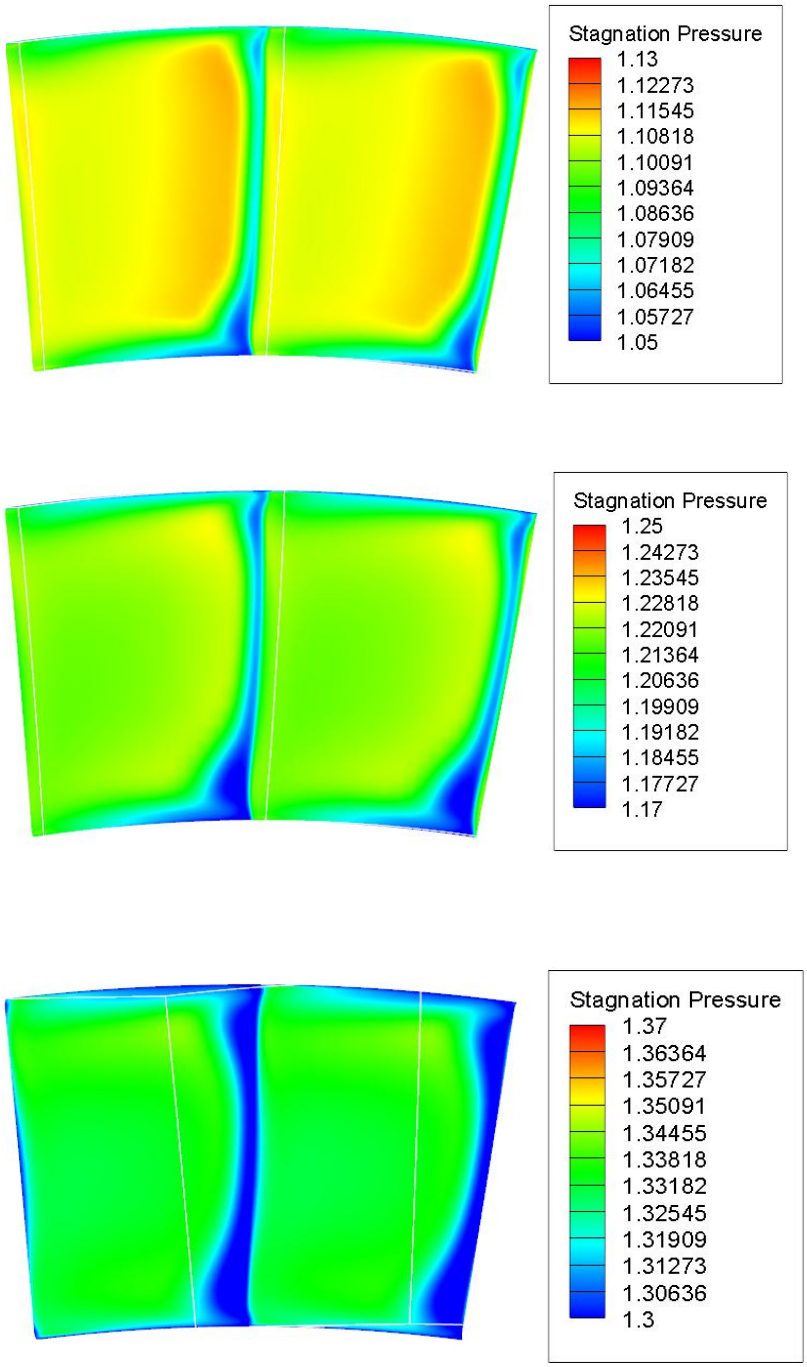

Figure 3.111: Stator exit total pressure contours at Peak Efficiency Loading condition. S1 exit (top), S2 exit (middle), S3 exit (bottom).

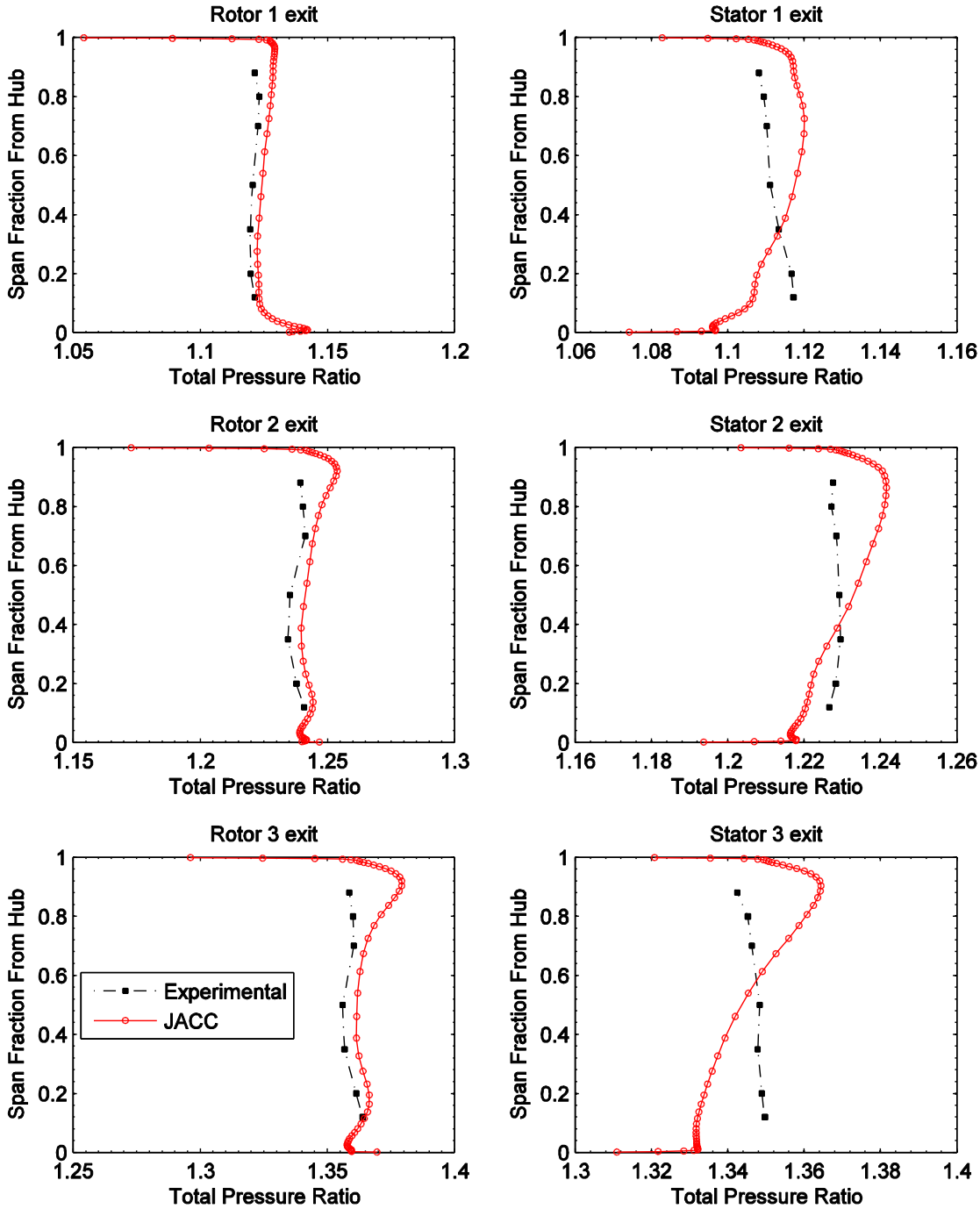

Figure 3.12: Radial profile comparison at High Loading condition.

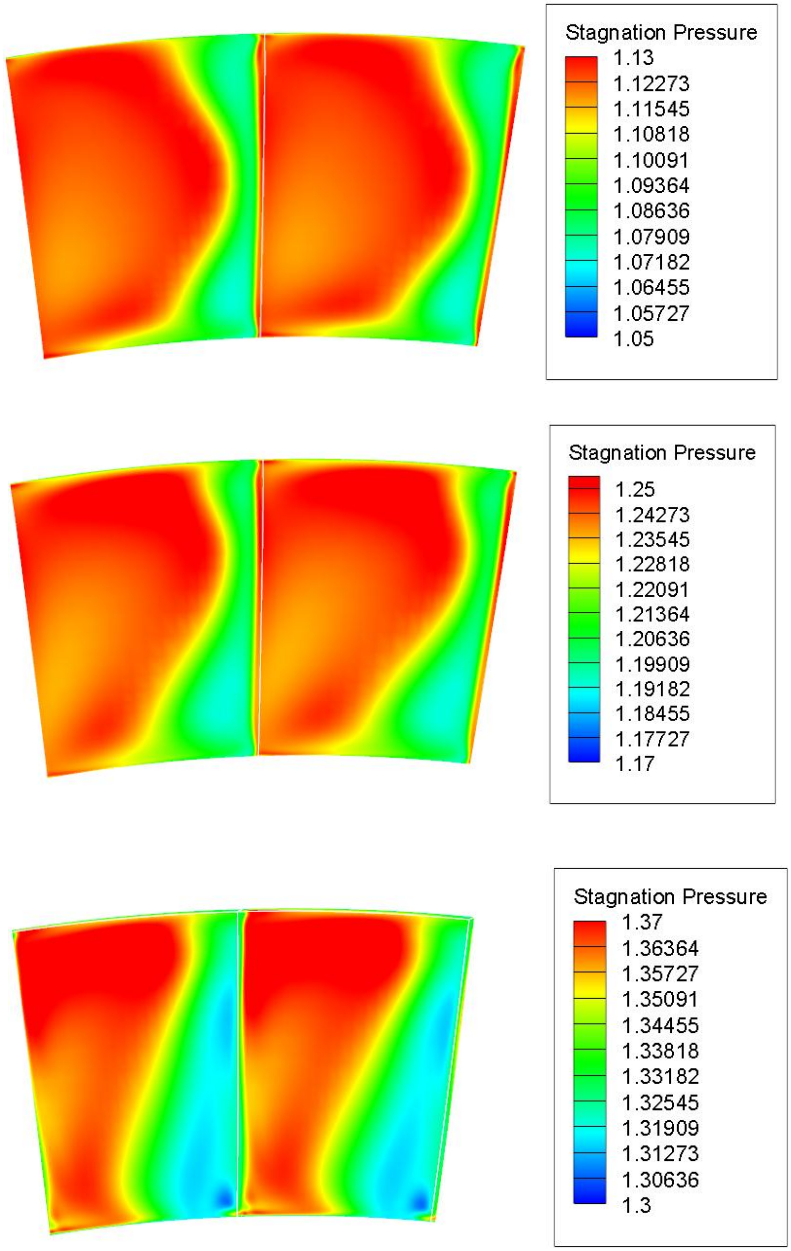

Figure 3.13: *JACC* total pressure contours at High Loading. S1 exit (top), S2 exit (middle), S3 exit (bottom).

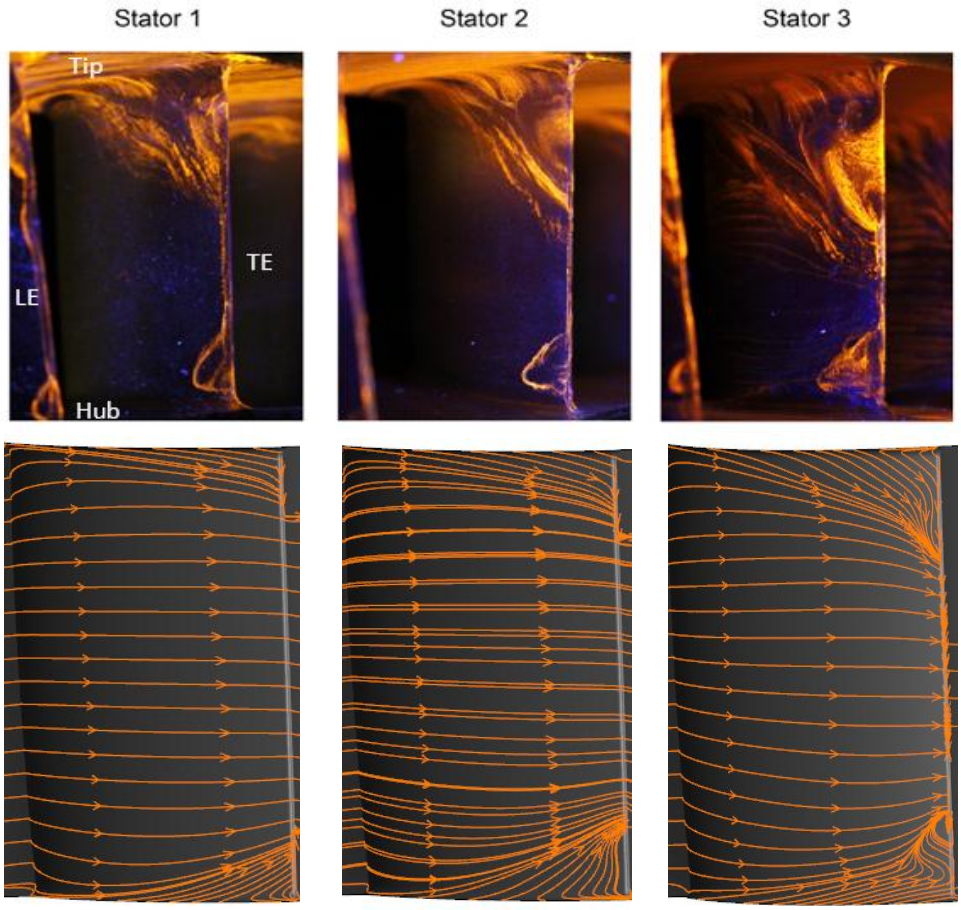

Figure 3.14: Comparison of separation patterns on suction surface at Nominal Loading. Experimental (top), *JACC* (bottom).

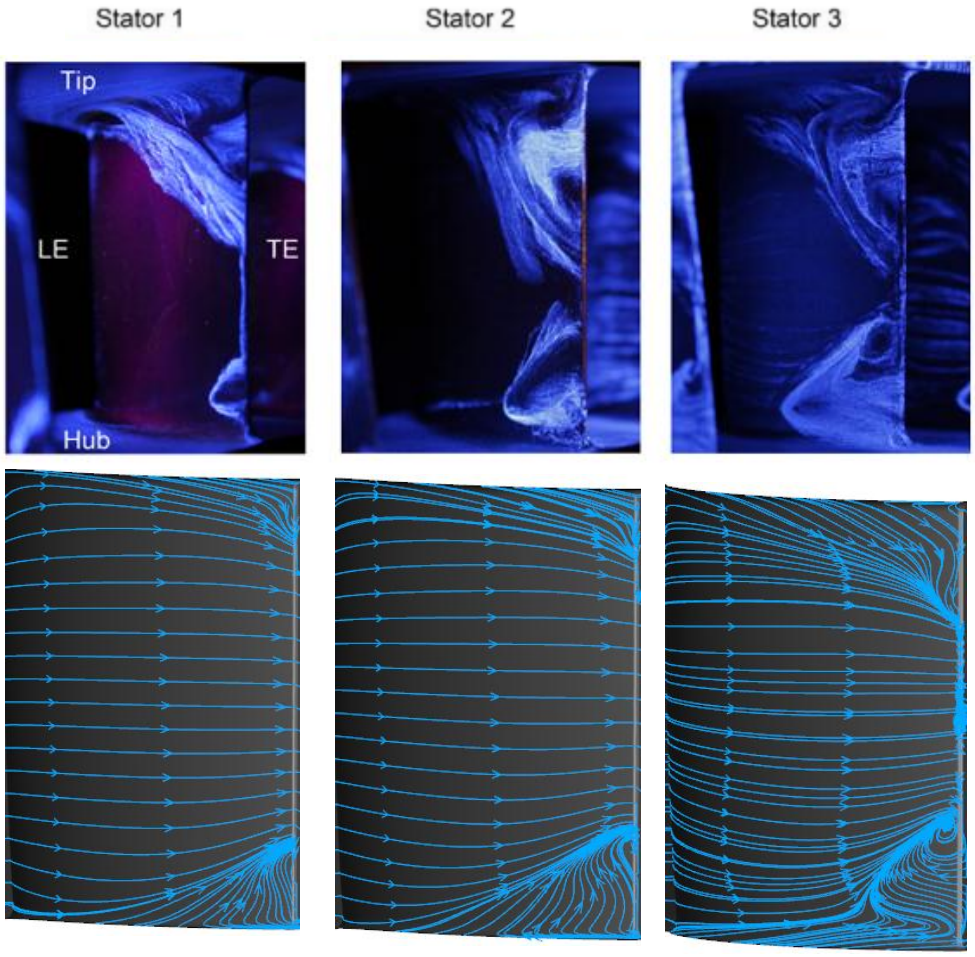

Figure 3.15: Comparison of separation patterns on suction surface at Peak Efficiency Loading. Experimental (top), *JACC* (bottom).

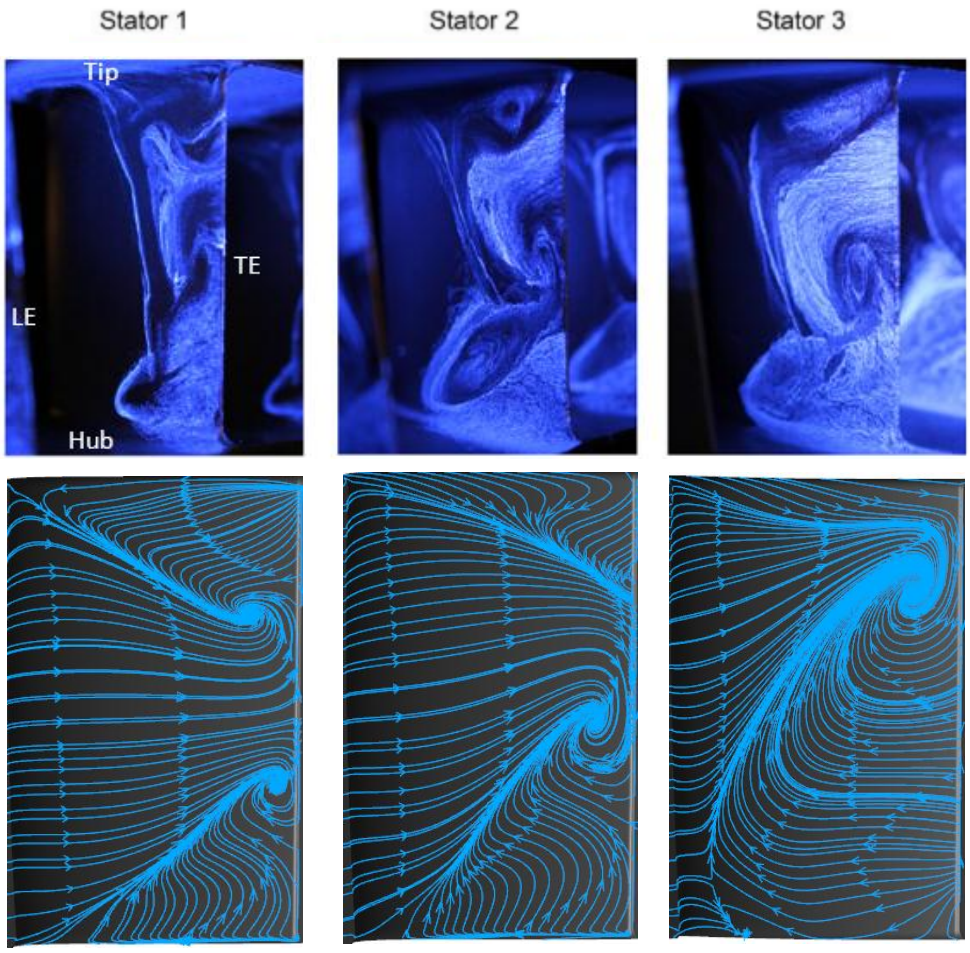

Figure 3.16: Comparison of separation patterns on suction surface at High Loading. Experimental (top), *JACC* (bottom).

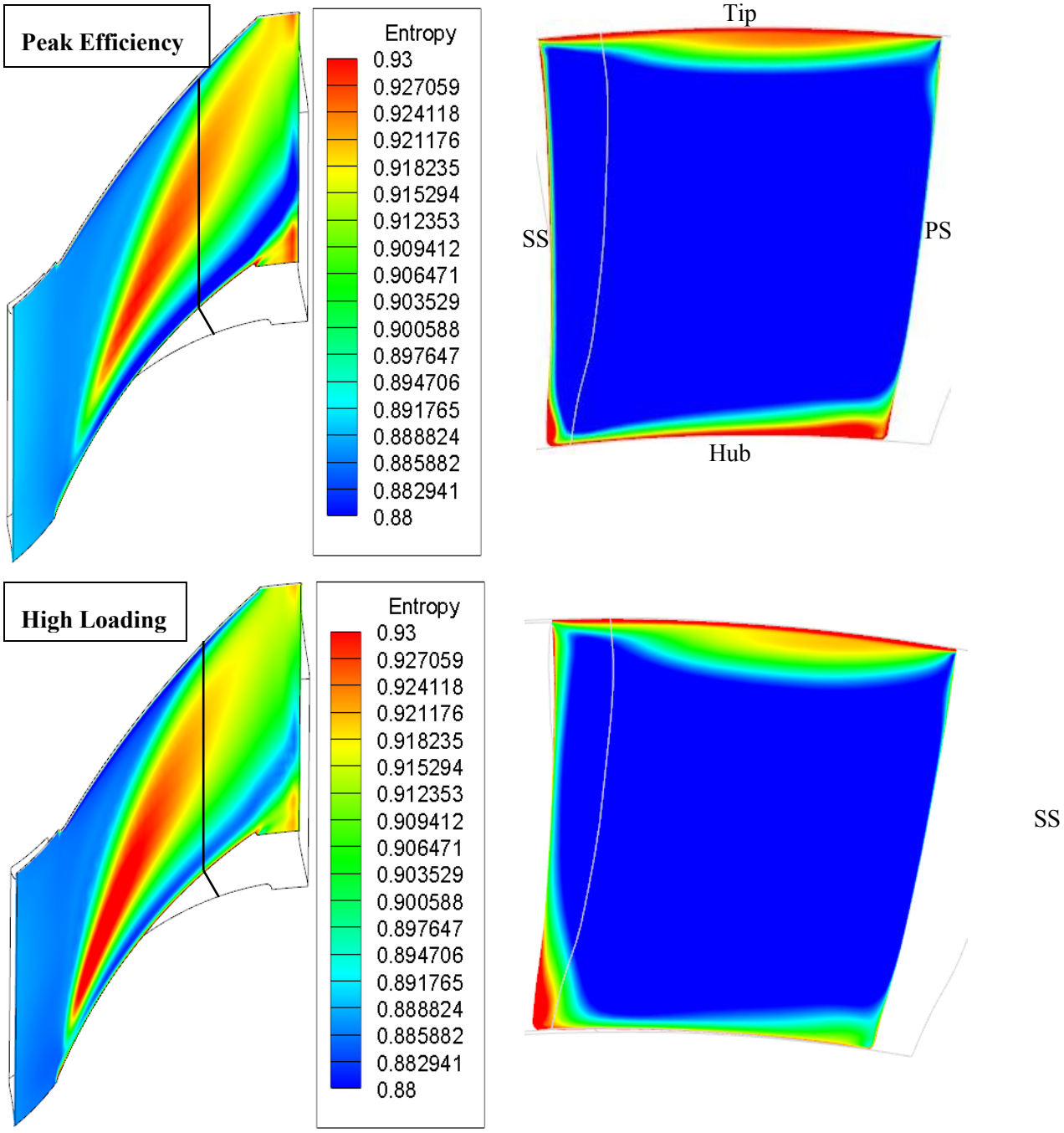

Figure 3.17: Computational results showing losses due to tip leakage vortex. 95% Span (left) 66% axial chord, marked by black line on left (right).

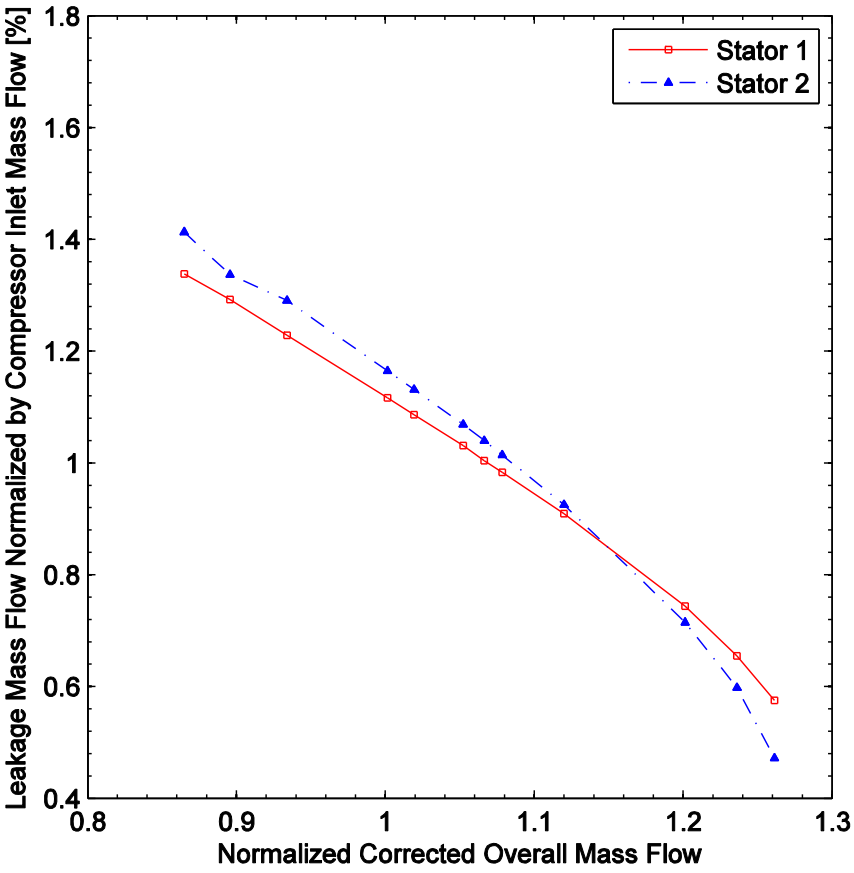

Figure 3.18: Normalized stator cavity leakage mass flow rates.

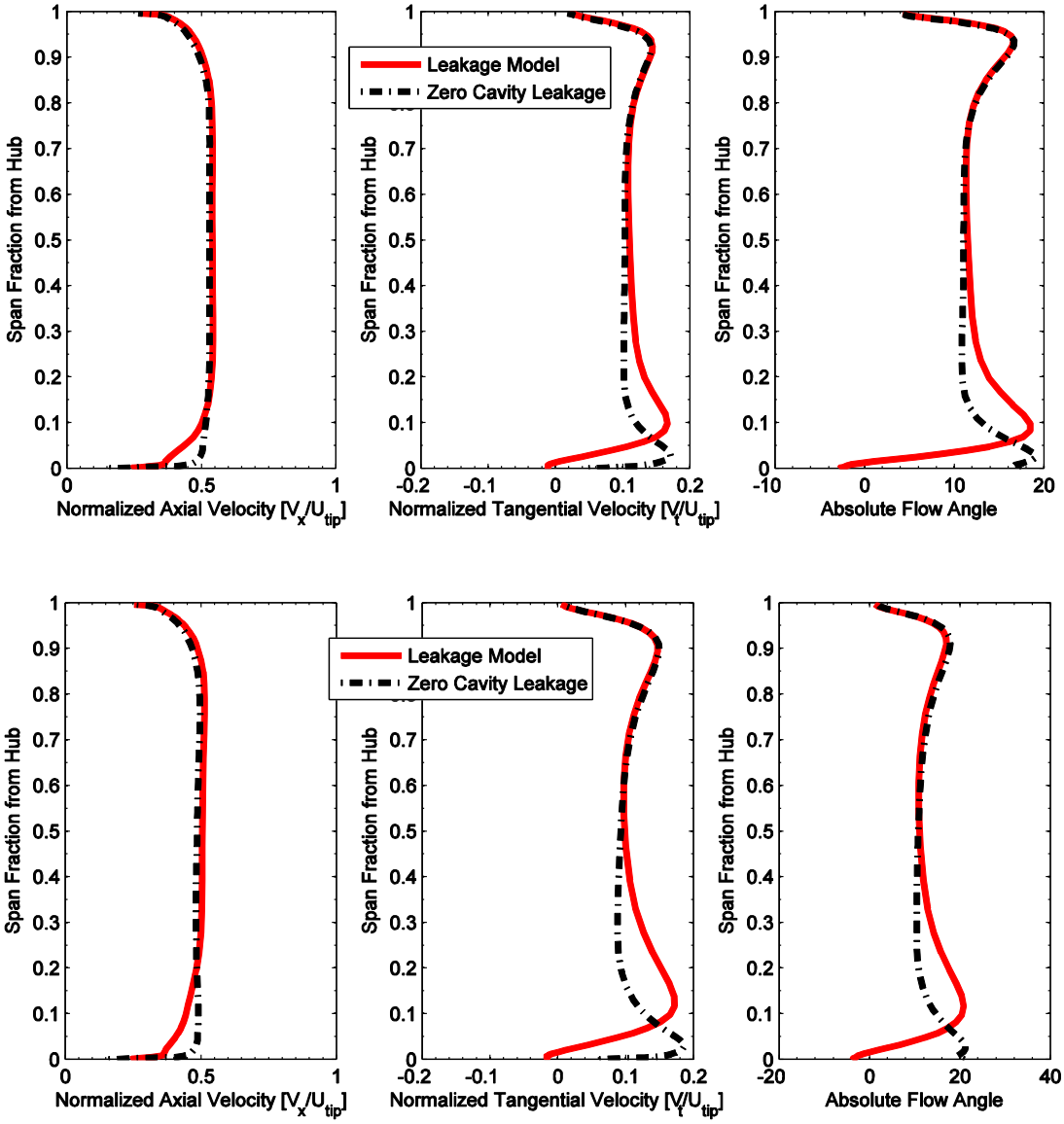

Figure 3.19: Comparison of flow properties at stator exit. S1 (top), S2 (bottom).

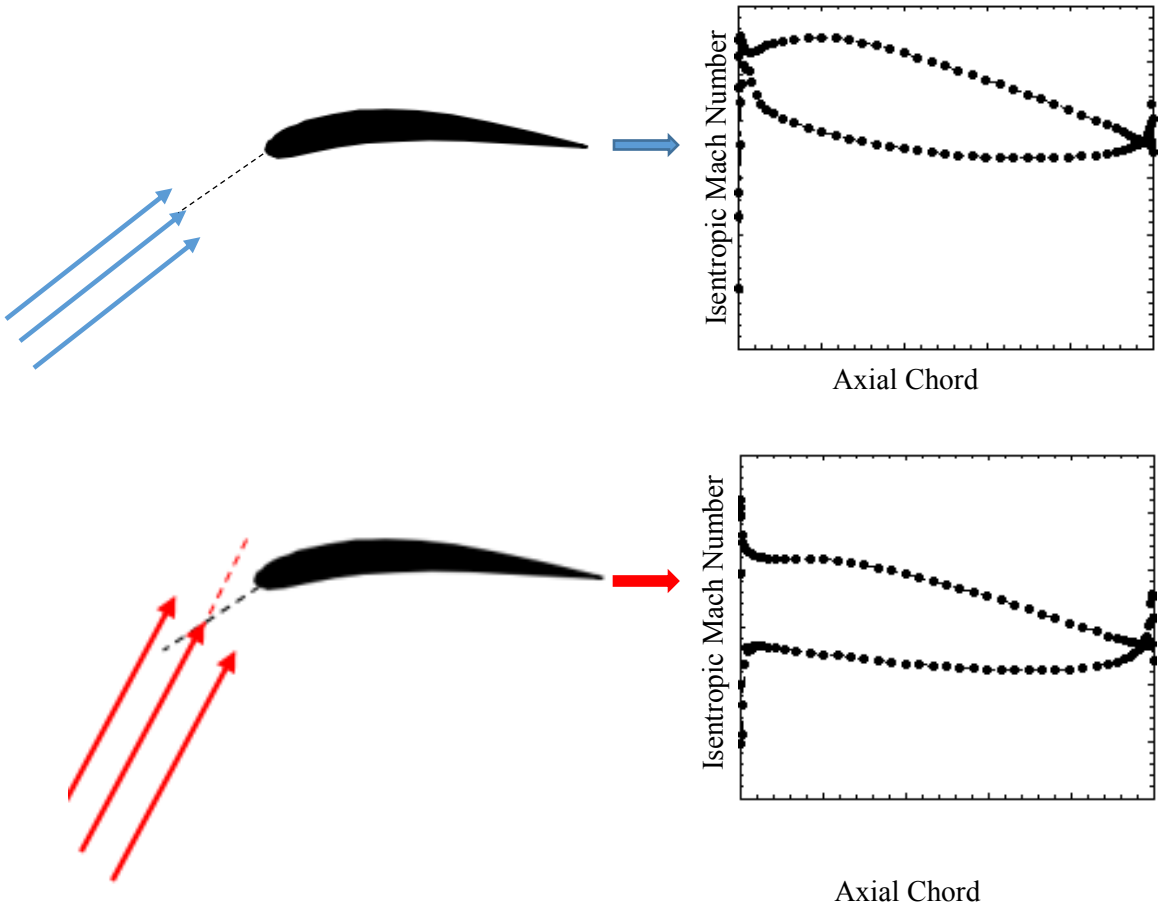

Figure 3.20: Effect of incidence on isentropic Mach number plots.

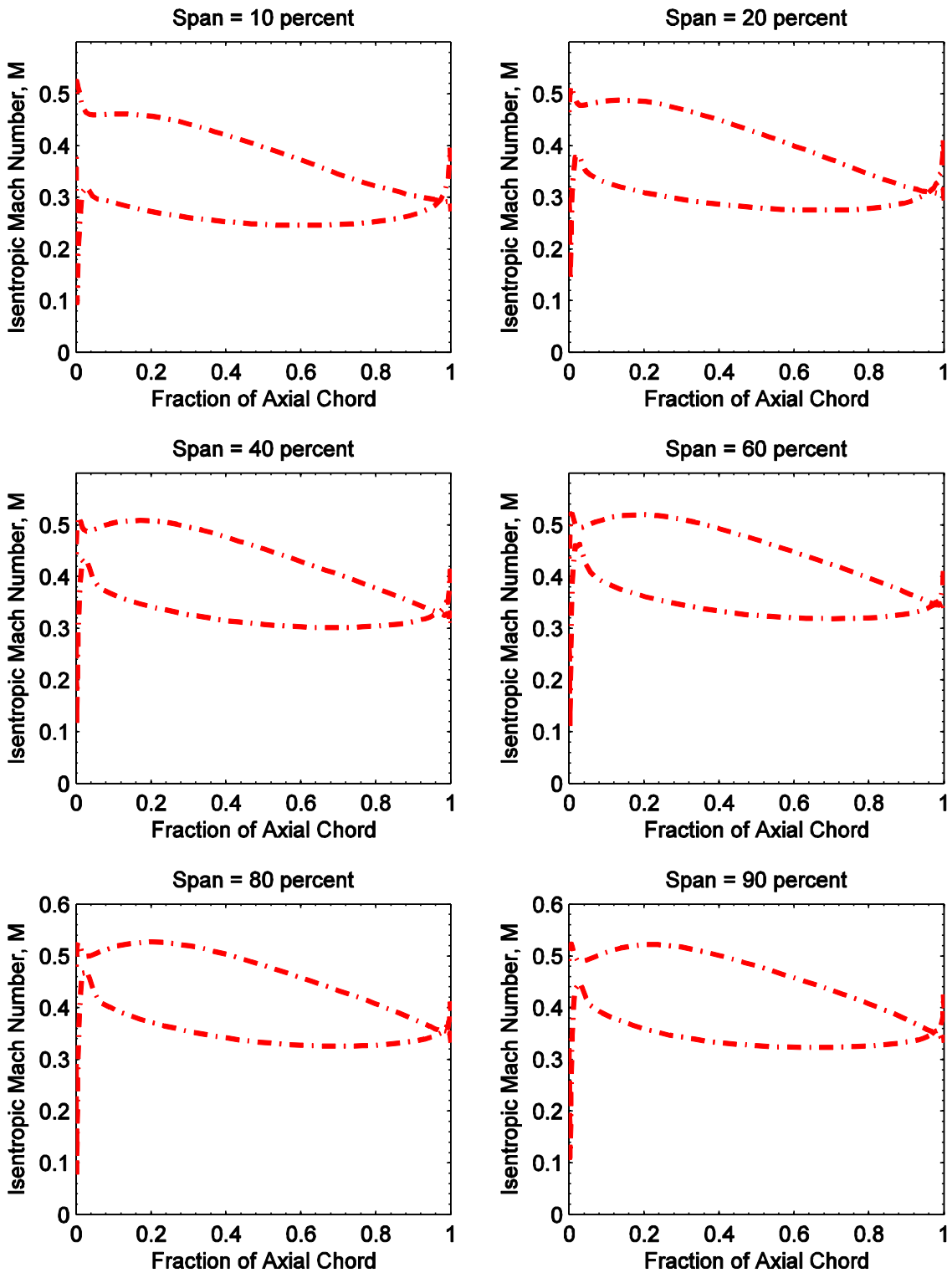

Figure 3.21: R2 isentropic Mach number plots at Peak Efficiency Loading.

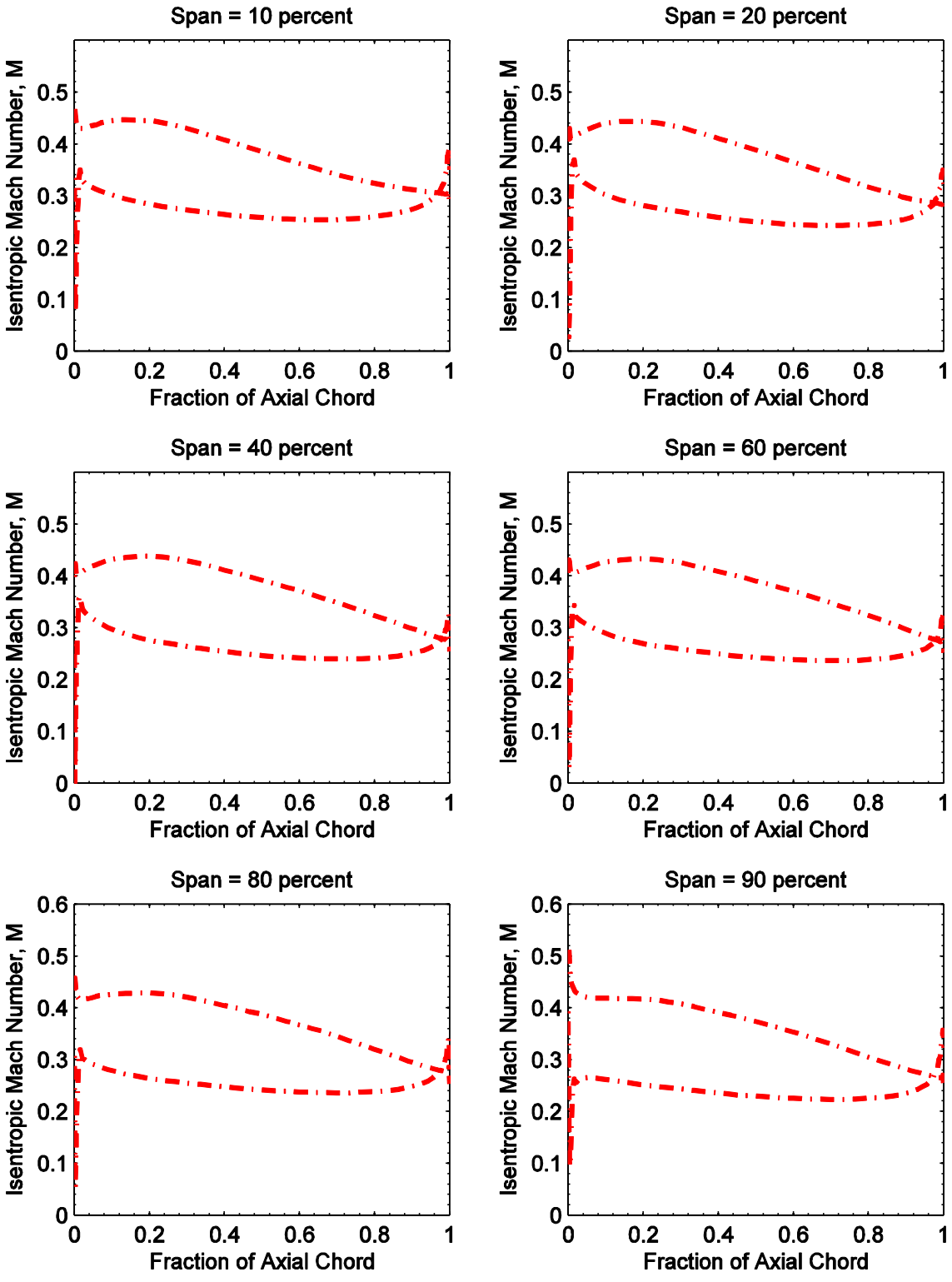

Figure 3.22: S2 isentropic Mach number plots at Peak Efficiency Loading.

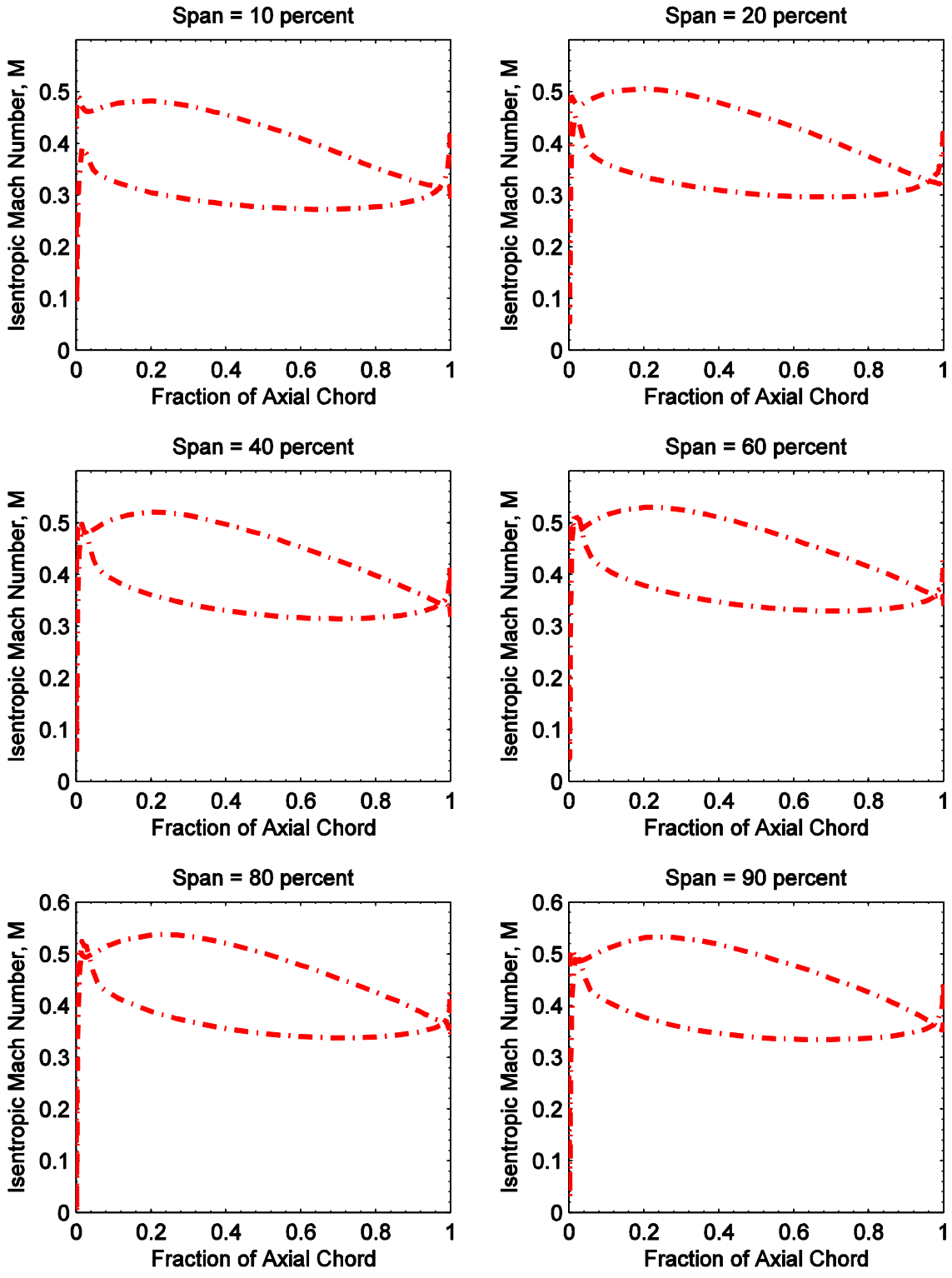

Figure 3.23: R2 isentropic Mach number plots at Nominal Loading.

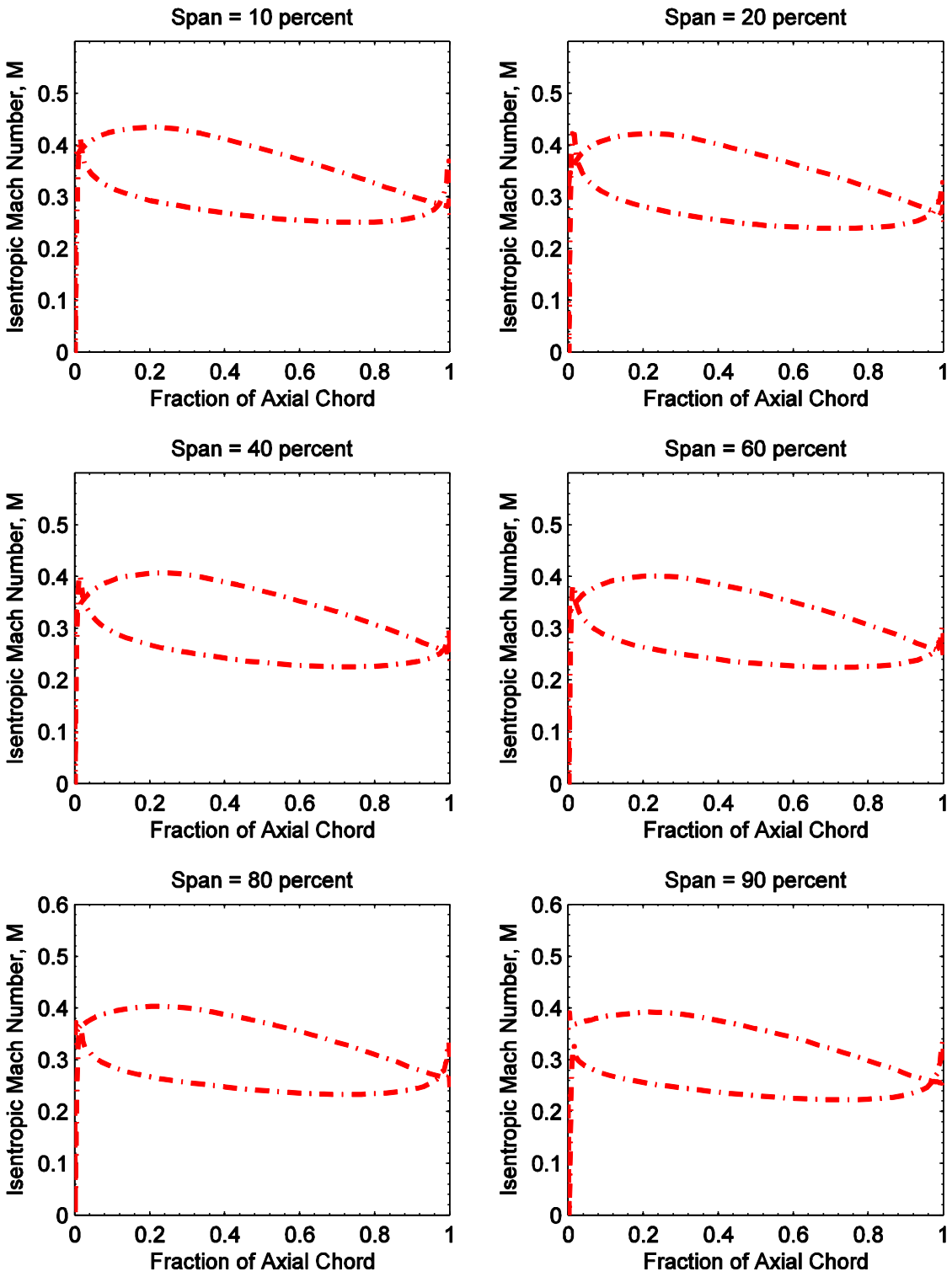

Figure 3.24: S2 isentropic Mach number plots at Nominal Loading.

CHAPTER 4: AEROMECHANICAL ANALYSIS OF ROTOR 2

Computational modeling of compressor forced response is a critical aspect of the design phase with engine companies relying more heavily on these computational results. The expense of conducting experimental forced response investigations throughout the design process is often prohibitive. At the same time, however, discovering unforeseen forced response phenomena during whole engine testing can set a program back many months or even a year. Therefore, it is imperative that computational modeling of aeromechanical behavior be reliable such that potentially dangerous resonant operating conditions can be identified and designed around. The difficulty in modeling these aeroelastic phenomena is the coupled interaction of unsteady fluid dynamics and structural dynamics. The unsteady nature of air flow through a compressor creates fluctuating surface pressures on the PS and SS of rotor blades. The two fluid disturbances most likely to excite rotor vibrations are viscous wakes from upstream stator rows and potential fields from both the upstream and downstream vane rows. Both of these flow structures contribute to unsteady surface pressures on the rotor blade, creating an oscillating blade force. As a rotor blade rotates it encounters these flow disturbances at a frequency dependent upon the rotational speed of the compressor. When a compressor rotates at a speed such that the rotor blades encounter these disturbances at a frequency associated with a blade mode of vibration, dangerous vibrations can occur.

Few complete data sets exist in open literature characterizing forced response in a high-speed multistage compressor. A recent experimental campaign at Purdue University has provided such a dataset, characterizing the forced response of the embedded rotor passing through resonance at the 1st Torsion mode (Murray, 2014 a). As both Stator 1 and Stator 2 have 44 vanes,

the 44EO excitation line on the R2 Campbell Diagram excites the 1T mode at 3710 rpm, Figure 4.1. Murray (2014, a) utilized both steady and unsteady instrumentation to measure the vortical and potential forcing functions which excite the vibrational response. A non-intrusive stress measurement system (NSMS), consisting of 8 light probes flush-mounted in the casing over R2 trailing edge, measured the vibrational amplitudes of each individual blade. This comprehensive data set provides a benchmark for which fluid-structure interaction computer codes can be validated. A comparison at loading conditions at which data are compared is shown in Table 4.1.

Figure 4.2 shows computational results of vortical and potential disturbances at 50% span for the Nominal Loading case. Only the S1-R2-S2 blade rows are considered in this simulation of the R2 forced response. Entropy contours in the top image are useful in tracking the convection of vortical disturbances through downstream bladerows. At any given instant, there exist one to two Stator 1 wakes in the Rotor 2 passage. The interference of the S1 wakes with R2 surfaces create an unsteady pressure distribution that causes a cyclic force on the blades. The bottom image of Figure 5.2 shows static pressure contours between R2 trailing edge and S2 leading edge. Increased regions of static pressure near the S2 leading edge indicate the potential field, which propagates upstream as acoustic waves to excite the R2 1T mode.

4.1 Vortical Forcing Function

The aerodynamic forcing due to the convection of upstream wakes is the strongest source of forcing. As such, it is important for computational models to predict with relative accuracy the size and strength of the vortical gusts, which are commonly measured in terms of total pressure and velocity deficits. These flow structures are also the most difficult to accurately predict as they are influenced heavily by turbulence levels, transitions, boundary layer growth and blade row

interactions, which can be difficult to capture with the mesh resolution commonly employed in turbomachinery simulations.

Figure 4.3 shows the absolute velocity for 80% span at the sliding plane mid-gap between S1 and R2. Even though the 44 S1 vanes are symmetrically spaced and the flow at the inlet of S1 is essentially uniform, the absolute velocity profile is very much non uniform. Blade row interactions create this non-uniformity. The potential field generated by the downstream rotating rotor row interacts with the S1 wakes creating a sinusoidal pattern in the total velocity wake profile. The influence of R2 is further evident in the frequency spectrum of this wake structure, shown in Figure 4.4. As expected the vane pass frequency (VPF) and its harmonics dominate the frequency spectrum with large amplitude peaks at 44/rev, 88/rev, 132/rev, etc. Also present in the frequency domain is the R2 blade pass frequency (BPF) and its harmonics. Distinct amplitude peaks are present at frequencies of 33/rev, 66/rev, and 99/rev, though the amplitude of these harmonics decay rapidly and are inconsequential after 99/rev. Direct comparisons to S1 wake measurements taken on the Purdue multistage compressor are best accomplished by analyzing CFD results in the steady state. In this manner any R2 harmonics are removed and the results uniquely characterize the S1 vortical disturbances.

Figure 4.5 compares the experimentally measured total pressure wake profile to the steady-state computationally predicted profile at Nominal Loading. At midspan the predicted profile is very similar in wake width, but clearly larger in the depth of the total pressure deficit, while at 80% span the wake profile is wider and shallower than the measured wake. This introduces an interesting trend in the computed results. The 80% span wake profile has a shallower wake deficit than the midspan profile. The aeroelastic CFD solver predicts a larger separation in the tip region of S1 than experimental measurements indicate. Recirculating fluid in the separated region enhances mixing and dissipation, leading to a modest total pressure recovery

of the wake profile in this region. This trend is not followed in the experimental measurements as the 80% span wake is moderately deeper than at the midspan wake structure. Wake profiles at High Loading are shown in Figure 4.6, with similar trends to those at NL. Midspan wakes compare reasonably well in both width and depth while the predicted wake at 80% span is wider and shallower than experimental measurements. These results again show that the computational model predicts a slightly larger separation in the tip region at HL, leading to an increased wake dissipation and shallower total pressure deficit. The effect of these wake shape differences on the aerodynamic forcing can be analyzed by investigating the frequency content. The mode of interest in this analysis is the 1st Torsion mode, excited by 44EO excitation line. This excitation line corresponds to the 44/rev component of the frequency spectrum. Hence, the amplitude of the 44/rev component is the driving vortical force which excites the 1T blade mode at an RPM of 3710.

Figure 4.7 presents the frequency spectrum of the steady-state total pressure wakes at NL. First, note that the 0th harmonic amplitude (associated with the signal mean level) was too large to fit on an appropriate scale and is, therefore, not included in these figures. At the 44/rev component, differences in the amplitude are small, a 20% increase at midspan and only 5% at 80% span. Differences on this scale would not be expected to make a noticeable difference in aerodynamic forcing on the R2 blades. The predicted midspan wake (Figure 4.5) was deeper and narrower than the measured profile, meaning that more energy (total amplitudes) should exist in the frequency domain. This is evident by a higher computational amplitude at each of the 7 harmonics shown in the plot. At 80% span the predicted wake was wider and shallower. Thus, less total energy should be present in the computational results. Even with reduced overall amplitudes, the wider wake shape forces more energy into the lower harmonics and is evident by larger CFD amplitudes at the first two harmonics. At High Loading the differences in the frequency spectrum are more substantial, Figure 4.8. At midspan the predicted 44/rev component

is 25% lower than experimentally measured while at 80% span the computed amplitude is nearly 55% lower than the measured amplitude. This is attributed, in part, to the difficulty of CFD to predict accurate aerodynamics as near stall conditions are approached. Since numerical stall always occurs at lower loadings than actual compressors stall, matching the experimental HL condition is closer to a near stall condition in the computational domain. Thus, CFD results at this HL condition may have larger discrepancies than at NL. As the computed wake at midspan was deeper than the measured, the computed spectrum has an overall greater amplitude sum. The reverse is true at the higher spanwise location.

A second common method of measuring the strength of vortical disturbances is to analyze the velocity wake profile. Wakes are characterized by a velocity deficit as the viscous nature of blade surfaces cause low momentum, boundary layer fluid to shed from the trailing edge. These velocity deficits are measured in the absolute frame of reference. In the relative, or rotational frame of reference (as experienced by a rotor), an absolute frame velocity deficit becomes an increase in relative frame flow angle and causes increased blade incidence. An increase in blade incidence changes the chordwise distribution of surface pressures on the rotor. Each instance a rotor blade chops through a propagating wake the surface pressures fluctuate, creating a cyclic force on the blades that can induce resonant vibrations when occurring at natural blade frequencies.

Figure 4.9 shows the absolute velocity wake profile at Nominal Loading. Although similar trends exist as were present in the total pressure profiles, the wake profiles in the freestream region agree more closely with velocity profiles measured in the compressor. At midspan the computed velocity wake is again slightly deeper and narrower, while at 80% span the CFD wakes are slightly wider and shallower. At High Loading the trends are again similar, Figure 4.10. At the midspan location the computed wake aligns very closely in depth to the

measured profile, but is still significantly narrower. Wake profiles near the tip region follow prior trends, with a higher level of wake dissipation present in the CFD wake structure to produce a shallower velocity deficit.

The frequency spectra of the velocity wakes are presented in Figure 4.11 for Nominal Loading and Figure 4.12 for High Loading. The difference in the 44/rev component amplitude at NL is less than 10 % at midspan and 35% at 80% span. Observing the trend of the frequency spectrum at 80% span, the computational results follow very closely the experimental results measured on the Purdue compressor. At HL the 44/rev difference at quite significant, with relative errors on the order of 60%. The driving force behind these computational differences is the narrowness of the velocity wake at midspan and the lack of wake depth at 80% span.

Analyzing S1 wakes yields valuable insight into the nature of the vortical disturbance which excites the rotor resonance conditions. The aeroelastic CFD code used in this work tended to predict deeper and narrower wakes at midspan and wider and shallower wakes at 80% span. However, analyzing the frequency content of the vortical disturbances showed that at the 44/rev frequency component the predicted amplitudes matched quite well at NL conditions. Therefore, the predicted unsteady surface forces on R2 due to vortical gusts should be very comparable to actual surface forces present in the compressor. Comparisons made at High Loading were not as reliable, suggesting that the predicted forced response may underestimate, to a degree, the forced response of Rotor 2 at the 1T mode.

4.2 Potential Forcing Function

The second aerodynamic forcing contribution comes from potential fields, or acoustic waves, caused by the presence of solid bodies in a moving fluid. The presence of a solid body

causes streamlines to shift, generating an increased static pressure region in close proximity to the airfoil leading or trailing edge. Both S1 and S2 generate potential fields, though the relative strength of the S1 potential field is small and, therefore, is neglected in this analysis. The strength of potential disturbances are generally analyzed by viewing the static pressure field across a vane passage or by analyzing the change in absolute flow angle caused by the potential field. These acoustic disturbances decay exponentially in time. However, modern trends in compressor design minimize the axial spacing between adjacent blade rows, strengthening the potential forcing and increasing its contribution to forced response. Murray (2014, a) analyzed both the casing static pressure mid gap between R2 and S2, as well as flow angles at two spanwise locations between R2 and S2, to characterize the strength of the potential forcing on R2.

Figure 4.13 compares casing static pressure measurements for a single vane passage at a location mid-gap between R2 TE and S2 LE. Both Nominal and High Loading conditions are considered. The computed potential field is much stronger than the measured values. At NL, the strength of the potential field increases the normalized static pressure by 0.09, nearly three times the measured increase. In this configuration the leading edges of S2 would be located at 0% Vane Passage and 100% Vane Passage, marked by increased static pressure. As noted previously, the overall total pressure ratio is larger in the CFD model than actually occurs in the compressor. As a result, the pressure at the exit of R2 will be larger in the computational results. As the predicted normalized static pressure will be larger than measured values, analyzing the difference between the maximum and minimum normalized static pressure provides a better comparison of the potential field strength. At High Loading conditions, the static pressure field follows a similar trend. Again, the predicted normalized static pressure has much larger variations than the measured static pressure field, indicating a stronger predicted potential forcing function. The predicted profile for a single vane passage has a normalized static pressure variation of 0.012, nearly twice that of the measured static pressure profile. The foregoing analysis suggests that

CFD over-predicts the potential forcing strength from the downstream stator row on R2. However, analyzing the effect of the potential field on the absolute flow angle yields a much closer comparison.

Figure 4.14 shows the measured and computed absolute flow angles at NL. The shape of the computed profile matches very closely the shape of the measured profile. In this configuration, the leading edge of the S2 vane is at about 20% Vane Passage. At 50% span the flow angle shift caused by the potential field is exactly the same between CFD and actual measurements, at 2.16°. Likewise, at 80% span the potential field causes a flow angle shift of 2.65° while measured results show a shift of only 0.5° more. Figure 4.15 shows the same results at the High Loading condition. Again, the midspan predicted potential field produces very similar flow angles to measured results. Murray (2014, a) measured a 3.12° change in absolute flow angle as a result of the S2 potential field, compared to 2.91° degrees predicted computationally. The shape of both flow angle profiles agree well. The largest discrepancy occurs at 80% span where the measured change in absolute flow angle is 1° greater than that predicted by the aeroelastic CFD code.

Comparing the strength of the S2 potential field in terms of its effect on the absolute flow angle shows that the predicted forcing function is very close to the measured parameters. The differences between maximum and minimum flow angles across a S2 vane passage are small, with the CFD results slightly under-predicting the angle shift. Using these results, the relative forcing of the S2 potential field on R2 compares well to experimental measurements.

4.3 R2 Vibrational Response

The unsteady aeroelastic code utilized in this work is used to estimate the resonant response of the rotor to aerodynamic forcing. Unsteady surface pressures on the rotor blades are converted into modal forces at each time step. Fully-coupled fluid-structure simulations permit the ability to calculate blade deflections at each time step. To save enormous computational cost, only a partially-coupled analysis was performed in which modal forces are calculated and recorded at each time step, allowing maximum vibrational amplitudes to be found in the post-processing stage. This maximum resonant amplitude is then found from the following generalized equation, (Vahdati et al., 2007);

$$X_{\max} = \frac{\Theta Q \Phi_{\max}}{\omega_r^2}. \tag{4.1}$$

Θ is the amplitude of modal force at the frequency of interest; Φ_{max} represents the largest modeshape element and is determined from an FEA modal analysis; and Q is the Q-factor which represents the sum total of damping, according to the equation:

$$Q = \frac{1}{2\zeta}. \tag{4.2}$$

The Q-factors used in this analysis were taken from NSMS measurements performed on the Purdue compressor (Murray, 2014 a). These tip-timing measurements found the average R2 circumferential blade deflection at NL to be 7.5 mils. However, this value represents a total circumferential displacement, which takes into account responses at all nodal diameters. As the difference in blade counts between R2 and the upstream and downstream vane rows is 11, the 11ND resonant response is the largest. The comparison of predicted vibrational amplitudes to measured amplitudes for an 11ND response is given in Figure 4.16. At NL, CFD predicts the R2 circumferential vibrational amplitude to be 2.051 mils compared to a measured amplitude of 1.82

mils, a difference of only 0.23 mils. As anticipated from the good match between measured and predicted forcing functions at NL, the CFD predicted displacement amplitude at Nominal Loading matches very closely with measured deflection at 11ND. Analyzing the frequency content of the aerodynamic forcing functions showed that the aeroelastic CFD code predicted the 44/rev amplitudes with relative accuracy. Predictions in the aerodynamic forcing matched more closely at midspan than 80% span. The computed circumferential vibration amplitude at HL was under-predicted by 0.78 mil. This is consistent with the spectral analysis of the vortical forcing where experimental measured showed considerably higher amplitudes at the 44/rev frequency component.

It is believed that the excessive mixing due to stator tip separations is a large contributor to the displacement discrepancy at HL. The mixing created an artificial wake dissipation that does not occur in the compressor. Wake profiles at 80% span and HL show total pressure and velocity deficits that are roughly half the depth measured experimentally. A more accurate wake prediction at HL would surely decrease the gap between predicted and measured vibration amplitudes.

Overall, the results at Nominal Loading show that the aeroelastic CFD code used in this work is capable of accurately predicting forced response phenomena present in the rear stages of core compressors. The predicted response measured the circumferential vibrational accuracy to within 0.23 mils of the measured response. The computed aerodynamic forcing components at NL matched closely to results presented by Murray (2014, a). It is believed that minor modifications to the near-blade surface mesh could improve the vortical forcing predictions, most especially at HL, such that wake shapes and amplitudes match more closely to measured values.

Table 4.1: Comparison of operating conditions.

	Case	$\dot{m}_c/\dot{m}_{c,\text{Peak Efficiency}}$	R_c/W_c
Nominal Loading	Experimental	0.746	0.0780
	CFD	0.75595	0.0779
High Loading	Experimental	0.66525	0.0884
	CFD	0.6776	0.0885

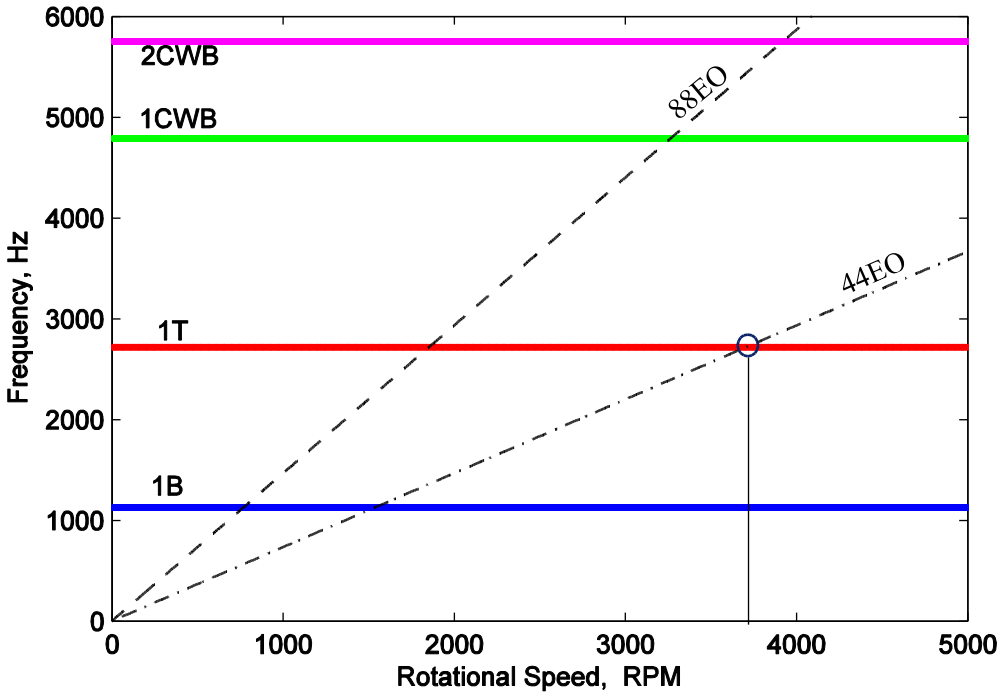

Figure 4.1: R2 Campbell Diagram with 1T crossing highlighted.

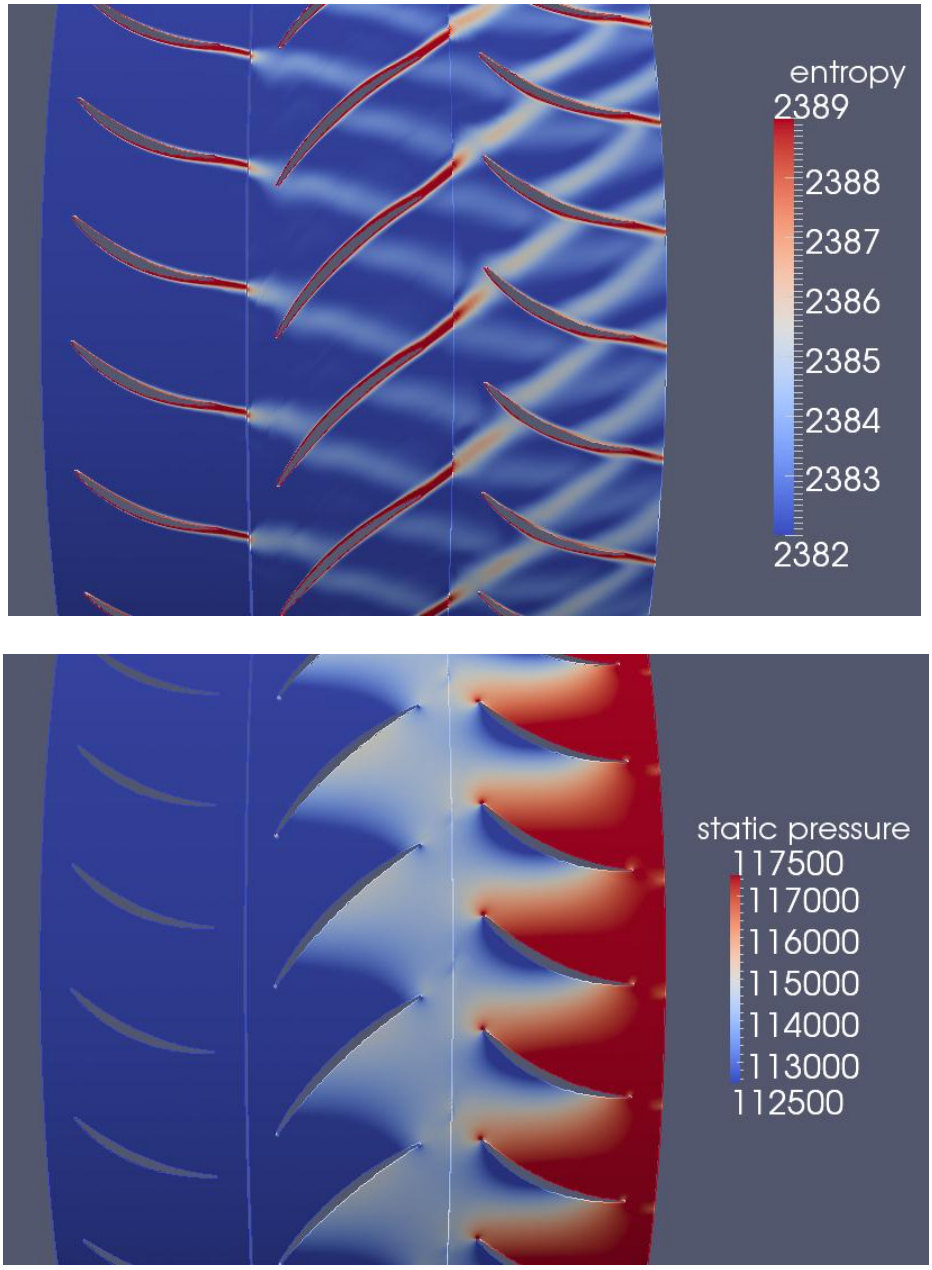

Figure 4.2: Instantaneous forcing functions on R2 at midspan: vortical disturbances (top), potential disturbances (bottom)

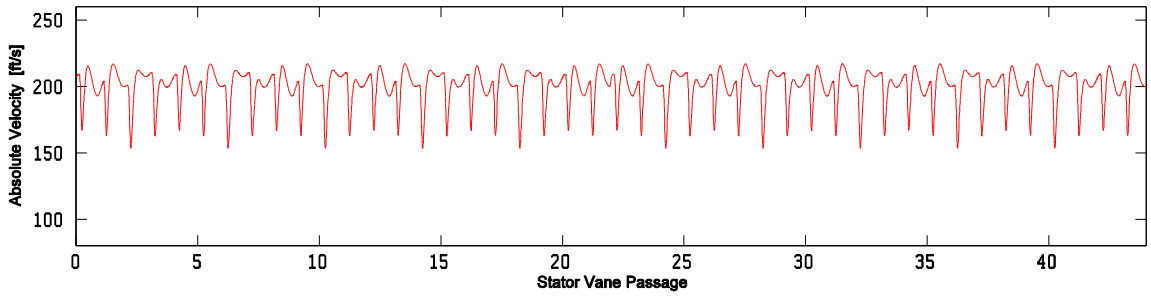

Figure 4.3: Unsteady full annulus absolute velocity wake structure at 80% span, NL.

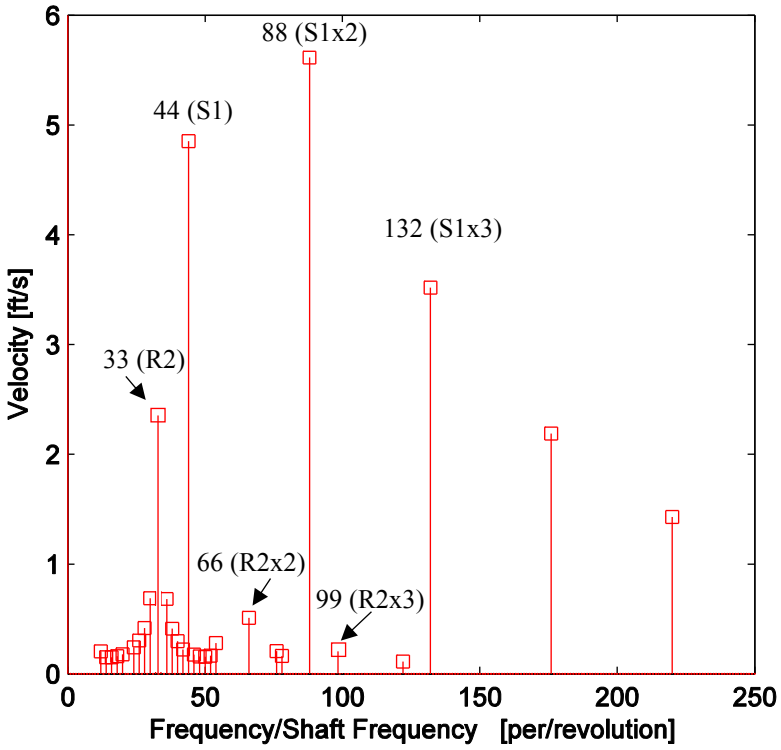

Figure 4.4: Frequency spectrum of unsteady total velocity wake structure.

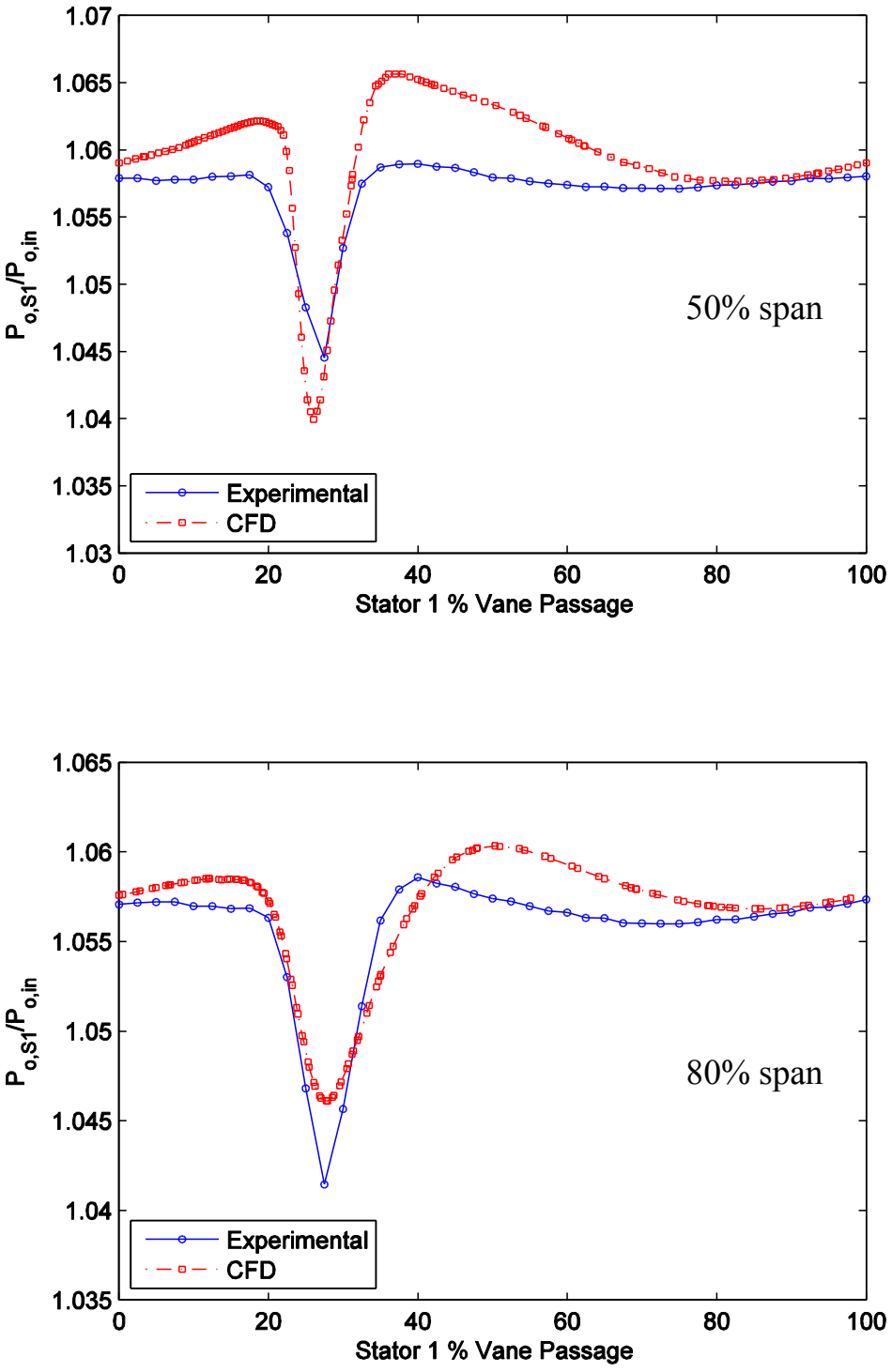

Figure 4.5: Steady-state total pressure wake comparison at NL.

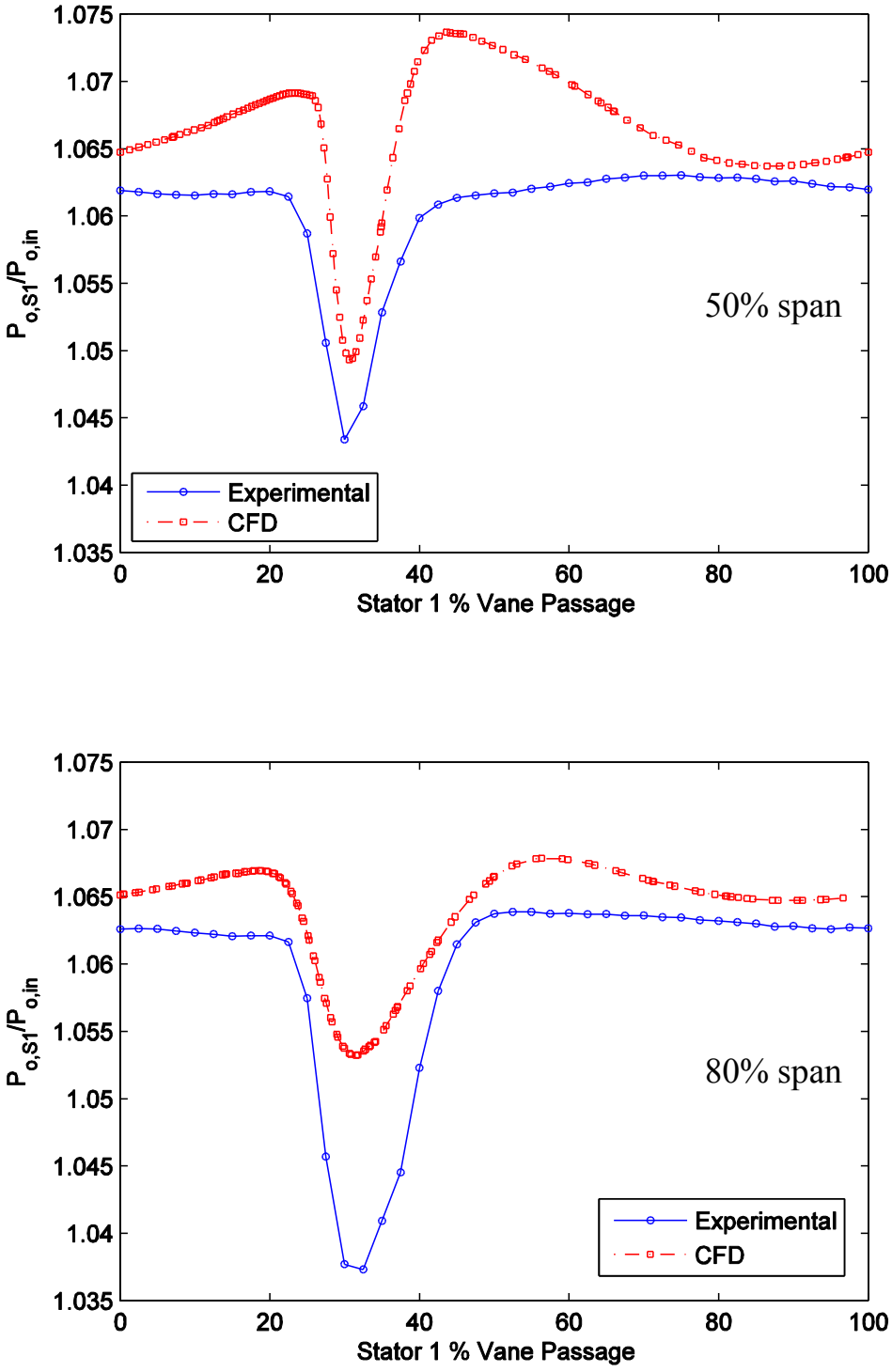

Figure 4.6: Steady-state total pressure wake comparison at HL.

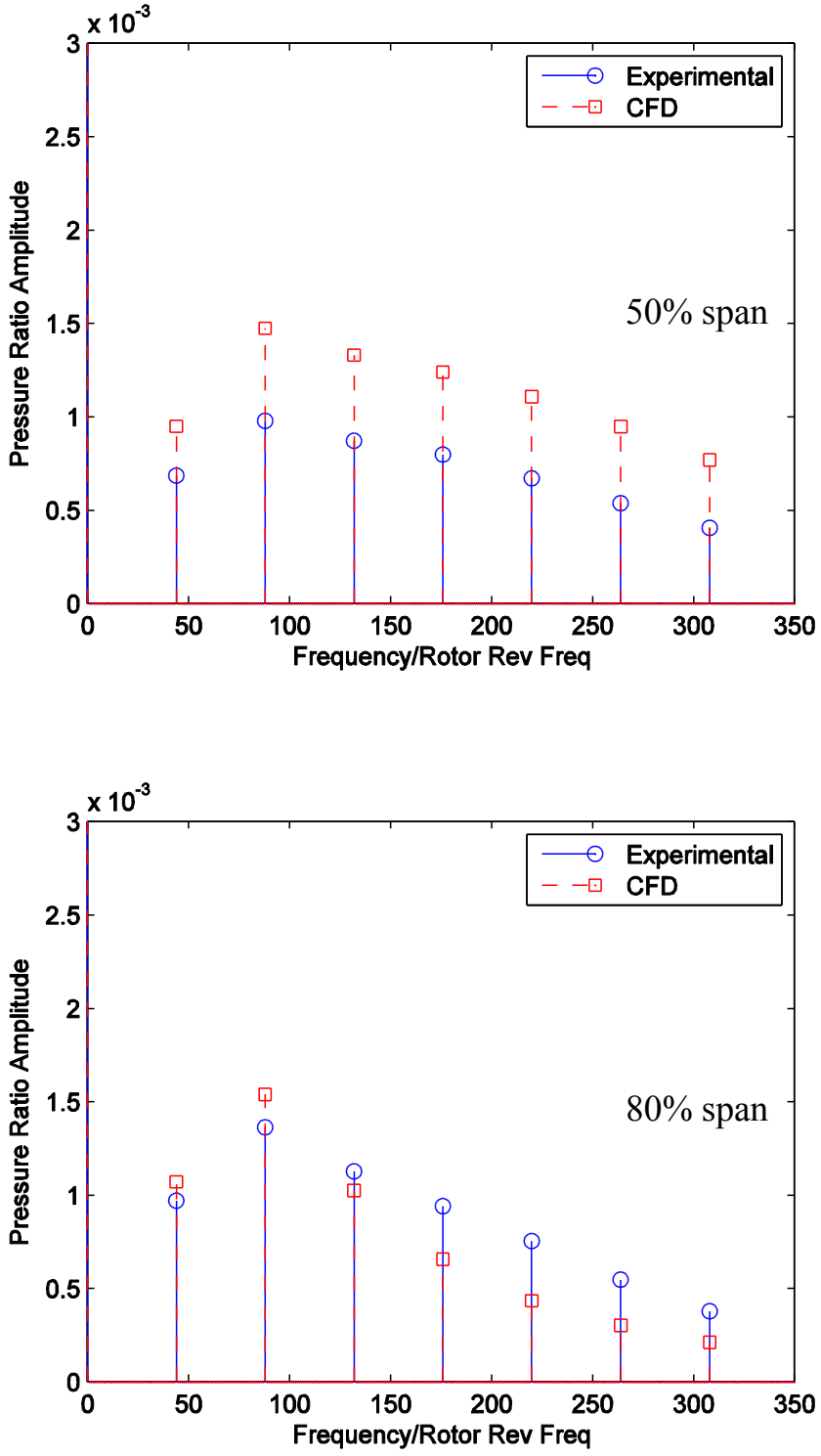

Figure 4.7: Steady-state total pressure frequency spectrum at NL.

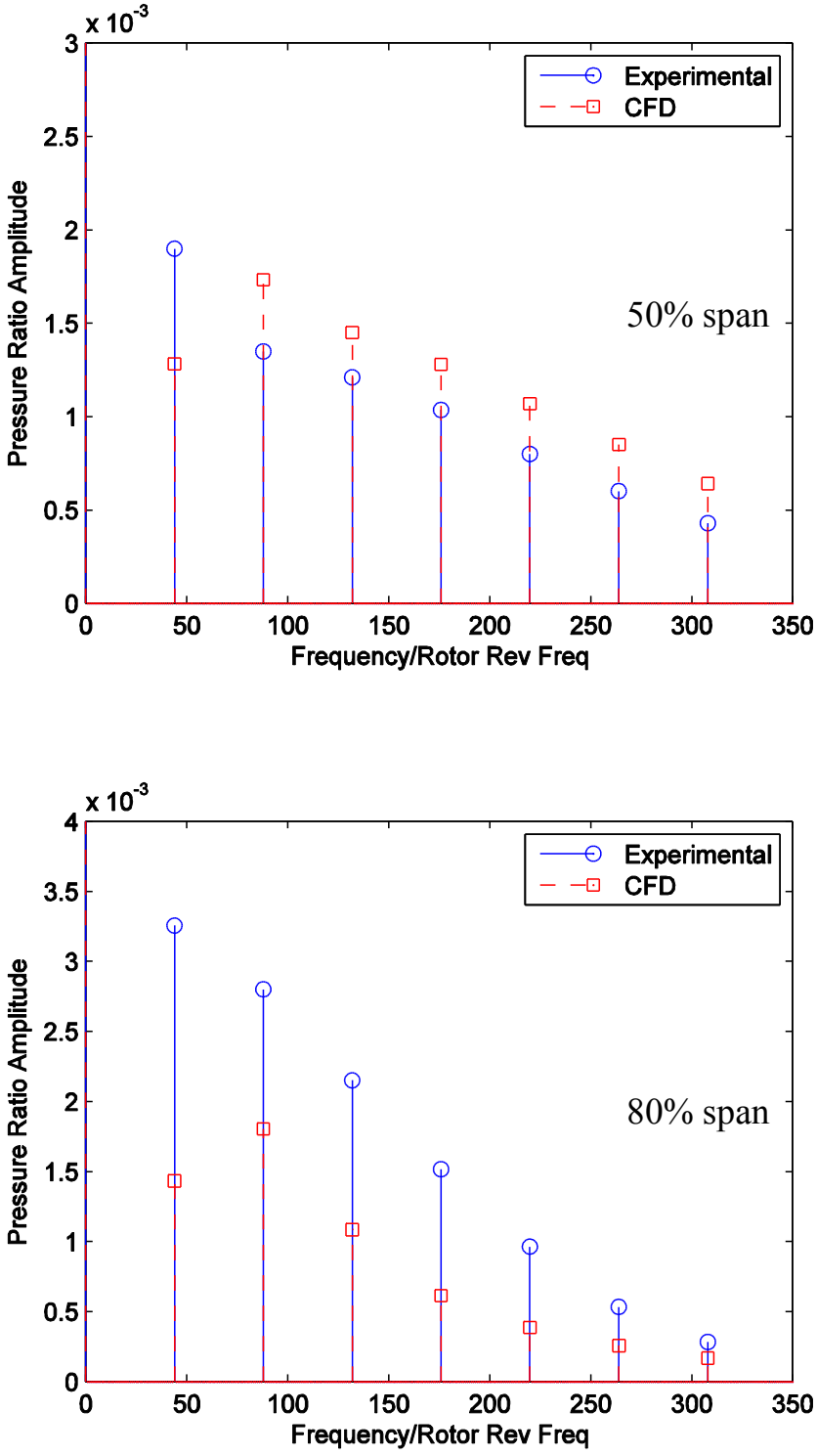

Figure 4.8: Steady-state total pressure frequency spectrum at HL.

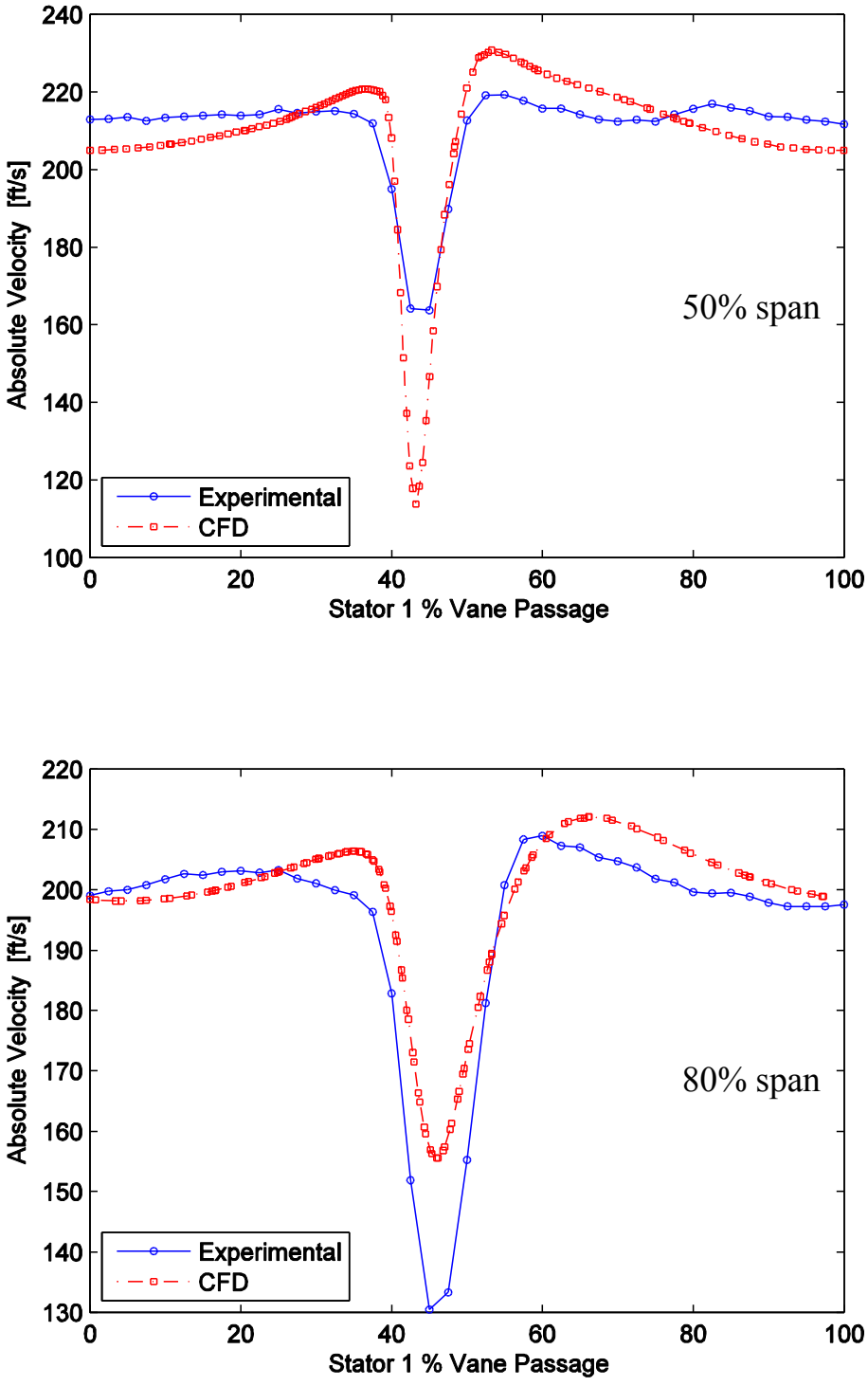

Figure 4.9: Time-averaged measured absolute velocity wake compared to steady CFD wake at NL; midspan (top), 80% span (bottom).

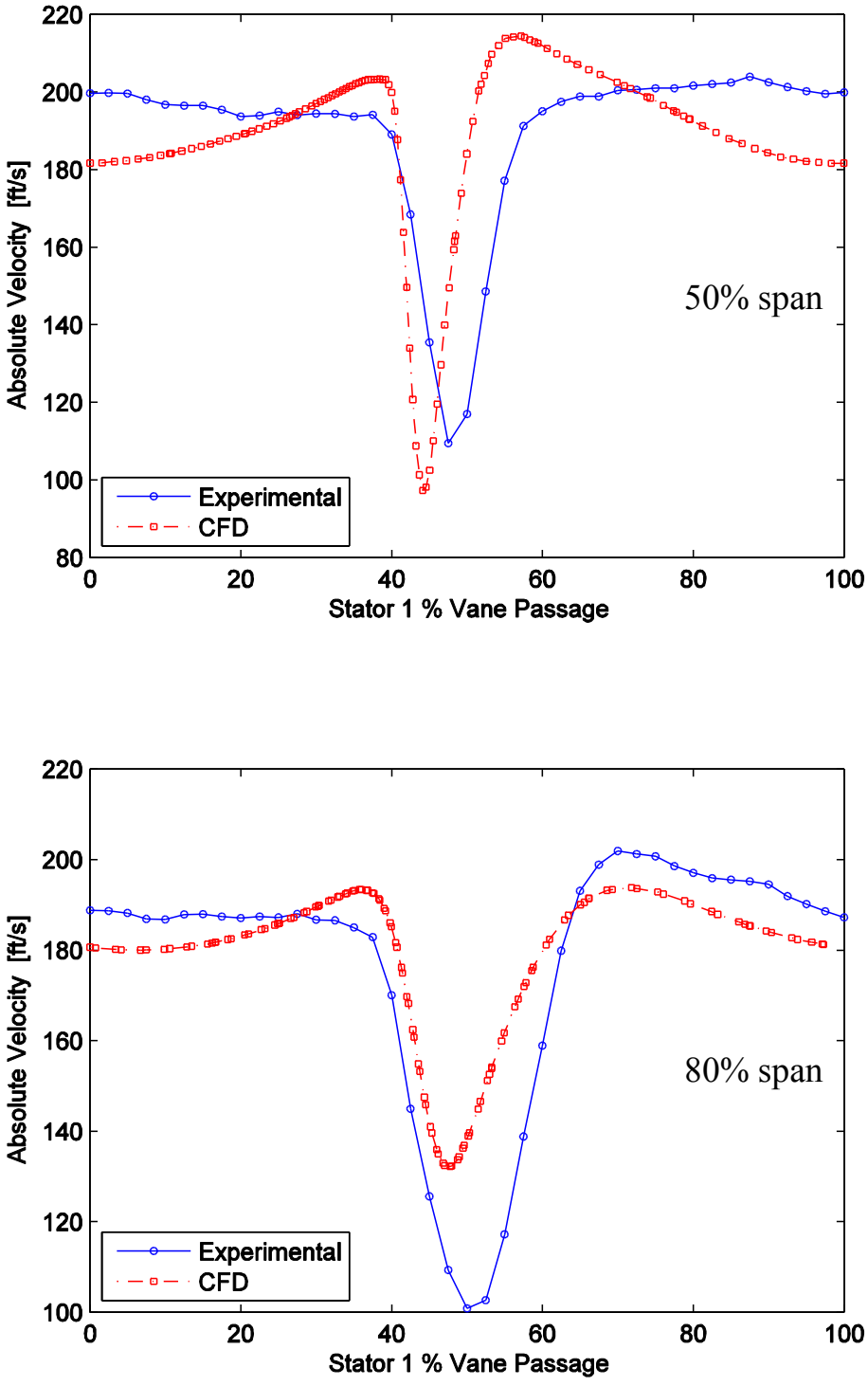

Figure 4.10: Time-averaged measured absolute velocity wake compared to steady CFD wake at HL; midspan (top), 80% span (bottom).

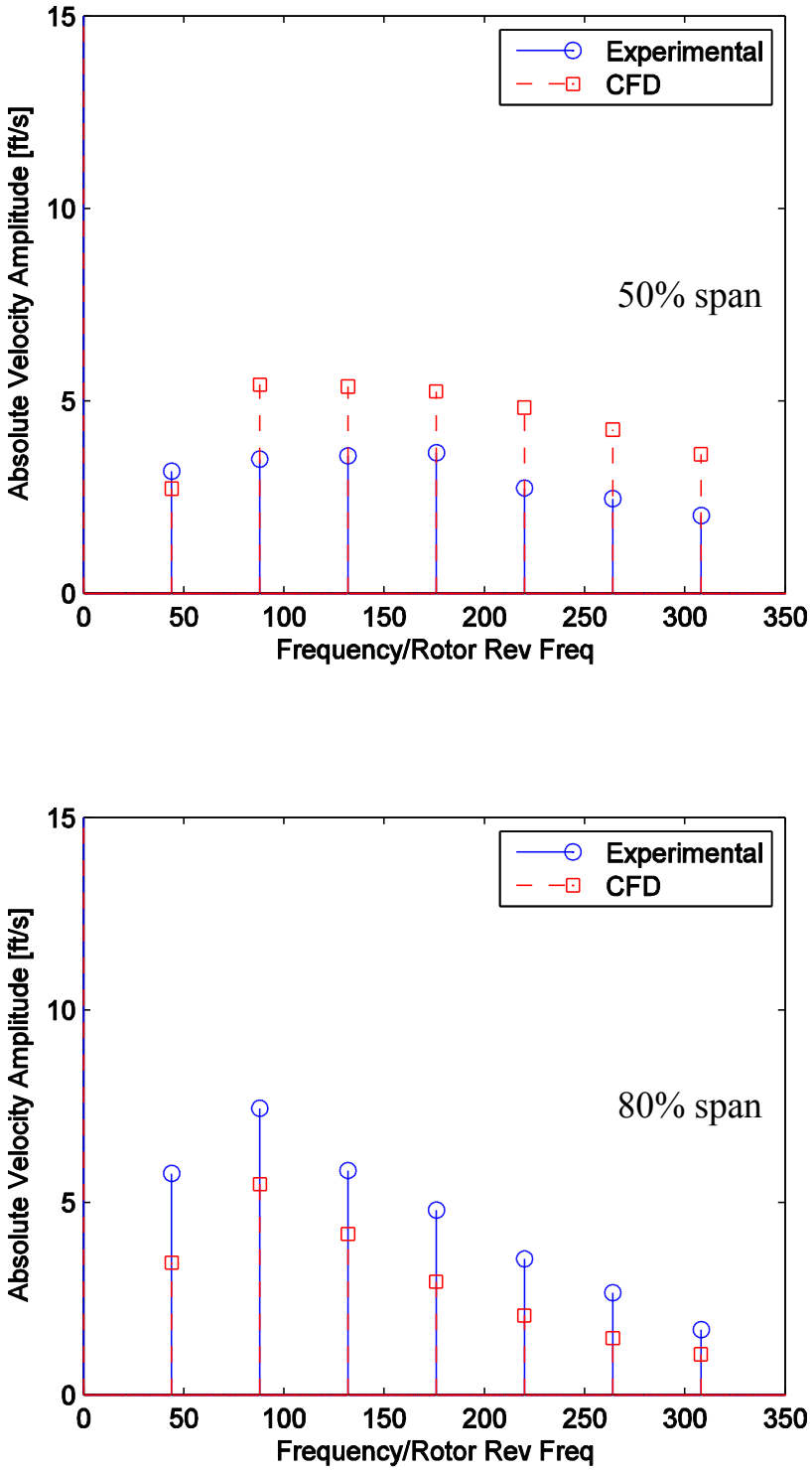

Figure 4.11: Absolute velocity frequency spectrum at NL; midspan (top), 80% span (bottom).

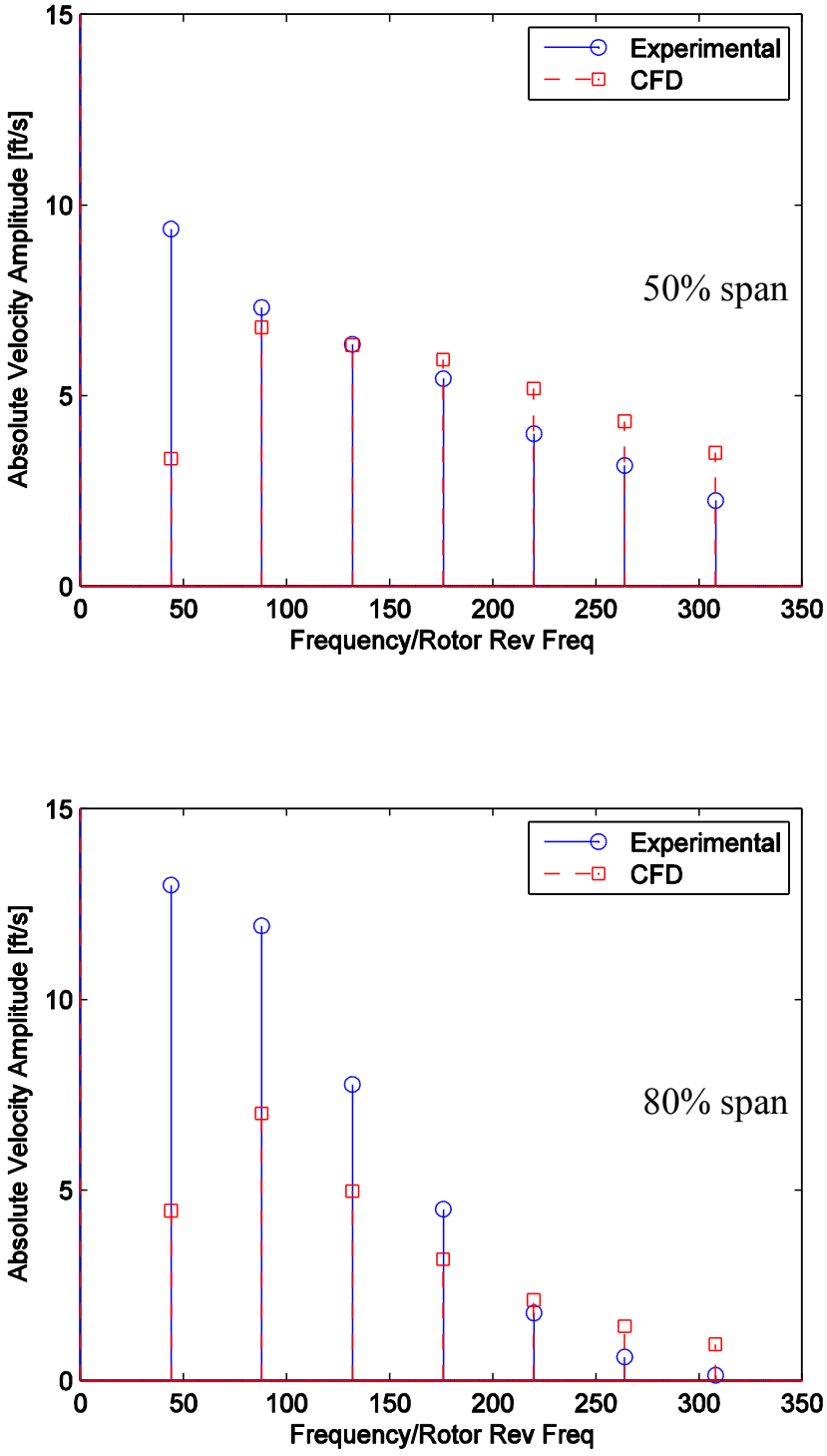

Figure 4.12: Absolute velocity frequency spectrum at HL; midspan (top), 80% span (bottom).

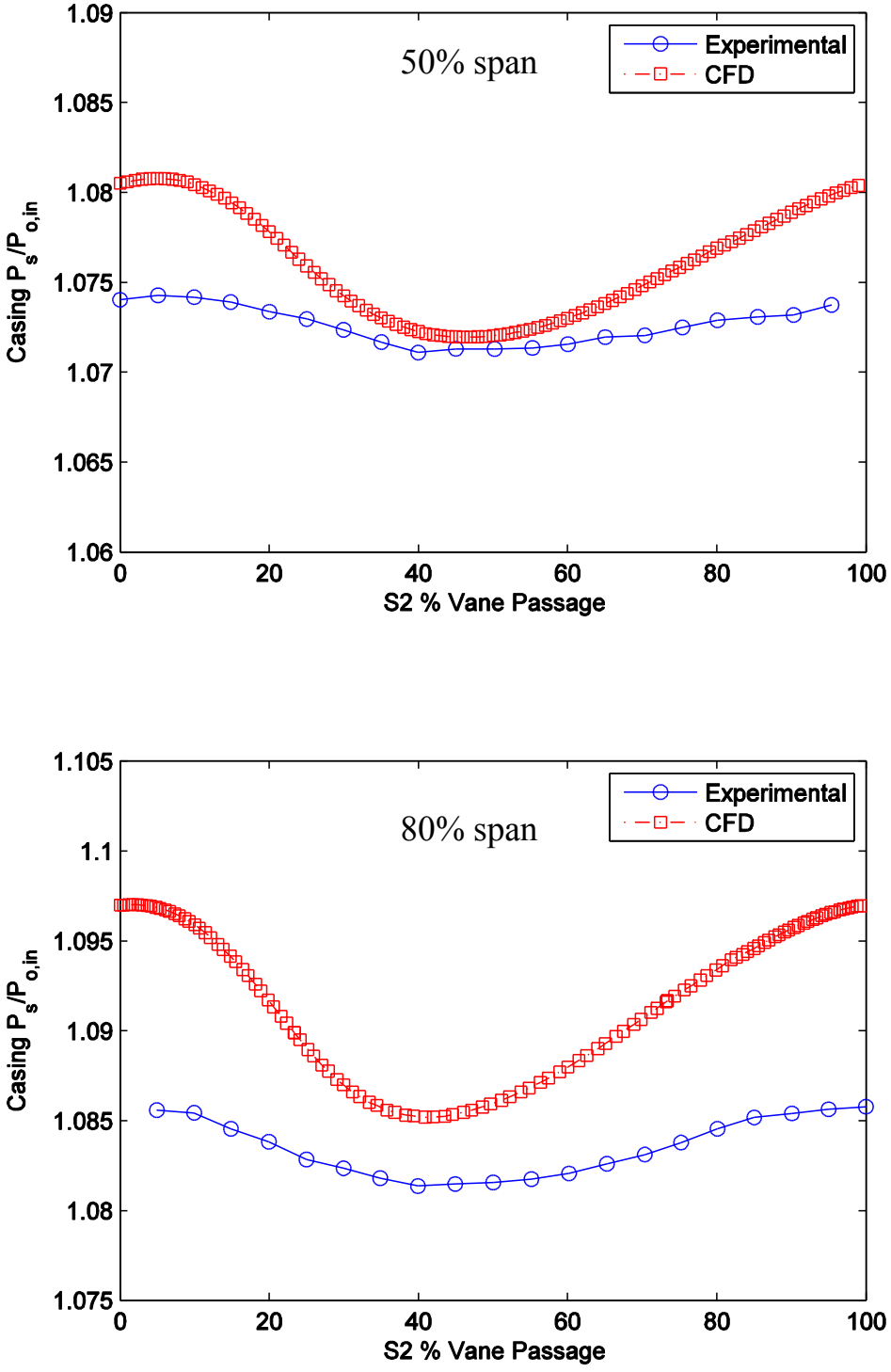

Figure 4.13: Potential field measure by casing static pressure, mid-gap between R2 and S2; NL (top), HL (bottom).

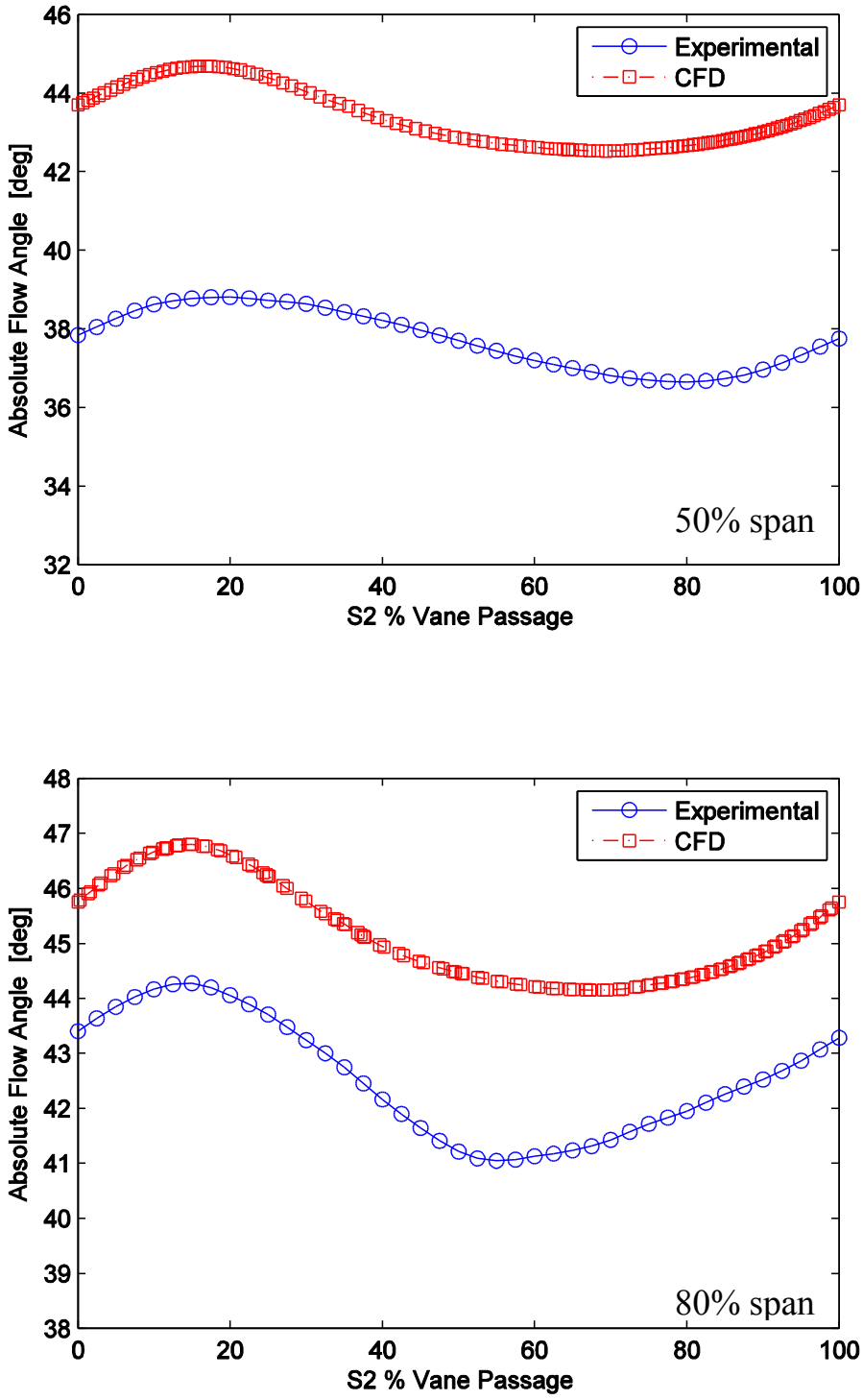

Figure 4.14: S2 potential field measured by absolute flow angle at NL.

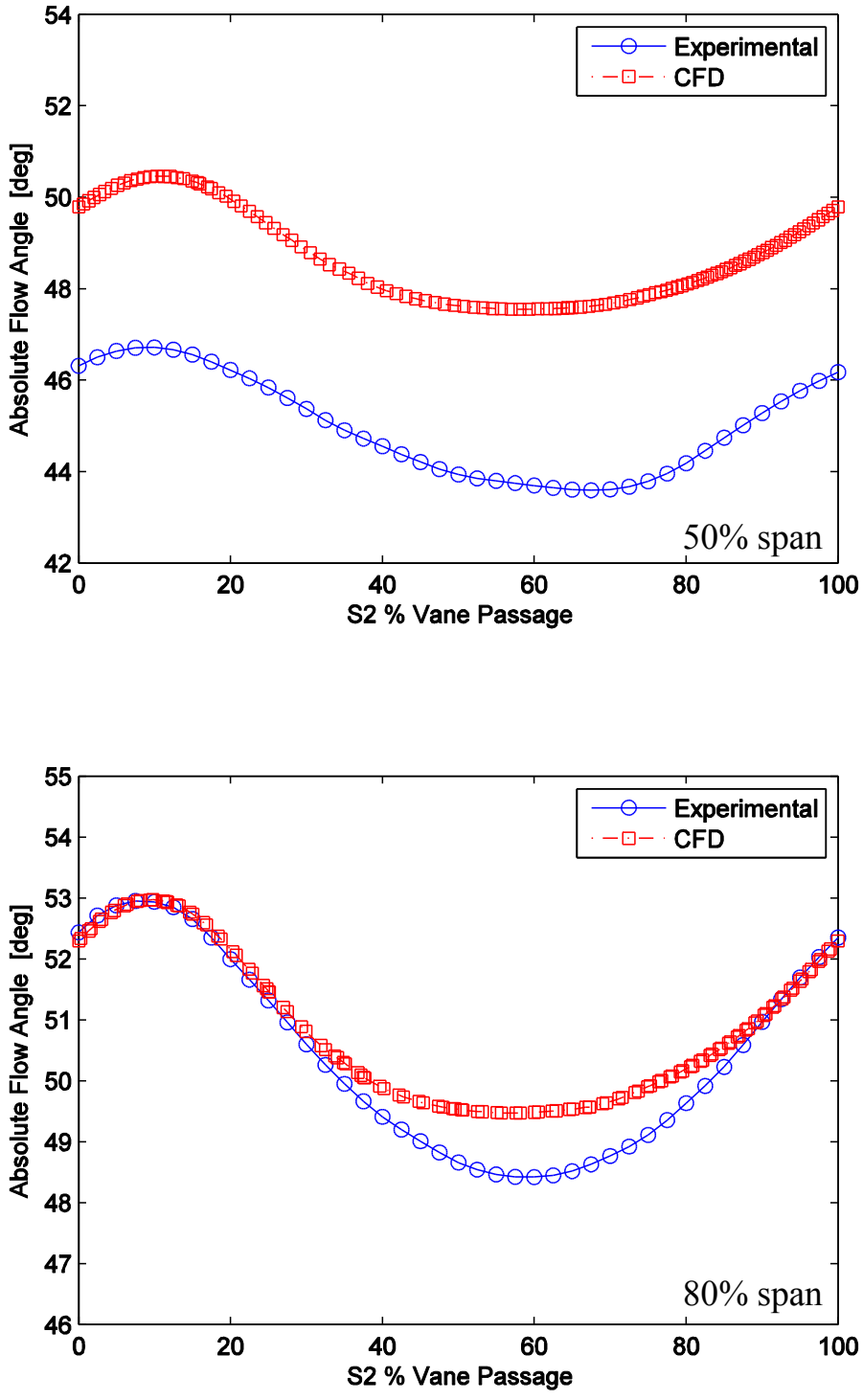

Figure 4.15: S2 potential field measured by absolute flow angle at HL.

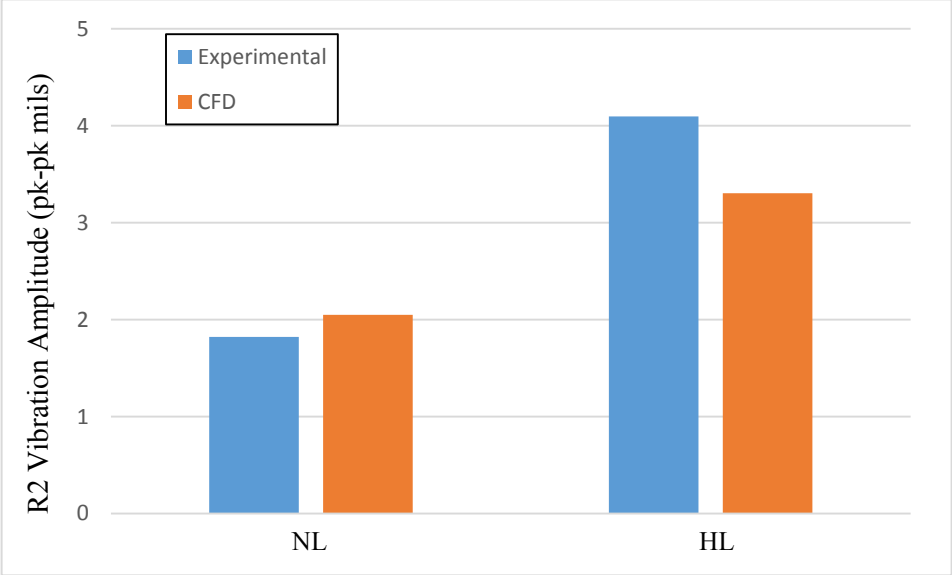

Figure 4.16: Comparison of vibrational amplitudes.

CHAPTER 5: DESIGN OF A NEW SYMMETRIC AND ASYMMETRIC S1

To further investigate the aeromechanical response of Rotor 2, a new reduced vane Stator 1 was designed, thereby altering the vortical forcing on R2. Reducing the number of S1 vanes has the effect of increasing the crossing speed on the Campbell Diagram of the new lower Engine-Order excitation line with the 1st Torsion mode of R2. A higher Campbell Diagram crossing speed increases the overall pressure rise of the compressor as well as the vortical wake deficit and potential fields forcing R2. Larger vortical and potential disturbances should provide a more measureable aerodynamic forcing function. Additionally, an asymmetric configuration of the new reduced vane S1 was designed to investigate methods of reducing the vibrational response of rotors operating near resonant conditions. Modeling the aeromechanical behavior of Rotor 2 with both of these new Stator 1 designs provides additional insight into forced response phenomena in compressors.

5.1 Design of Reduced Count Symmetric Stator 1

5.1.1 Aerodynamic Considerations

By reducing the vane count of Stator 1, there will no longer be equal vane counts upstream and downstream of R2, resulting in multiple nodal diameter disk excitations of the R2 blisk. One benefit of this configuration is the ability to isolate the effects of both the upstream and downstream aerodynamic forcing. Computational models can separate the nodal diameter components of the modal forces, thereby determining the relative effect of both the vortical

upstream forcing and the downstream potential forcing. The reduction in vane count will also increase the rotational speed of the Rotor 2 Campbell diagram crossing.

The design objective was to reduce the S1 vane count to the greatest extent without significantly altering the vane row aerodynamics. As vane aerodynamics are largely influenced by solidity, a ratio of the chord length to vane spacing, the initial aim was to keep solidity constant and explore how many vanes could be removed while increasing the chord length to accomplish this. However, the current compressor configuration has a defined slot width for the Stator 1 ring that limited the maximum axial chord length of the new design. By reducing the fillet size of the vanes at the hub and tip from 3/32" to 1/16", an increased axial chord length of 0.07" could be achieved. This was not enough to keep solidity constant, but helped in limiting the solidity increase. Using *JACC* as the performance prediction tool, the aerodynamic performance of different S1 vane counts was analyzed. Figure 5.1 shows the area-averaged diffusion factor and the solidity of Stator 1 as the vane count is decreased. Based on recommendations from aero designers at RR, a reduction to 36 vanes resulted in a diffusion factor above standard practice, indicating that the vane row would have insufficient stall margin. Thus, in the following analysis, the results for three vane counts are presented: 38 vanes, 40 vanes, and the Baseline case with 44 vanes.

The overall performance of the compressor at 100% corrected speed shows that there are negligible changes in the overall compressor pressure ratio and efficiency for the different S1 vane counts, Figure 5.2. Figure 5.3 shows the Stage 1 performance for the three vane counts. The Stage 1 total pressure ratio is nearly identical for all three vane counts, but the Stage 1 efficiency varies with S1 count. The higher vane count (44) does better at high loading compared to the reduced vane counts. However, for the majority of the speedline, the 44 baseline count has slightly lower efficiency compared to the rest of the cases. Figure 5.4 compares CFD results of

flow angles and radial profiles at the stator exit for the different vane counts. Aerodynamic properties at stator 1 exit are minimally changed by the modification in stator vane count. Total pressure and total temperature radial profiles do not show any noticeable changes between the Baseline and new designs. However, a small difference does occur in the exit absolute flow angles. For the 38-vane design, the flow angles differ by about one-quarter of a degree, caused by slightly greater deviation due to the decreased solidity. Differences in the diffusion factor are also indicated. The isentropic Mach number near the vane surface is shown along the chord at several spans for the different vane counts, Figure 5.5. Differences between the 38-vane increased chord design and the baseline design are small.

Reducing the Stator 1 vane count to 38 vanes is shown to minimally affect the aerodynamic performance of the vane row. Additionally, increasing the axial chord length by the maximum allowable distance of 0.07" helped maintain acceptable diffusion factor and solidity values, a 6% increase in diffusion factor and a 9% decrease in solidity. Thus, in terms of aerodynamic performance a reduction to 38-vanes is a viable design option for increasing the resonance speed of the R2 1T excitation.

5.1.2 Aeromechanical Considerations

Although a new Stator 1 with 38 vanes is acceptable by aerodynamic considerations, it must also be evaluated in terms of the Rotor 2 response at the 38EO Campbell diagram crossing for the Rotor 2 1T mode. Previous aeromechanics research on the Purdue compressor show that R2 has a significant response at the 44EO 1T crossing (Murray, 2014). Therefore, caution must be taken to ensure that the increase in resonance speed at the R2 1st Torsion mode does not lead to unsafe aerodynamic forcing and resultant vibrational responses.

Figure 5.6 shows the R2 Campbell Diagram, highlighting the increase in crossing speeds of the Rotor 2 1T mode between the baseline 44EO excitation (3700 rpm) and the proposed 38EO excitation (4285 rpm) – a 15% increase in resonance speed. To determine if the new Stator 1 forcing functions are within acceptable limits, it is necessary to analyze the shapes and frequency content of the wakes for the new design.

All CFD results were obtained with the Rolls-Royce code *JACC*, solving the single-passage multi-bladerow computational domain. For the initial wake analysis, flow properties across the vane passage were taken at an axial location several grid points downstream of the Stator 1 trailing edge and at spanwise locations of 50% and 80% span. Data were taken sufficiently close to the trailing edge to ensure adequate grid resolution to capture wake behavior. Figure 5.7 shows the Baseline Stator 1 mesh near the trailing edge from a vantage point of the casing looking radially inward.

Wake comparisons were made at four loading conditions: Open Throttle, Nominal Loading, High Loading, and Near Stall. The Baseline 44-vane case was run at the Rotor 2 44EO 1T crossing speed of 3710 RPM, while the 38-vane design was run at the 38 EO 1T crossing speed of 4285 RPM. The compressor characteristics for these two speeds are given in Figure 5.8, with the symbols indicating comparable loading conditions used for this analysis. Figure 5.9 shows the comparison of wake profiles between the 44-vane design and the 38-vane design for these four loadings at 50% span. Wake depths are larger for the 38-vane design, but the wake widths are smaller when compared to the Baseline design. Similar results occur at 80% span, as shown in Figure 5.10.

The effect of the increased S1 wake depth on the resonant response of Rotor 2 was explored by investigating the spectrum associated with vortical disturbances shed from Stator 1. A Fourier transform of the S1 wake was computed. CFD grids typically employ uneven grid

spacing between blades and vanes, with much smaller spacing towards the blade/vane surface. Therefore, to generate pressure and velocity data at equally spaced intervals across the vane passage, the CFD wake passage data were resampled to provide 200 points uniformly spaced across the passage.

Figure 5.11 compares the spectral results of total pressure for the two stator designs at midspan. The principal harmonic occurs at a frequency of 2713 Hz, with the first 10 harmonics shown. The 0^{th} harmonic amplitude (associated with the mean level) was too large to fit on the scale of the plot and, therefore, is not shown in these figures. Each loading condition shows that the Baseline (44-vane) amplitude is greater than the 38-vane design at the first harmonic. Even though the wake depth of the 38-vane design is larger than the Baseline stator, the first harmonic amplitude is less than the Baseline 44 vane stator. This suggests that the fundamental harmonic forcing from S1 is reduced by the 38-vane design. The reduction occurs because the reduced-vane wake shape is narrower and acts as more of an impulse, spreading more of the lower harmonic energy into the higher harmonics.

Both total pressure and total velocity can be used as a measure of vortical disturbance strength. As both methods generally generate similar results, only total pressure will be used in the foregoing analysis. A similar analysis was performed at 80% span, Figure 5.12. At this spanwise location, the new stator design no longer has a smaller 1^{st} harmonic amplitude at all loading conditions. The "High Loading" condition shows the principal harmonic amplitude is nearly equal to the Baseline stator, and at "Near Stall" conditions the lower vane count does indeed have a larger 1^{st} harmonic amplitude. Therefore, it is expected that the reduction in Stator 1 vanes will cause an increased Rotor 2 vibrational response at "Near Stall" loading.

To ensure that the results are representative of what Rotor 2 will encounter, and not skewed by the close proximity of the wake data to the stator trailing edge, Fourier transforms of

the wakes were also computed at an axial location midway between Stator 1 trailing edge and the mixing plane. The axial location for which wake data were taken is shown in Figure 5.13. Results for total pressure only, at both 50% and 80% span locations are presented in Figures 5.14 and 5.15. Results agree with those acquired near the trailing edge; the only loading condition with increased levels in the 1st harmonic amplitude for the 38-vane design is the Near Stall loading at 80% span. As no plans exist to take aeromechanical data at near stall operating conditions, the predicted increase in aerodynamic forcing due to the reduced-vane design at near stall loading is not deemed critical to the analysis. Therefore, with steady CFD predicting equal or decreased aerodynamic forcing at all loading conditions of interest, a reduced-vane S1 with 38 vanes passes the aeromechanical analysis.

5.1.3 Mechanical Analysis

With prior analyses showing acceptable aerodynamic and aeromechanical behavior, a mechanical analysis of the new vane design was then conducted. The aerodynamic design did not change the thickness-to-chord ratio of the vanes from the current stator design, which was robustly designed. Therefore, no stress analysis was performed on this reduced-count vane design. A modal analysis was performed to investigate the change in mode shapes and frequencies brought about by the slight modification in vane count and chord length. This analysis was conducted on both the current 44-vane stator and the reduced 38-vane stator design. The analysis was performed using the ANSYS Workbench software package. A CAD model of a single vane sector of the stator was loaded into ANSYS. Cyclic symmetry constraints were applied on the sector faces to represent a full stator ring. Cyclic symmetry constraints model one vane passage as a repeating sector of a 360° ring. This is not the true constraint since the stator is split into two half-rings, but it is the most accurate boundary condition available without

exponentially increasing the mesh size and analysis time required to model the entire stator half. Both stators were meshed using triangular elements, with node counts at roughly 53,000 nodes. As the mesh was nearly identical between the two stators, only the 38-vane stator is shown in Figure 5.16. Zero-displacement boundary conditions were applied to the O-ring grooves to simulate the effect of the casing.

The modal analysis shows that only minor variations are introduced in the reduced vane count design. Figure 5.17 compares mode shapes for the first two modes. Mode shapes appear to be identical between the two stator designs. A comparison of the modal frequencies is presented in Table 5.1. The slightly increased chord length in the 38-vane design changes the modal frequencies only a small degree. Mode 1 and Mode 2 frequencies are decreased 1.7% and 2.6%, respectively. Mode 3 and Mode 4 frequencies are both increased in the reduced vane design by 2.3% and 2.7%, respectively. Of biggest importance are the changes in Campbell Diagram crossing speeds associated with the frequency changes. Figure 5.18 presents the Stator 1 Campbell Diagram, with the 36EO line representing the 36-blade Rotor 1 and 33EO line representing the 33-blade Rotor 2. Modal frequencies for both stator designs are shown. The largest change in mode crossing speed occurs for the 33-EO excitation of Mode 2, which reduces the current stator mode crossing speed by 66 rpm. Only the first two modes have crossing speeds within the operating range of the compressor, as the Mode 3 crossing occurs at over 10,000 rpm.

The foregoing analyses predicts that reducing Stator 1 to 38 vanes does not significantly alter the aerodynamic performance of the vane row, does not increase the vortical forcing on R2 at loading conditions of interest, and also does not introduce additional vane mode shapes or frequencies. Therefore, this new S1 design is adequate and acceptable for additional research into forced response in the embedded stage of the Purdue compressor.

5.2 Design of an Asymmetric Stator 1

Experimental campaigns to measure compressor forced response are becoming increasingly expensive. Often these measurements are not taken until full-scale engine testing occurs for new engine designs. While computational predictive capabilities continue to advance, designers still look for any method available to reduce the aerodynamic forcing and forced response within a compressor. One such method explored in recent years is the introduction of geometric asymmetries as a means of altering the frequency content of the vortical and potential disturbances. While asymmetries can take many forms, two were analyzed as potential designs for Stator 1 in the Purdue compressor: non-uniform vane spacing (NUVS) and different vane counts on each stator half (with symmetric spacing on each half-ring). The effect of Stator 1 asymmetry on R2 forced response is investigated initially by comparing the frequency content of the asymmetric stator wakes to the symmetric 38-vane S1 results at a nominal loading. Full annulus S1 wake structures were constructed out of single passage steady CFD results. This was accomplished by joining together the S1 passage total pressure wake profiles and computing the Fourier Transform (FT). Because both of the asymmetric concepts modify the spacing between vanes, simulations with different Stator 1 vane counts were run so that the wake profiles of the asymmetric geometry are representative of the different solidities present in each asymmetric configuration. These single passage wake profiles were then repeated in different patterns to form full-annulus wake structures. A FT of steady CFD solutions reveals the frequency content of the S1 vortical forcing functions. All CFD simulations were run on the Rolls-Royce code *JACC*. A view of the Stator 1 mesh and axial plane at which the total pressure profile is measured is shown in Figure 5.19. The analysis presented in Section 5.1.2 showed that DFT results of the S1 velocity wake follow the same trends as the total pressure wakes and, therefore, only the total pressure results are presented.

5.2.1 NUVS Asymmetry

The non-uniform vane spacing (NUVS) concept alternates long and short vane passages across a stator vane. In essence, this creates a long passage - short passage pattern that repeats around the annulus. The simplest way to construct this asymmetry is to modify the passage size of the symmetric 38 vane S1 in MATLAB by multiplying its passage length by a scaling factor. The short vane passage is then reduced by the scaling factor and the long passage is extended by the same factor. In this manner, each 2-vane long-and-short passage combination occupies the same circumferential extent as two symmetric 38 vane passages. As wake depths and structures are greatly influenced by solidity, the wake shape and depth in the larger passage will differ from that of the short passage. To have representative wake shapes, single-passage multi-bladerow CFD simulations were performed for 32 vane, 36 vane, 40 vane, and 44 vane Stator 1 vane counts (in addition to the 38 vane symmetric stator). As an example, for a NUVS geometry with a scaling factor of ± 20%, the larger passage most closely matches the size of a 32-vane stator spacing while the shorter passage most closely matches the spacing of a 40-vane stator 1. Hence, the total pressure wake profiles from simulations with these Stator 1 vane counts were used. The two wake profiles were joined together to form a two-passage profile. The profiles were then resampled to ensure equal spacing between data points and repeated 19 times to form a representative 38 vane NUVS wake profile. An example full-annulus representation of the ± 20% NUVS geometry is shown in Figure 5.20.

DFT results of the NUVS geometry with scaling factors of 10%, 20%, and 30% were analyzed, shown in Figure 5.21. First, the principal harmonic of the NUVS asymmetry is shifted to 19/rev, instead of the 38/rev in the symmetric case. For the ± 10% vane spacing shown in the left column of Figure 5.21, the minor asymmetry yields virtually no amplitude change at the 38/rev excitation. The ± 20% case demonstrates interesting results. At midspan, the reduction in

amplitude for the 38/rev component is almost 50%, while essentially no reduction occurs at 80% span. The increase in the 38/rev component from midspan to 80% span is caused by a slight change in shape of the total pressure profile in the freestream region outside of the wake, with the 80% span profile more flat in this freestream region. The final NUVS case, ± 30%, shows a significant reduction in the 38/rev amplitude from the symmetric stator 1. At midspan this reduction is roughly 60% while at 80% span the reduction is 40%. Thus, increasing the magnitude of the NUVS asymmetry further reduces the forcing at the 38/rev excitation. However, aerodynamic stability must also be considered. As the scaling factor is increased, the solidity of the larger vane passage decreases while the diffusion factor increases. Eventually, these values will exceed acceptable values for efficient and stable operation. Table 5.2 shows the spanwise-averaged solidity and diffusion factor values for each case. It is clear that the ± 30% NUVS geometry exceeds limits of stable operation. The ± 20% vane spacing has the most significant benefit in terms of reducing the stator 1 aerodynamic forcing while maintaining more reasonable values of solidity and diffusion factor.

5.2.2 Stator Halves of Different Vane Counts

The second asymmetric concept redistributes the 38 vanes unequally between the two stator halves, creating two stator halves with different vane counts. Two combinations of vane counts were considered in this analysis, stator halves of 18 vanes and 20 vanes as well as stator halves of 16 vanes and 22 vanes. Since single-passage CFD simulations exist for each of these Stator 1 vane counts, representative wake shapes were used to build a full annulus wake structure without modifying the passage size. To build the full annulus waveform, single-passage total pressure profiles for each vane count were duplicated to form stator halves of different vane counts. To ensure that the distance between data points was identical between all stator halves,

the constructed half-annulus wake structures were resampled with an equal number of data points. The combinations of stator halves were then joined together to form a full annulus. Figure 5.22 shows the representative wake structure for the vane count combination of 16 vanes and 22 vanes.

A DFT of this asymmetric concept was conducted for vane combinations of 18 and 20 vanes as well as stator halves of 16 and 22 vanes. The results are presented in Figure 5.23. The asymmetry of Stator 1 eliminates the 38/rev principal harmonic of the symmetric stator as energy is instead shifted into neighboring frequencies. For the stator half combination of 18 and 20 vanes (left column of Fig. 5.24), the 38/rev harmonic is shifted into distinct amplitude peaks at 36/rev and 40/rev. These peaks are spread ± 2/rev from the symmetric 38/rev first harmonic, equal to the difference in vanes between the two stator halves. Likewise, for the combination of 16 and 22 vane stator halves, the difference of 6 vanes shifts the symmetric first harmonic ± 6/rev into amplitude peaks at 32/rev and 44/rev. For both cases, the deconstruction of the symmetric first harmonic eliminates the 38/rev component of frequency entirely and shifts the rotor 2 1T excitation onto different EO lines on the Campbell Diagram, Figure 5.24. Shifting the EO excitation line means that the operating speed at which R2 1T is excited is now shifted away from 4285 rpm of the symmetric S1. However, even at these new resonant operating speeds the amplitude of aerodynamic forcing from S1 is reduced from the baseline symmetric case. For the 18 and 20 stator vane combination, the 40/rev component observes the smaller amplitude reduction of 25% at midspan and reduction of 10% at 80% span. The 36/rev component has a larger reduction of 55% at midspan and 35% at 80% span. As in the first asymmetric concept, increasing the magnitude of the asymmetry increases the reduction in aerodynamic forcing. When compared to the 38/rev magnitude of the symmetric stator, the 44/rev component of the 16-22 vane combination is reduced 20% at midspan and 15% at 80% span while the 32/rev component is reduced 90% at midspan and 70% at 80% span.

Again, aerodynamic stability must be considered in addition to the reduction in aerodynamic forcing from S1. Table 5.3 lists the solidity and diffusion factors of the lower vane count stator half compared to the solidity and diffusion factor of the symmetric 38-vane stator, as well as changes in compressor efficiency as derived from single passage calculations. Values for the 18-vane stator half differ minimally from the symmetric S1 while solidity and diffusion factor for the 16-vane stator half have likely exceeded limits for aerodynamic stability. Likewise, the compressor efficiency for the 16-vane stator half is significantly lower than the symmetric stator.

5.2.3 Mechanical Analysis of Asymmetric Design

Although both asymmetric S1 design concepts demonstrate the ability to reduce the magnitude of aerodynamic forcing, the non-uniform vane distribution between stator halves yields a greater benefit at a lower aerodynamic performance cost. Therefore, a S1 consisting of 18-vane and 20-vane stator halves was selected as the design for which to proceed with detailed aeromechanical investigations.

With the decision to move forward with an asymmetric stator geometry consisting of 18 equally spaced stator vanes on one half-ring and 20 equally spaced vanes on the second half ring, a mechanical modal analysis was conducted. The modal frequencies were compared to those of the symmetric 38 vane stator design, as well as the Baseline 44 vane design. The industry standard for computing mode shapes and frequencies is to impose cyclic symmetry constraints on a single sector of the vane row. This allows the finite element software to solve a single sector as if it were repeated to form a full ring, greatly reducing the computational cost. Since the asymmetric configuration prevents the use of cyclic symmetry, the full stator was modeled in ANSYS to compute mode shapes and frequencies. Figure 5.25 shows the asymmetric stator ring solid model, as well as a multi-vane section of mesh. Mode shapes are presented in Figure 5.26.

From a qualitative standpoint, the first two mode shapes of the asymmetric S1 are nearly identical to the results of the symmetric S1. Comparing the specific mode frequencies shows essentially no change in resonance frequency between the symmetric and asymmetric reduced vane stator, shown in Table 5.4. As only the first two modes of S1 have Campbell Diagram crossings within the operating range, only frequencies for these modes are presented in the table for the asymmetric S1 due to the enormous size of the computation. The redistribution of vanes from the symmetric to the asymmetric configuration changes the mode frequencies by only 1-3Hz. Thus, no mechanical concerns arise from distributing the 38 vanes unequally, forming an asymmetric S1 geometry with an 18-vane stator half and a 20-vane stator half.

5.3 Future Research on New Symmetric and Asymmetric Stator 1

The newly designed reduced-vane symmetric and asymmetric Stator 1 configurations will be used as part of ongoing research on the forced response analysis of the embedded rotor in the Purdue multistage compressor. Research presented in this thesis will computationally investigate the reduction in vibrational amplitude of R2 operating at the 1T resonant condition as a result of the asymmetric configuration. An unsteady, aeroelastic CFD code is used to capture the fluid-structure interaction of Rotor 2. Additionally, future research at Purdue University will investigate experimentally the forced response behavior of Rotor 2 in the presence of both the symmetric and asymmetric S1 configurations. As such, orders were placed for the manufacturing of both stator rings.

Table 5.1: Mode frequency comparison between 44-vane and 38-vane stators.

	Mode 1 (Hz)	Mode 2 (Hz)	Mode 3 (Hz)	Mode 4 (Hz)
Baseline (44) Stator	708.91	2100.9	6186	6898.3
38 Vane Stator	689.96	2063.5	6325.7	6714.6

Table 5.2: Spanwise-averaged values of solidity and diffusion factor for NUVS asymmetry.

	Avg. Solidity	Avg. D-Factor
Symmetric	1.223076	0.54244
+10% spacing	1.11469	0.558556
+20% spacing	1.05427	0.568138
+30% spacing	1.00848	0.57541

Table 5.3: Spanwise-averaged values of solidity and diffusion factor for stator halves with unequal vane counts.

	Avg. Solidity	Avg. Diffusion Factor	Efficiency Δ
Symmetric S1	1.223076	0.54244	
18 Vane Stator-half	1.158976	0.551534	- 0.0003
16 Vane Stator-half	1.030152	0.571963	- 0.0055

Table 5.4: Mode frequency comparison between all stator geometries.

	Baseline Stator 1 (44 Vanes)	Symmetric Stator 1 (38 Vanes)	Asymmetric Stator 1 (38 Vane Full stator)
	Hz	Hz	Hz
Mode 1	708.91	689.96	686.47
Mode 2	2100.9	2063.5	2064.4
Mode 3	6186	6325.7	
Mode 4	6898.3	6714.6	
Mode 5	7405.4	7040.5	

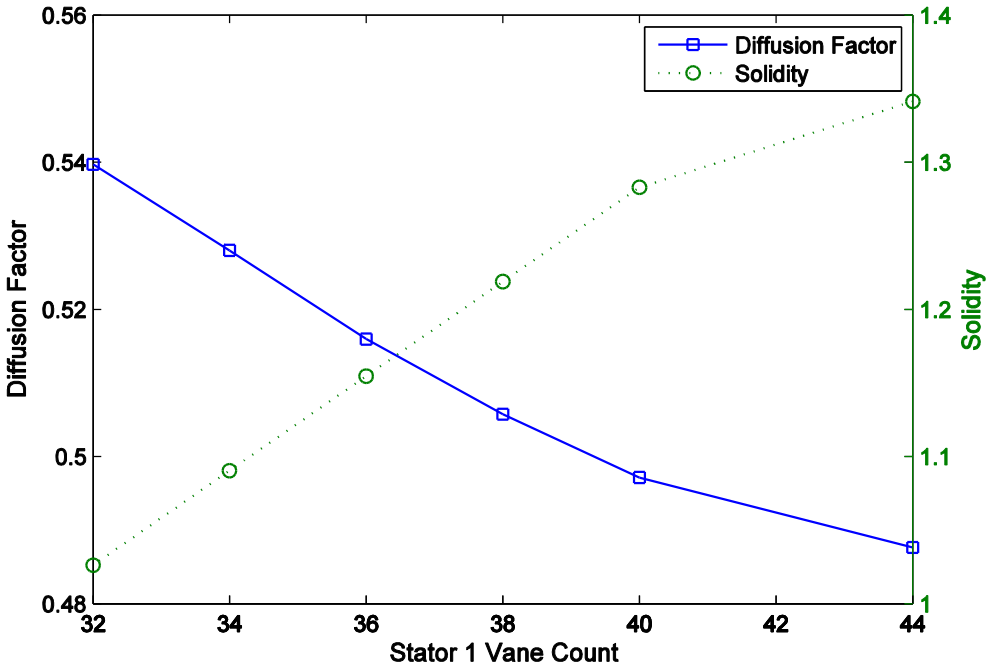

Figure 5.1: Area-averaged diffusion factor and solidity for S1 designs with different vane counts.

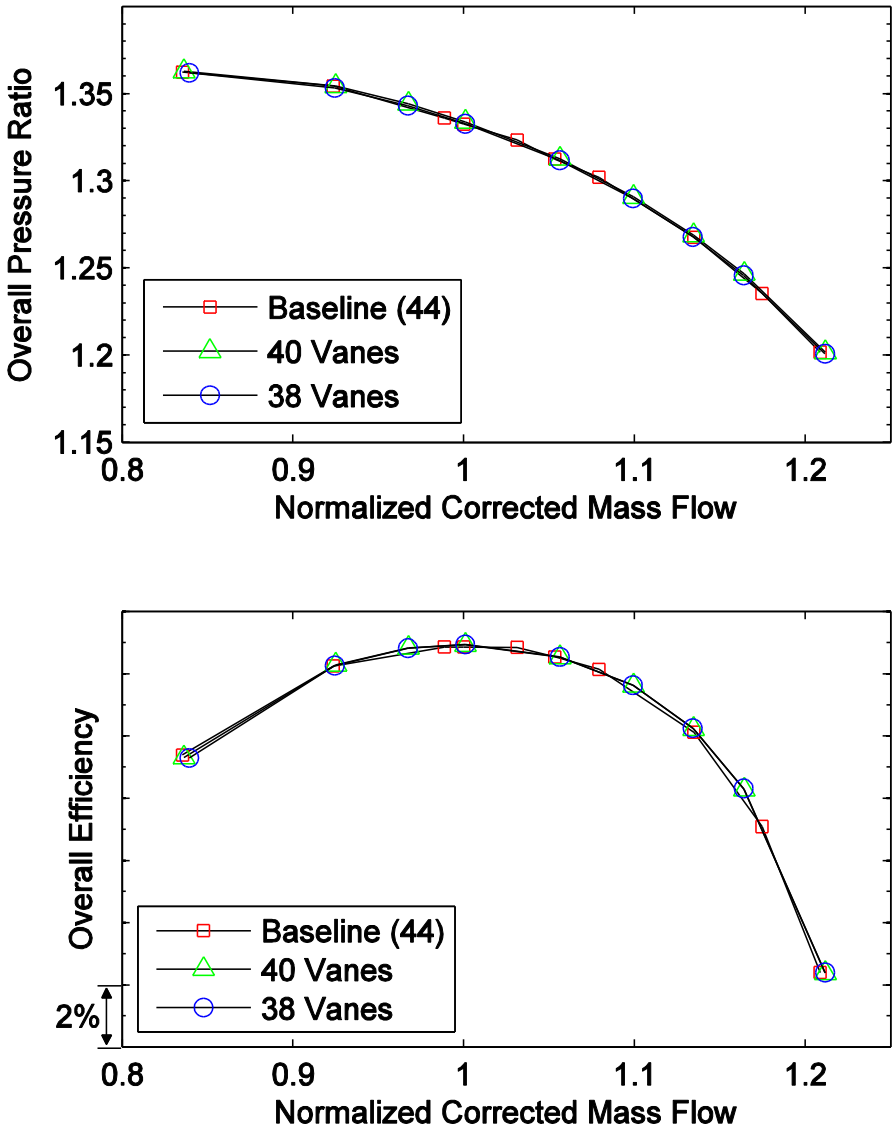

Figure 5.2: Overall compressor performance for different S1 counts.

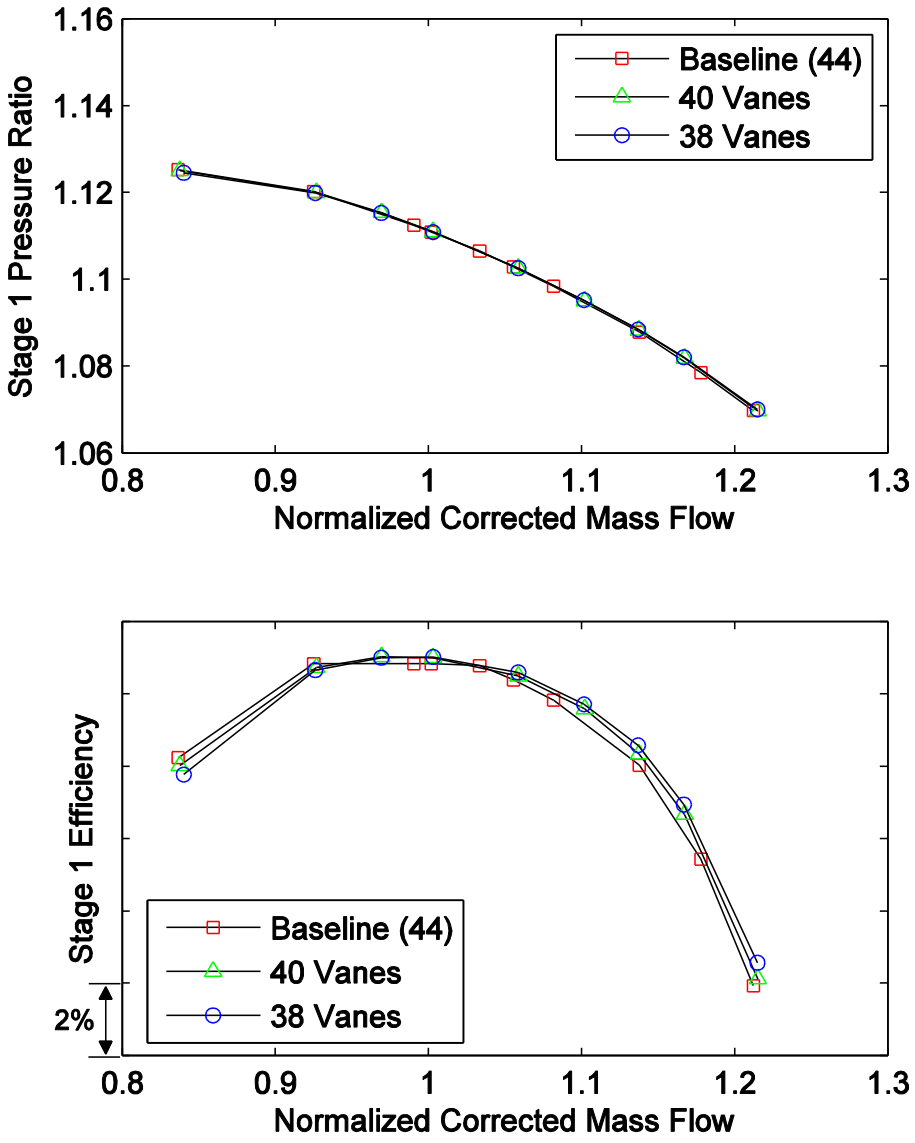

Figure 5.3: Stage 1 performance (IGV inlet to S1 exit) for the three S1 counts.

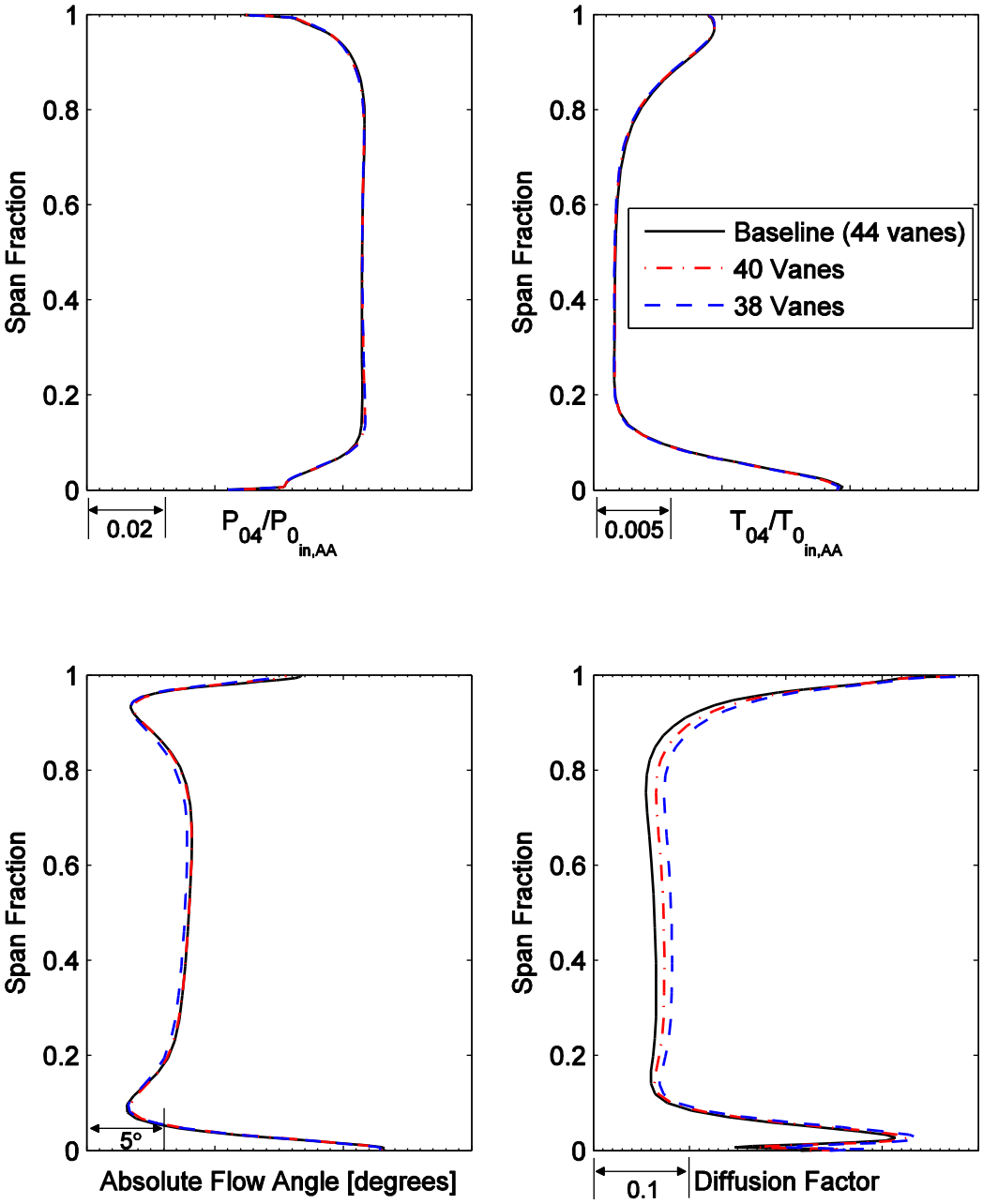

Figure 5.4: Stator 1 exit flow properties for Baseline (44), 40, and 38 count vane designs

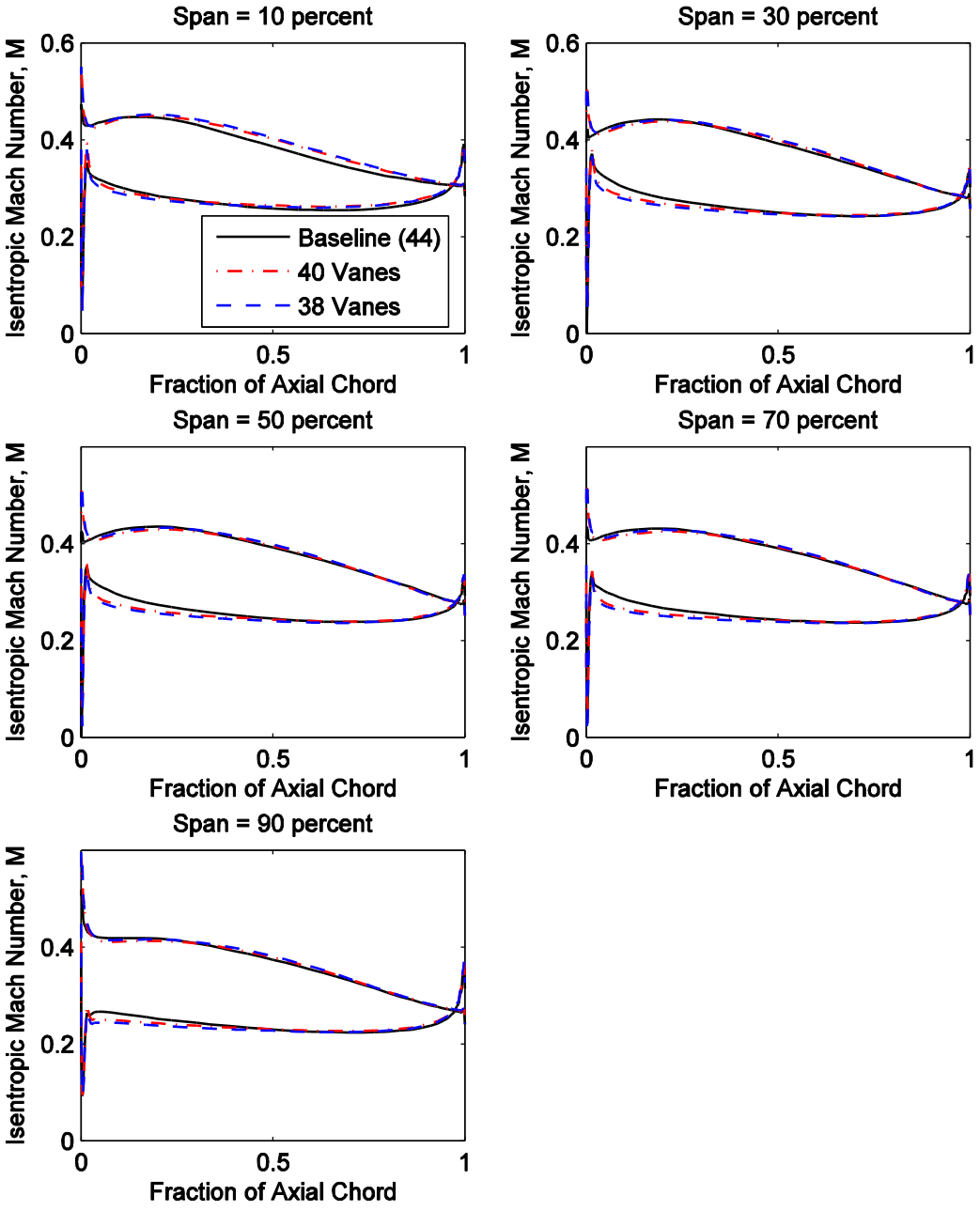

Figure 5.5: Isentropic Mach number distribution along chord for three vane counts.

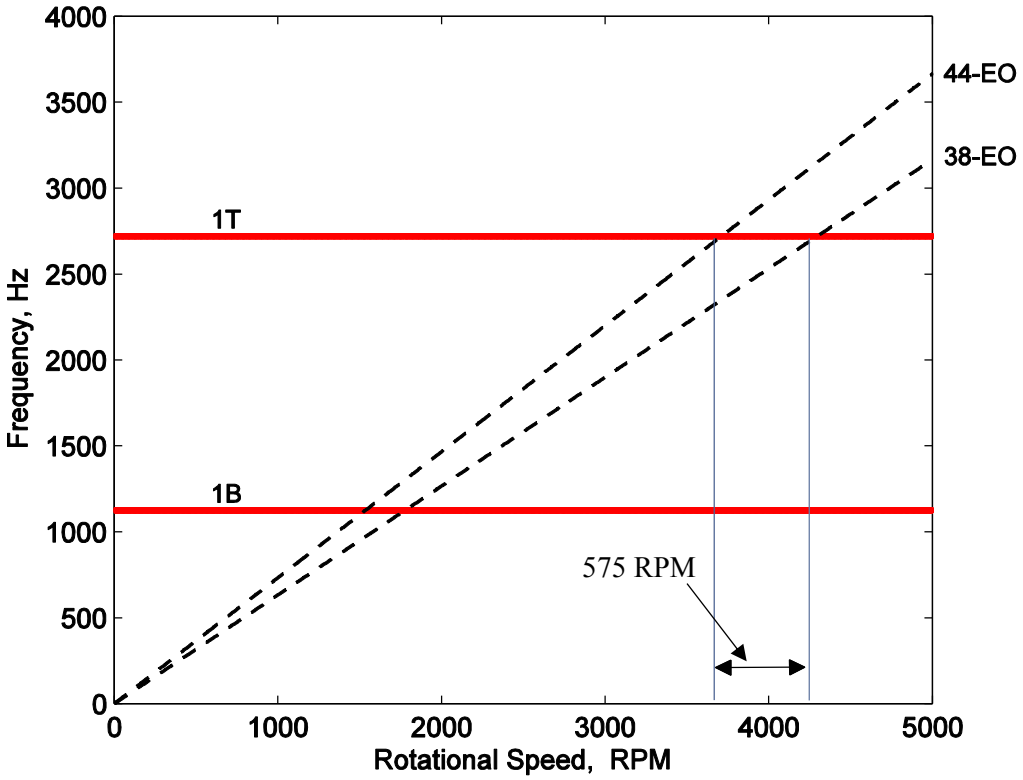

Figure 5.6: Rotor 2 Campbell Diagram.

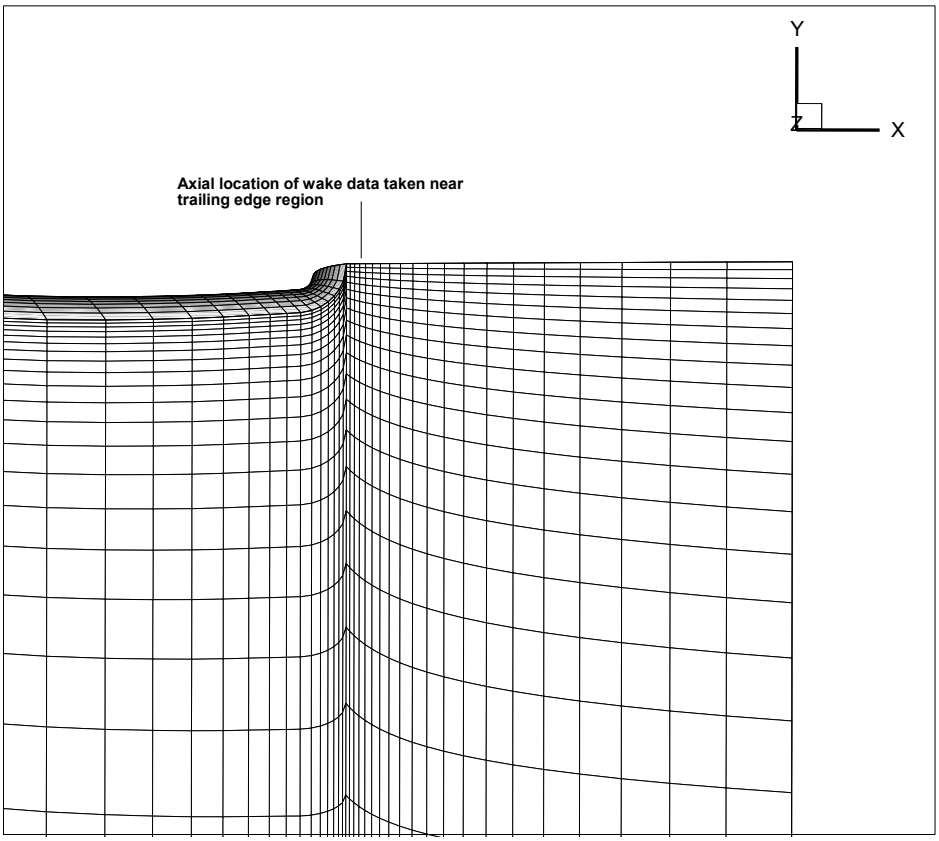

Figure 5.7: Computational mesh at Stator 1 trailing edge region.

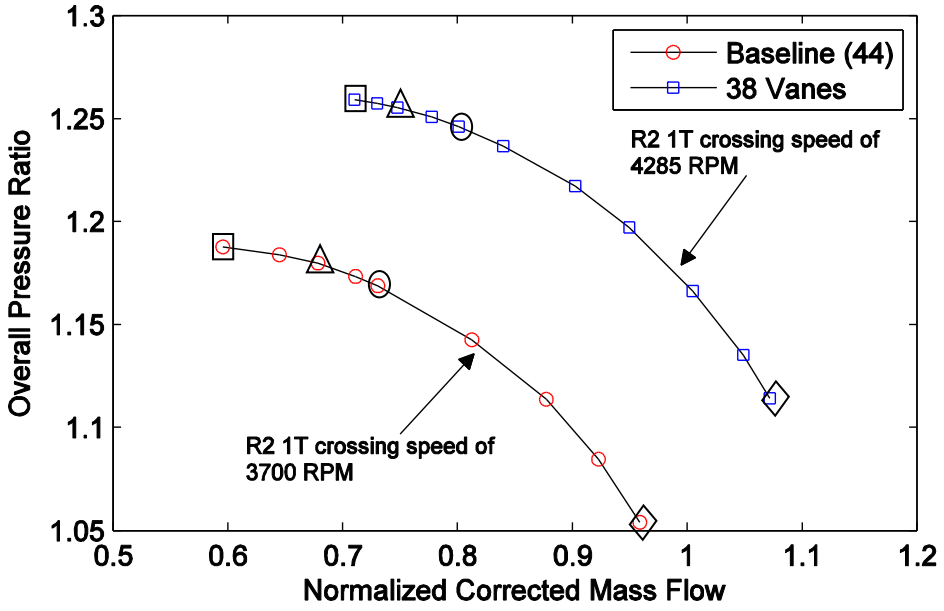

Figure 5.8: Compressor characteristics at R2 1T crossing with comparative loading conditions.

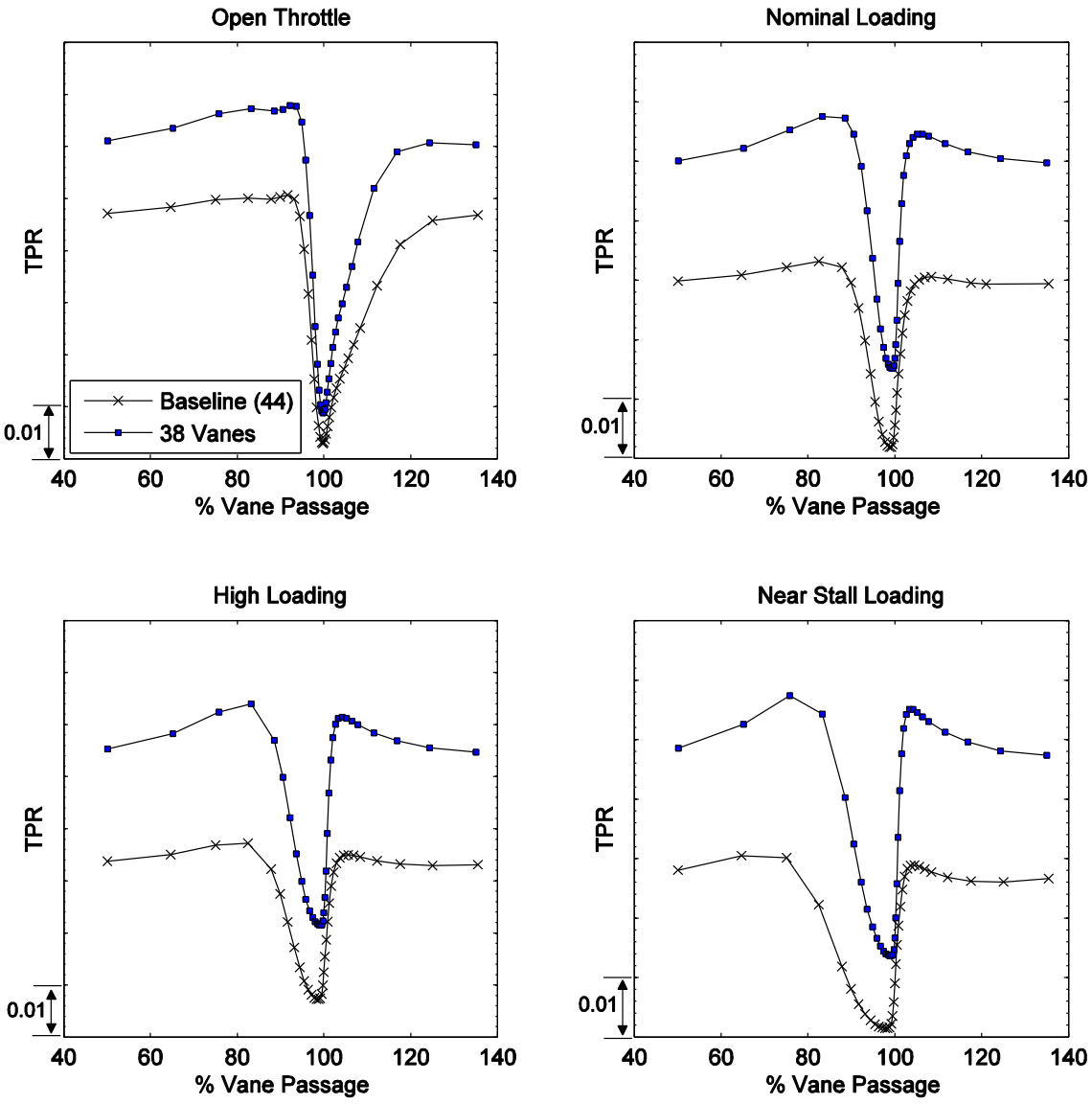

Figure 5.9: Mid-span total pressure S1 wake profiles at several loading conditions.

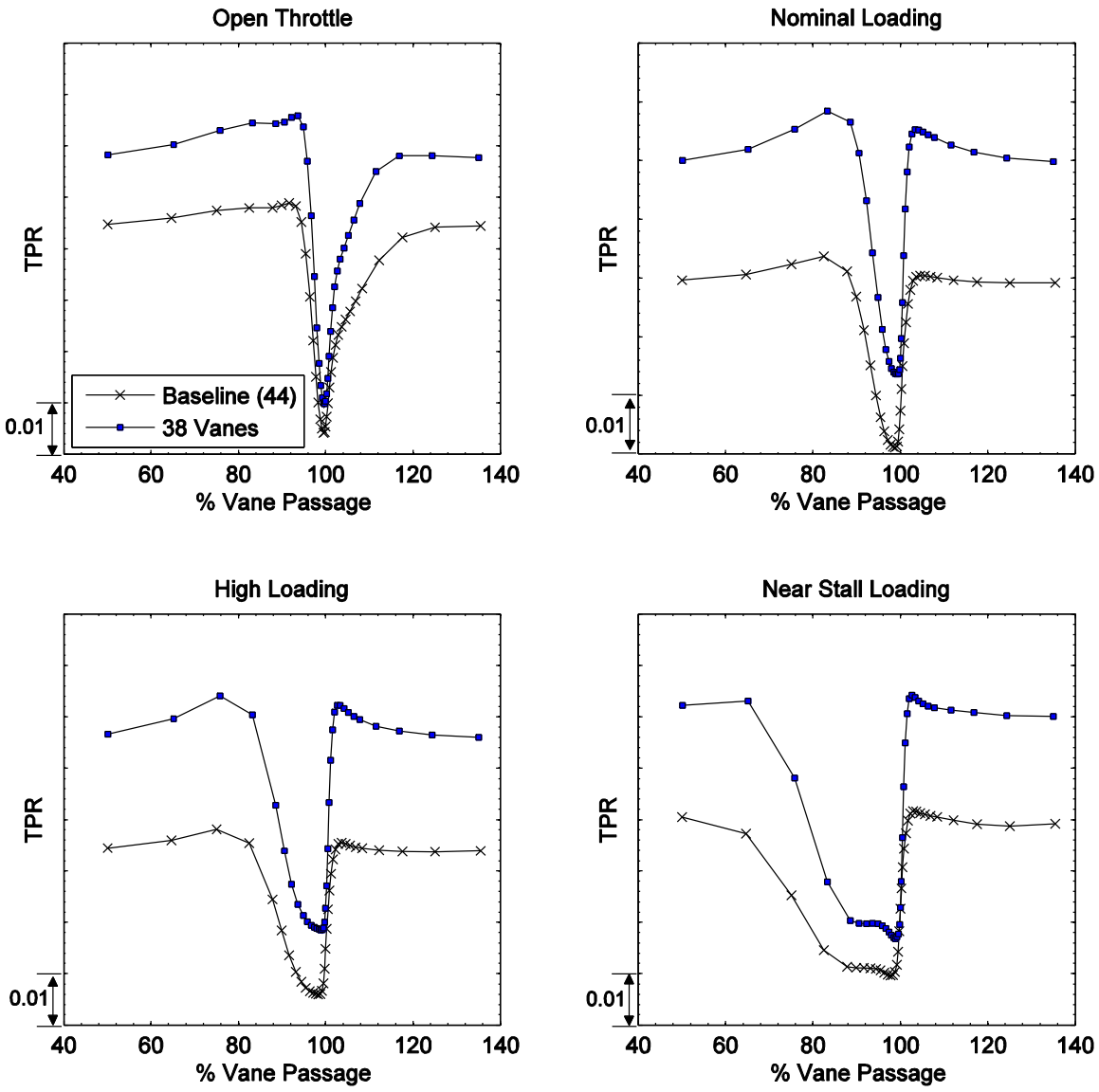

Figure 5.10: S1 wake profiles at 80% span for several loading conditions.

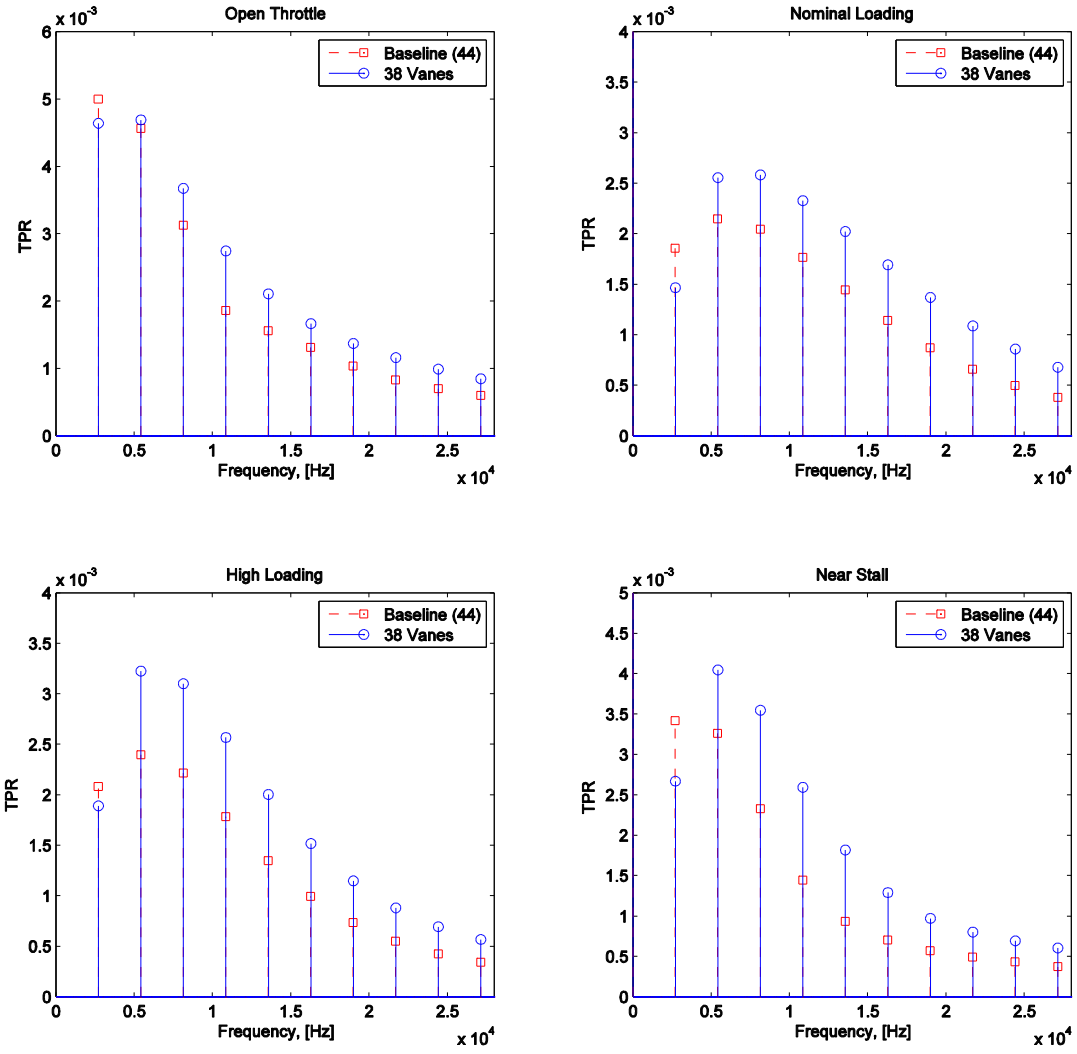

Figure 5.11: Spectrum of total pressure wakes at mid-span for several loading conditions.

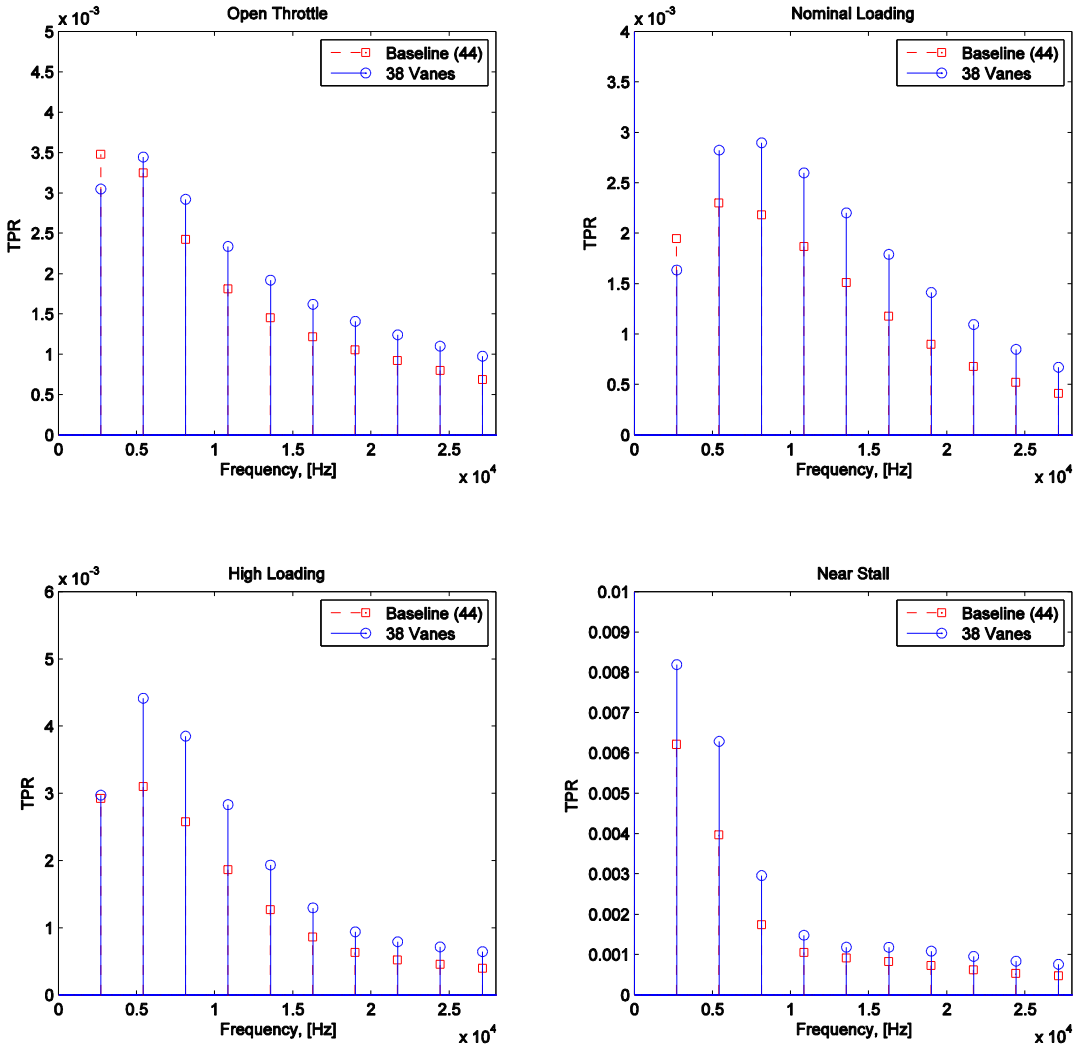

Figure 5.12: Spectrum of total pressure wakes at 80% span for several loading conditions.

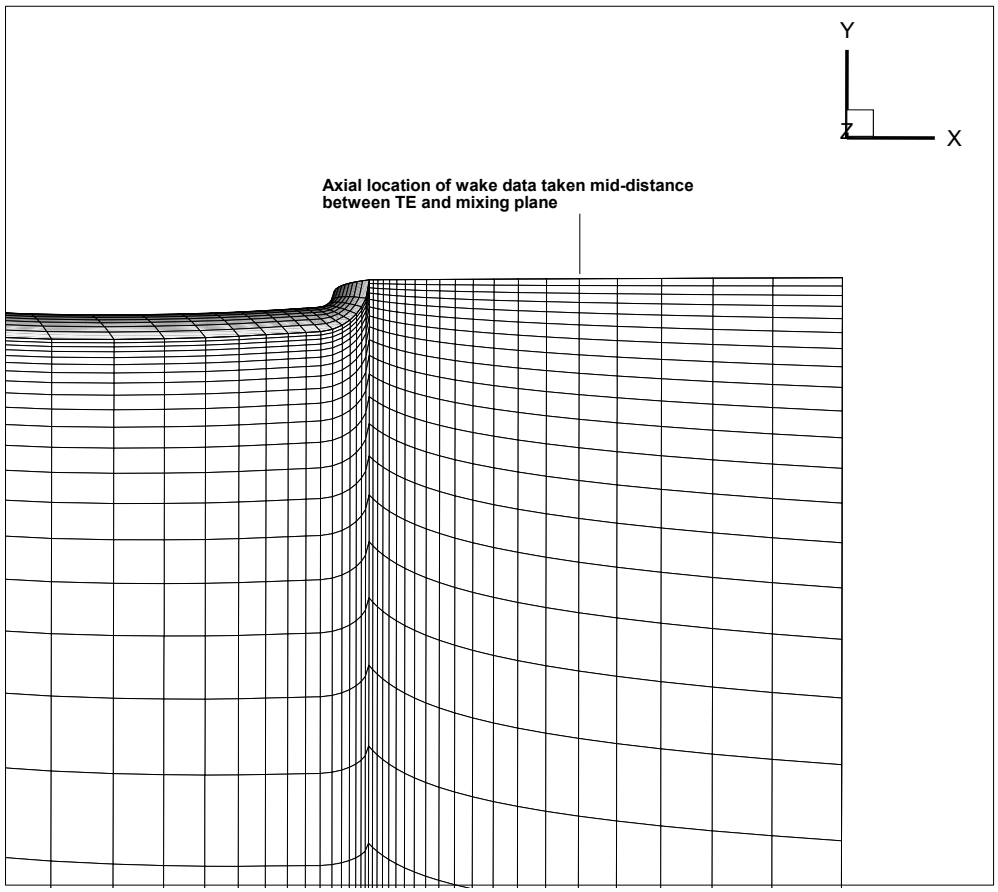

Figure 5.13: Computational mesh showing axial location of data sampled half way between TE and mixing plane.

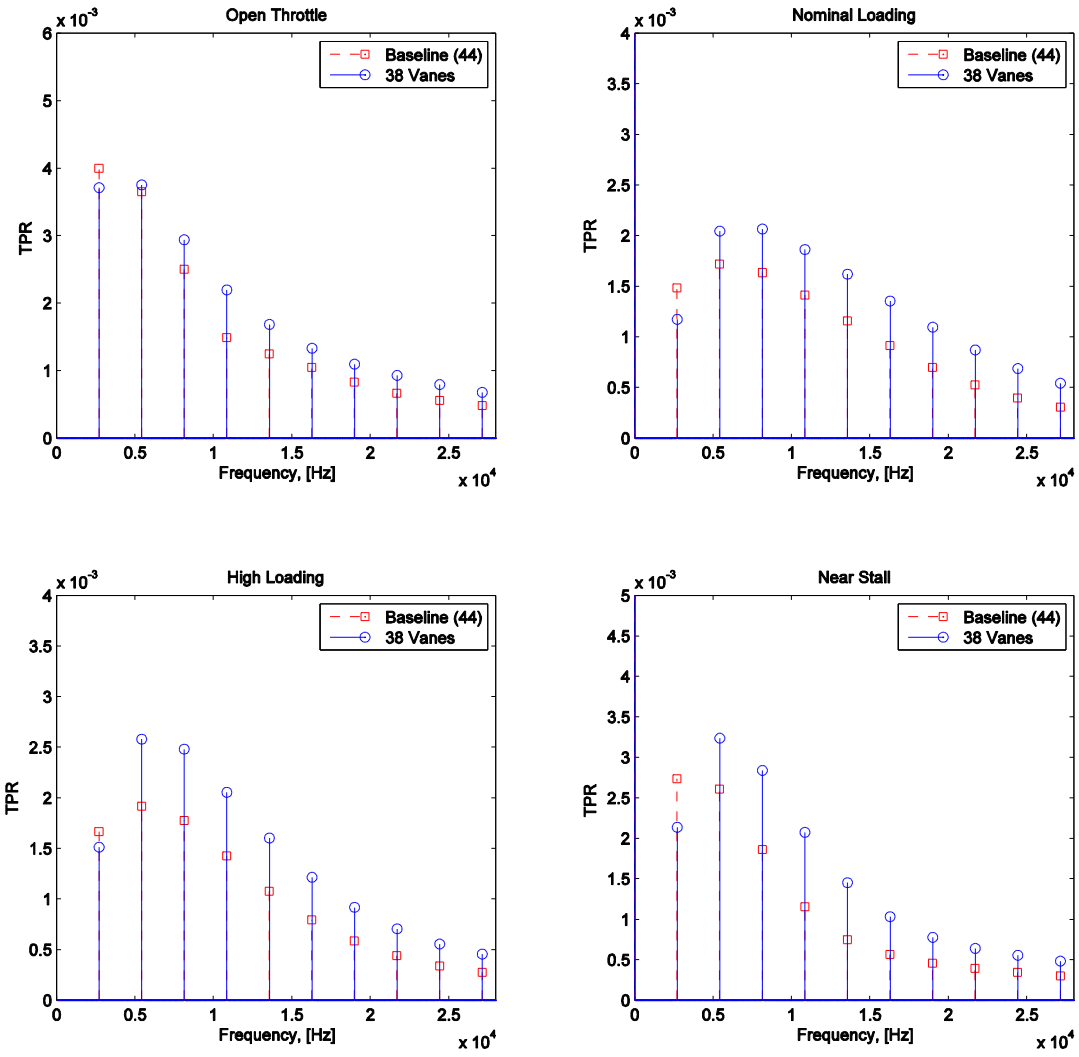

Figure 5.14: Spectrum of total pressure wakes at 50% span for several loading conditions at an axial location halfway between the trailing edge and mixing plane.

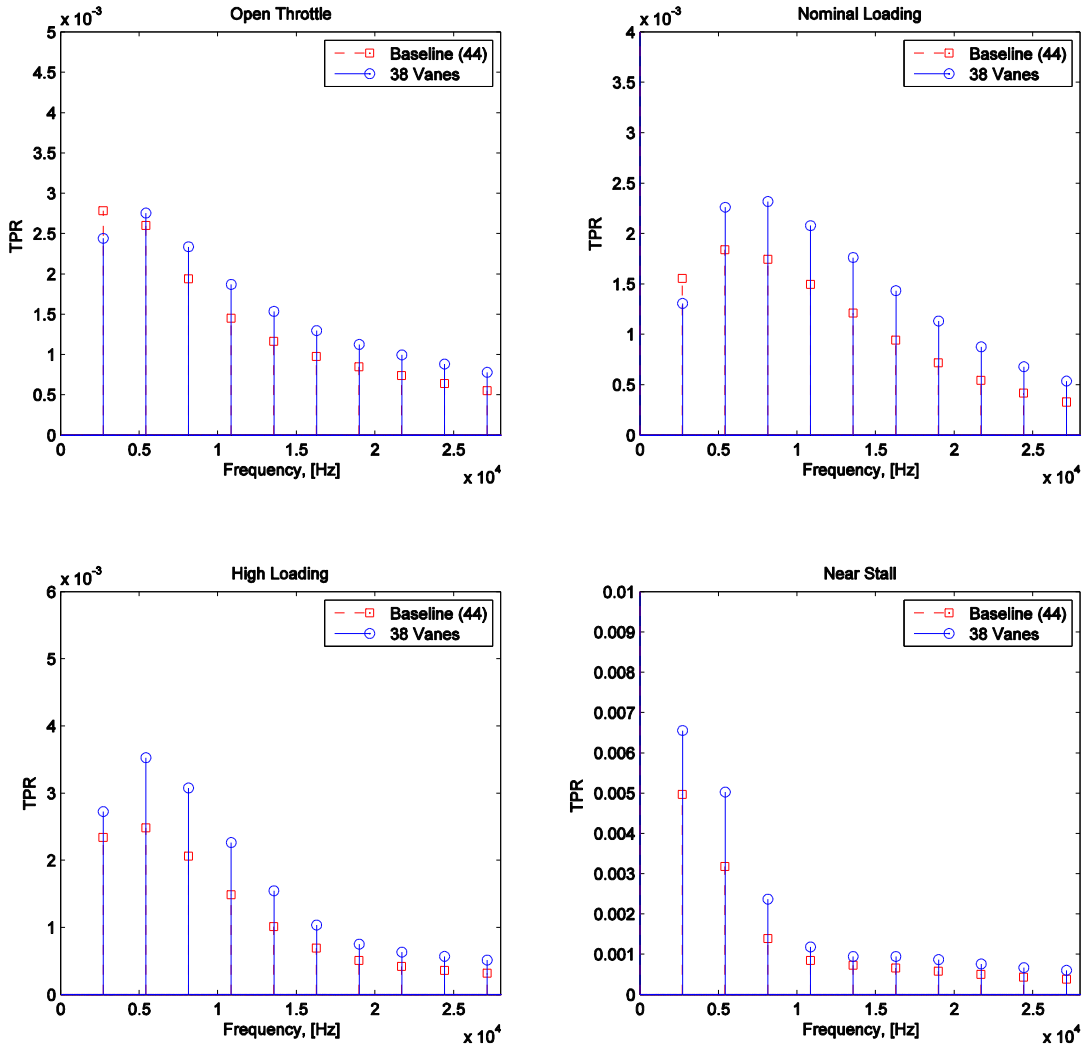

Figure 5.15: Spectrum of total pressure wakes at 80% span for several loading conditions at an axial location halfway between the trailing edge and mixing plane.

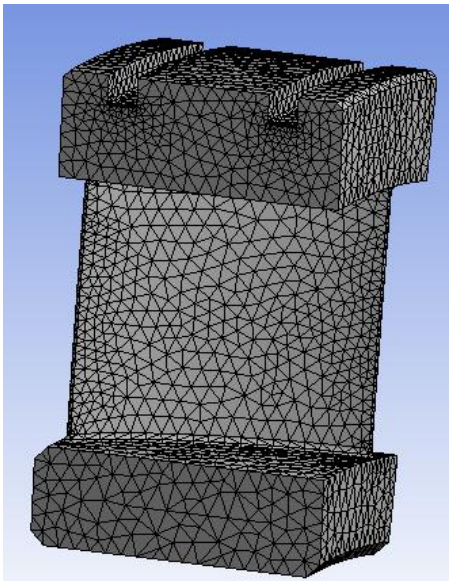

Figure 5.16: Stator 1 modal analysis mesh.

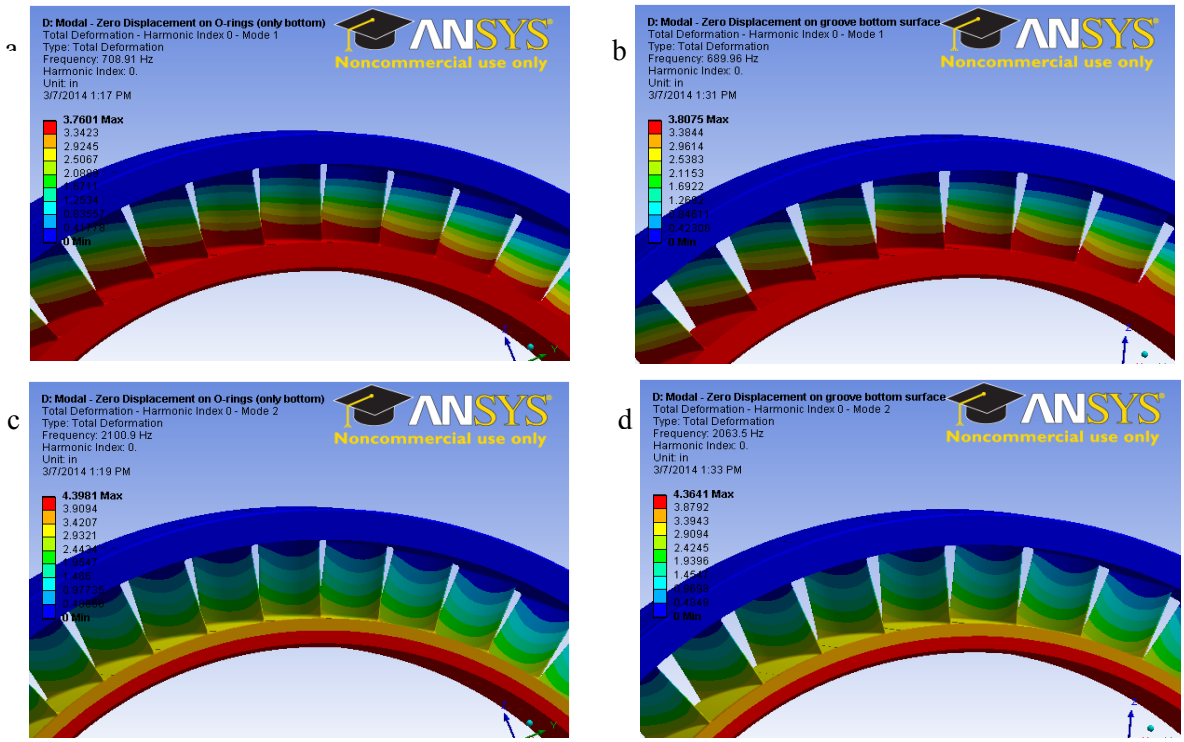

Figure 5.17: a) Mode 1–44 vanes, b) Mode 1–38 vanes, c) Mode 2– 44 vanes, d) Mode 2–38 vanes.

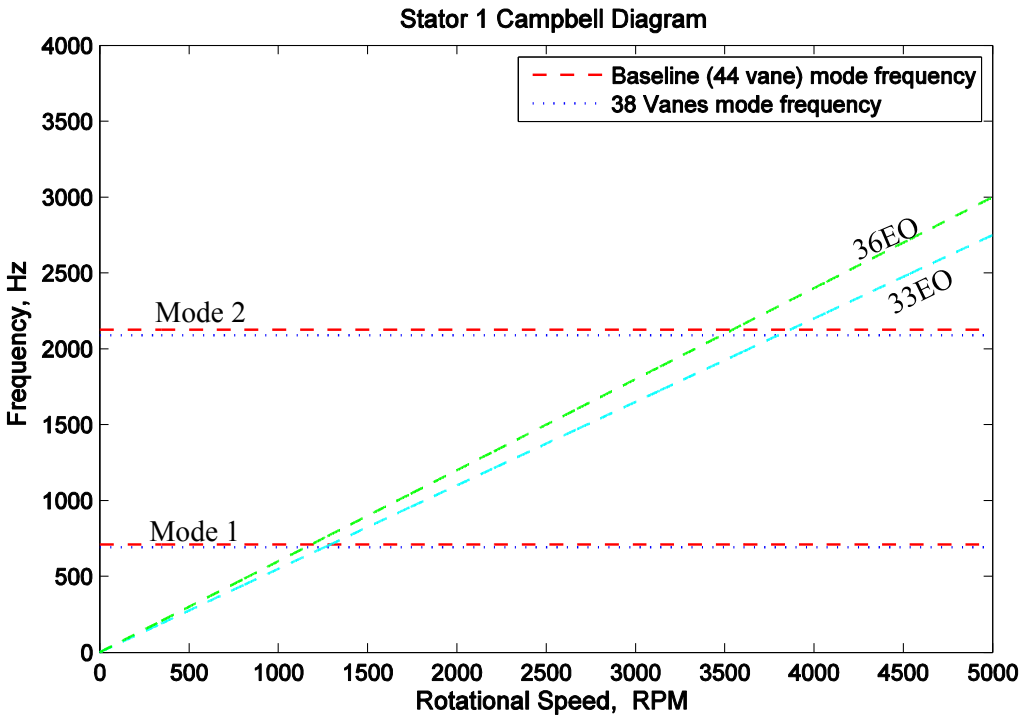

Figure 5.18: Stator 1 Campbell Diagram showing new stator design

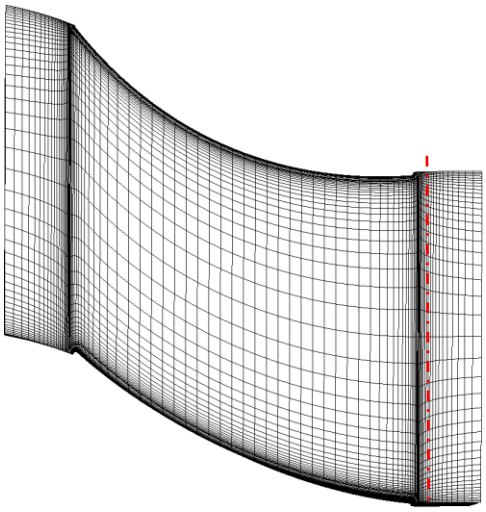

Figure 5.19: Location where wake data taken.

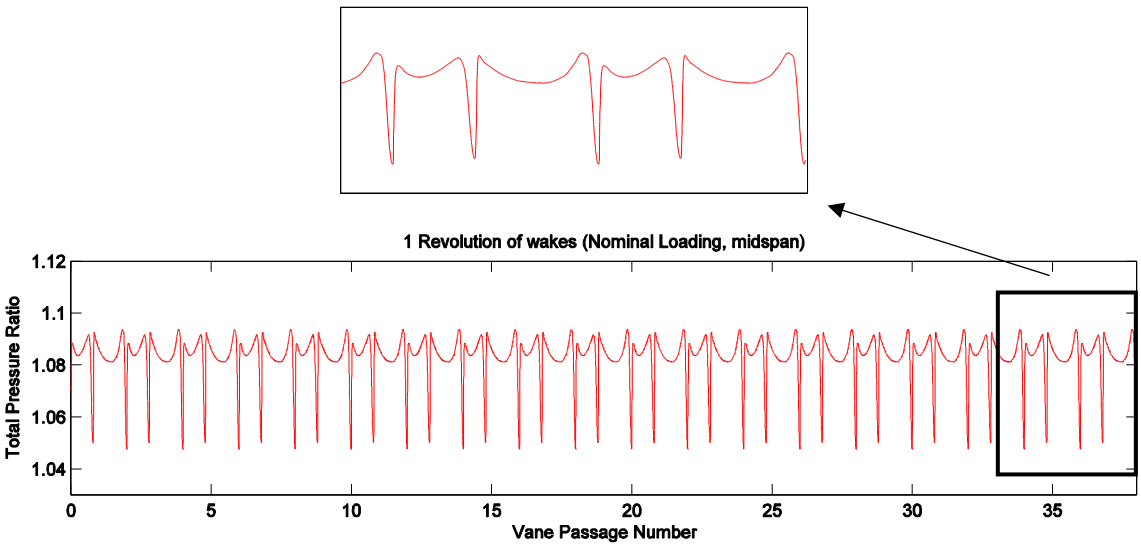

Figure 5.20: Full-annulus wake structure for (+/-) 20% NUVS geometry, midspan.

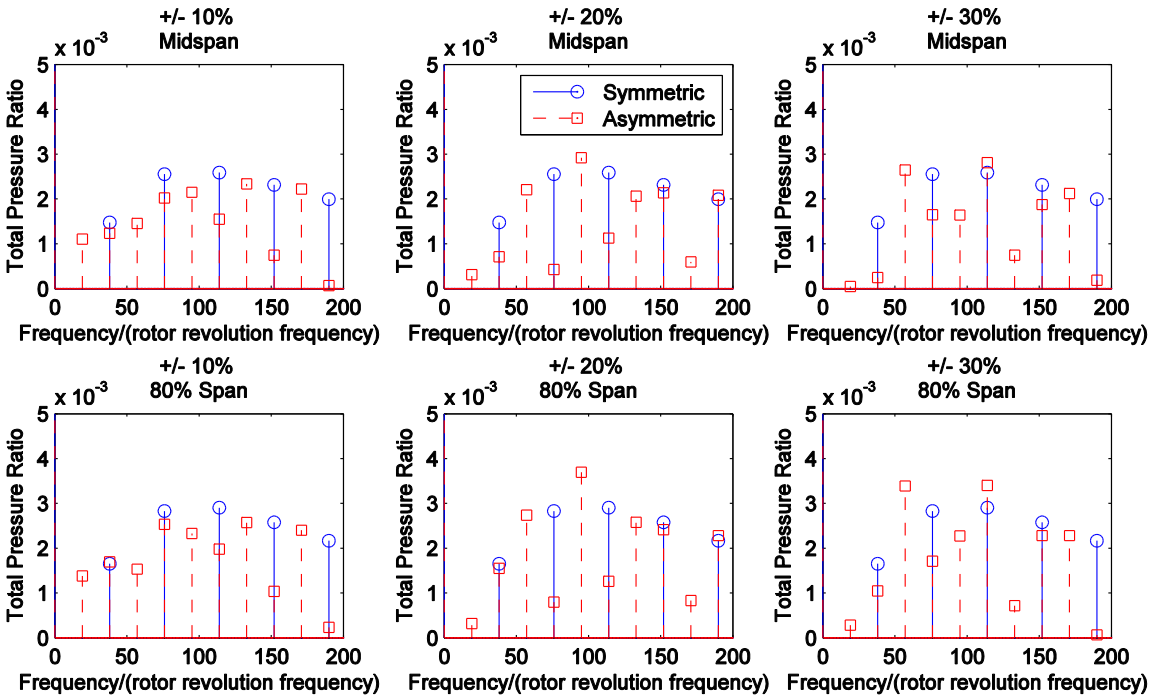

Figure 5.21: DFT of NUVS asymmetric wake, +/- 10% (left); +/- 20% (middle); +/- 30% (right).

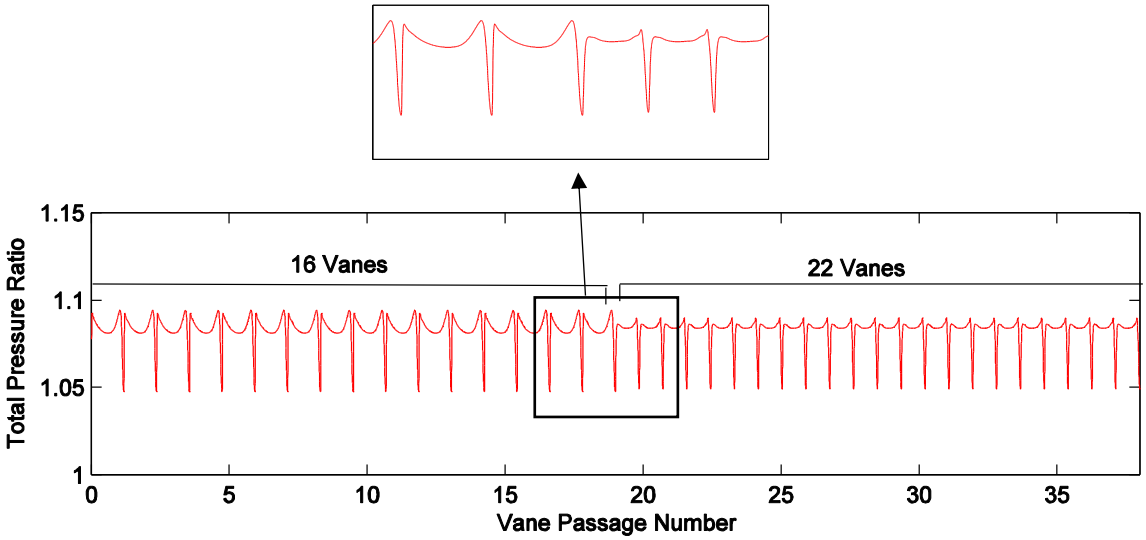

Figure 5.22: Representative full annulus wake structure asymmetric stator (midspan).

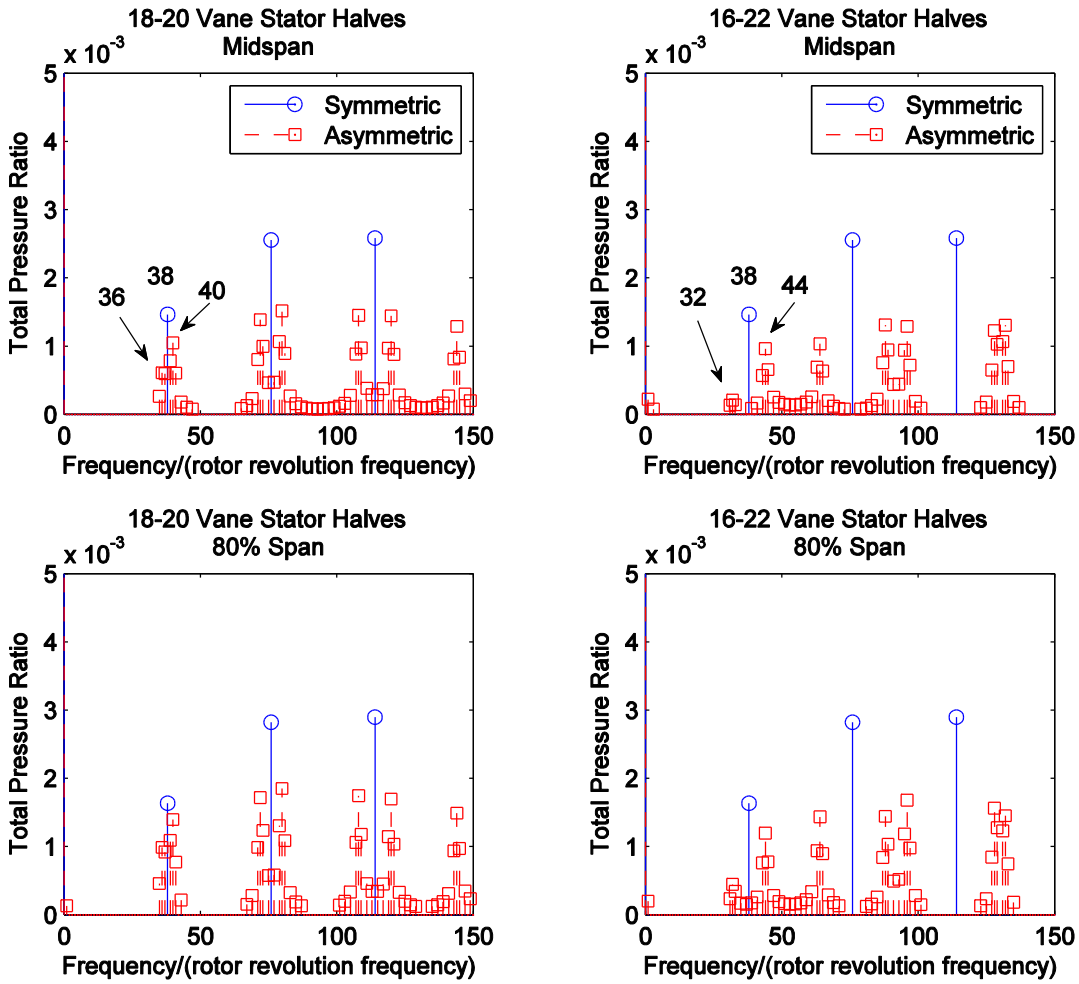

Figure 5.20: DFT of S1 wakes for stator halves with different vane counts; 18-20 vane combination (left), 16-22 vane combination (right).

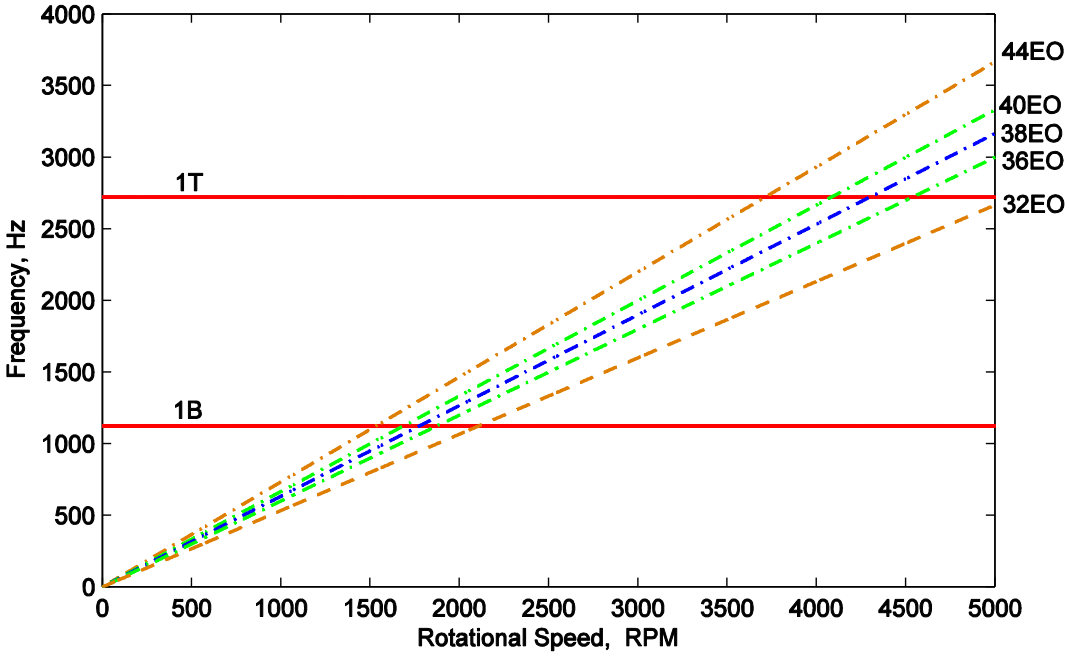

Figure 5.24: Rotor 2 Campbell Diagram, showing EO excitations from stator asymmetry.

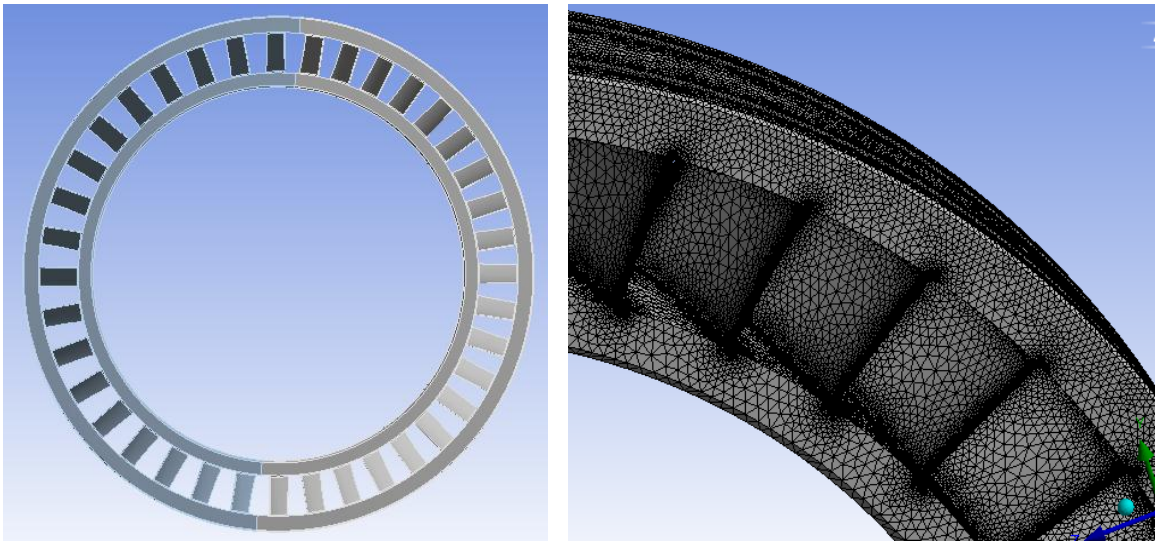

Figure 5.25: Solid model of asymmetric stator ring (left), view of computational mesh (right).

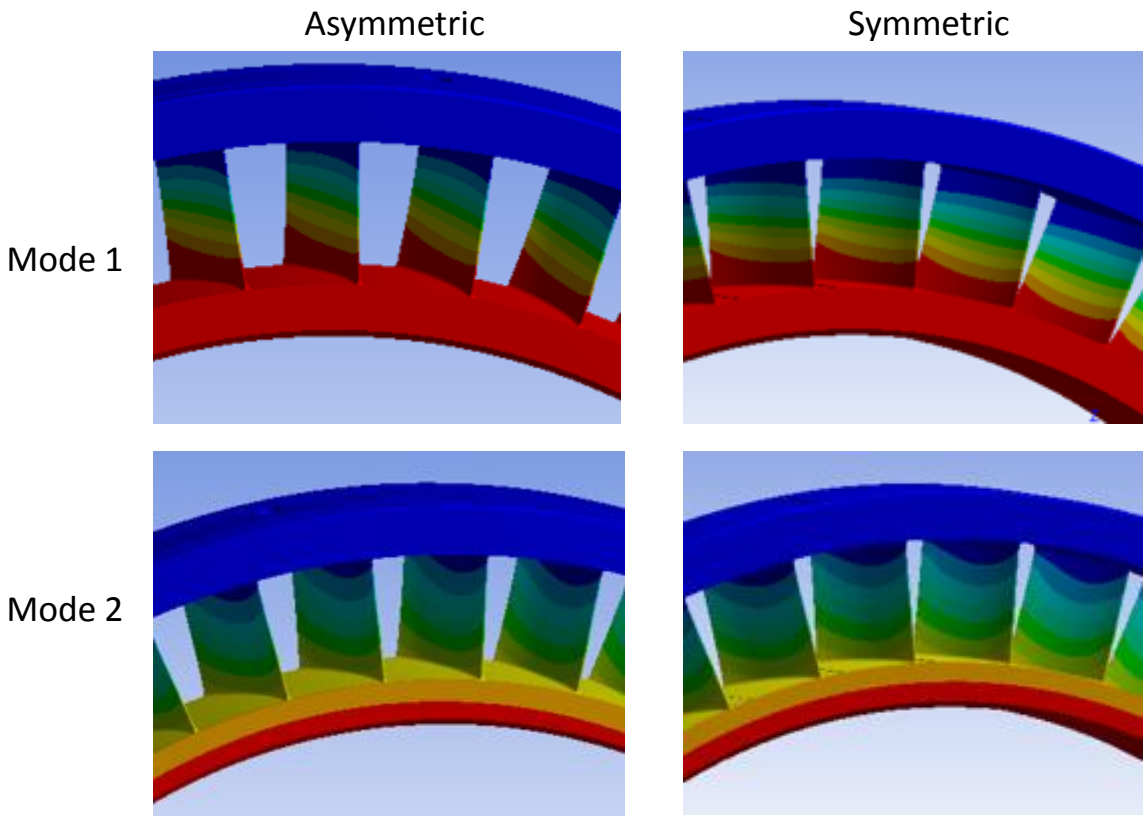

Figure 5.21: Mode shapes of first two modes for 38-vane symmetric and asymmetric S1.

CHAPTER 6: EFFECT OF S1 ASYMMETRY ON R2 FORCED RESPONSE

Further analysis was performed to investigate the effect of Stator 1 asymmetric vane spacing on the aerodynamic forcing and forced response of Rotor 2 at the 1st Torsion mode. Identifying and preventing forced response-induced HCF failures is a costly and critical aspect of the compressor design program. Engine failures due to forced response-induced HCF have received national attention throughout the years and have led to significant financial losses and lengthy investigations. El-Aini et al. (1997) postulates that while 90% of potential HCF problems are uncovered during the engine development and testing program, the few that are not discovered account for nearly 30% of the total development cost. These can be especially harmful in industrial turbomachines that are designed to run in continuous operation. Mazur (2008) reported a heavy-duty steam turbine which experienced a turbine blade failure after operating at an unknown resonance speed for just 7 seconds. The risk of forced response and HCF is well understood. As forced response vibrations are excited by aerodynamic flow disturbances, designers are constantly searching for methods to reduce the strength, or forcing, of these disturbances.

Viscous wakes shed from upstream stator rows provide the strongest source of aerodynamic forcing. The work presented in Chapter 5 outlined the design of an asymmetric stator in which half-annulus sectors with different vane counts were placed together to form a full stator ring. The final design consisted of an 18-vane stator half and a 20-vane stator half, shown in Figure 6.1. By modifying the vane spacing of the stator, and thereby creating an asymmetric configuration, the frequency spectrum of the vortical disturbances are altered. Comparing spectral amplitudes of the vortical field at the 1T mode frequency, between the symmetric and asymmetric

38-vane S1, will determine the effect of asymmetry on the vortical forcing functions. The initial analysis presented in Chapter 5 revealed that the asymmetric configuration decomposes the 38/rev principal harmonic of the symmetric S1 and shifts energy instead into 36/rev and 40/rev components. This results in new 36EO and 40EO excitation lines on the R2 Campbell Diagram (Figure 5.25) and two new resonant operating speeds. A detailed computational analysis is now performed in which steady and unsteady, full annulus geometries were considered to determine the effect of asymmetric and aerodynamic forcing. The simulations were run at the 38EO crossing speed for the symmetric S1 and both the 36EO and 40EO crossing speeds for the asymmetric S1 geometry. Both cases are run at Nominal Loading.

6.1 Analysis at 40EO Crossing Speed

This first analysis compares the vortical forcing of the symmetric S1 at the 38EO crossing speed of 4285 rpm with the asymmetric configuration at the 40EO crossing speed of 4080 rpm. As would be expected the higher RPM of the symmetric case at the resonance crossing produces a higher total pressure ratio and absolute velocity at the S1 exit plane. Figure 6.2 compares the full annulus total pressure wake structures in the steady state at both midspan and 80% span. The asymmetry is clearly shown as the wake troughs of the asymmetric S1 do not align with the symmetric S1 geometry. Since the symmetric 38EO crossing speed is over 200 rpm higher than the 40EO crossing speed, the wakes are larger in depth (total pressure deficit). Figure 6.3 shows the wake comparison for just 3 stator passages, presenting a more detailed comparison. In this circumferential window the wakes line up closely with each other. The width of the total pressure wakes does not change significantly between the two S1 configurations.

Figure 6.4 presents the frequency spectra of the total pressure wakes. Even though the asymmetric S1 still has 38 vanes, the asymmetric vane spacing eliminates the 38/rev frequency

component and shifts energy into neighboring frequencies. Distinct amplitude peaks occur at 36/rev and 40/rev, corresponding to the 18-vane and 20-vane stator half-sectors. At midspan the asymmetry significantly reduces the total pressure amplitudes at the frequency components of interest. At the 36/rev component, the amplitude is reduced by 32%, while at the 40/rev frequency component, the total pressure amplitude is decreased by over 40%. This amplitude reduction is not isolated to the principal harmonic. Each of the five harmonics shown in the figure experience significant amplitude reductions at midspan. The frequency spectrum at 80% span shows that principal harmonic is nearly eliminated. The 38/rev amplitude of the symmetric stator is reduced to less than one-fifth of the midspan amplitude. Analyzing the amplitudes of the asymmetric stator show that the 40/rev amplitude is 8% larger than the symmetric S1 principal harmonic. However, with the relative amplitudes of the principal harmonic at such decreased levels, this increase is inconsequential and would not be expected to create a measurable increase in the vortical forcing on R2.

Analyzing the absolute velocity wakes yields similar conclusions. Figure 6.5 compares the full annulus absolute velocity wake structure. Note the effect of the asymmetry on the velocity wake depth. The interface between the 18-vane and 20-vane half-stator sectors occurs at 120° and 270°, which are the same circumferential locations of minimum velocity wake depth. This effect is more noticeable at midspan, though it does exist, to a lesser extent, at 80% span. The depth of the velocity wakes is also comparable between the symmetric and asymmetric configurations, shown clearly in Figure 6.6.

Computing the frequency spectra of the absolute velocity wakes shows that the overall amplitude in each of the harmonics is decreased by the vane spacing asymmetry as shown in Figure 6.7. At both spanwise locations, the 40/rev component (the frequency of interest

corresponding to the 40EO excitation) is decreased by over 40%. Such a decrease in amplitude is significant and should provide measureable reductions in R2 vibrational response.

Analyzing the wake profiles in the unsteady state also gives insight into the vortical forcing functions. The benefit of unsteady CFD is that blade row interactions are captured. It is a more realistic, high-fidelity, estimate of the flow physics occurring inside the compressor. Unlike the mixing plane approach of the steady simulations where flow properties are averaged out across adjacent mesh blocks, the unsteady approach interpolates flow properties onto adjacent mesh blocks so that flow structures propagate undistorted across mesh boundaries. As vortical forcing is the focus of this work, the propagation of these flow structures and their interaction with Rotor 2 is important to understand. Figure 6.8 shows entropy contours at 80% span for the asymmetric stator operating at the 40EO crossing speed. The reduced frequency of the velocity field at R2 inlet and at this spanwise location is computed to be k=1.65, meaning that 1.65 S1 wakes exist in the R2 passage at any instant in time. Also noticeable in this figure is the S2 potential field. The potential field propagating from the middle S2 vane in this image distorts the R2 wake as it begins to impinge on the vane leading edge. One interaction that is difficult to discern is that of the R2 leading edge potential field with the S1 wakes. A DFT of the absolute velocity field at the sliding plane interface between S1 and R2 highlights this rotor-stator interaction. Figure 6.9 compares the asymmetric S1 geometry steady frequency spectrum to the unsteady frequency spectrum. The most noticeable difference is the addition of the R2 BPF, which appears at 33/rev, 66/rev, 99/rev, etc. Amplitudes at the first three harmonics are changed the least in the unsteady spectrum. The 40/rev component at 80% span is increased only 5% in the unsteady case and 10% at midspan.

6.2 Analysis at 36EO Crossing Speed

Analyzing the vortical wake profiles of the asymmetric S1 geometry operating at the 40EO crossing speed showed that the asymmetry reduces the amplitude of the symmetric S1 principal harmonic by decomposing the energy from the 38/rev and harmonics into neighboring frequencies. The decrease in amplitude does not come as a complete surprise as the crossing speed of the 40EO excitation line on the R2 Campbell diagram is less than the crossing speed of the symmetric S1 38EO excitation. A lower crossing speed means the S1 wake profile will be at a lower pressure with smaller total pressure and absolute velocity wake deficits. The bigger question to answer is whether this same amplitude reduction occurs at the 36EO crossing speed, where the resonance speed is nearly 250 rpm higher than the 38EO crossing speed.

Figure 6.10 compares a multi-passage section of the S1 total pressure wakes for the asymmetric S1 at 4533 rpm to the symmetric S1 at 4285 rpm. In this circumferential window the wakes line up well, allowing a qualitative comparison of wake shapes between the two cases. Wake width and depth appear to be very similar. In fact, total pressure wake shapes change very little on the asymmetric S1 between the 18-vane stator half and the 20-vane stator half. A spectral analysis of the total pressure wakes is shown in Figure 6.11. As with the 40EO results, the addition of asymmetry reduces the total amplitude of the spectrum, especially in the higher harmonics. At midspan, the 36/rev frequency component is reduced 18% from the symmetric first harmonic. At 80% span, the 36/rev amplitude is increased 70% from the 38/rev component. However, the overall amplitude at this frequency is small, and the relative amplitude increase in the asymmetric S1 will not have a significant effect on the R2 1T response. At all higher harmonics, the asymmetric S1 total pressure amplitudes are reduced by at least 40%.

Figure 6.12 compares the full annulus absolute velocity wakes. Again, note the variation in midspan wake depth of the asymmetric wake profile in the transition region between the 18-

vane stator half and the 20-vane stator half. The wake depth variation is less apparent at 80% span. A more detailed view of the absolute velocity wake shapes is given in Figure 6.13. The midspan velocity wakes appear much narrower and more of an impulse shape than the total pressure wake profiles. The asymmetric wakes appear to be slightly narrower than the symmetric S1 wakes within this circumferential window.

Analyzing the DFT of these profiles shows that the asymmetric stator reduces the absolute velocity amplitude at both spanwise locations and for all harmonics, Figure 6.14. The 36/rev component of the midspan wake is reduced 25% from the principal harmonic of the symmetric stator. At 80% span the 36/rev frequency component is reduced by 40%.

The present analysis concludes that the introduction of asymmetry has a noticeable benefit in reducing the critical vortical frequency components in the wakes shed from S1. Combining stator half-sectors of 18-vanes and 20-vanes shifted energy away from the 38/rev principal harmonic of the symmetric configuration and into amplitude peaks at 36/rev and 40/rev. These two new principal harmonics correspond to resonant speeds of 250 rpm above and 205 rpm below the resonant speed of the symmetric S1, respectively. The work presented, however, confirms that even at higher resonant operating speeds the asymmetric configuration reduced the vortical amplitudes at the frequencies of interest.

6.3 Rotor 2 Vibrational Response

The vibrational response of R2 at the 1T mode is calculated to quantify the change in vibrational amplitudes caused by the S1 vane spacing asymmetry. As presented in Chapter 4, vibrational amplitudes are dependent upon several parameters, including modal force magnitudes,

Q-factors, mode shape amplitudes, and resonance frequencies (see Equation 4.1). Modal forces are computed in the CFD simulation by integrating surface pressures of the R2 blade at each time step. A time-history of the modal force shows the cyclic nature of this forcing, which results in blade vibration cycles. The time-history of modal force for the 38-vane symmetric S1 is shown in Figure 6.15.

The S1 vane reduction from the Baseline 44-vane S1 presented in Chapter 4 to the 38-vane symmetric S1 presently analyzed changed the nodal diameter excitation of the R2 disk. The difference in blade counts – 33 R2 blades and 38 S1 vanes, now creates a 5ND excitation. Determining the nodal diameter excitation of the asymmetric S1 is slightly more complex, and the R2 response now shifts to two separate ND excitations. The response to the 18-vane stator half occurs as if the 18-vane half were a full 36-vane stator. This creates a 3ND excitation of the R2 disk. Likewise, the 20-vane stator half creates a 7ND excitation of R2 as if it were a full 40-vane stator. The 3ND response will occur at the 36EO excitation while the 7ND response occurs at the 40EO excitation speed. As a comparison the symmetric 38-vane vibrational response, the 5ND response is also computed at both the 36EO and 40EO excitation crossings. The asymmetric geometry decomposes the 38/rev frequency component dominant in the symmetric case and spreads energy in to neighboring frequencies. However, the 38/rev frequency component is still present in the frequency spectra for the asymmetric configuration at 36EO and 40EO excitation crossings and will excite a minor vibrational amplitude. As phasing and resonance frequency change with nodal diameter, the 5ND vibrational amplitude is not additive to the 3ND or 7ND responses at their respective EO crossings.

Additionally, only the vibrational response caused by the S1 vortical disturbances is considered. The upstream propagating potential field from S2 creates an additional forcing of R2. However, as S2 is comprised of 44 vanes the 44EO excitation line excites the R2 1T mode at a

different rotational speed. The focus of this study is to isolate only the effect of S1 asymmetry on the vortical forcing and resulting vibrational response.

Table 6.1 presents the total blade displacement amplitudes for each S1 geometry discussed. Blade displacement results presented in Chapter 4 computed only the circumferential displacement amplitude to allow a direct comparison to NSMS tip timing measurements. The present study computes the total blade displacement. The 38-vane symmetric S1 response at the 38EO crossing is considered the baseline response amplitude, and each of the asymmetric S1 responses are measured against this baseline. Asymmetric responses are measured at both the 36EO and 40EO Campbell Diagram crossing speeds, and for the 3ND and 7ND excitations, respectively. The peak-to-peak vibrational amplitude for the asymmetric S1 at the 40EO crossing is reduced by roughly 50% at the 7ND disk excitation. As the 40EO crossing occurs at a lower rotational speed than the baseline 38EO crossing, this was expected to experience the larger reduction. However, even at the increased rotational speed of the 36EO crossing, a large reduction is observed. The 3ND response at this crossing experiences a 35% reduction in maximum peak-to-peak blade displacements. Also present in Table 6.1 are the vibrational amplitudes of the 5ND diameter response at the both the 36EO and 40EO crossings. Compared to the symmetric 38-vane 5ND response, the asymmetry creates an 88% and 92% reduction of the 5ND response at the 36EO and 40EO crossings, respectively.

These results are consistent with the CFD-predicted decreases in the strength of vortical disturbances, resulting from the stator asymmetry. The magnitude of the reductions in vibrational amplitude, though, is greater than the computed reduction in the vortical forcing components. This is believed to be caused by relative phasing between the vortical disturbances and the potential disturbances propagating upstream from S2. If the potential disturbance is out of phase

with the vortical disturbances – which does occur due to the difference in vane counts, the two disturbances will in effect dampen the response of the rotor.

The analysis presented in this study confirms that the introduction of asymmetry in an upstream stator reduces the forced response in rotors. The specific stator asymmetry investigated combined an 18-vane stator half and a 20-vane stator half to form a full 38-vane stator ring. This difference in vane counts changed the frequency spectrum of the resulting wake structures by shifting energy out of the 38/rev principal harmonic of the symmetric stator and into 36/rev and 40/rev frequency components. This frequency spreading reduced the vortical forcing amplitudes compared to the symmetric stator and resulted in significantly lower R2 vibrational responses at the 1T mode. Interestingly, the higher harmonics experienced even greater vortical forcing amplitude reductions. It would then be expected that vibrational responses at higher EO harmonics and higher-order modes would experience greater reductions. Other forms of S1 asymmetry could also be implemented, each with the intent to modify the frequency spectrum of the aerodynamic forcing functions. Other concepts include varying the vane spacing in adjacent stator passages, altering the stagger angle of adjacent vanes, or fluctuating the trailing edge metal thickness. One significant benefit to the asymmetric concept implemented in this study is that the vane aerodynamics and performance are minimally changed from the symmetric baseline stator performance. Creating similar vibrational reductions with the other asymmetric concepts would likely result in greater changes in the aerodynamic performance of the stator. It is, therefore, asserted that implementing stator asymmetry in the form of stator halves with different vane counts creates a viable option for reducing dangerous vibrations and forced response issues in modern compressor systems.

Table 6.1: Summary of total blade displacements for asymmetric S1.

S1 Geometry	EO Excitation	Resonant Speed (RPM)	Blade Displacement (mils)	% reduction
Symmetric 38-vane S1: 5ND	38EO	4285.0	1.82388	
Asymmetric 38-vane S1: 7ND	40EO	4080.0	1.21461	49.16
Asymmetric 38-vane S1: 5ND	40EO	4080.0	0.20243	91.53
Asymmetric 38-vane S1: 3ND	36EO	4533.3	1.55872	34.76
Asymmetric 38-vane S1: 5ND	36EO	4534.3	0.29644	87.59

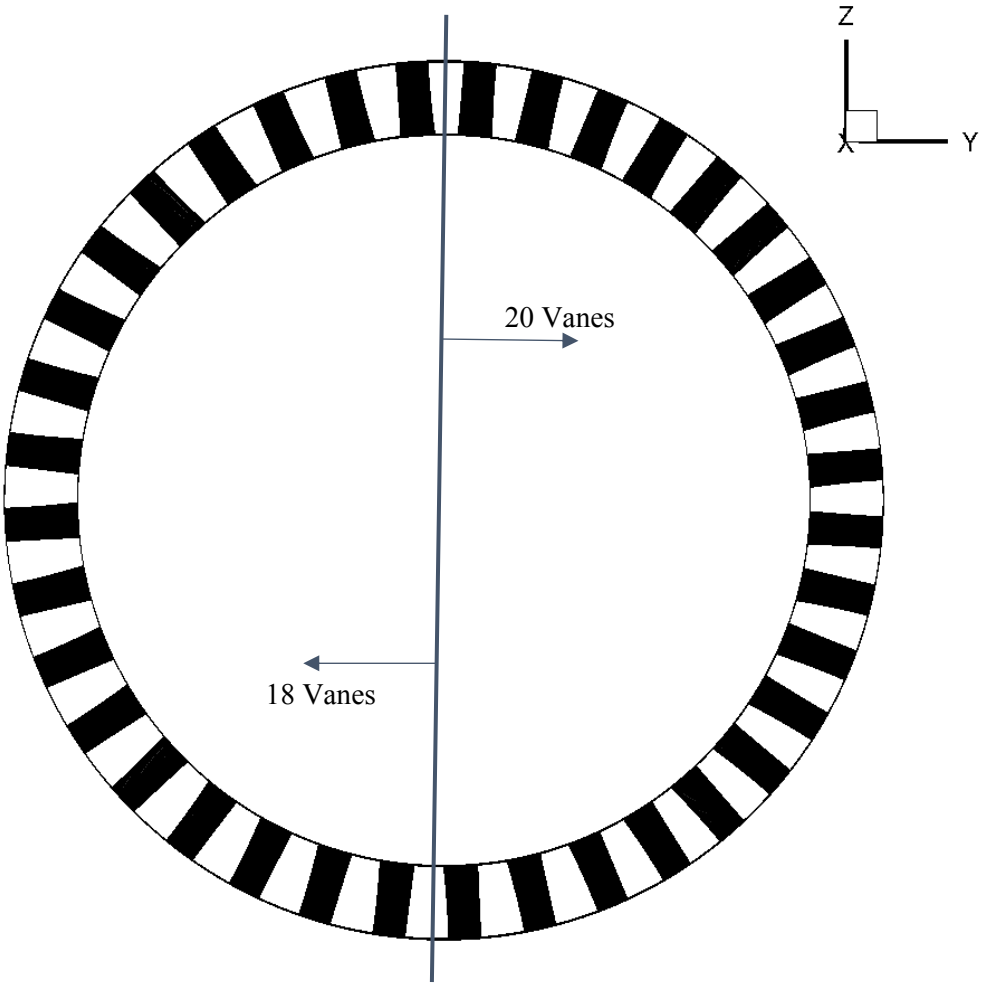

Figure 6:1: Asymmetric S1 geometry.

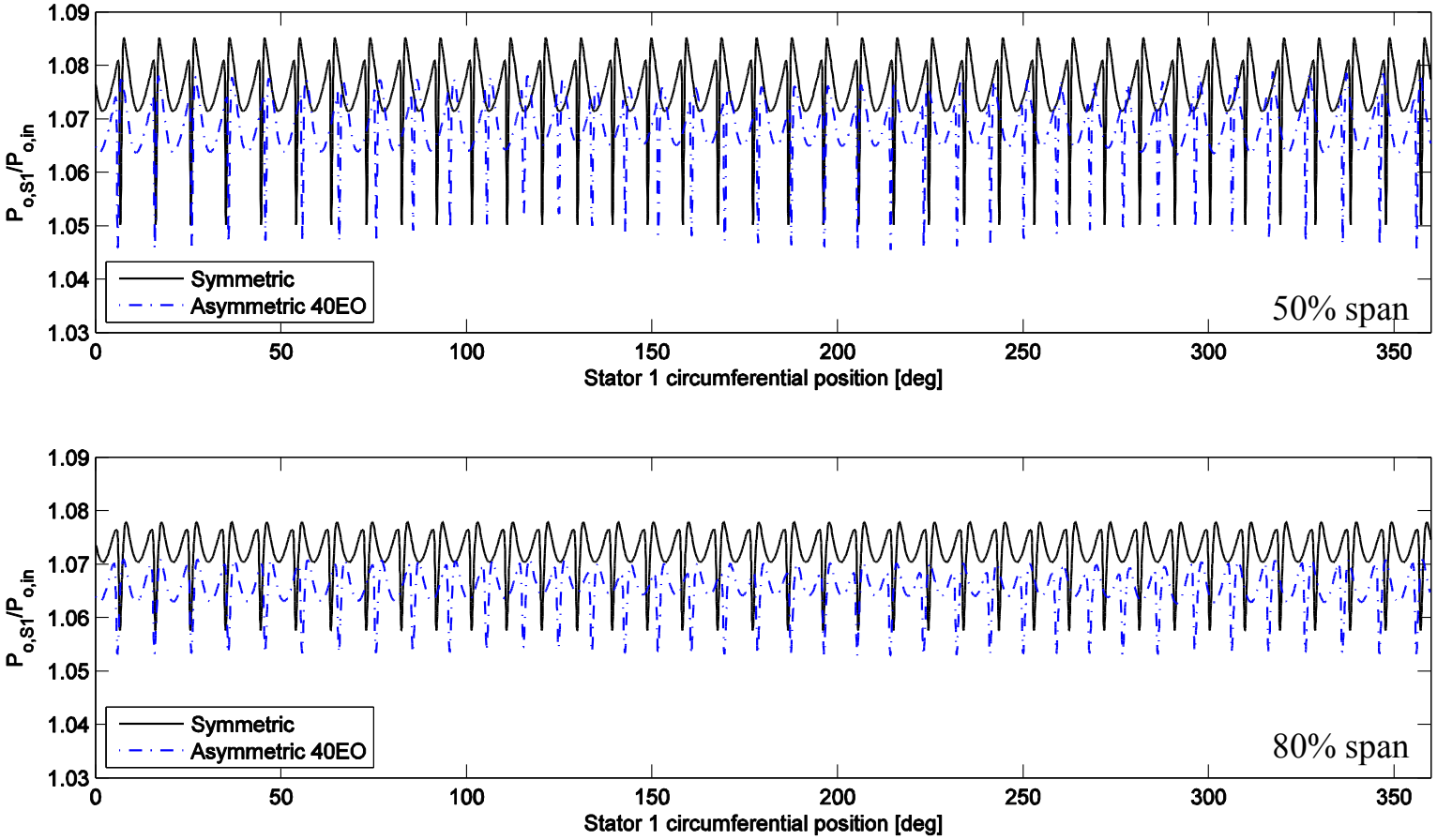

Figure 6:2: Total pressure wake profile comparison: midspan (top), 80% span (bottom).

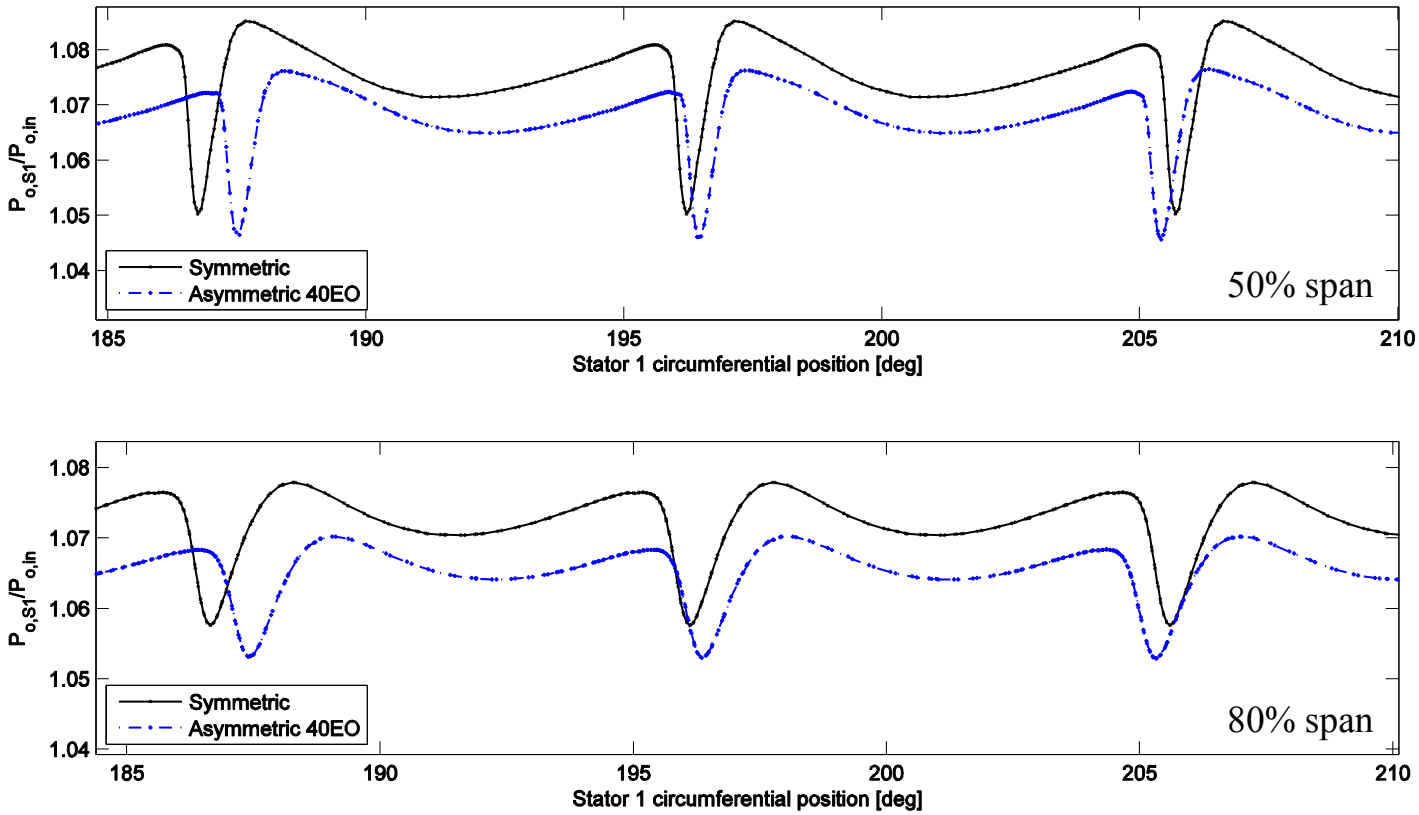

Figure 6:3: Zoomed in view of multiple stator passage total pressure wakes: midspan (top) 80% span (bottom).

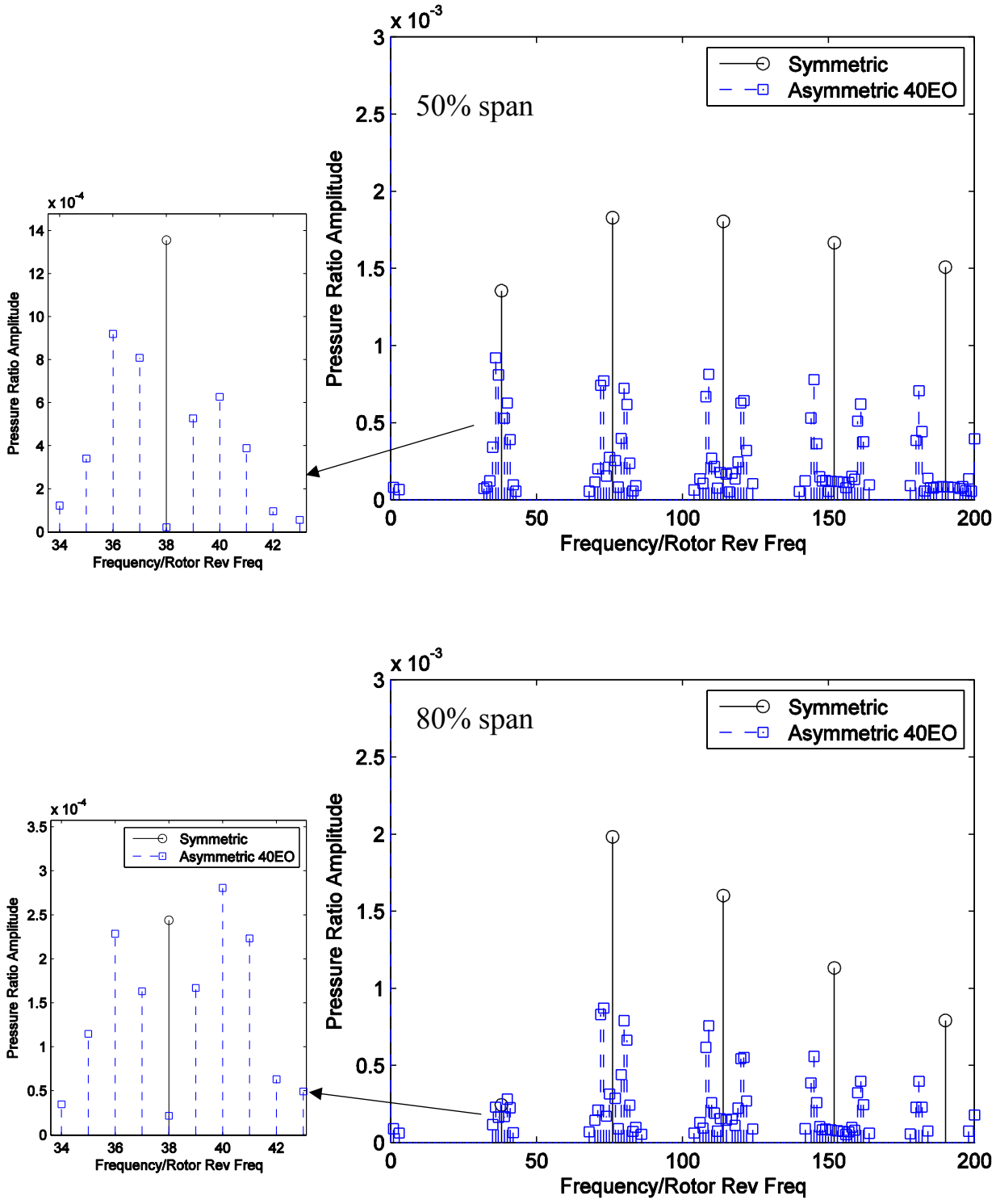

Figure 6:4: Frequency spectrum comparison of total pressure wakes: midspan (top), 80% span (bottom).

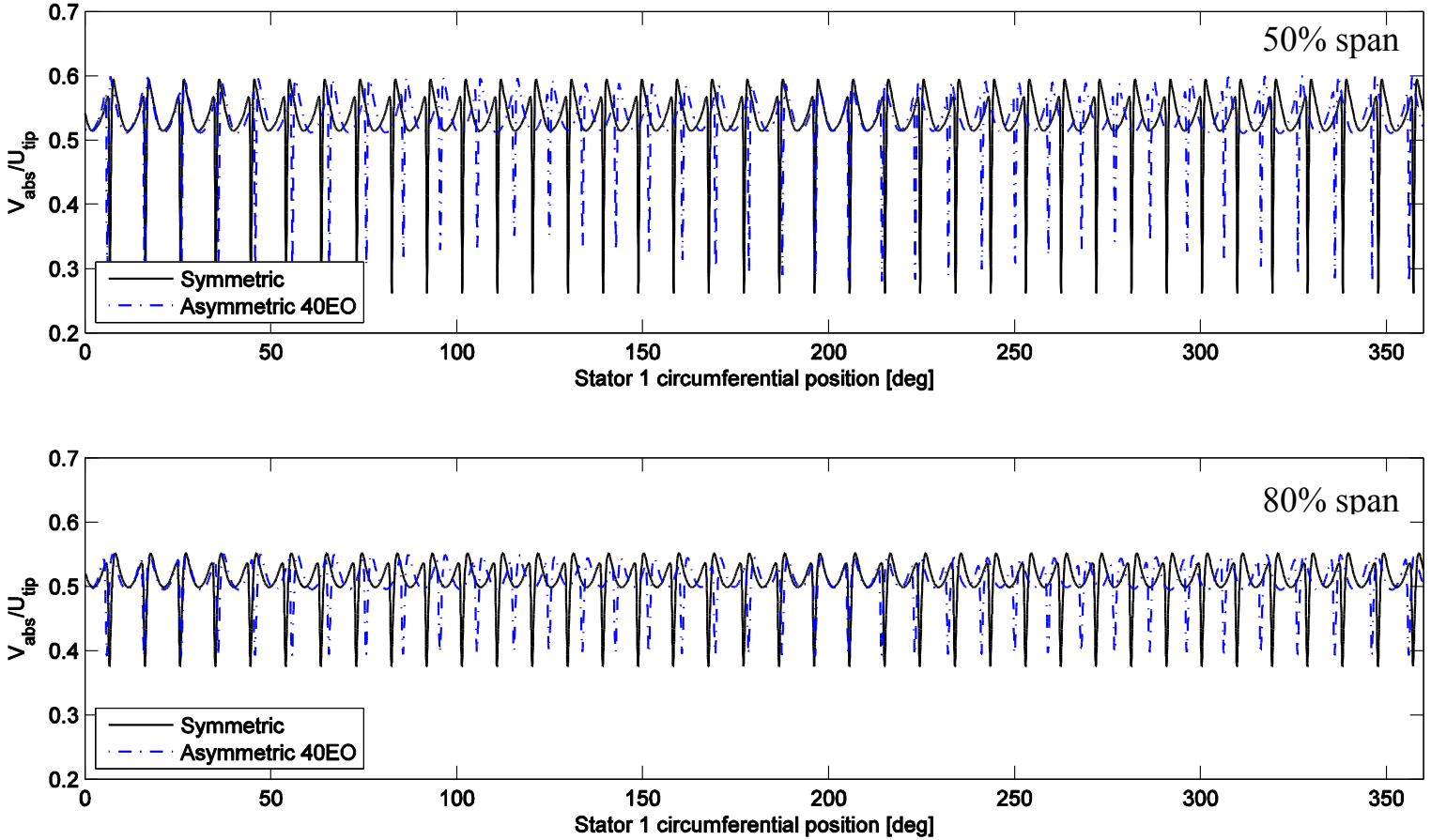

Figure 6:5: Full annulus total velocity wake structure: midspan (top), 80% span (bottom).

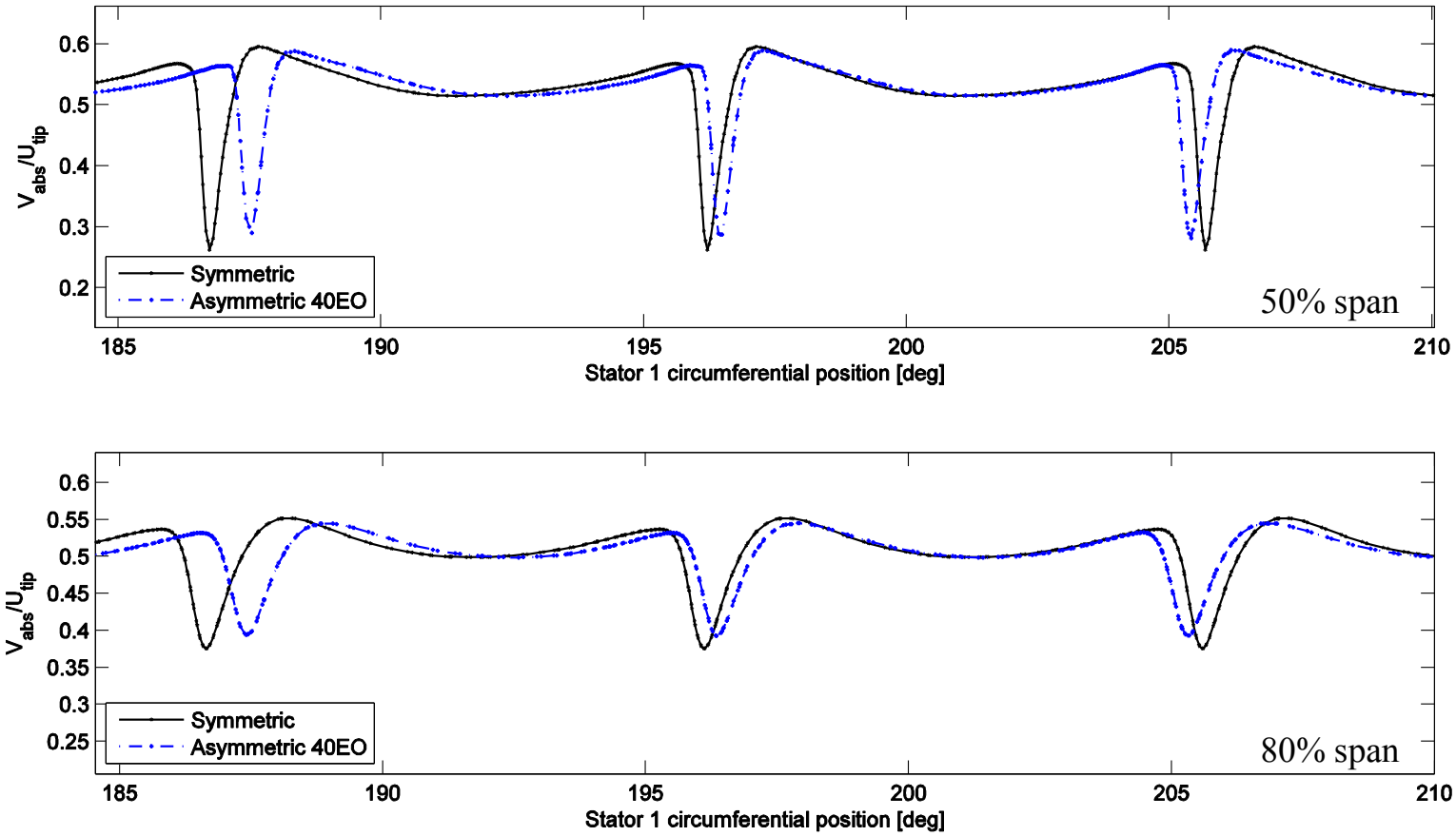

Figure 6:6: Zoomed in view of multiple stator passage absolute velocity wakes: midspan (top) 80% span (bottom).

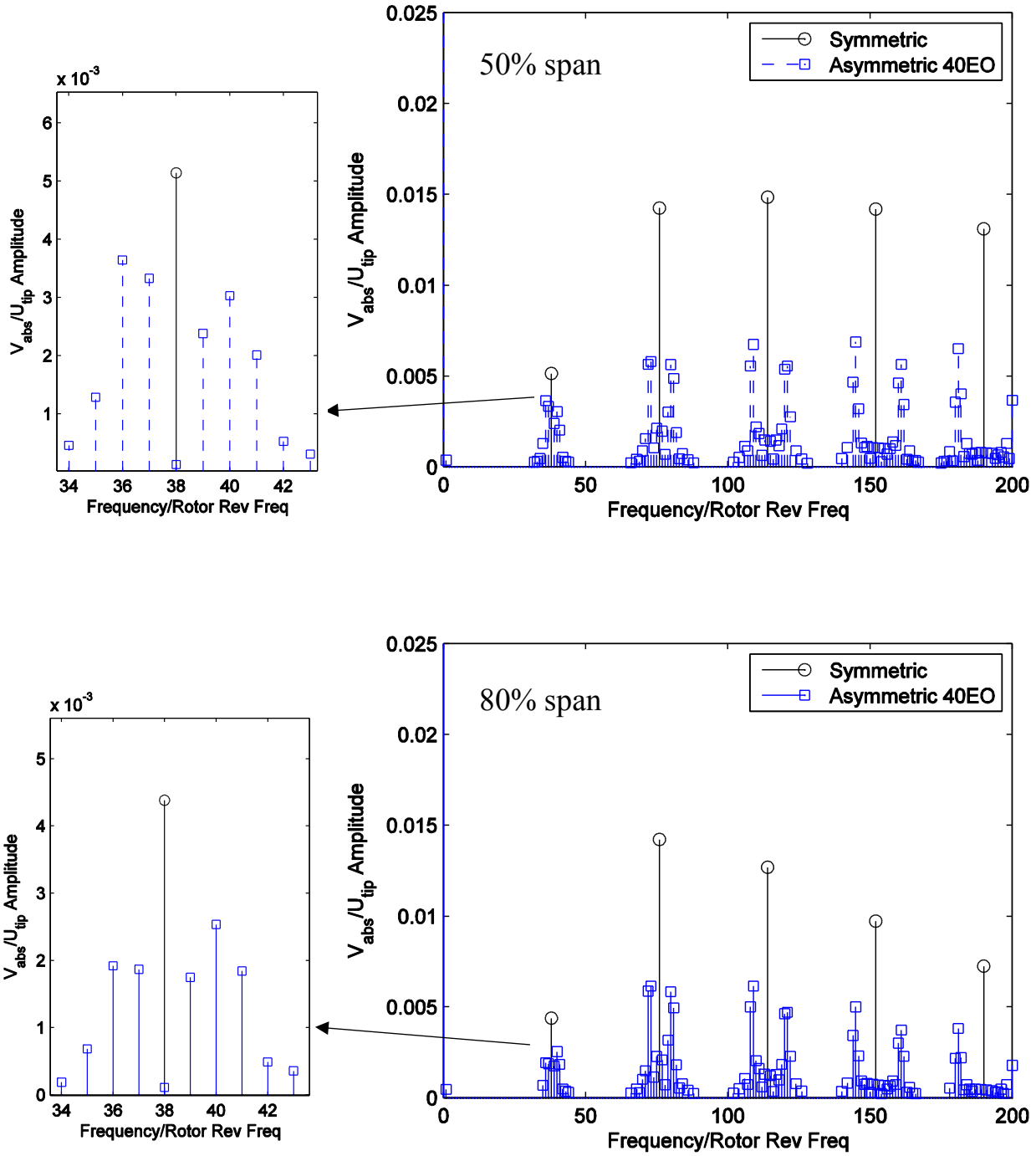

Figure 6:7: Frequency spectrum comparison of absolute velocity wakes: midspan (top), 80% span (bottom).

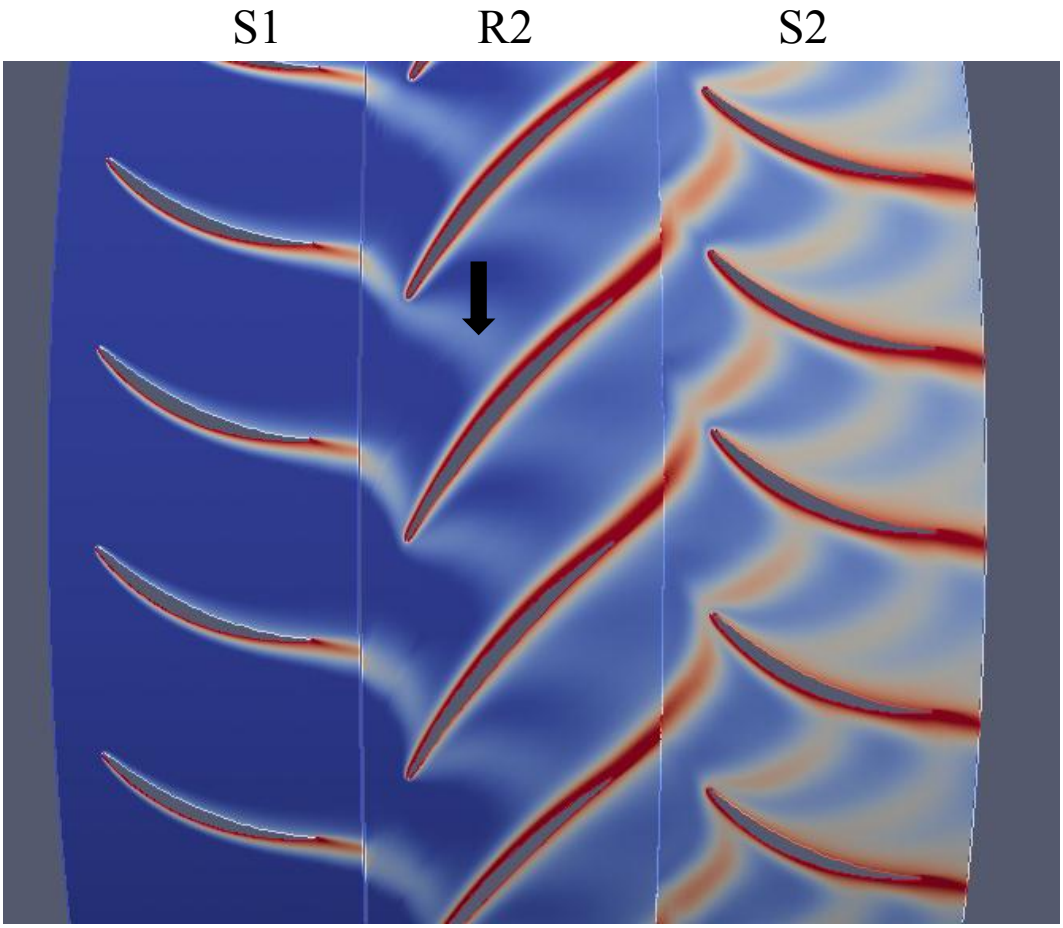

Figure 6:8: Instantaneous entropy contours for asymmetric S1 geometry at 80% span.

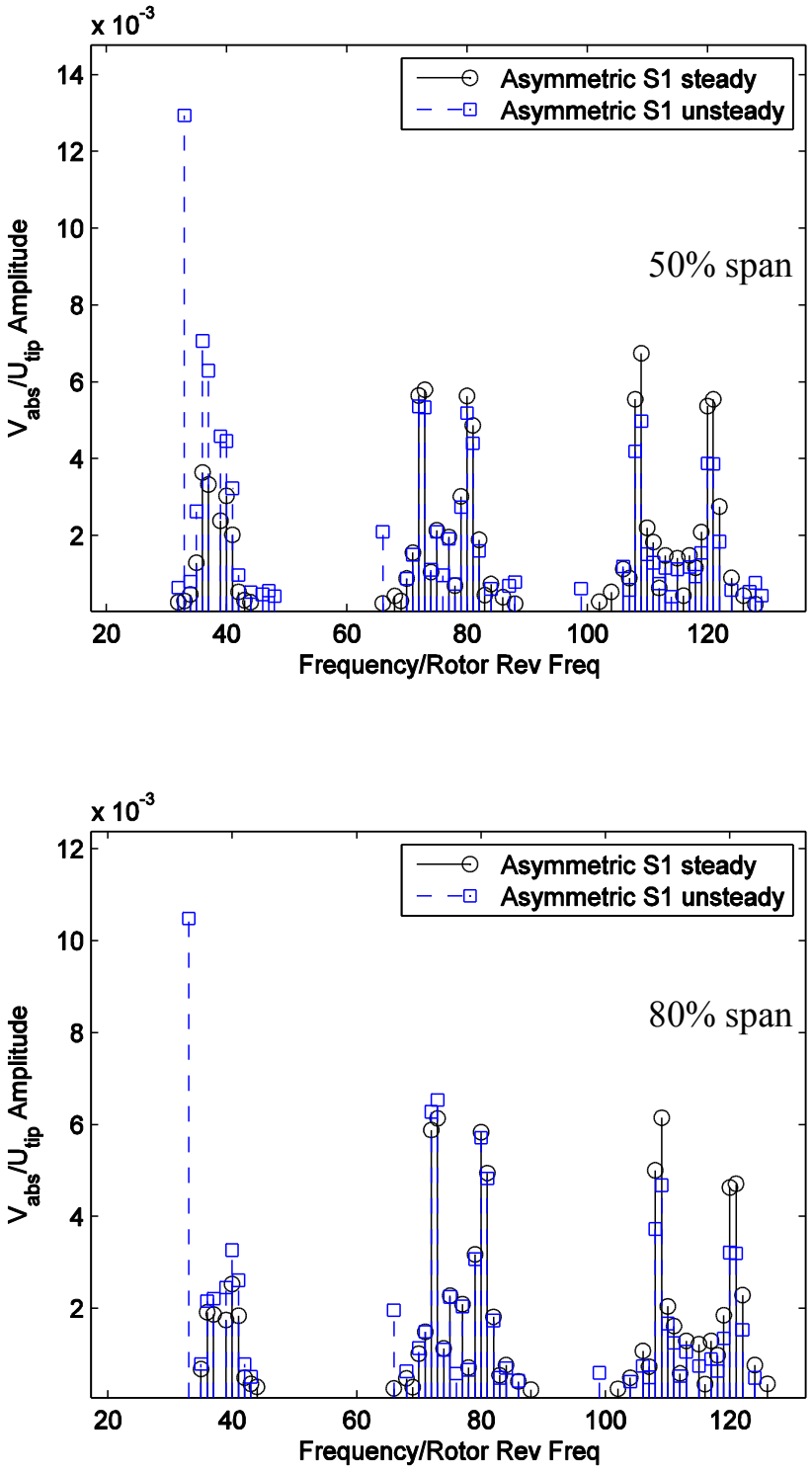

Figure 6:9: Comparison of steady and unsteady absolute velocity wakes: midspan (top), 80% span (bottom).

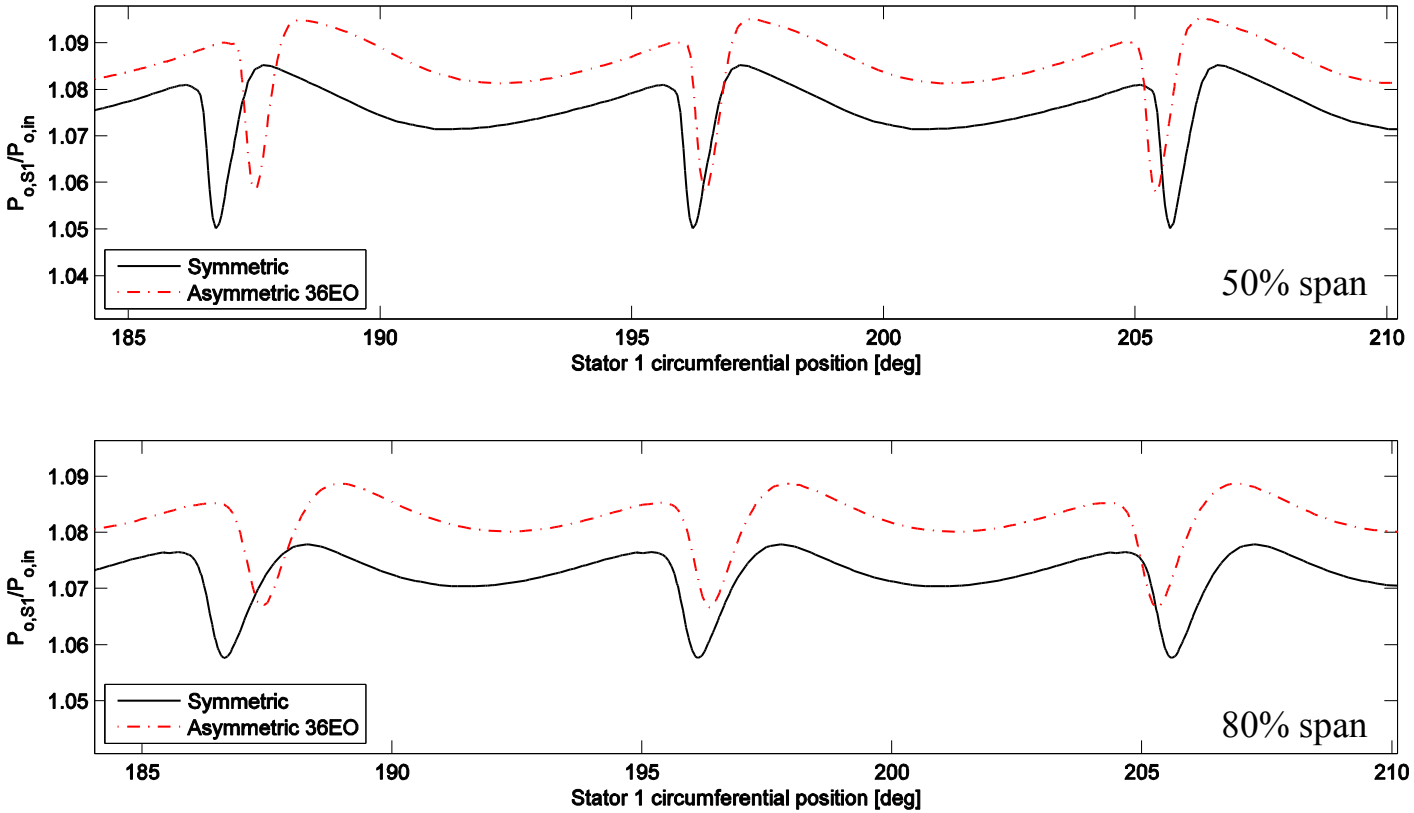

Figure 6:10: Zoomed in view of multiple stator passage total pressure wakes: midspan (top) 80% span (bottom).

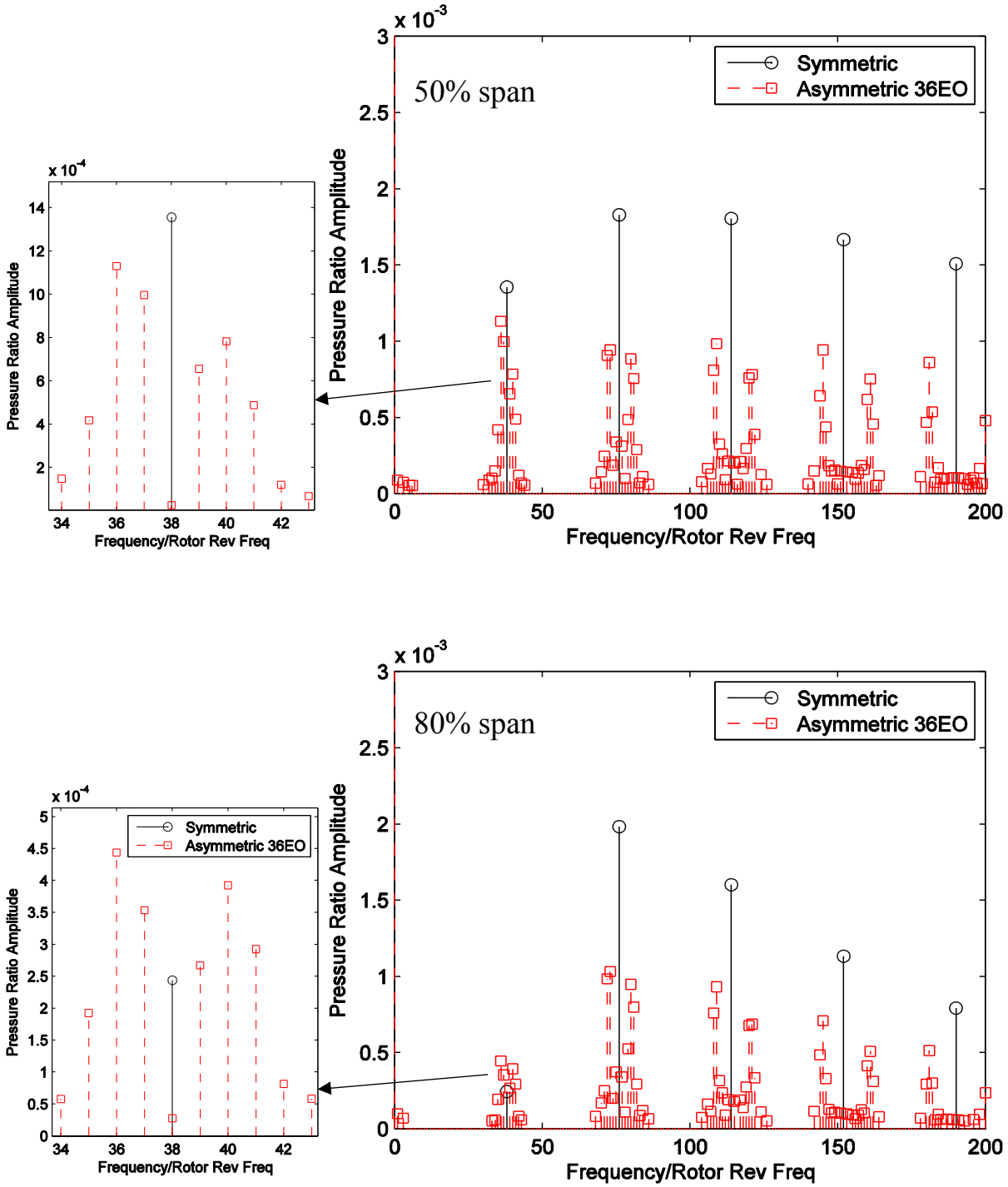

Figure 6:11: Frequency spectrum comparison of total pressure wakes: midspan (top), 80% span (bottom).

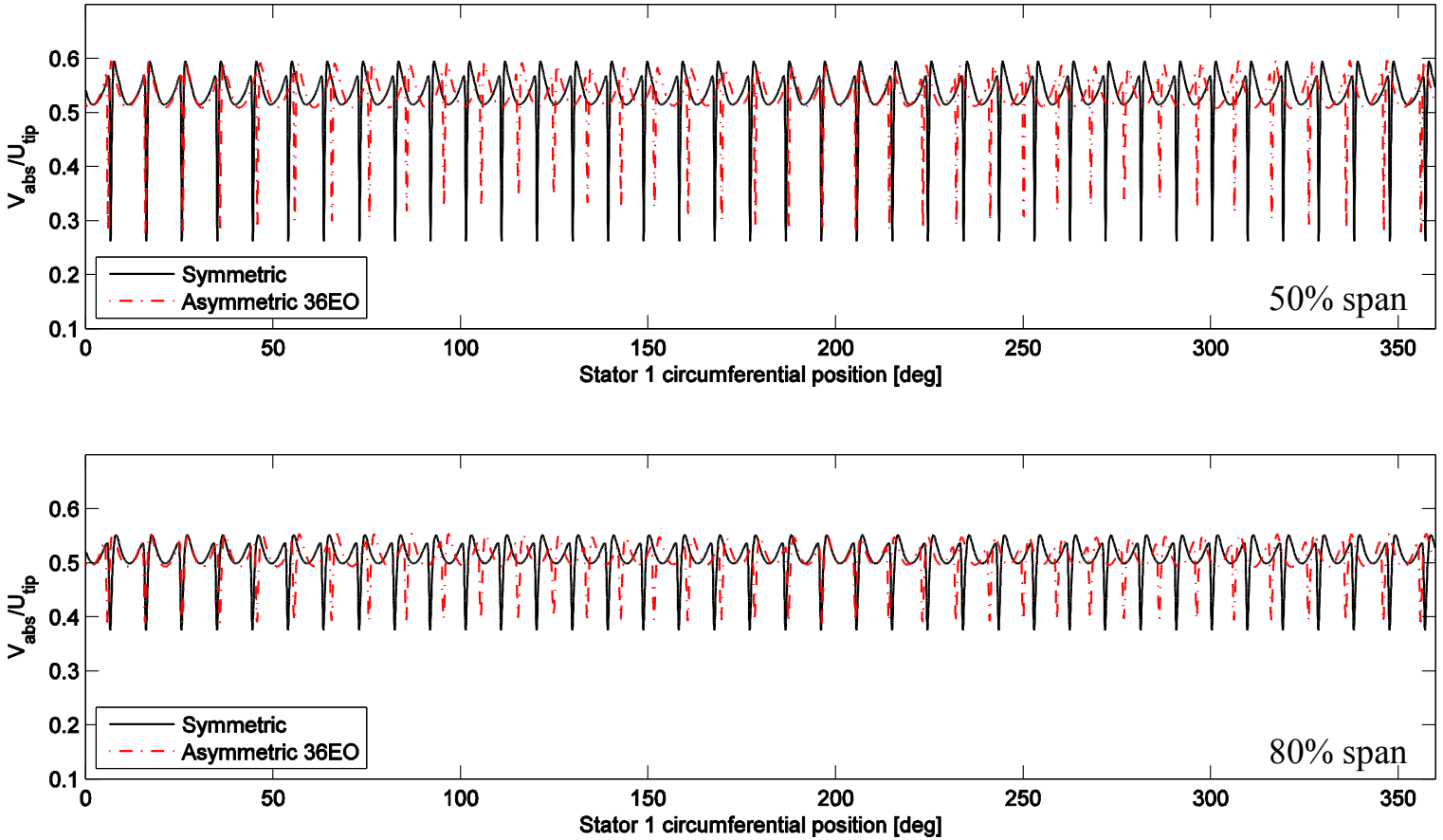

Figure 6:12: Full annulus total velocity wake structure: midspan (top), 80% span (bottom).

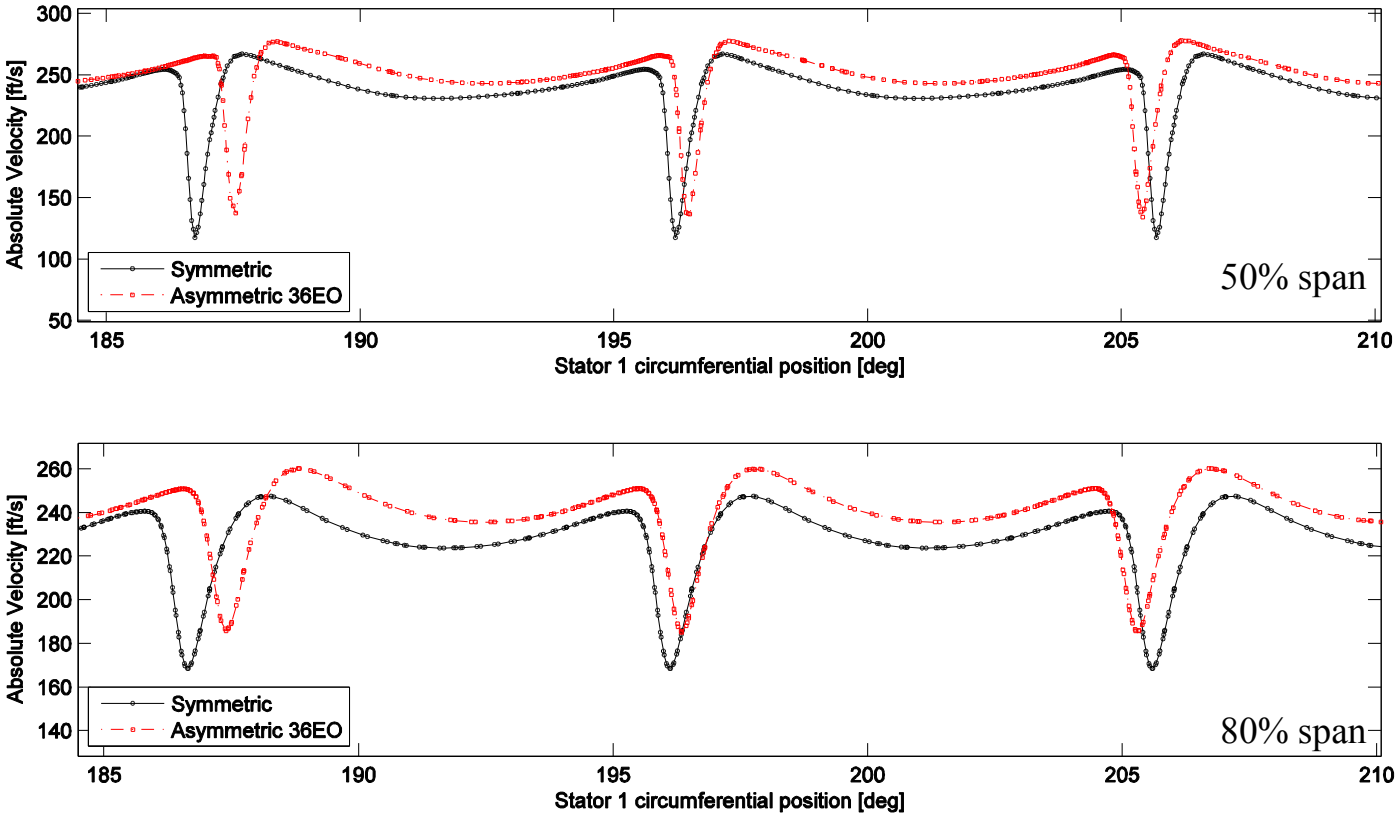

Figure 6:13: Zoomed in view of multiple stator passage absolute velocity wakes: midspan (top) 80% span (bottom).

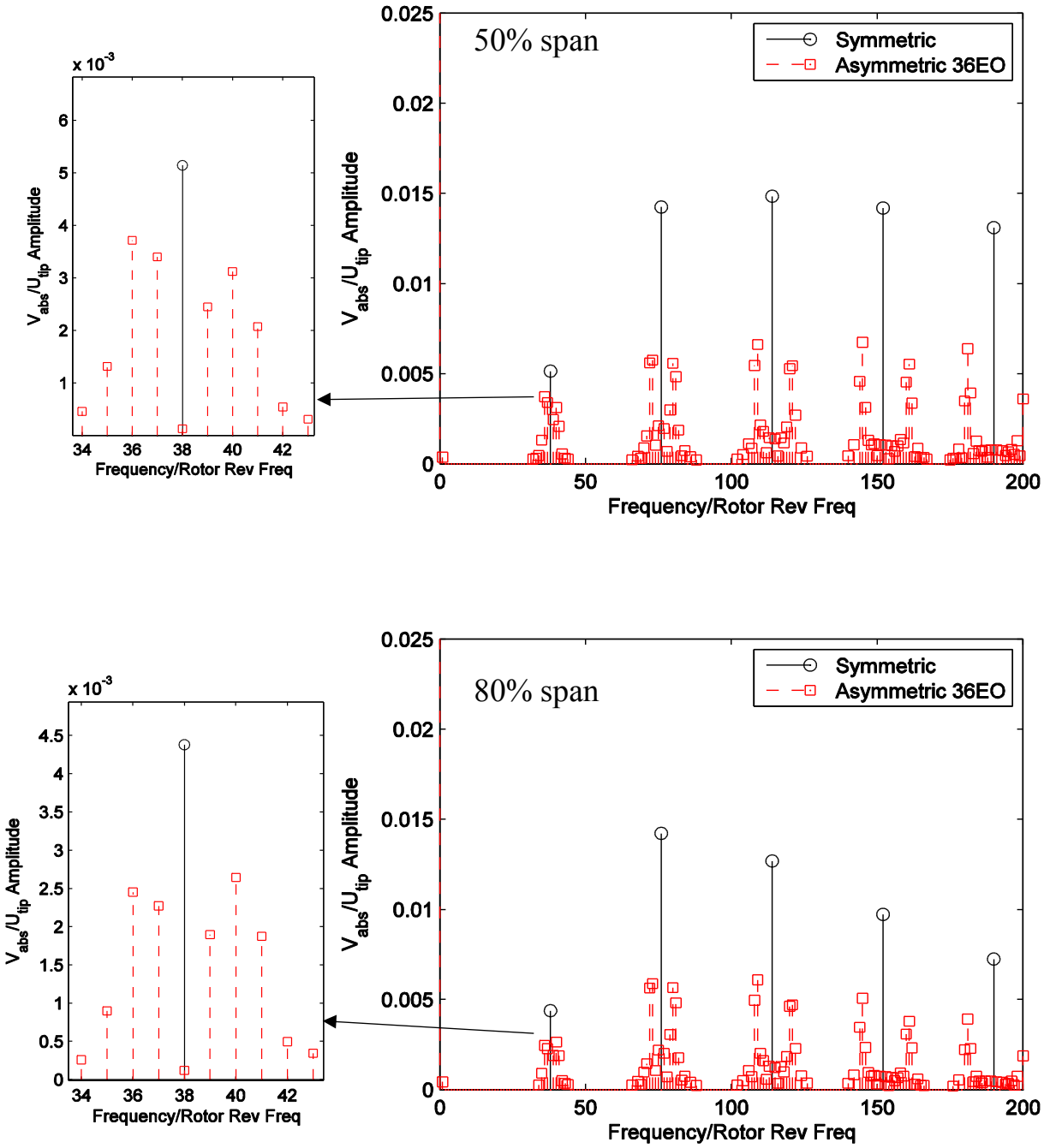

Figure 6:14: Frequency spectrum comparison of absolute velocity wakes: midspan (top), 80% span (bottom).

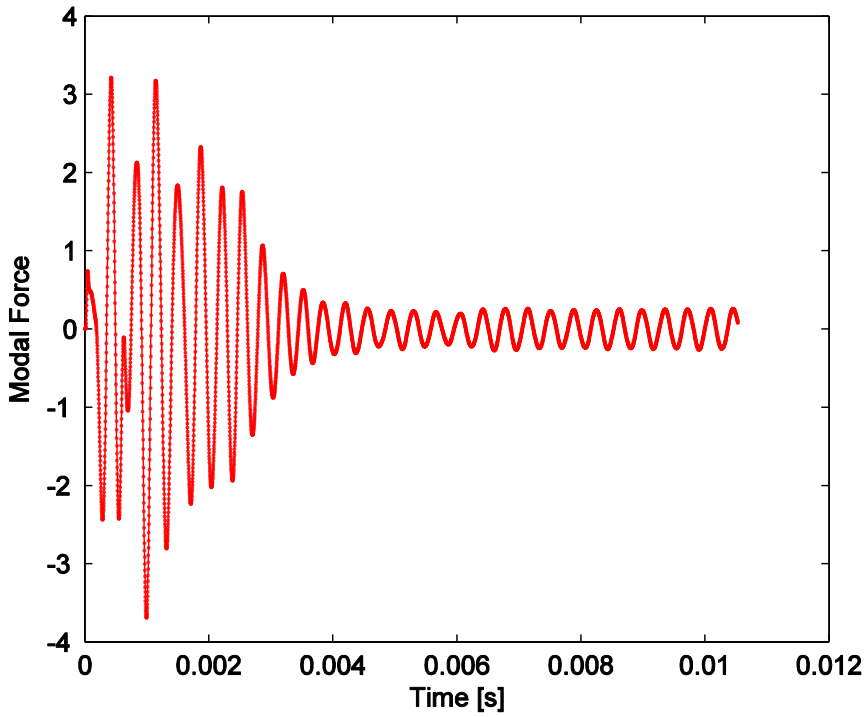

Figure 6:15: R2 mode force time history for symmetric 38-vane S1 configuration.

CHAPTER 7: SUMMARY AND CONCLUSIONS

The work contained in this thesis has focused on the computational modeling of the aerodynamic and aeromechanical behavior of the Purdue multistage compressor. As current trends continue to push compressor performance limits, the ability for CFD to accurately predict aerodynamic and aeromechanical behavior is vital. Confidence in such predictions increase through validation with experimental data. Fortunately, the multistage axial compressor at Purdue University has accumulated an expansive data set detailing the flow physics as well as the structural and vibrational characteristics.

Accurate modeling of the compressor flow physics highly depends on the ability to capture mixing and losses associated with viscous phenomena such as boundary layers and wakes, as well as secondary flow interactions. The bulk flow inside of the compressor – the inviscid flow, is well understood and reasonably simple to model and predict. It is the viscous and secondary flow structures that require excessive mesh resolution and computing time. To fully resolve these fluid regions, mesh scales must be smaller than the fluid length scales associated with such turbulent fluid behavior. Therefore, designers most often compromise between high mesh resolution and reasonable simulation run times. Continued advances in computing power have decreased the size of this gap and led to the development of CFD codes with improved performance capability. The bulk of this work utilized modern CFD codes to model the aerodynamic and aeromechanical behavior of the Purdue multistage compressor, and complements existing experimental data. Additional work was performed in analyzing a novel concept for reducing forced response vibrations in modern core compressors.

7.1 Aerodynamic Analysis

The aerodynamic analysis of the Purdue multistage compressor was computed using *JACC*, an in-house CFD code maintained by Rolls-Royce. The inlet total pressure and total temperature profiles used in the simulations were modified such that the predicted radial profiles matched experimentally measured profiles at the IGV leading edge. Overall performance of the compressor was predicted very well in the computational model. *JACC* computed the compressor mass flow rate 1-2% higher than experimental measurements for comparable loading conditions. However, the shape of the compressor characteristic matched closely the experimentally measured characteristic. Looking more closely at the individual stage characteristics, *JACC* predictions differ most greatly at high loadings. Actual measurements in the Purdue compressor show Stage 1 as the weakest stage - the stage that first encounters performance deterioration as the compressor is throttled. The computational model predicts Stage 3 as the weak stage, with performance deterioration occurring at the final two loading conditions. Stage 2 has the best overall agreement with the predicted stage performance closely following the measured performance.

Individual bladerow performance was more accurately predicted in the rotors than in the stators. Total pressure profile comparisons for the rotors showed that *JACC* predictions matched experimental profile shapes very well, with minor exceptions in the tip regions. Experimental measurements show the total pressure profiles begin to fall over, or decrease in pressure rise above roughly 80% span. Computational results show no performance deterioration until 90% span or above. However, the predicted rotor performance for the majority of the span follows very closely the measured performance. Stator performance was not predicted as closely. The computational results show significant losses in the hub regions of the stators at Peak Efficiency Loading and High Loading, with increasing pressure loss at each subsequent stator. Experimental

measurements show the opposite trend, significant pressure losses in the tip regions with very strong hub performance.

Observing stator surface streamlines from CFD results helps identify the cause of this discrepancy. The computational model shows large separations occurring in the hub regions on the stator vanes, especially at Peak Efficiency and High Loading. The separated region is typically smallest in S1 and increases in size for S2 and S3. Flow visualization experiments in the Purdue compressor allow a similar analysis of the actual flow physics. These images show large separations initiating in the tip region of S1 and increasing in size through the compressor. High predicted stator cavity leakage rates contribute to the size and magnitude of the predicted stator hub separations. It is believed, however, that the primary cause for the discrepancy in stator aerodynamic behavior is *JACC* not fully capturing the losses and blockage associated rotor tip leakage vortex structures. The predicted increase in blockage in the rotor tip sections does not increase significantly between PE and HL conditions. Tip leakage vortex structures commonly grow in size and strength as stall conditions are approached and increase blockage in the tip region. Increased tip blockage and losses in the computer model would generate larger stator tip separations and force more flow down to the hub region, alleviating to a degree the large separation present in this region. *JACC* predicts the overall aerodynamic behavior of the Purdue compressor well.

7.2 Forced Response Analysis

The aeromechanical behavior of the embedded rotor in the Purdue compressor was analyzed by utilizing an advanced aeroelastic CFD code. This code performs both steady single-passage, multi-bladerow simulations and unsteady full-annulus, multi-bladerow simulations. The first was used initially to define the flow field at the R2 1T resonance operating conditions and

then the steady-state results interpolated onto inlet and exit surfaces as boundary conditions for the full-annulus S1-R2-S2 unsteady simulations. Both the S1 exit wake profiles and the S2 potential field profiles were analyzed for the Baseline 44-vane S1 configuration and compared to experimental measurements previously acquired in the compressor. Computed wake profiles measured between S1 and R2 tended to predict a slightly deeper and narrower midspan wake than measured wake profiles. At 80% span the CFD code predicted slightly larger separations which led to increased wake dissipation and moderately wider and shallower wake profiles. The midspan wakes had a much closer agreement to measured profiles than at 80% span. These differences were not significant as the computed frequency spectrum of the wake profiles agreed reasonably well to measured values.

The strength of the potential field propagating from S2 was also investigated. The computed static pressure field at the compressor casing mid-gap between R2 and S2 indicated a much stronger potential field than experimentally measured. However, comparisons of the absolute flow angle at midspan and 80% span at this same axial location matched much better. The predicted difference between minimum and maximum flow angles as a results of the potential field matched to within a single degree, and were identical at midspan in the NL case. The results of these predictions led to the calculation of R2 vibrational amplitudes at the NL and HL operational conditions. Predicted blade displacements matched well to measured displacements. At NL the aeroelastic code predicted a maximum 11ND peak-to-peak displacement of 2.051 mils, compared to a measured value of 1.82 mils, a different of only 0.23 mils. At HL, the predicted maximum peak-to-peak vibrations at the 11ND response was found to be 3.315 mils, compared to a measured deflection of 4.094 mils, a difference of only 0.78 mils. Thus, the aeroelastic code used was found to give valid predictions for vibrational responses at the R2 1T mode in the Purdue compressor.

7.3 Effect of Stator 1 Asymmetry on Rotor 2 Forced Response

With confidence in the predictive capability of the aeroelastic CFD code, a study was performed on the effect of introducing asymmetries in S1 as a means of reducing the forced response in R2. The asymmetric concept analyzed investigated the effect of stator halves with unequal vane counts. A new 38-vane S1 was designed with symmetrically spaced stator vanes to act as a baseline. Then, an additional stator was designed in which the 38 vanes were distributed unequally such that 18 vanes were placed on one half-sector and 20 vanes on the other half-sector. Such an asymmetric geometry modifies the vortical structures which excite vibrations in R2. Analysis of this asymmetric geometry showed that the frequency content of the wakes shifted energy out of the 38/rev principal harmonic of the symmetric geometry and into 36/rev and 40/rev frequency components. This decomposition of the symmetric S1 harmonics created two additional excitation lines on the R2 Campbell Diagram of 36EO and 40EO and created two new resonant operating speeds. Unsteady CFD simulations were then run at the 38EO 1T crossing for the symmetric S1 and at 36EO and 40EO crossings for the asymmetric S1 configuration. The frequency spectrum of both the total pressure and absolute velocity wake profiles demonstrated that the shifting of energy to the 36/rev and 40/rev frequency components reduced the amplitudes of the vortical disturbances. Vortical forcing amplitudes were reduced 15%-40% on average. Amplitude increases were observed for the 36/rev component of the total pressure wakes at 80% span, but the symmetric S1 wake amplitude was already small enough that the slight increase would have negligible effects on the resonant response.

R2 peak-to-peak vibrational responses decreased in all cases as a result of the S1 asymmetry. At the 40EO excitation crossing of the R2 1T mode, a 48.6% and 51% decrease in maximum blade displacements was predicted for the 7ND and 3ND disk excitations, respectively.

At the 36EO excitation crossing, a 31% peak-to-peak vibrational amplitude was predicted at both nodal diameter excitations.

7.4 Suggested Future Research

The most notable discrepancy between *JACC* aerodynamic performance predictions and experimentally measured data in the Purdue compressor was the location of large separations. It is believed that *JACC* predicts large separations in the stator hub region in large part because significant losses associated with the rotor tip leakage vortex are not being fully captured. It is recommended to investigate this further. Modifying the mesh to include more points in the tip gap, or switching to more complex turbulence models are a few paths that could lead to more accurate predictions of the separation behavior in the compressor. A more accurate prediction of the stator separations would improve the overall model and would likely lead to very accurate performance predictions.

The predicted reduction in R2 forced response due to S1 asymmetry was very significant at the 1T mode crossings. Amplitude reductions of 30% and 50% were found at the 36EO and 40EO crossing speeds. The analysis of the vortical wake structures showed that the asymmetry has even larger forcing function reductions in the higher harmonics. If such large vibrational reductions occurred at the 1st harmonic, which had smaller vortical forcing reductions, it would be very interesting to investigate the vibrational reductions at higher harmonics. Additionally, it is recommended to investigate the reduction in forced response for the higher-order modes such as 1st and 2nd chord-wise bending modes. The results presented in this work would suggest that the vibrational reduction would be even more significant than the 30%-50% found at the 1T mode.

LIST OF REFERENCES

LIST OF REFERENCES

Adamczyk, J.J., 1999: Aerodynamic Analysis of Multistage Turbomachinery Flows in Support of Aerodynamic Design, Freeman Scholar Lecture.

Adamcyzk, J. J., 1985, “Model Equation for Simulating Flows in Multistage Turbomachines”, ASME Paper No. 85-GT-226.

Adamczyk, J. J., Celestina, M. L., Beach, T. A., and Barnett, M., 1990, "Simulation of Three-Dimensional Viscous Flow Within a Multistage Turbine," *Journal of Turbomachinery*, Vol. 112, pp. 370-376.

Adamczyk, J. J., Celestina, M. L., and Greitzer, E. M., “The Role of Tip Clearance in High-Speed Fan Stall,” *Journal of Turbomachinery*, Vol. 115, 1993, pp 28-38.

Baldwin, B.S. and T.J. Barth, 1990, “A one-equation turbulence transport model for high Reynolds number wall-bounded flows”. TM 102847, NASA

Baldwin, B.S. and H. Lomax, 1978: Thin-layer approximation and algebraic model for separated turbulent flows. Paper 78-257, AIAA

Ball, P. R., 2013, “An Experimental and Computational Investigation on the Effects of Stator Leakage Flow on Compressor Performance”, Master’s Thesis, Purdue University, West Lafayette, IN

Brossman, J.R., Ball, P.R., Smith, N.R., Methel, J.C., Key, N.L., 2014, "Sensitivity of Multistage Compressor Performance to Inlet Boundary Conditions," *AIAA Journal of Propulsion and Power*, 30(2), pp.407-415.

Chen, S.H. and Eastland, A.H., 1990, “Forced Response on Turbomachinery Blades due to Passing Wakes,” AIAA-90-42781, 1-11.

Chima, R. V., 1998, “Calculation of Tip Clearance Effects in a Transonic Compressor Rotor”, *Journal of Turbomachinery*, Vol. 120, pp. 131-140

Choi, Y.S., Key, N.L., and Fleeter, S., 2008, “Vane Clocking Effects on the Resonant Response of an Embedded Rotor,” Presented at the 44th AIAA/ASME/SAE/ASEE Joint Propulsion Conference, AIAA-2008-4793.

Cumpsty, N., 2004, Compressor Aerodynamics, Krieger Publishing Company, Malabar, Fl.

Dawes, W. N., 1985, "A Pre-processed Implicit Algorithm for 3D Viscous Compressible Flow," in: 6th GAMM Conference on Numerical Methods in Fluid Mechanics, Gottingen, DFVLR, Sept.

Denton, J. D., 2010, “Some Limitations of Turbomachinery CFD”, Proceedings of ASME Turbo Expo 2010, June 14-18, Glasgow, UK, GT2010.

El-Aini, Y., deLaneuville, R., Stoner, A., and Capece, V., 1997. “High Cycle Fatigue of Turbomachinery Components – Industry Perspective”. AIAA Paper No. 97-3365, July, 33rd AIAA/ASME/SAE/ASEE Joint Propulsion Conference.

Freeman, C., 1985, “Tip clearance effects in axial turbomachines”, VKI Lecture Series 1985-05

Gorrell, S.E., Car, D., Puterbaugh, S.L., Estevadeordal, J., Okiishi, T.H., “An Investigation of Wake-Shock Interactions in a Transonic Compressor with DPIV and Time-Accurate CFD” Proceedings of ASME Turbo Expo 2005, June 6-9, Reno, NV GT2005-69107

Griffin, L. W., and Dorney, D. J., 2000, “Simulations of the Unsteady Flow Through the Fastrac Supersonic Turbine”, Journal of Turbomachinery, April, Vol. 122, pp. 225-233

Hall, E.J., Hidegger, N.J., and R.A. Delaney, “JACC v1.0: User’s Manual”, NASA-CR- 1999-206600, 1999.

King, A. J., 2013, Personal communication Rolls-Royce compressor aerodynamicist.

Mansour, M. L., Gunaraj, J., and Goswami, S., “Validation of Steady Average-Passage and Mixing Plane CFD Approaches for the Performance Prediction of Modern Gas Turbine Multistage Axial Compressor”, Proceedings of ASME Turbo Expo 2008, June 9-13, Berlin, Germany, GT2008-50653.

Mazur, Z., García-Illescas, R., and , Porcayo-Calderón, J., 2008, “Last Stage Blades Failure of a 28MW Geothermal Turbine”. *Engineering Failure Analysis*. August, pp 1120-1032.

Miller, R.J., Moss, R.W., Ainsworth, R.W., and Harvey, N.W., 2003,"Wake, Shock, and Potential Field Interactions in a 1.5 Stage Turbine-Part 1: Vane-Rotor and Rotor-Vane Interaction," ASME Journal of Turbomachinery, 125, 33-39.

Mulac, R.A., 1988, "A multistage mesh generator for solving the average-passage equation system", NASA-CR-179539.

Murray, W. L., and Key, N. L., 2014 (a), "Experimental Investigation of a Forced Response Condition in a Multistage Compressor". Proceedings of AIAA Joint Propulsion Conference, July 28-30, Clevelend, OH AIAA-2014-3735

Murray, W. L., and Key, N. L., 2014 (b), "Detection of Rotor Forced Response Vibrations Using Stationary Pressure Transducers in a Multistage Axial Compressor". *International Journal of Rotating Machinery*, Accepted for publication Nov., 2014.

Pope, S. B., 2000, Turbulent Flows, Cambridge University Press, New Delhi, India

Pullan, G., Young, A., Day, I., Greitzer, E., and Spakovszky, Z, "Origins and Structure of Spike-Type Rotating Stall", ASME IGTI Turbo Expo, Copenhaven, Denmark, 2012; GT2012-68707.

Rai, M. M., 1989, "Three-Dimensional Navier-Stokes Simulations of Turbine Rotor-Stator Interaction: Part 1—Methodology," Journal of Propulsion, Vol. 5, No. 3, p. 305.

Richards, S. K., Ramakrishnan, K., Shieh, C., 2012. "Unsteady Acoustic Forcing on an Impeller Due to Coupled Blade Row Interactions," ASME Journal of Turbomachinery, 134, 061014-1 – 061014-9.

Sayma, A.I., Vahdati, M., Sbardella, L., and Imregun, M., 2000, "Modeling of Three-Dimensional Viscous Compressible Turbomachinery Flows Using Unstructured Hybrid Grids", AIAA Journal, Vol. 38, No. 6, June, pp. 945-954

Sayma, A.I., Vahdati, S., Lee, J., and Imregun, M., 2003, "Forced Response Analysis of a Shaft-Driven Lift Fan", J. of Mechanical Engineering Science, Vol. 217 part C.

Smith, N. R., and Key, N. L., 2014, "Utilization of Flow Visualization in a Multistage Compressor", International Journal of Rotating Machinery.

Spalart, P.R. and S.R. Allmaras, 1994, "A one-equation turbulence model for aerodynamic flows. Recherche Aérospatiale 1, 5-21.

Talalayev, A., 2011, On the Renovation of the Three-Stage Axial Compressor Research Facility for Compressor Performance Research, Master's Thesis, Purdue University, West Lafayette, IN.

Tipton, D.L., Scott, T.E., and Vogel, R.E., 1986, "Labyrinth Seal Analysis. Vol. III – Analytical and Experimental Development of a Design Model for Labyrinth Seals", Allison Gas Turbine, Division of General Motors Corporation, Indianapolis, IN, Jan. (also AFWAL-TR-85-2103 Volume IV)

Tucker, P.G., 2011, "Computation of Unsteady Turbomachinery Flows: Part1 – Progress and Challenges", Progress in Aerospace Sciences, Oct., Vol. 47, Issue 7, pgs. 522-545.

Wellborn, S.R., and T.H. Okiishi, 1999, "The Influence of Shrouded Stator Cavity Flows on Multistage Compressor Performance", *Journal of Turbomachinery*, July, Vol. 121 Pgs. 486-497

Wellborn, S.R., and T.H. Okiishi, 1996, "Effects of Shrouded Stator Cavity Flow on Multistage Axial Compressor Aerodynamic Performance", NASA Contractor Report 198536

Wellborn, S. R., Tolchinsky, I., and Okiishi, T. H., 2000, "Modeling Shrouded Stator Cavity Flows in Axial-Flow Compressors", *Journal of Turbomachinery*, Jan.Vol. 122, pp 55-61.

Wisler, D.C, 1985, "Aerodynamic Effects of Tip Clearance, Shrouds, Leakage Flow, Casing Treatment and Trenching in Compressor Design Blading Design in the Endwall Region", VKI-Lecture series, 1985-05.

Wisler, D.C., 1985, "Loss reduction in axial-flow compressors through low-speed model testing." Trans. ASME Journal of Engineering for Gas Turbines and Power. 107, 354-363

Vahdati, M., and Imregun, M., 1996, "Modeling of Three-Dimensional Viscous Compressible Turbomachinery Flows Using Unstructured Hybrid Grids", Proceedings of the Institution of Mechanical Engineers, Part C: Journal of Mechanical Engineering Science, November, pp. 549-564.

Vahdati, M., Sayme, A.I., Imregun, M., and Simpson, G., 2007, "Multibladerow Forced Response Modeling in Axial-Flow Compressors", ASME J. of Turbomachinery, Vol. 129, pp 412-420.

Vahdati, M., Breard, C., Sayma, and A., Imregun, M., 2002, "An Integrated Time-Domain Aeroelasticity Model for the Prediction of Fan Forced Response due to Inlet Distortion", ASME J. Eng. Gas Turbine Power, Vol 124, pp 196-208

Vo, H., Tan, C., and Greitzer, E, 2008, “Criteria for Spike Initiated Rotating Stall”, Journal of Turbomachinery, Vol. 130, January 2008. [DOI: 10.1115/1.2750674]